HEAT TRANSFER AND FLUID FLOW ANALYSIS

OF HYDROGEN-COOLED PANELS

AND MANIFOLD SYSTEMS

By F. M. Walters and O. A. Buchmann

ABSTRACT

This report describes an analytical study of the performance of flat, hydrogen-cooled heat exchanger panels, as part of a comprehensive investigation of problems associated with design and fabrication of efficient regeneratively cooled structural panels. Heat exchangers were designed and performance was calculated for several panel concepts in a range of loads from 10 to 500 Btu/sec-ft^2 (114 to 5680 kW/m^2). Factors that influence heat exchanger and manifold system design, such as state of the art, materials, and fabrication techniques are set forth. Parametric data on the performance of a broad array of coolant passage geometries are presented. The potential for coolant conservation and reduction of temperature differentials by use of various methods of flow manifolding, flow folding, multiple stacking of heat exchangers, and insulation are discussed. Analytical and experimental studies of rectangular and triangular flat-manifold systems show the effects of geometry variation on pressure drop and panel flow distribution.

FOREWORD

This report was prepared by AiResearch Manufacturing Company, a division of The Garrett Corporation, Los Angeles, California, for the Langley Research Center of the National Aeronautics and Space Administration. Results of an analytical study performed under Task Order No. 2, Heat Transfer and Fluid Flow Analysis of Heat Exchanger Surfaces and Manifold Systems, are presented as part of a comprehensive analytical and experimental study of regeneratively cooled panels accomplished under Contract NAS 1-5002. This program was under the cognizance of Dr. M. S. Anderson and Mr. J. L. Shideler of the Aerothermoelasticity Section, and Mr. R. R. Howell and Mr. H. N. Kelly of the 8-Foot High-Temperature Structures Tunnel Branch of the Structures Division, Langley Research Center.

CONTENTS

CONTENTS (Continued)

HEAT TRANSFER AND FLUID FLOW ANALYSIS OF

HYDROGEN-COOLED PANELS AND MANIFOLD SYSTEMS

By F. M. Walters and O. A. Buchmann
AiResearch Manufacturing Company
a division of The Garrett Corporation

SUMMARY

As part of a comprehensive investigation of problems associated with design and fabrication of efficient regeneratively cooled structural panels, an analysis was made of the heat transfer and the fluid flow performance of flat, hydrogen-cooled heat exchangers. In addition, the fluid flow performance of selected manifold concepts was investigated analytically and experimentally.

Within ground rules established as compatible with the state of the art for materials and fabrication techniques, a large variety of conceptual designs for heat exchanger panels were investigated to determine specific design features and ranges of applicability. Performance of a broad array of heat exchanger geometries was determined over a range of heat fluxes to 500 Btu sec-ft^2 (5680 kW/m^2), and is presented in terms of coolant flow rate, flow length, cross-sectional temperature difference, and pressure drop. Potential advantages of various heat exchanger geometries and methods of flow manifolding, flow folding, multiple stacking of heat exchanger elements, and insulation were investigated qualitatively and quantitatively, in terms of coolant conservation and temperature differential reductions.

In general, the investigations were made assuming fixed uniform heat fluxes over the exposed surface of the panel. However, for coolant conservation studies a uniform recovery temperature was assumed. A hydrogen coolant inlet temperature of 100°R (55.5°K) and various outlet temperatures from 1400°R to 1900°R (778° to 1055°K) were used. The inlet pressures were varied, as required--subject to a maximum pressure limitation of 1000 psi (6880 kN/m^2)--to maintain a coolant outlet pressure of 250 psi (1720 kN/m^2).

Although the single-pass heat exchanger was found generally applicable to the entire range of conditions studied, two heat exchanger concepts appeared attractive for coolant conservation: (1) insulation on the heat exchanger hot surface and (2) flow folded in the panel width dimension with counterflow in alternate passages. Typical hydrogen flow rate reductions of 5 to 10 percent are achieved by use of folded flow at heat fluxes below 100 Btu/sec-ft^2 (1135 kW/m^2) and recovery temperatures below 7000°R (3890°K). Hydrogen flow reductions of 20 percent or more can be achieved by use of insulation throughout the range of heat flux for this study.

In addition to the parametric analysis of heat exchanger panels, detailed performance was calculated for selected panel concepts. The concepts evaluated were (1) a single-sandwich configuration that provides for both structural load carrying capability and coolant containment and flow routing, (2) a composite configuration in which the coolant-pressure-containing surface heat exchanger is metallurgically bonded to the structural-load-carrying sandwich panel, and (3) a cooled-shingle configuration in which the surface heat exchanger is mechanically attached to low-temperature load-carrying structure.

The manifold analyses and testing performed as part of this program demonstrated that serious flow distribution problems can occur in regeneratively cooled panel applications. Geometry variations affecting manifold pressure drop and heat exchanger panel flow distribution were investigated experimentally, and means of improving the flow distribution are indicated.

INTRODUCTION

Vehicles traveling at hypersonic speeds are exposed to severe thermal environments. Maintaining the temperature of structural elements of these vehicles within the limit of current material technology becomes a serious problem. For spacecraft and research aircraft where the heating period is short and refurbishment is not a problem, acceptable thermal limits have been maintained by designing the vehicle as a heat sink or by ablatively cooling the surface. For hypersonic cruise aircraft where heating periods are much longer and refurbishment is a problem, these means of thermal protection are no longer sufficient.

Major portions of a hypersonic aircraft can and will be radiatively cooled; however, in many areas the radiation equilibrium temperatures will exceed the material limitations and some active means of thermal protection must be provided. One of the more attractive means of active cooling for this application is regenerative cooling (use of the fuel as a coolant). This technique appears especially attractive for the hypersonic cruise vehicle because cryogenic hydrogen, which has been proposed as a fuel, is an excellent coolant.

Regenerative cooling has been used successfully for hydrogen-fueled rocket engines. However, in contrast to rocket engine applications, which are characterized by small areas, high heat fluxes, and short operating times, air breathing hypersonic cruise aircraft will have large areas of low to moderate heat flux and will be expected to operate for much longer periods of time. Conservation of coolant and minimization of weight become paramount for these vehicles.

Therefore, a study has been initiated to investigate problems associated with design and fabrication of efficient regeneratively cooled structural panels The overall study is concerned with practical engineering problems of material applications and fabrication, structural design and analysis, heat transfer and fluid flow analysis, and the integration and interaction of various aspects of

2

the general design problem. In an initial investigation, reported in ref. 1, analytical studies were conducted of a wide array of conceptual designs for flat, hydrogen-cooled panels operating at heat fluxes from 10 to 500 Btu/sec-ft² (114 to 5680 kW/m²) and normal pressures from 6.95 to 250 psi (48 to 1720 kN/m²). Procedures for integrating the heat transfer and structural design and minimizing configuration weight were developed, and ranges of applicability of the various conceptual designs were determined.

In a companion investigation, reported herein, the heat transfer and fluid flow performance of flat, hydrogen-cooled heat exchanger panels was studied analytically; the performance of associated manifolding systems was studied both analytically and experimentally. Various influences on heat exchanger performance were examined and potential advantages of various methods of flow manifolding, flow folding, multiple stacking of heat exchanger elements, and insulations were investigated qualitatively and quantitatively, in terms of coolant requirements and heat exchanger temperature differentials. In addition, parameteric data were generated on the performance of circular, rectangular, interrupted rectangular, and pin-fin coolant passages.

Although the present investigation was closely allied with the configurations of ref. 1, the types of problems encountered and investigated are representative of those that will arise in the design of hydrogen-cooled panels for application to hypersonic vehicle or engine surfaces. Furthermore, the data presented encompass the ranges of applicability for both exterior and interior surfaces and provide the basic quantities of interest for specific design or tradeoff studies.

SYMBOLS AND PARAMETERS

A = area, ft² (m²)

A = fluid designation in four-fluid heat exchanger program

b = fin or web spacing, or width, in. (cm)

C = ratio of heat exchanger thermal conductances at 2000°R (1111°K) and at T_{CO}, dimensionless; fluid designation in four-fluid heat exchanger program

C_p = specific heat at constant pressure, Btu/lb-°R (J/g-°K)

D = diameter, in. (cm)

f = fin effective thickness factor, or friction factor, dimensionless

G = fluid designation in four-fluid heat exchanger program

g = g_c = 32.2 lb (mass) ft/lb (force) sec² (980.7 cm/sec²)

H   =   enthalpy, Btu/lb (J/g)

H   =   fluid designation in four-fluid heat exchanger program

h   =   height, in. (cm) or heat transfer coefficient, $Btu/sec\text{-}^\circ R\text{-}ft^2$ $(kW/^\circ F\text{-}m^2)$

j   =   Colburn modulus, $St(Pr)^{2/3}$, dimensionless

K   =   pressure drop coefficient for turning, expansion, or contraction

k   =   thermal conductivity, $Btu/hr\text{-}^\circ R\text{-}ft$ $(W/m\text{-}^\circ K)$

L_o =   offset length (uninterrupted flow length), in. (cm)

ℓ =   panel length, or hydrogen flow length, in. (cm)

l_{fin} =   effective fin length, in. (cm)

N   =   number of fins/unit of heat exchanger width

P   =   pressure, psi (kN/m^2)

Pr   =   Prandtl number, $\mu C_p/k$, dimensionless

Q   =   velocity head, $W^2/A_f^2 2g_c\rho$, lb/in^2 (kN/m^2)

q   =   heat transfer rate, Btu/sec (kW)

R   =   resistance to flow, dimensionless; gas constant in equation for density

Re   =   Reynolds number, $\dfrac{4r_h W}{\mu A_f}$, dimensionless

r   =   radius, in. (cm)

r_h =   hydraulic radius, in. (cm)

St   =   Stanton number, $\dfrac{hA_f}{WC_p}$, dimensionless

T   =   temperature, $^\circ R$ $(^\circ K)$

TC, TH =   fluid temperatures in four-fluid heat exchanger program, $^\circ R$ $(^\circ K)$

T1,T2,
...   =   metal temperatures at nodes 1, 2, ..., in four-fluid heat exchanger program, $^\circ R$ $(^\circ K)$

t   =   thickness, in. (cm)

W $\quad$ = $\quad$ flow rate, lb/sec (kg/sec)

WC, WH = $\quad$ fluid flow rates in four-fluid heat exchanger program, lb/sec (kg/sec)

w $\quad$ = $\quad$ panel width, or hydrogen flow width, in. (cm)

X $\quad$ = $\quad$ variable width, in. (cm), in dimensionless core flow width, X/W

α $\quad$ = $\quad$ thermal expansion coefficient, in./in.-$^\circ$F (m/m-$^\circ$K)

γ $\quad$ = $\quad$ material density, lb/in^3 (kg/m^3)

Δ $\quad$ = $\quad$ change in, increment of

ϵ $\quad$ = $\quad$ strain, in./in. (m/m)

η $\quad$ = $\quad$ fin effectiveness

η_o $\quad$ = $\quad$ overall fin effectiveness

μ $\quad$ = $\quad$ viscosity, lb/sec-ft (kg/sec-m)

ρ $\quad$ = $\quad$ density, lb/ft^3 (kg/m^3)

ρ_a $\quad$ = $\quad$ density at average pressure and temperature

σ $\quad$ = $\quad$ stress, psi (kN/m^2), or ratio of density at average temperature and pressure, lb/ft^3 to standard density of I lb/ft^3

Subscripts:

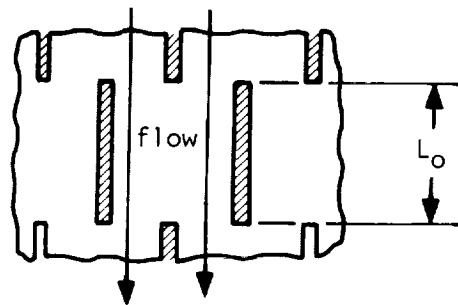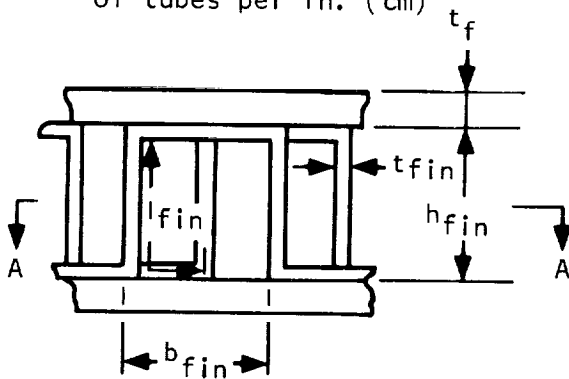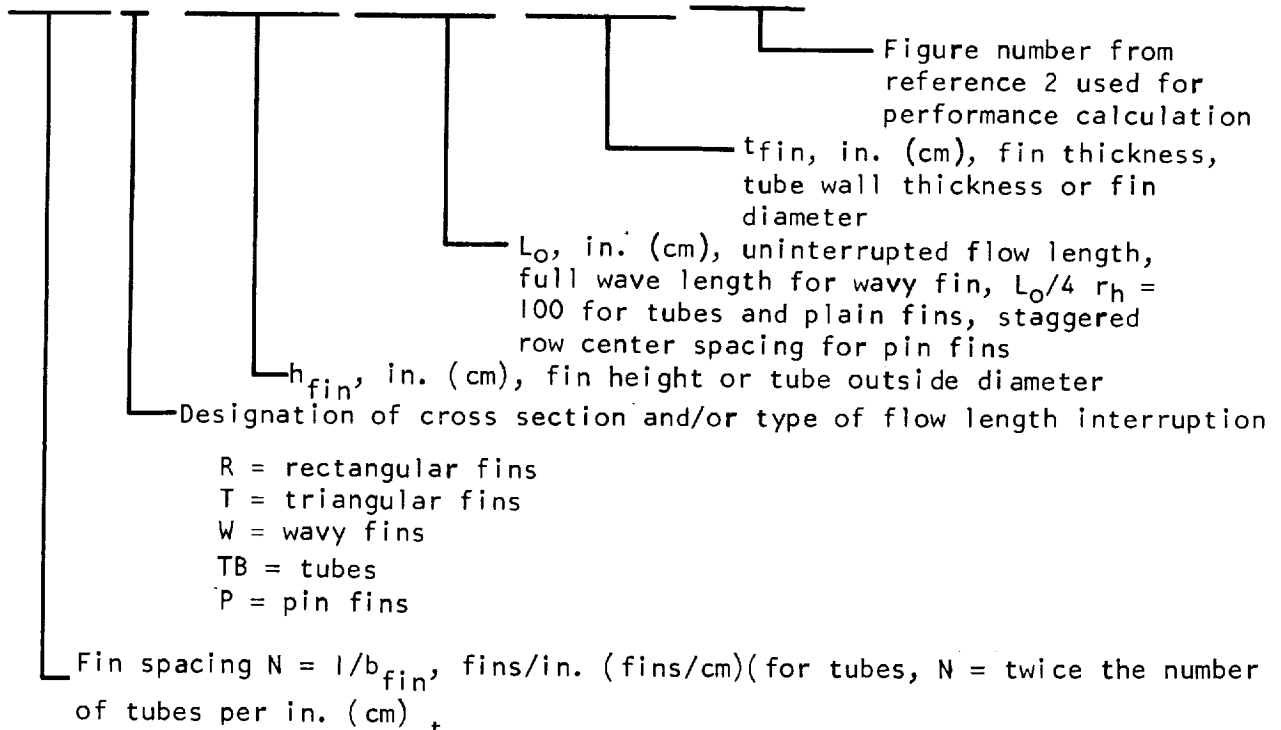a $\quad$ = $\quad$ average

C $\quad$ = $\quad$ coolant

c $\quad$ = $\quad$ core

DMW $\quad$ = $\quad$ design maximum wall

E $\quad$ = $\quad$ effective

F $\quad$ = $\quad$ fin tip (location in heat exchanger most remote from aerodynamic surface)

f $\quad$ = $\quad$ face sheet, flange, friction as in ΔP_f, flow as in A_f, at film temperature as in k_f, μ_f, C_{pf}

fin $\quad$ = $\quad$ fin

G $\quad$ = $\quad$ hot gas
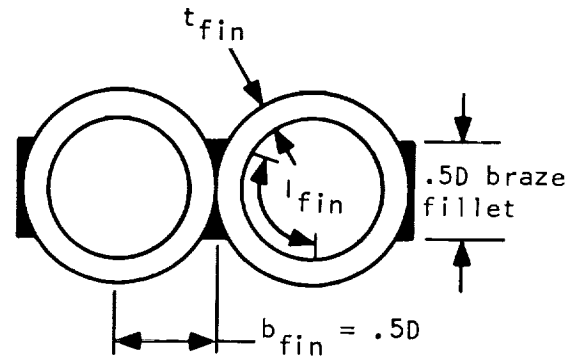
HF	=	horizontal fin
HM	=	hydrogen temperature between folded and single-pass panels
HT	=	hydrogen temperature at 180^{0}-turn in folded-flow routings
I	=	inlet
i	=	insulation
LP	=	longest path
M	=	manifold
m	=	momentum
max	=	maximum
min	=	minimum
0	=	outlet
o	=	overall
p	=	port
R	=	recovery or adiabatic wall
req	=	required
SP	=	shortest path
std	=	standard
T	=	total
W	=	hydrogen-cooled surface of hot wall
WH	=	aerodynamic-heated surface of hot wall
1, 2, 3, 4, 5	=	flow distribution test unit test station numbers

6

Fin geometry is designated with a six-part nomenclature:

20(7.9)R-.100(.254)-.125(.318)-.004(.010) (10-61)

Figure number from reference 2 used for performance calculation

t_{fin}, in. (cm), fin thickness, tube wall thickness or fin diameter

L_o, in. (cm), uninterrupted flow length, full wave length for wavy fin, $L_o/4\ r_h = 100$ for tubes and plain fins, staggered row center spacing for pin fins

h_{fin}, in. (cm), fin height or tube outside diameter

Designation of cross section and/or type of flow length interruption

R = rectangular fins
T = triangular fins
W = wavy fins
TB = tubes
P = pin fins

Fin spacing $N = 1/b_{fin}$, fins/in. (fins/cm)(for tubes, N = twice the number of tubes per in. (cm)

Rectangular offset fins

Tubular fins

HEAT EXCHANGER GEOMETRY NOMENCLATURE

7

STATEMENT OF PROBLEM

Objectives

The objectives of this study were to examine the heat transfer and fluid flow characteristics of heat exchangers and manifolds for flat, hydrogen-cooled panels and to provide useful data for the design of panels of this type. The desired capabilities of an efficient heat exchanger panel and manifold system were considered to be: (1) to limit maximum temperature for strength or corrosion resistance, (2) to limit steady-state ΔT throughout the structure for acceptable thermal stresses, (3) to limit coolant flow rate and, thereby, increase efficiency and reduce vehicle weight, (4) to make efficient use of pressure drop for obtaining maximum heat transfer coefficient and limiting required pumping power, and (5) to establish flow distribution to fit the heat flux distribution across the panel width.

Environmental Conditions and Design Constraints

During this study, the environmental conditions applied were considered representative of conditions that may be encountered on external and internal (i.e., inlet, duct, and engine wall) surfaces of hypersonic cruise vehicles. The design constraints imposed were those considered representative of good engineering practice, and they were based on present day materials and fabrication technology. Limiting conditions used in the study presented herein are

- Panel length--up to 5 ft (1.525 m)

- Panel configuration--flat

- Coolant--hydrogen

- Cooling method--forced convection

- Net heat flux--0 to 500 Btu/sec-ft^2 (0 to 5680 kW/m^2)

- Coolant pressure--250 to 1400 psi (1720 to 9650 kN/m^2)

- Coolant temperature--100° to 1900°R (55.5° to 1055°K)

Heating condition.-- For the purpose of this study, it was assumed that heating occurred from one side only. When two-sided panel heating occurs, heat fluxes will generally differ significantly on the two sides and special coolant controls will be required to permit two-sided heating of a single panel with acceptable thermal stresses. Also, installation requirements may lead to the use of separate panels for each of two surfaces with different heat fluxes.

Two different heating conditions were considered. For the majority of cases, a uniform heat flux was assumed over the surface of the panel. Due to temperature variation along the length of a cooled panel, this condition is

8

approached for a uniform external environment only as recovery temperature becomes very large relative to wall temperature. Therefore, the term infinite recovery temperature is used herein to refer to the uniform heat flux condition. For the remaining cases, the panel was assumed to be exposed to a hot gas with a uniform finite recovery temperature so that the effects of panel surface temperature could be considered. The nominal level of heating for these cases was defined by the heat flux at the cold end of the panel, which was assumed to be operating at a hot wall temperature of $500°R$ ($278°K$). The actual heat flux along the panel varied directly with the difference between the local hot wall temperature and the hot gas recovery temperature; therefore, the average heat flux to the panel was less than the nominal value. Uniform finite recovery temperatures of $3000°$, $5000°$, and $7000°R$ ($1670°$, $2780°$, and $3890°K$) were used for these studies.

Coolant Pressure.-- For this study, the minimum coolant pressure that occurs at the outlet manifold was chosen to allow for a pressure differential that can be used to inject the hydrogen into an engine combustor section. The use of supercritical outlet pressures allows the assumption of forced-convection, single-phase, heat transfer coefficients throughout the study. The coolant inlet pressure selected was that pressure required to produce the necessary coolant flow through the heat exchanger. The upper limit on inlet pressure was usually taken to be 1000 psi (6895 kN/m^2), although inlet pressures up to 1400 psi (9650 kN/m^2) were considered.

Temperature.--A hydrogen inlet temperature of $100°R$ ($55.5°K$) was used during this study. It was assumed that hydrogen would be stored at $40°R$ ($22.2°K$) or less and would undergo a temperature increase due to heat leak and/or compressor energy input of about $60°R$ ($33.3°K$). A hydrogen outlet temperature of $1600°R$ ($889°K$) was usually assumed, although outlet temperatures from $1400°$ to $1900°R$ ($778°$ to $1055°K$) were considered.

Practical structural operating temperatures have been limited to approximately $2000°R$ ($1111°K$) by current state of the art in materials and fabrication of heat exchangers and structures. This temperature was used throughout the program as the maximum permissible temperature at any point on regeneratively cooled structures.

Materials.-- Use of superalloys such as Hastelloy X, Inconel 625, and Waspaloy was dictated by strength-at-temperature and low-cycle-fatigue characteristics. The important material property for heat transfer analysis is thermal conductivity. Thermal conductivities for these three materials are shown in fig. 1.

Heat exchanger geometry.-- Table I specifies the limiting dimension for each of the heat exchanger geometry variables and the primary limiting conditions. The table of Symbols and Parameters defines these geometry variables and descriptive terminology.

Hydrogen Properties.-- The transport and thermodynamic properties referenced throughout this study are those of parahydrogen gas at 500 psi (3450

kN/m^2), as shown in fig. 2. The use of parahydrogen properties is based on the assumption of liquid hydrogen storage and insufficient time or catalytic reaction between storage and panels for conversion to equilibrium hydrogen.

RESULTS AND DISCUSSION

Heat Exchanger Performance

The important variables and parameters related by the various performance analyses are

- Heat flux, q/A, and recovery temperature, T_R

- Hydrogen flow length, ℓ

- Hydrogen flow rate per width of panel, W/w

- Hydrogen inlet pressure, P_{CI}

- Hydrogen pressure drop, ΔP_C

- Maximum heat exchanger temperatures, T_{WH} and T_W

- Maximum structure temperature, T_F

As detailed in Appendix A, operating characteristics of typical panel heat exchangers permit simplifying combinations of the seven performance parameters listed above. However, the important relationships among these variables and parameters are well summarized for all flow routings and geometries by the following statement: panel heat exchanger performance is good when small temperature differences result with low pressure drop and low coolant flow rate.

Recovery temperature effects.--From the basic equation for convective heat transfer from a hot gas to an exposed surface (eq. 1 of Appendix A) it can be seen that the heat flux to a panel surface is directly proportional to the difference between recovery temperature of the hot gas, T_R, and the temperature of the hot surface of the panel, T_{WH}. If the hot surface temperature can be increased to approach the recovery temperature more closely, the heat flux to the panel will be reduced and consequently (see eq. 2 of Appendix A) the coolant flow rate can be reduced.

Using eqs. 1 and 2 of Appendix A, a cooling efficiency factor has been established to provide an insight into the effects of hot gas recovery temperature on the thermal performance of cooled panels and to provide a criterion to assist in evaluation of various cooling configurations. The cooling efficiency factor is defined as the ratio of coolant flow rate required for a panel with a uniform hot wall temperature of 2000°R (1111°K) to the flow rate required for a panel with some other average hot wall temperature, T_{WH}. (A temperature of

10

2000°R (1111°K) was selected as a reference because it represents a practical maximum temperature for structural applications of superalloy materials.) Since coolant flow rate and average best flux are linearly proportional, the cooling efficiency factor is also the ratio of average heat fluxes into the two panels.

The cooling efficiency factor has been evaluated for selected average hot wall temperatures and the results are presented in fig. 3 as functions of the hot gas recovery temperature. Hot wall temperatures of less than 2000°R (1111°K) are representative of typical uninsulated panels in which the hot wall temperature varies from some low value to the maximum allowable temperature of 2000°R (1111°K) as the coolant temperature increases along the panel. An average temperature of 1000°R (555°K) can be considered as a limiting case for single-pass, straight-through cooled panels where the hot wall surface temperature varies linearly from 0°R (0°K) to 2000°R (1111°K). Average temperatures between 1000°R (555°K) and 2000°R (1111°K) can be obtained with sophisticated flow routings or coolant passage contouring, which permits the surface temperature to approach the permissible maximum nearer the inlet end of the panel, or through the use of insulation on the hot face of the panel. Average temperatures greater than 2000°R (1111°K) cannot be obtained with flow routing or passage contouring alone; these temperatures are representative of cases where nonstructural insulating material has been added to the hot face of the panel to increase the surface temperature. A temperature of 2500°R (1389°K) appears to be a practical maximum temperature limit for nonstructural metallic type insulation for design life in the tens of hours.

It is apparent from fig. 3 that the cooling efficiency is a relatively strong function of wall temperature at the lower recovery temperatures, but becomes insensitive to wall temperature at the higher recovery temperatures and converges to a cooling efficiency of 1.0 at an infinite recovery temperature. As a consequence, an infinite recovery temperature has been assumed for a majority of the heat transfer calculations because it permits the heating conditions to be defined by heat flux alone and avoids the iterative, incremental analysis required to account for variations in the hot surface temperature along the panel length. At recovery temperatures of 7000°R (3889°K) or greater, the coolant flow rate obtained by assuming the entire surface of a panel is at the maximum allowable temperature of 2000°R (1111°K) differs by less than 15 percent from that obtained when surface temperature variations are considered. For lower recovery temperatures, the differences resulting from such an assumption become progressively larger and more detailed incremental calculations involving the hot wall and recovery temperatures are required for accurate prediction of coolant requirements.

The recovery temperature of the hot gas must always be specified to evaluate the coolant conservation potential of various flow routings and insulations. It is apparent from fig. 3 that the potential for improvements in cooling efficiency due to sophisticated flow routing or insulation decreases rapidly as the recovery temperature increases. For example, at a recovery temperature of 5000°R (2778°K), an increase in the average surface temperature from 1000°R (555°K) to 3000°R (1667°K) will increase cooling efficiency by approximately 75 percent; whereas, at a recovery temperature of 7000°R (3889°K) the same change in surface temperature nets a 45-percent increase in cooling efficiency. It should be

noted, however, that the quantity of coolant conserved is the same at both recovery temperatures. Thus, although the percentage of coolant that can be conserved by a given increase in average hot wall temperature varies with recovery temperatures, the actual quantity of coolant that can be conserved is directly related to the increase in hot wall temperature that the flow routing or insulation provides and is independent of recovery temperature. Furthermore, for a given hot wall temperature, the heat flux to the panel increases as the recovery temperature increases; consequently the thickness of insulation required to attain that hot wall temperature decreases. Therefore, although the coolant efficiency decreases, the efficiency of the insulation in terms of coolant reduction per unit weight of insulation actually increases with recovery temperature.

Single-pass heat exchanger panels.-- As discussed in detail in ref. 1, panel stress is caused by normal pressure, dynamic pressure, coolant internal pressure, and various temperature gradients, both transient and steady-state, which may exist in all three panel dimensions. The temperature gradient through the heat exchanger thickness causes important thermal stresses and is defined as the sum of the temperature differences through the hot face sheet or the tube wall, $T_{WH} - T_W$, and the fins, $T_W - T_F$, as indicated in fig. 4.

For a 0.010-in. (0.025-cm) thick superalloy heat exchanger face sheet, $T_{WH} - T_W$ ranges from $160^{\circ}R$ ($89^{\circ}K$) at the cold end to $100^{\circ}R$ ($55.5^{\circ}K$) at the hot end with a heat flux of 500 Btu/sec-ft^2 (5680 kW/m^2). The face sheet ΔT variations are due to superalloy thermal conductivity variations with temperature, and are obtained as specified in Appendix A.

In ordinary heat exchangers, where the heat flux is lower than that considered here, the fin ΔT is much smaller than the wall-to-bulk-fluid ΔT. In fact, the fin tip most remote from the heated surface is at approximately the same temperature as the directly heated prime surface. However, for heat flux rates above 10 Btu/sec-ft^2 (114 kW/m^2), the fin tip attached to the back sheet is essentially at the coolant local bulk temperature and $T_W - T_F$ is equal to or greater than 95 percent of $T_W - T_C$. At heat flux near the high end of the design range for this program, approximately one-half of the entire fin is at the local coolant temperature. Therefore, since it was assumed that there was no heat loss out of the backside of the structure supporting the heat exchanger, the temperature of this structure was the same as the local coolant temperature and the maximum hydrogen temperature was also the maximum temperature of the supporting structure. The primary thermal stresses occur because the hot face sheet of the heat exchanger, which is at a higher temperature, is constrained to remain flat and hold the planform dimensions of the supporting structure.

The basic function of heat exchanger geometry is control of thermal conductance and pressure drop. Thermal conductance is that property of the coolant-and-geometry combination that controls temperature differential between the hot-gas heated surface and the structure, i.e., $T_W - T_F$. Pressure drop and outlet pressure together control pressure-containment strength requirements and determine pumping power required for panel systems. The heat exchanger

geometry must provide a lightweight and fabricable configuration, contain the hydrogen pressure, maintain acceptable heated-surface temperatures, and provide cross section temperature differences within the thermal stress limitations of available materials.

The heat exchanger geometries considered for use in hydrogen cooled panels are shown in fig. 5. Geometries with discrete passages such as round and rec-tangular tubes may be distinguished from those geometries formed from corrugated tension members brazed between two flat sheets. Smooth aerodynamic surfaces can be obtained with the heat exchanger geometry in which corrugated metal fins are brazed between flat sheets. The aerodynamic and heat transfer effects of the rough surface presented by tubes are adverse factors in some applications.

The important geometry characteristics that allow variations in thermal conductance and pressure drop, and which apply equally to all geometries, are: (1) cross section shape, (2) uninterrupted flow length (offset length), (3) types of flow length interruption, (4) fin height, (5) fin spacing, (6) fin thickness, and (7) thermal conductivity. "Tube" or "tube wall" can be substi-tuted for the word "fin" in the previous sentence.

Because heat exchanger geometry efficiency is measured in terms of hydrogen flow rate, pressure drop, and material weight, high thermal conduc-tance at a given pressure drop is usually sought. High thermal conductance reduces fin ΔT and permits the hydrogen temperature to be maximized within the constraints of the maximum heat exchanger face-sheet temperature, T_{WH}, and the maximum structural temperature, T_F.

Fin ΔT is reduced and pressure drop is increased (1) by reducing uninterrupted flow length, fin height, and fin spacing, or (2) by increasing fin thickness. Frequent interruption of the hydrogen boundary layer along the passage walls (e.g., by use of offset fins) can be used to achieve high thermal conductance. Increasing fin thermal conductivity will decrease fin ΔT without increasing pressure drop. Although discrete passage geometries inherently can withstand internal pressure better than corrugated tension members brazed between two flat sheets, the typical hydrogen inlet pressures required for regenerative panel applications are within the pressure capabilities of the latter configuration.

For the tubular heat exchanger geometries without braze fillets, the corrugated surface area is 57 percent greater than the planform area, $w\ell$. In the limit, an increase in heat flux and hydrogen flow rate of 57 percent over flat surfaces can be postulated. In half-tube-diameter braze fillets, as assumed, and as defined in the Symbols and Parameters table, exposed area is 18 percent greater than $w\ell$. In this case, heat flux and hydrogen flow rate increases of up to 18 percent greater than those for flat surfaces can be postu-lated. Hydrogen thermal conductance was estimated for both of the above surface condition assumptions; however, no increase in heat flux or hydrogen flow rate was assumed because of increased exposed area. Hydrogen pressure drop is not affected since plain, round, inside surfaces were assumed for all tubes. Tubes have higher thermal conductance without braze fillets than with braze fillets.

13

Without braze fillets, half of the tube inside circumference was assumed to be fin area transferring heat to the hydrogen. With the more realistic assumption of half-tube-diameter braze fillets, three-fourths of the tube inside circumference was assumed to be fin area transferring heat to the hydrogen. The fin ΔT values, $T_W - T_F$, were assumed to occur in one-fourth of the tube inside circumference without braze fillets and in three-eighths of the tube inside circumference with half-tube-diameter braze fillets. By comparison, fin length for rectangular fins is taken as the fin height plus half the fin spacing.

The above considerations led to emphasis on the rectangular-offset-fin configuration throughout the analyses. Work was done with the other geometries, however, to point out their strengths and weaknesses, but they were not studied extensively.

The performance of heat exchangers with single-pass flow routing was calculated by the method described in Appendix A for the seven important geometry variables previously listed. A somewhat smaller range of geometry variables was examined more intensively (Appendix B) to provide temperature and pressure data for heat exchangers studied in ref. I. Figs. 6 through 15 show heat exchanger performance in terms of hydrogen thermal conductance per unit of panel projected area and density-adjusted pressure drop per unit of hydrogen flow length, both as functions of hydrogen flow rate per unit of panel width. Plots of density-adjusted pressure drop and fin ΔT as functions of heat flux, with panel length as a parameter, are presented in figs. 16 through 20. Fig. 21 shows the effect of temperature-dependent fluid properties on thermal conductance and density-adjusted pressure drop.

Since only friction pressure drop is presented in the performance curves, overall panel pressure drop must be calculated by adding manifold pressure drop as well as heat exchanger core entrance, exit, and flow-acceleration pressure drops. The flow-acceleration pressure drop in hydrogen-cooled panels is about 6 percent of the friction pressure drop. The core entrance and exit pressure drops are usually so small as to be negligible for the panel geometries considered. They will, of course, represent a somewhat larger percentage of the friction pressure drop for smooth tubular surfaces than for frequently interrupted surfaces such as rectangular offset fins. To make the heat exchanger pressure drop curves applicable at any hydrogen gas density, all pressure drops were multiplied by a density ratio. Viscosity variations also affect frictional pressure drop; however, as indicated by the small variations with temperature of the density-adjusted pressure drops for offset fins shown in Figure 21, the effects of viscosity variations are insignificant for the temperature range and flow rates of interest. At flow rates lower than those shown in fig. 21, heat exchanger pressure drop is less than 2 percent of a typical panel inlet pressure of 500 psia (3450 kN/m^2).

Flow routing.--Cooling flow rate can be reduced (cooling efficiency improved) by increasing average wall temperature, T_{WH}. Use of a more complex hydrogen flow routing than the single-pass concept (fig. 22a with one inlet)

14

produces higher wall temperatures and higher cooling efficiencies. The single-pass flow routing concept is distinguished by:

- Coolant flow parallel or counter to external hot-gas flow

- Hydrogen flow length equal to panel length

- Inlet and outlet manifolds located at opposite ends of the panel

- Average wall temperatures between 1000° and $1500^\circ R$ (555° and $834^\circ K$), depending upon hydrogen outlet temperature and heat flux, under the boundary conditions specified for this program

Preceding a detailed discussion of the flow routing concepts depicted in fig. 22, some of the results of flow routing studies are presented to summarize cooling efficiency. Table 2 shows that flow routings more complex than single-pass yield significant increases in cooling efficiency only at low flux and low recovery temperature. At and above recovery temperatures of $5000^\circ R$ ($2780^\circ K$) and heat flux of 250 Btu/sec-ft^2 (2840 kW/m^2), cooling efficiency is essentially equal for all flow routings, although the folded-in-width configuration (fig. 22d) is best. The cooling efficiencies at recovery temperatures of 3000° and $7000^\circ R$ (1670° and $3890^\circ K$) resulted from preliminary analyses of heat exchangers with unequal flow length. The cooling efficiencies at a recovery temperature of $5000^\circ R$ ($2780^\circ K$) result from more exact analyses of heat exchangers with equal flow length. An example illustrating the method of heat exchanger system design for folded flow, as used to obtain the cooling efficiencies at recovery temperature of $5000^\circ R$ ($2780^\circ K$), is presented later in this section. Although flow folding increases cooling efficiency over only a limited range of the boundary conditions that were investigated in this study, its potential use-fulness will depend upon the following considerations:

- The extent of the vehicle or engine surfaces operating at low heat fluxes. In general, large portions of external surfaces and engine inlets will be operating at low heat fluxes. Given this situation and a requirement for regenerative cooling, significant reductions in coolant flow requirements could be achieved by flow folding.

- The complexity involved in providing for folded flow.

- Off-design performance of and coolant control in folded-flow panels.

Multiple inlets: Heat exchanger length in a single panel may be divided with all parts connected in parallel, as shown in fig. 23, or with parts connected in series, as shown in fig. 22a. Compared to single-pass flow, connecting parts in parallel provides a large pressure drop reduction and no increase in cooling efficiency. Series connection of the parts produces significant increases in cooling efficiency and some reduction in pressure drop.

Where the flow length is a fraction of panel length, the number of inlet and outlet manifold sets may be equal to the number of flow length subdivisions as shown in fig. 23a. The total number of manifolds can be held to a minimum

by using common inlets and outlets as shown in fig. 23b. While thermal stresses are less severe with common inlets and outlets, the only structurally acceptable configuration generally has an inlet at each end of the panel and a common hot outlet at the center of the panel. In addition, the panel length-to-width ratio should be at least 2. Since a panel length of 3 ft (0.915 m) and pressure drop of $\leq$ 700 psi (4840 kN/m^2) at P_{CO} = 300 psia (2070 kN/m^2) can be obtained with the single-pass configuration at the highest heat flux considered in this study, the need for manifolding in the middle of panels is limited to systems with lower pressure drop limits. Some advantages in reduced manifold weight may be obtained by use of midpanel hot manifolds.

Increasing average wall temperature by injecting part of the total hydrogen flow at the inlet and at subsequent points along the length of the panel, as shown in fig. 22a, causes the sawtooth temperature profiles depicted in fig. 24. The thermal stresses may become unacceptable, but are less severe than for fig. 23a. Separating a multiple-inlet panel into several separate single-pass panels does increase efficiency with acceptable thermal stress, but is complex. In the limit, an infinite number of injection points or short panels will allow the entire surface to be at the maximum temperature, which for this study is 2000°R (1111°K).

Figure 24a depicts periodic injection and removal of hydrogen to keep mass flow rate constant, thereby maximizing coolant temperature while reducing pressure drop. Increasing fin height in a series of steps (fig. 24b) reduces pressure drop by providing greater flow area. For concepts shown in figs. 24a and 24b, a temperature sensor located at the end of each section controls a cold coolant valve at the beginning of that section. These concepts were rejected for purposes of this study because of control and manifold intricacy, which result in high weight and fabrication complexity. The heat exchanger concept of fig. 24c has multiple coolant inlet from a cold heat-exchanger layer that is insulated from the hot heat-exchanger layer. Instead of controllable valves, the fixed orifice position must be designed to provide the necessary flow rates. The practical problems of connecting two heat exchangers that are operating at very different temperatures make this concept appear impractical for inlets spaced at intervals of a few inches. Difficulties in obtaining a match between design point flow apportionment and off-design conditions also make this system appear unattractive. Again, excessive weight and fabrication complexity caused rejection of this concept for purposes of this study.

Flow folded in depth: The folded-in-depth concept (fig. 22b) increases cooling efficiency when heat flux from the hotter layer to the colder layer exceeds the aerodynamic heat flux to the hotter layer on a substantial fraction of the panel length. By changing heat exchanger geometry, the heat exchanger thermal conductance can be changed relative to any given hot-gas thermal conductance. Reducing the thermal conductance of the cooler heat exchanger layer reduces the heat transfer from the hotter to the colder layer and, thus, reduces average wall temperature and cooling efficiency. In the limit, the thermal conductance of the cooler heat exchanger layer can be zero. Then, no heat is transferred from the hotter layer to the colder layer, single-pass temperature profiles result throughout the hotter layer, and the colder layer is entirely at the hydrogen inlet temperature.

16

For analyses in this study, the sheet metal layer between the hotter and colder heat exchanger layers was assumed to have zero resistance perpendicular to the thickness. As the resistance of this layer is increased, or if insulation is used between the two heat exchanger layers, the heat transferred from the hotter layer to the colder layer is reduced. Effectively zero resistance can be obtained if the hotter and colder heat exchanger layers are connected by a single sheet metal thickness. In this case, however, thermal stresses resulting from hydrogen inlet and outlet temperature differentials become a limitation. If the hotter and colder fin layers are not metallurgically bonded to a single intermediate sheet, a high and usually nonuniform thermal resistance is introduced and acts in the same manner as insulation between the layers.

An important conclusion from the above studies is that insulation should never be placed between the heat exchanger layers if cooling efficiency is to be increased. However, insulation will always increase cooling efficiency if applied between the heat exchanger and the hot-gas heat source. Use of the upper fin layer as an insulation fin without hydrogen flow will provide equal or greater increases in cooling efficiency than folded-in-depth flow for the same weight. In fact, a primary reason for rejecting the folded-in-depth flow route configuration is that it has two heat exchanger layers, and is thus about twice as heavy as single-layer heat exchanger configurations (such as the single pass and the folded in width).

Folded flow with multiple injections: Use of folded flow with muliple injections (fig. 22c) was conceived to reduce cross-section ΔT's that occur in the folded-in-depth concept and at the same time maintain the beneficial high surface temperatures. Some examples of panel systems using this concept are shown in fig. 25. This figure indicates the fabrication difficulty, control complexity, and, therefore, excessive weight associated with this concept. The major limitation on fabrication practicality is the need for injection slots with widths of less than 0.004 in. (0.010 cm).

As noted in fig. 22c, tne excess flow at the right-hand edge of the panel may be equal to or greater than zero. The pressure drop is lower, wall and hydrogen temperatures are higher, and cooling efficiency is greater for the system that has some excess cold flow.

Flow folded in width: The concept shown in fig. 22d has many counterflow streams interspersed across the panel width. A plain-fin or rectangular-tube configuration is required, since the streams must remain separate between panel ends. Use of offset plate fins or pin fins is eliminated, but wavy fins or inserts in the plain passages may be used to increase thermal conductance. This concept is called folded-in-width when the inlet and outlet are at the same end of the panel (solid lines). It is also possible to have an inlet and outlet at both ends of the panel (dashed lines). Both methods of manifolding counterflow in adjacent passages develop the same overall performance. The concept with an inlet and outlet at both ends of the panel was rejected because of thermal stresses caused by a temperature profile similar to that for a single-pass configuration with a common hot outlet at the panel center and inlets at both ends.

Initial work with folded-flow panels was based on achieving wall temperatures of 2000°R (1111°K) and hydrogen outlet temperatures of 1760°R (978°K) at a heat flux of 10 Btu/sec-ft² (114 kW/m²), or a hydrogen outlet temperature of 1600°R (888°K) at higher heat fluxes. The relative cooling efficiency obtainable with various flow routings was of primary interest. To do this in the simplest way, the panel length that could be cooled with a specific flow rate and fin geometry was determined. Panels of unequal length resulted. Typical temperature profiles and panel length dimensions are shown in fig. 26. With this technique, the flow length at high flux (not shown) was between 4 and 8 in. (10 and 20 cm).

Fig. 26 points out the following characteristics of typical folded-in-width performance for panels of unequal length:

(a) The difference between coolant outlet temperature and maximum coolant temperature at the hot (folded) end of the panel increases as hydrogen inlet and outlet temperatures increase, but decreases as the hydrogen inlet and outlet temperature differential decreases.

(b) The maximum metal temperature may be reached at the hot end of the panel, but further use of the coolant thermal capacity can be obtained in a shorter, downstream panel with a smaller hydrogen inlet and outlet temperature differential without exceeding the maximum wall temperature. Longer panel segments result with higher hydrogen temperature for the same difference between inlet and outlet temperature.

A direct comparison of folded-in-width and single-pass concepts was also made for panels with a fixed length of 2 ft (0.61 m). This comparison was drawn at a recovery temperature of 5000°R (2780°K) and at the hydrogen temperatures and pressures noted in fig. 27 for high and low fluxes. Results of this analysis in terms of cooling efficiency are presented in table 2. Two different hydrogen outlet temperatures were used because of differences in the strength of superalloys selected for high- and low-flux panels during this part of the study. Plain-rectangular fins were used for folded-flow and offset-rectangular fins for single-pass panels. The Hastelloy X fin and wall (face sheet) thermal conductivity was varied as a function of local temperature. A heat exchanger hot-wall and cold-wall thickness of 0.010 in. (0.025 cm) was used in all calculations.

A single-pass panel was associated in series with a folded-flow panel so that identical hydrogen outlet temperatures would prevail for the two concepts compared. To obtain maximum coolant outlet temperature, a single-pass panel must be used to end a series of efficient folded-flow panels of equal length. Only by use of unequal length or low cooling-efficiency folded-flow panels can the maximum desired coolant temperature be obtained with folded-flow panels. If a low efficiency folded-flow panel were substituted for the single-pass panel in series with the folded panel, the overall cooling efficiency of the system would increase above the value reported in table 2. The system of two single-pass panels was connected in parallel to allow half the hydrogen to flow through each panel. This minimized the pressure drop but did not maximize cooling efficiency. As pointed out for panels with multiple inlets, cooling efficiency would have been increased with part flow through one panel and total flow through the other panel.

18

For high-flux panels discussed here, all material temperatures were within the design limits if the single-pass panel metal temperatures were within these limits. The maximum hot-wall temperatures for single-pass and folded-flow panels are compared in fig. 28 as functions of flow rate, with fin geometry as a parameter, for high flux conditions. The folded-panel system always had lower maximum wall temperature than the all-single-pass system. In the system with two single-pass panels for heat flux of 500 Btu/sec-ft^2 (5680 kW/m^2), maximum wall temperature for some fin heights is above the limit for this study: 2000°R (1111°K). The maximum allowable cold-wall temperature of 1600°R (888°K) occurred at the outlet end of all single-pass panels.

Fig. 28 also indicates that both single-pass panel and folded-panel cooling efficiency improves when fin height is increased. In single-pass panels, cooling efficiency also improves when fin spacing is increased. However, cooling efficiency is lowered in folded panels when fin spacing is increased because less heat can be transferred from hotter to colder hydrogen. Performance differences between folded and single-pass panels with an increase in fin spacing are due to the special function of the hot and cold walls in the folded heat exchanger. These 0.010-in. (0.025-cm) thick walls act as fins that conduct heat from the hotter to the colder hydrogen in adjacent passages. When fin spacing is reduced, more heat is transferred from hotter to colder hydrogen, thus increasing hot-wall temperature and reducing flow rate.

In fig. 29, inlet pressure is plotted as a function of flow rate and fin height for both single-pass and folded-flow systems at high heat flux. The folded-flow system always had higher pressure drop and, hence, higher inlet pressures than the all-single-pass system. The flow rates quoted for the system with a single-pass and a folded-flow panel are one-half the actual flow rate per unit width in the panel, and are quoted in this manner for direct comparison with the flow rates quoted for the system with two single-pass panels. The actual flow rate in the system with a folded-flow and a single-pass panel is twice the quoted flow rate because it cools a 4-ft (1.22-m) total panel length compared to the flow rate quoted for the system with two single-pass panels, which cools a 2-ft (0.61-m) flow length. Some short fins in the folded-flow system have inlet pressure above the design limit in this study of 1000 psia (6900 kN/m^2).

The design maximum wall temperature and hydrogen inlet pressure data from figs. 28 and 29 were combined in fig. 30 with fin-allowable pressure to show that all high flux designs had adequate strength as well as near-minimum weight. Minimum weight occurs for all configurations where fin-allowable pressure is equal to hydrogen inlet pressure. Minimum weight was a secondary goal in this part of the study, since cooling efficiency was known to increase with increasing fin weight.

The comparison among all flow routings is summarized in the following relationships. The pressure drop for single pass is less than for folded-in-width, which in turn is less than for folded-in-depth. The cross section temperature difference for single pass is less than for folded-in-width, which in

turn is less than for folded-in-depth. These relationships make single-pass flow a clearcut choice whenever cooling efficiency is not an important criterion for panel system design. However, hypersonic vehicle cooling hydrogen flow requirements are usually greater than fuel hydrogen flow requirements, so folded-in-width flow routing is still of use at low flux and low recovery temperature.

Temperature profiles: Analysis of flow routing with counterflow in adjacent passages, for both folded-in-depth and folded-in-width concepts, has indicated similarities in temperature profile as a function of flow length. The hydrogen and maximum metal temperature profiles of single-pass, folded-in-depth, and folded-in-width flow routing are compared in fig. 31 at the same hot-gas and hydrogen-inlet conditions and for the same panel length. For the folded-flow routings, the coolant outlet temperature is lower than both the hotter and colder hydrogen stream temperatures along most of the panel. The heat flux from the hotter-to-colder hydrogen stream must be greater than the heat flux to the panel to produce temperature profiles of this kind. Only with this relative flux situation does folded flow increase cooling efficiency. As the ratio of aerodynamic heat flux to heat flux from the hotter-to-colder hydrogen stream is increased for the same heat exchanger geometry and hydrogen flow rate, the slopes of the hydrogen temperatures are reduced until the average-wall and hotter-hydrogen-stream temperatures for folded flow are essentially equal to the average-wall and hydrogen temperatures for single-pass flow. This explains the fact that cooling efficiency for folded flow is significantly higher than for single-pass flow at low aerodynamic heat flux, and negligibly higher at high aerodynamic heat flux.

To maintain an efficient relationship of temperature profiles, acceptable cross section ΔT, and thermal stress at the cold end of folded-flow panels, the hydrogen outlet temperature is well below the allowable maximum. Similar hydrogen outlet temperatures are used for single-pass flow to provide a realistic comparison in fig. 31. More than one-half of the available hydrogen thermal capacity remains. One or more additional series-connected panels, either single-pass or folded, must be used for efficient utilization of the remaining hydrogen thermal capacity.

The need to obtain moderate thermal stresses places a severe limitation on the cross section temperature difference that is acceptable in all flow routings. Fig. 32 shows typical cross section ΔT profiles that prevail for the temperature profiles in fig. 31. At the hot end of the folded-in-depth concept, the cross-section ΔT is equal to the single-pass cross section ΔT, because there is no heat transfer from hotter to colder hydrogen. At the cold end of the folded-in-depth concept, the cross section ΔT is greater than the single-pass ΔT but less than the sum of the single-pass ΔT plus the local difference between hotter and colder hydrogen streams. With the folded-in-width flow routing, the local maximum surface temperature can be below the local hotter hydrogen stream temperature along a substantial length of the panel (fig. 31). Also, the local minimum surface temperature on the adiabatic surface of the heat exchanger can be substantially above the local colder hydrogen stream temperature. Therefore, the cross section ΔT for folded-in-width flow routing can be less than 25 percent of the local difference between hydrogen stream temperatures.

20

High average surface temperature and increased cooling efficiency can be obtained in single-pass heat exchangers by use of a thick heat exchanger (tall fins) with low thermal conductance and large hydrogen flow area; this obtains the large temperature differences primarily responsible for high wall temperatures. However, unacceptable thermal stresses occur in such a design because the low-strength hot end of the panel has almost the same cross section ΔT as the high-strength cold end of the panel. This is in contrast to folded flow, which provides a more acceptable small cross section ΔT at the low-strength hot end of the panel, and relatively high cross section ΔT at the high-strength cold end of the panel.

Insulation.-- Although insulation adds weight and reduces coolant flow (increases cooling efficiency) at all recovery temperatures lower than infinity, the tradeoff between insulation weight and hydrogen flow reduction can be implemented only for a specific vehicle and mission analysis. The efficiency of insulation increases as heat flux increases because the insulation thickness (weight) required to achieve a given decrease in coolant flow is inversely proportional to heat flux. Insulation may be powder, batt, foam or solid ceramic, a stagnant gas, or, simplest and heaviest, increased heat exchanger face sheet thickness.

Fig. 33a depicts a layer of insulating material with a thin refractory alloy or superalloy sheet covering, which is in turn held in place by discrete attachments. Use of bare ceramic insulation on panels may be limited by the need to provide containment, protection from aerodynamic effects, or from handling. Oxidation-resistant or coated refractory alloy shields for fibrous, powder, or solid insulation are then required. Oxidation-resistant coatings for refractory alloys are being developed for long term use. Use of oxidation-resistant metallic insulation such as Hastelloy X, even though limited to temperatures around $2500^\circ R$ ($1390^\circ K$), was considered because only a thin layer is required and it can be included in the brazed panel assembly.

Fig. 33b shows an overlapping shingle array of metal plates, in which the sheets are held in place at their corners. The attachment points consist of one fixed support point combined with a set of slotted, oversize holes to provide support and yet allow for differential expansion of the shingle with relation to the hydrogen-cooled surface. A major defect of this insulation concept for hydrogen-cooled panels is the nonuniformity of thermal resistance between the shingles and the heat exchanger face sheet. This nonuniform resistance can cause uneven shingle temperatures and oxidation rates or local hot spots in the heat exchanger, which are detrimental to cycle life through increased thermal stresses. The surface roughness inherent in the overlapping shingle concept will be a disadvantage in some applications where smooth aerodynamic surfaces are required.

A metallic sheet that is held away from the hydrogen-cooled surface by pin fins is shown in fig. 33c. The pin fins hold the metallic sheet and provide a uniform heat path with a good thermal resistance to weight ratio. The face sheet can be made up from many small elements where the differential expansion between them and the hydrogen-cooled surface can be absorbed by lateral bending

of the pins in any direction. The use of the same cross section area in plate fins of either the plain or offset rectangular type can provide the same insulation effects for equal weight, but will have bending flexibility in one direction only: perpendicular to the corrugations.

A recovery temperature of 5000°R (2780°K) was selected as typical for many hydrogen-cooled panel applications to illustrate the effects of metallic insulation. Typical insulation performance is listed in table 3, as obtained by the method described in Appendix A. The tabulated hot-gas heat transfer coefficients were used for both insulated and uninsulated surfaces because the hot-gas heat transfer coefficient is a weak function of wall temperature. The heat fluxes resulting at the hot end of the panel with and without insulation are for the tabulated local wall temperatures. A realistic maximum temperature for nonstructural superalloys of 2500°R (1390°K) permitted a panel hot-end heat flux reduction of 20 percent. In this case, the hydrogen flow rate and average heat flux were reduced more than the local heat flux at the panel hydrogen outlet end, because superalloy thermal conductivity increases with increasing temperature. The flow rates in table 3 apply for the integrated heat flux on the entire panel length.

A Hastelloy X hot wall with a thickness greater than 0.010 in. (0.025 cm) can provide the required insulation but is heavy. Insulation weight can be reduced using a fin layer and a thin face sheet instead of solid metal. The thin insulation closure sheet provides a smooth aerodynamic surface, and conductivity of the stagnant gas in the fins will be negligible compared with conductivity of the metal fins. For the typical sheet and fin insulation geometry analyzed under typical conditions, less than 0.7 lb/ft² (3.4 kg/m²) of insulation can reduce hydrogen flow rate more than 20 percent.

Typical fins, such as 20/in. (7.9/cm) with a thickness of 0.006 in. (0.015 cm) or 40/in. (15.8/cm) with a thickness of 0.003 in. (0.008 cm), have a solidity of 0.12 and an effective thermal conductivity about 8.3 percent that of solid metal. Use of equation 10 in ref. 5 indicates that air conduction and radiation will increase the effective fin conductivity noted by less than 3 percent and 1 percent, respectively, at the hydrogen outlet end of the panel. Therefore, the average effective thermal conductivity of the fins described above is 8.6 percent of solid metal conductivity, and is practically equal to the effective thermal conductivity based on metal conduction alone.

Insulation fin temperature differences are less than the overall insulation temperature differences because the insulation hot wall has a significant ΔT at high heat flux. The insulation fin height provides for a length of metal between fin roots equal to that required for the insulation fin ΔT, since fin thickness was added to wall thickness to obtain wall ΔT. Insulation fin heights are shorter than those normally used in fluid passages, but the heights cited have been fabricated. Weight and thermal resistance of braze material have not been included in the tabulated values. Since insulation thickness is based on allowable maximum surface temperature at the hot end of the panel, the tabulated weights per unit area are independent of overall panel dimensions and depend only on the density of the insulation fin material. A density of 0.3 lb/in.³ (830 kg/m³) was used.

22

Manifold Performance

The objective of the manifold study was to provide estimates of pressure loss and flow nonuniformity resulting from various manifold concepts for use in panel concept evaluation and tradeoff studies. A low manifold pressure drop is desirable since the manifold contributes to the overall pressure drop of the cooled panel. However, pressure drops greater than the minimum attainable may be required to provide proper flow distribution with low manifold weight. For a uniform heat flux (which was generally assumed in this study), a uniform flow is desirable to prevent nonuniform temperatures. The effect of a typical type of flow nonuniformity is shown in fig. 34, where 10 percent more flow occurs in the center of the panel than at the panel edges. The temperature is higher along the edges of the panel than in the center. This nonuniform temperature results in (1) thermal stresses than can easily attain large values, which must be allowed for in design, and (2) overheating of the starved areas of the panel. Since maximum temperature capabilities of materials are limited, it becomes necessary to increase the total coolant flow by 5 percent, for this example, to prevent overheating (ref. 1). However, thermal stresses attributable to temperature nonuniformity in the panel width are not eliminated by simple increases in coolant flow. With uniform heat flux, increases in thermal stress and coolant flow rate are avoided only with uniform flow. Thus, correct manifold design provides a match between cooling requirements and coolant flow distribution across panel width to minimize thermal stresses and coolant flow rate requirements.

Manifold concepts suitable for the special requirements of regeneratively cooled panels are presented in ref. 1. Three basic concepts, shown in fig. 35, were selected for use in this program. The upper corrugation or fin is the heat exchanger core fin in all of the concepts depicted. The two types of flat manifold provide pressure containment by fins similar to those used in the heat exchanger core. Cylindrical manifolds of the type shown can be used to obtain low pressure drop and uniform distribution, but result in relatively large unsupported spans that must accommodate high coolant pressures.

The selection of these three basic manifold concepts was based on the need for assembly of adjacent panels with the use of edge seals to prevent hot gas flow into regions in back of the panel. Additionally, the concepts provide for coolant flow and high thermal conductance in all parts of the panel surface exposed to hot gas.

Basic assumptions and constraints.--The flat rectangular manifold (fig. 35a) was selected as a reference configuration, with uniform flow (zero maldistribution) as the design objective. The rectangular manifolding was chosen to take advantage of previous design layout and analysis work accomplished for this configuration. It was assumed that the trends established from analyzing the rectangular manifold would be representative of the tapered manifold also. Consequently, pressure drop calculations were performed only for the rectangular manifolds. The cylindrical manifold was not considered beyond the initial stage of the study because the concept has a definite weight disadvantage for containing coolant pressure.

It is possible for uniform flow to occur through a cooled panel, independent of the properties of a manifold, if the panel pressure drop is very large compared to the manifold pressure drop. When this occurs, any nonuniformity in the pressure drop through the manifold is negligible compared to the uniform resistance across the width of the panel heat exchanger core. For this manifold study, however, it was assumed that heat exchanger pressure drop would be low enough that a variation in pressure drop through the manifold would have an effect on flow distribution. Thus, if uniform flow is achieved in the manifold, the ratio of heat exchanger panel pressure drop to overall pressure drop can have any value, and uniform flow will still occur.

Uniform flow in the manifold dictates that the resistance between the manifold inlet port and the heat exchanger panel be equal for all paths. Therefore, all paths except the maximum length paths that feed the edges of the panel require some source of pressure drop in addition to the pressure containment fins. Two methods for obtaining equal pressure drop for all flow paths are: (1) variation of the resistance in the vertical fin (the fin between the upper edge of the port and the heat exchanger core fin) and (2) incorporation of an orifice plate with large free-flow area in series with the longest, most highly restrictive paths at the edges, and small flow areas in series with the shortest, least restrictive paths adjacent to the ports. This study considers the second method.

The large number of dimensional variables involved in manifold design require selection of additional guidelines and assumptions for size and construction in order to facilitate calculation of pressure drop and weight. Accordingly, the pressure drop analyses were based on the following geometric features shown conceptually in fig. 35a:

(a) The configuration is flat rectangular.

(b) One manifold port feeds the full heat exchanger width.

(c) The manifold port and associated piping diameters are sized to provide a ratio of core free-flow area to port free-flow area of 1. Specification of this ratio provides a convenient basis for sizing the piping relative to the heat exchanger.

(d) The overall vertical fin flow length of 1.5 in. (3.81 cm) is divided into two parts: 0.5 in. (1.25 cm) from the top edge of the port to the bottom surface of the panel, and 1 in. (2.54 cm) parallel to the panel surface and underneath it. This 1-in. (2.54-cm) length contains three 90-deg bends and accommodates the seals, preventing hot gas flow to the region behind the panels. These dimensions are typical values and were selected with the aid of layout design work presented in ref. 1.

(e) Pressure containment in the manifolds results from plain rectangular fins, 10 per in. (3.94 per cm) of 4-mil (0.010-cm) Hastelloy X and manifold face sheets of 0.010-in. (0.025-cm) Hastelloy X. These selections are adequate for pressure containment of 500 psi (3450 kN/m^2) at 1600°R (888°K) and represent minimum gauge limits.

24

(f)   Manifold fin heights of 0.250 and 0.050 in. (0.634 and 0.127 cm) are used to provide an adequate design range for both high and low flux panel applications.

(g)   Inlet and outlet manifolds are identical in size, although typical design point densities require that the design be based on the outlet manifold, which contributes 97 percent of the total manifold pressure drop. When inlet and outlet manifolds are the same size, the weight penalty is small, and fabrication is simplified. Also, off-design operation benefits from equal manifold sizes.

(h)   The port-shoulder-radius to port-diameter ratio is 0.1 at the transition point between the inlet or outlet pipe and manifold. This value was selected to provide a calculation basis, although its effects are only approximated in the calculation procedure.

Analytical results.--Using the assumptions and constraints just discussed and procedures described more fully in Appendix C, pressure drop and weight were calculated for specific manifold configurations. Manifold performance was related by a flow rate parameter that combines heat flux and panel dimensions and is proportional to hydrogen flow rate, specific heat, and temperature change. This parameter, $(q/A)(\ell/w)$, permits flow rate to be indicated without a separate curve for each flow rate in each panel width. Fig. 36 shows the combined inlet and outlet manifold pressure drop as a function of the flow rate parameter for three different manifold widths and port diameters. The results are for an inlet coolant temperature of $100^\circ R$ ($55.5^\circ K$) and an outlet temperature of $1600^\circ R$ ($888^\circ K$). Other inlet and outlet hydrogen temperatures will cause a negligible difference in $_\sigma\Delta P$. This is because manifold friction pressure drop is a weak function of viscosity, and friction does not exceed one-half the manifold pressure drop. The outlet pressure used to calculate the pressure drops shown in fig. 36 was 250 psi (1560 kN/m^2). Consequently, the curves in fig. 36 indicate pressure drops slightly higher than these that occur with high flux panels and slightly lower than those that occur with low flux panels because the inlet pressure used in developing the data was 500 psi (3120 kN/m^2). The inlet manifold pressure drop is about 3 percent of the combined inlet and outlet manifold pressure drop at the pressure and temperature conditions that form the basis for fig. 36. Inlet manifold pressure drop, although linearly proportional to hydrogen inlet pressure, is considered constant because it is such a small fraction of the combined inlet and outlet manifold pressure drop.

The limiting value of the flow rate parameter at any particular manifold width is noted when the port pressure drop is equal to the overall manifold pressure drop allotment. This limit requires a zero pressure drop, infinite fin-height manifold. Work in support of the studies in ref. I, for example, used a pressure drop allotment of 45 psi (310 kN/m^2) for the manifold and assumed that 40 percent of the manifold pressure drop occurred in the port. On this basis, the manifold pressure drop allotment is equaled by the port pressure drop when the combined inlet and outlet manifold pressure drop is 112 psi (770 kN/m^2). Fig. 36 shows that the limiting value of the flow rate parameter is 600 Btu/sec-ft^2 (6810 kW/m^2) for a manifold width of 2 ft.

For flow rate parameters greater than the above limit, two options are available. One is to increase the port diameter and the other is to reduce manifold width by increasing the number of ports in the panel width of 2 ft (.61 m). The option of more than one port per panel width was exercised. Table 4 lists the selected number of manifold width segments and ports, manifold fin height, pressure drop, and port diameter. Manifold widths of 8 and 12 in. (20.3 and 30.5 cm) were used for the 500 Btu/sec-ft^2 (5680 kW/m^2) heat flux with a 3-ft (.914-m) flow length to illustrate the change in manifold fin height that occurs. The 8-in. (20.3-cm) segment width, which yields a shorter manifold fin height, was used for subsequent analysis.

Calculated manifold weight as a function of manifold width is shown in fig. 37 for tapered and rectangular manifolds. The port diameter is plotted because of the fixed ratio of port diameter to manifold width. Tapered manifolds are lighter than rectangular manifolds because the 0.5-in. (1.27-cm) vertical fin length between the top of the port and the bottom surface of the panel was tapered. The possible weight reduction afforded by use of tapered manifolds is most important at low heat-flux, low normal-pressure load design points, where the manifolds are a larger fraction of the total panel weight (ref. 1). Fig. 38 combines results from figs. 36 and 37 to show the trade between: (1) installation and ducting complexity, and (2) manifold weight and pressure drop. As the manifold width fed by single duct is increased to simplify installation, the manifold pressure drop and/or weight increases. For the geometry assumed, as manifold width increases, pressure drop increases much faster than manifold weight. Other assumptions for geometry (larger fin height and port diameter) can provide wider manifolds with no increase in pressure drop but at a higher rate of weight increase.

The manifold pressure drops shown in fig. 36 are based on uniform flow distribution across the width of the manifold. As already discussed, this is a convenient and practical approach to the manifold design problem. Fig. 39, however, shows the type of flow distribution obtainable in a typical manifold when no special provisions are made to obtain uniform flow. Table 5 shows the manifold geometry and operating conditions used in calculating the flow distribution of fig. 39. The pressure drops associated with the three widths of manifolds are shown in fig. 40. The maximum-to-minimum flow rate ratios and the ratio of core pressure drop to overall pressure drop are also noted. As shown in the experimental results, the core-to-overall pressure drop ratio is the most useful parameter for providing an indication of flow distribution in terms of maximum-to-minimum flow ratio. Only with the relatively high pressure drop ratios noted in fig. 40 can the relatively small flow nonuniformities indicated in figs. 39 and 40 be achieved.

Experimental results.--A completely analytical treatment of the manifold flow distribution problems has not proved successful in the past, even for relatively simple configurations. The purpose of tests performed during this program was to evaluate the performance of manifold configurations considered practical for application to regeneratively cooled panels. A widely applicable configuration is the flat manifold, rectangular or tapered, attached to the regeneratively cooled surface at right angles (figs. 35a and 35b). This was the reference configuration selected for evaluation. Table 6 lists the test

specimen geometries evaluated with the referenced configuration. Dimensions shown were obtained by measuring the parts. The test apparatus and procedures are described in Appendix D.

The maximum-to-minimum flow ratio through the core (the regeneratively cooled surface) is the characteristic flow uniformity parameter. Preliminary analysis indicated that the geometric manifold parameters of interest were the inlet or outlet port diameter, plate spacing (manifold fin height), manifold width parallel to panel width, and port radius-to-diameter ratio. Figs. 41 and 42 summarize the experimental investigation of the effect of these geometric parameters on flow uniformity and on pressure drop. Appendix D gives details of the data analysis as well as detailed performance data for the various test specimens. In general, the data reveal that increased flow uniformity results from manifold geometries with reduced pressure drop (resistance), because resistance is unequal in the various manifold flow paths.

In addition to pressure drop ratio, geometric similarity also provides a good first-order indication of flow distribution uniformity. Specimen 12 is twice the size of Specimen 2 in manifold width, port diameter, fin height, fin spacing, and fin thickness. Rather close agreement in flow rate ratio is obtained with W_{max}/W_{min} of 1.88 for Specimen 2 and 1.69 for Specimen 12.

Fig. 41 shows that flow is more uniform as port diameter is increased, as manifold width is reduced, as port radius-to-diameter ratio is increased, and as fin height is increased. Although changing port r/D provides as much change in flow uniformity as port diameter, the reason for this is not primarily a change in port loss coefficient but a change in horizontal fin friction and flow-turning pressure drop between the horizontal fin and vertical fin. With large port diameter or large r/D, the width of the horizontal fin adjacent to the port is approximately the same. Specimens 4 and 7 have practically equal flow nonuniformity (fig. 41) and horizontal fin flow width, but have markedly different port diameters (table 6). Even for the relatively narrow spans evaluated as part of the experimental program, flow distribution ratios (maximum flow to minimum flow at any station) of up to 5.75 were experienced (fig. 41). One reason for this is that the configurations were selected so as to highlight the problem rather than to minimize it. For example, the manifold plate spacing (fin height) for most of the specimens was set at 0.052 in. (0.132 cm); this resulted in relatively severe pressure drops and large maldistribution. In general, the weight penalty associated with greater plate spacings is small, so that use of such plate spacings appears quite feasible. Use of isothermal air was a second characteristic of the experimental evaluation that exaggerated flow nonuniformities. Both inlet and outlet manifolds contributed significantly to flow nonuniformity. For the boundary conditions used in the heat transfer analysis work of $T_{CI} = 100°R$ (55.5°K) and $T_{CO} = 1600°R$ (888°K), flow distribution is largely controlled by the lower density hydrogen in the outlet manifold.

The lowest test value for maximum-to-minimum flow ratio of 1.32 will probably not be acceptable for any operational application because of hydrogen flow rate and stress increases. Extrapolation of the curves to higher ratios of core to overall ΔP indicates that maximum-to-minimum flow ratios of 1.1 or

less require a core to overall-ΔP ratio greater than 0.5. Uniform flow will occur at a ΔP ratio of 1.0. In general, both analysis and test results indicate that manifolds for use in regeneratively cooled panels, even where the ΔP ratio is above 0.5, will require means for equalizing resistance in all manifold flow paths.

The experimental data can be used to make first estimates of flow distribution for configurations other than those tested. Appropriate correcting devices can then be designed for experimental evaluations. Any correcting device for configurations of the complexity required for panel manifolding will require iteration of the design based on test results.

CONCLUDING REMARKS

The heat transfer and fluid flow aspects of hydrogen-cooled flat panels have been evaluated. Pressure drop and thermal conductance data for a wide variety of coolant passage configurations were obtained. Application of data to integrated panel design was undertaken and is illustrated for typical cases in the present report.

Selection of a heat transfer design for a given application generally requires consideration of other factors. These factors include weight, thermal stress, structural life, system pressure levels, coolant consumption, manufacturing methods, and installation. No single performance figure of merit has been found that permits selection of coolant passage geometry, even if heat flux, thermal stress, coolant consumption, and coolant pressure drop are retained as the only parameters. Recourse to basic thermal conductance and pressure drop data, on the other hand, can quickly serve to narrow the selection to a limited and manageable number of candidates.

Various schemes for conserving coolant were investigated. Insulation is a logical candidate at all times for reducing heat load to the coolant. The benefits of flow folding by various techniques were also evaluated. As with insulation, flow folding aims at raising the average temperature of the heated surface and, hence, reducing heat load. At low heat fluxes, and at recovery temperatures below 7000°R (3890°K), cooling efficiencies can be increased by 5 to 10 percent. As heat flux and recovery temperature increase, the benefits are reduced. The complexity associated with any of the flow folding schemes can, therefore, be justified only where large areas operating at low heat-flux levels constitute a substantial part of a total flight system heat load. Preliminary analysis of the problem, prior to availability of the detailed analysis program, indicated much more substantial benefits from flow folding. The final results obtained were, therefore, somewhat disappointing in view of expected benefits.

The concern in typical panel applications with coolant conservation, thermal stress, pressure drop, envelope, and weight requires consideration of not only the panel proper, but of the manifolds. Indeed, the benefits

28

obtained by careful optimization of the coolant passage geometry and by the use of insulation and flow folding can be completely obviated by relatively small amounts of flow maldistribution in the manifolds.

The manifold studies presented in this report provide pressure loss and flow nonuniformity data resulting from use of various manifold concepts. Extension of this data to configurations other than those specifically evaluated is feasible, but will generally require experimental verification and iteration of the design. As a starting point for design, core (panel)-to-overall pressure drop ratios of 0.5 or higher appear necessary for satisfactory manifold performance, with maximum-to-minimum flow ratios of 1.1 or less across the width of the manifold. Even at these pressure drop ratios, efficient manifold design, i.e., light weight and low volume, may require use of special inserts or orificing to equalize pressure drops and flow rates across the panel.

All performance data presented in this report are based on the use of fluid properties evaluated at coolant bulk temperatures. The selection of reference temperature and basic performance correlation can significantly influence predictions relating to panel wall temperature difference. This is particularly true where wall-to-bulk temperature ratios are large and where hydrogen temperatures are below $90^\circ R$ ($50^\circ K$). The type and form of correlation used in design must, therefore, be an important consideration in regeneratively cooled panel applications.

always used. For curves with heat flux as abscissa, W/w was based on the change in hydrogen enthalpy between $100°R$ ($55.5°K$) and $2000°R$ ($1111°K$) at 500 psia (3450 kN/m^2), i.e., $W/w = 0.0001477$ $(q/A)\ell$, lb/sec-ft ($W/w = 0.00022$ $(q/A)\ell$, kg/sec-m).

Heat exchanger thermal conductance, heat flux, and fin ΔT are related by eq. 3.

$$T_W - T_F = \Delta T_{fin} \simeq T_W - T_C = \frac{q/A}{\eta_o hA_T/w\ell} \tag{3}$$

A 10-percent margin for manufacturing and curve-reading tolerances is included in all estimates of $\eta_o hA_T/w\ell$ and $T_W - T_F$. That is, values of $\eta_o hA_T/w\ell$ presented in this report are 0.9 of the calculated values and values of $T_W - T_F$ given are 1.11 of the calculated values.

When the hot wall was evaluated as insulation, k_i was evaluated at $(T_{WH} + T_W)/2$, where $T_{WH} = 2500°R$ ($1390°K$) and $T_W = 2000°R$ ($1111°K$); i.e., panel hot end $k_{if} = k_{ifin} = 16.2$ Btu/hr-$°R$-ft (28 W/m-$°K$) at $2250°R$ ($1250°K$)

Use of a fin layer brazed under a thin cover sheet was also analyzed as insulation. The above constants, the values for panel hot-end heat flux from table 3, and an insulation ΔT of $500°R$ ($278°K$) were substituted in eq. 4 to solve for h_{ifin}. The insulation thickness and weight were then calculated from eqs. 5 and 6. Eq. 4 was developed for the assumption of an effective insulation wall thickness of $t_{if} + t_{ifin}$ and an effective insulation fin height of $h_{ifin} - 2t_{ifin}$.

$$\frac{q/A}{\Delta T_i} = \frac{k_{iE}}{t_{iE}} = \frac{\dfrac{k_{if}}{t_{if} + t_{ifin}}}{1 + \dfrac{k_{if}(h_{ifin} - 2t_{ifin})}{(t_{if} + t_{ifin})(k_{ifin})(N_{ifin})(t_{ifin})}} \tag{4}$$

$$t_i = t_{if} + h_{ifin} \tag{5}$$

$$W_i/A = \rho_i \left\{ t_{if} + t_{ifin} \left[1 + (h_{ifin} - t_{ifin}) N_{ifin} \right] \right\} \tag{6}$$

Single-Pass Heat Exchangers

All single-pass heat exchanger thermal conductances and pressure drops at infinite recovery temperature were calculated by a digital computer program using the method described below.

Except where noted, the heat exchanger thermal conductance data are for local conditions of hydrogen temperature and pressure at the hydrogen outlet (hot end) of the heat exchanger. The calculation procedure shown below is also for local conditions, since overall performance for panel heat exchangers is usually obtained by integration of a series of incremental calculations, each made at local conditions. Specific assumptions are listed relative to appropriate parts of the analysis.

The calculation procedure described here is based on pipe flow correlations and applies to single-phase flow only. Conclusion 2 in ref. 8 indicates the general correctness of using pipe flow equations with all fluid properties evaluated at film temperature when, as in this study, bulk temperatures are above $90^\circ R$ ($50^\circ K$). Ref. 2 suggests the use of bulk temperatures in frequently interrupted boundary layer heat exchanger geometries, although test data at large wall-to-bulk temperature ratios are lacking. Film temperature in this discussion is equal to the arithmetic average of wall and bulk temperatures. The general curves of thermal conductance and fin ΔT were developed with fluid properties from fig. 2 evaluated at $2000^\circ R$ ($1111^\circ K$), a value that may be considered bulk or film at the user's discretion. If the temperature is considered to be film temperature, the flow rate parameter, W/w, must be multiplied by the ratio of bulk-to-film temperature before reading thermal conductance.

Bulk temperature was used to obtain all of the performance curves with cross section ΔT or wall temperature. It is convenient to use the local bulk temperature because iteration is avoided. Iteration is required with use of film temperature or a wall-to-bulk temperature ratio. Use of bulk temperature and wall-to-bulk temperature ratio results in nearly the same hot-wall temperatures at $1600^\circ R$ ($888^\circ K$) hydrogen temperature. Wall temperature and fin ΔT are far higher when wall-to-bulk temperature ratio is used at a $100^\circ R$ ($55.5^\circ K$) hydrogen temperature. Use of wall-to-bulk temperature ratio gives essentially the same results as use of film temperature when all fluid properties are evaluated at film temperature, and the heat transfer coefficient is multiplied by the bulk-to-film temperature ratio to the 0.8 power.

The parameter j is defined by eq. 7 and read from curves as a function of Reynolds number (eq. 8).

$$j = St \, (Pr)^{2/3} = \frac{h \, A_f \, (Pr)^{2/3}}{W \, C_p} \tag{7}$$

$$Re = \frac{4 r_h W}{\mu A_f} \tag{8}$$

These j vs Re curves were developed from data on the same or geometrically similar fluid passage geometries reported in ref. 2. The specific figure from ref. 2 used for f and j data is noted as the last term in the various fin geometry designations. The fin geometry designations are defined in the Symbols and Parameters table.

Specific test data are available for the 16 fin/in. (6.3 fin/cm) and the 20(7.9)R - 0.100(0.254) - 0.125(0.318) - 0.004(0.010) fin geometries. Fig. 10-61 from ref. 2 was used for all other rectangular offset fin geometries. To make use of a single performance curve suitable for a broad variety of fin geometries, the ratio of offset length, L_o, to hydraulic radius, r_h, was held constant at 8. The strongest control of the level of j and f for a particular class of fin geometry is the ratio of offset length to hydraulic radius. The constant 8 is empirical; it is based on test data in ref. 2 for geometries with offset length of 0.125 in. (0.318 cm) or greater, 20 fins/in. (7.9 fins/cm) or less, height of 0.100 in. (0.254 cm) or greater, and thickness of 0.004 in. (0.101 cm) or greater. Fig. 43 shows relationships between spacing, height, thickness, offset length, and hydraulic radius for rectangular fins of interest in this study, for which performance was calculated by fig. 10-61 of ref. 2.

Eq. 9 was used throughout this study to calculate heat transfer coefficients. Eqs. 10 and 11 are widely used correlations that evaluate fluid properties at other than bulk temperature.

$$\text{bulk } h = \frac{j \, W \, C_p}{A_f \, (Pr)^{2/3}} \tag{9}$$

where all fluid properties are evaluated at local bulk temperature.

$$\text{film } h = \frac{j_f \, W \, C_{p\,f} \, (T_{bulk}/T_f)^{0.8}}{A_f \, (Pr_f)^{2/3}} \tag{10}$$

where all fluid properties are evaluated at the arithmetic average of wall and local bulk temperature.

$$\text{wall-to-bulk } h = \frac{j \, W \, C_p}{A_f \, (Pr)^{2/3} \left(\dfrac{T_w}{T_{bulk}}\right)^n} \tag{11}$$

where all fluid properties are evaluated at local bulk temperature. For Reynolds numbers less than 5000, n is 0.0; for Reynolds numbers greater than 5000, n is 0.55.

Overall heat transfer surface effectiveness is calculated by eq. 12 for fins with uniform thickness parallel to flow.

$$\eta_o = 1 - \frac{A_{fin}}{A_T} \left[1 - \frac{\tanh \left(\dfrac{2h}{k_{fin} \, t_{fin}}\right)^{0.5} (l_{fin})}{\left(\dfrac{2h}{k_{fin} \, t_{fin}}\right)^{0.5} (l_{fin})} \right] \tag{12}$$

34

where for rectangular corrugated fin geometry

$$A_{fin} = w\ell \left(2(N)(h_{fin} - t_{fin}) + (1 - t_{fin} N) \right) \tag{13}$$

$$A_T = A_{fin} + w\ell(1 - t_{fin} N) \tag{14}$$

$$k_{fin} = 10 \text{ Btu/hr-}^\circ\text{R-ft } (17.3 \text{ W/}^\circ\text{K-m}) \text{ unless otherwise noted}$$

$$1_{fin} = h_{fin} + 0.5 \left(\frac{1}{N} - 3t_{fin} \right) \tag{15}$$

$$A_f = w(1 - t_{fin} N)(h_{fin} - t_{fin}) \tag{16}$$

$$r_h = \frac{h_{fin} A_f}{A_T} \quad (= D/4 \text{ for round tubes}) \tag{17}$$

Friction pressure drop was calculated by eq. 18. The Fanning friction factor, f, was read from curves as a function of Reynolds number (eq. 8). These f vs Re curves were developed from data on the same or geometrically similar fluid passage geometries.

$$\Delta P_f = \frac{f \ell W^2}{r_h A_f^2 2g_c \rho_a} \tag{18}$$

Hydrogen properties (fig. 2) at 1050°R (584°K) and 500 psia (3450 kN/m^2) were used to estimate $\sigma\Delta P/\ell$, $\sigma\Delta P$, and ΔP. A 10-percent margin for manufacturing and curve-reading tolerances is included in the stated values of $\sigma\Delta P/\ell$, resulting in 1.1 times the calculated values.

Pressure drop due to change in momentum, calculated by eq. 19, was not included in any of the $\sigma\Delta P$ curves, but was included in the curves for P_{CI}. A constant ratio of $\Delta P_m/\Delta P_f = 0.06$ was used.

$$\Delta P_m = \frac{W^2}{A_f^2 2g_c} \left(\frac{1}{\rho_o} - \frac{1}{\rho_I} \right) \tag{19}$$

Flow Routing Analysis Methods

All flow routings herein discussed, including the single-pass configuration, were analyzed by means of digital computer programs. Fig. 22 shows that simultaneous heat transfer can occur between the hot gas and all coolant streams only in the folded-in-width concept. The other folded-flow configurations have heat transfer between the hot gas and only one coolant layer. Separate analysis programs were used for the two general cases.

Both programs permit only two of the fluids to have temperature changes. The other one or two fluids must have constant temperature, which implies infinite capacity rate. This occurs for some two-phase heat transfer processes, and is approached for aerodynamic heating at hypersonic flight conditions. The heat transfer coefficients for the infinite capacity rate fluids are input as constants. Passage geometry, flow rate, temperature, and pressure are assumed to be uniform in the flow width. Incremental analysis is used, with the maximum length and incremental length selected as inputs.

A three-fluid heat exchanger analysis program was used for the folded-in-depth concept, and is applicable to plate and rectangular-fin heat exchanger geometries, including those having no fins in either one or both of the edge fluids. The finite capacity rate fluids (central and one edge) may be any single-phase liquid or gas. One edge fluid must be of infinite capacity rate because it is analyzed as rejecting or absorbing heat without temperature change. A range of fluid flow rates and boundary temperatures was used with the fin geometries considered to find the combination that gives the desired heat exchanger length.

The heat exchanger geometry inputs are:

   Metal thermal conductivity

   Fin spacing, fin height, and fin thickness for each of three fluids

   Initial number, final number, and increment in number of fin layers (sandwiches) for each of three fluids in each three-fluid cycle

   Initial width, final width, and increment in width of heat exchanger

   Initial number of cycles, final number of cycles, and increment in number of three-fluid cycles

   Initial length, total heat exchanger length, and length increment between initial and total length at which calculations are to be made

   Colburn modulus, j, and Fanning friction factor divided by Colburn modulus, f/j, as functions of the Reynolds number for each of two fluids undergoing temperature change

The operating condition inputs are:

   Flow rate for both fluids undergoing temperature change

   Constant temperature for infinite-capacity-rate fluid and temperature at some point in the heat exchanger for the two fluids undergoing temperature change

   Heat transfer coefficient for infinite-capacity-rate fluid

Specific heat, density, dynamic viscosity, and (Prandtl number)$^{2/3}$/C_p for both fluids undergoing temperature change

The outputs are:

Input values of fluid flow rates and passage geometries

Calculated values of Reynolds number and heat transfer coefficient for the two fluids undergoing temperature change

A tabulation of fluid and wall temperatures, heat fluxes, temperature differences, and density-adjusted pressure drops as a function of position relative to one end of the heat exchanger for both a three-fluid heat exchanger and a two-fluid heat exchanger

The two-fluid heat exchanger is similar to the three-fluid heat exchanger except that in the former, the outer fin layer with a finite-capacity rate is deleted. This feature permits direct comparison for identical geometry and fluid inlet conditions of both a folded-in-depth and a single-pass heat exchanger in one computer output.

The analysis procedure for each length increment requires calculation of:

(a)   The flow passage geometry for each fluid in terms of free-flow area, hydraulic radius, fin heat transfer area, and plate heat transfer area from input dimensions

(b)   Heat transfer coefficient, thermal conductance, and $\sigma\Delta P$ for each of the two fluids undergoing temperature change from pipe-flow equations and j and f/j tables

(c)   Wall temperatures for the center fluid passage from a heat balance on these walls and the one-dimensional conduction equation applied to the fins connecting these walls

(d)   Temperatures of the finite-capacity-rate fluids at the end of the length increment (used as inlet to the next increment) by two simultaneous differential equations based on a heat balance of the finite-capacity-rate fluids and the wall temperatures from procedure (c)

(e)   Net heat fluxes and the other wall temperatures by use of the values obtained in steps (b) and (c) above

A four-fluid heat exchanger analysis program was used for the folded-in-width concept. A cross section and one flow configuration analyzed by this program are depicted in fig. 44. The four fluids are identified as G, C, H, and A. Flow directions of fluids G and A are unimportant because both fluids are infinite-capacity-rate; that is, each fluid has a constant temperature, whether heat is being added or removed. The heat transfer coefficients for fluids G and A are assumed to be constant and are inputs to the program. Fluids C and H

are in passages between fluids G and A, and may be any single-phase liquid or gas. They may flow parallel or counter to each other.

For fluids C and H, the input includes:

Flow passage geometry (cross section dimensions and metal thicknesses)

Tables of Fanning friction factor, f, vs Reynolds number, Re

Tables of Colburn modulus, j, vs Reynolds number, Re

Tables of fluid properties (specific heat, dynamic viscosity, and Prandtl number, all as functions of temperature)

Flow rates, WC and WH

Inlet temperature for fluid C, TC, and outlet temperature for fluid H, TH

Flow geometry (parallel or counterflow, folded or not folded, total length, and analysis increment size)

A table of metal thermal conductivity as a function of temperature

For fluids G and A, the input includes:

Temperature and heat transfer coefficient

The output includes:

All inputs of importance

At each station of interest:

20 metal and 2 fluid temperatures (locations indicated in fig. 44)

Heat flux and heat transfer rate to or from surfaces facing fluids G and A

$\sigma \Delta P$ for fluids C and H

Reynolds number, heat transfer coefficient, and heat transfer rate to or from fluids C and H

Although the input includes dimensions and flow rates for one complete passage of fluids C and H, the temperature distributions calculated are for the shaded area between the lines of symmetry in fig. 44. The analysis procedure for each increment involves calculation of:

(a) The free-flow areas, heat transfer areas, and hydraulic radii of the passages for fluids C and H from input dimensions.

38

(b) The heat transfer coefficient, thermal conductance, and $\sigma\Delta P$ for fluids C and H from pipe-flow equations, using j and f tables.

(c) A heat balance at nodes I and 2 to obtain TI and T2 in terms of the local fluid temperatures, heat transfer coefficients, and geometry. As a basis for this calculation, a one-dimensional fin temperature distribution analysis is applied to the partition fin in terms of TI and T2, TC, TH, and the heat transfer coefficients for fluids C and H. Also, a one-dimensional fin temperature distribution analysis is applied to passage walls acting as fins for the assumptions that all values of TI are equal and that all values of T2 are equal. Heat transfer coefficients and temperatures for fluids A and G are used in this part of the analysis.

(d) Temperatures TC and TH at the end of the increment (the inlet to the next increment) by two simultaneous differential equations based on a heat balance on fluids C and H.

(e) The five temperatures along the centerline of each passage wall from temperatures TI and T2, and the one-dimensional fin temperature distribution analysis mentioned in (c) above.

(f) The IO external surface temperatures and eight internal surface temperatures for the passage walls between the finite-capacity-rate fluids C and H and the infinite-capacity-rate fluids G and A, from a one-dimensional conduction analysis using the local fluid temperatures and heat transfer coefficients as well as the fin centerline temperatures from procedure (e).

(g) Net heat flux to or from the passage walls by use of the integrated fluid temperatures and the wall centerline temperatures.

(h) The values for metal thermal conductivity are obtained from the table at the passage wall centerline average temperature.

The nature of the program makes it necessary to use a partly graphical solution for finding the relation between flow rate and fin geometry (weight) for panels of equal length. The general procedure used to determine flow rate as a function of fin geometry was the same for both high- and low-flux folded-flow systems. First, the intermediate hydrogen temperature between folded-flow and single-pass panels was determined by graphical techniques from the computer output. Then, the fin geometries that had acceptable maximum design wall temperatures and inlet pressures were determined, also by graphical techniques. Finally, plotting of effective fin thickness, $\bar{t}$, as a function of flow rate for both panel systems permitted calculation of the cooling efficiencies.

The intermediate hydrogen temperature between single-pass and folded-flow panels was calculated by the following procedure: From the computer output for various fin geometries in the folded-flow panel, maximum wall temperature was plotted as a function of panel length with parameters of hydrogen flow rate and outlet temperature (fig. 45). Cross plots of hydrogen flow rate and outlet

temperature, both versus maximum wall temperature, were prepared with fin geometry as a parameter for a panel length of 2 ft (0.61 m)(fig. 46). Also from the computer output for single-pass flow, plots of hydrogen temperature as a function of length were prepared for various fin geometries with flow rate as a parameter (fig. 47). The single-pass panel hydrogen inlet temperature was then read as a function of flow rate at 2 ft (0.61 m) upstream from the length at which the design value of hydrogen outlet temperature occurred. Hydrogen outlet temperature from the folded panel and hydrogen inlet temperature to the single-pass panel were then plotted in fig. 48 for low-flux panels and fig. 49 for high-flux panels. The intersection of these curves is the locus of inter- mediate hydrogen temperatures for the flow rate and fin geometry combinations indicated. The narrow range of hydrogen flow rates that satisfy all boundary conditions of hydrogen temperatures, heat flux, and fin geometry was then avail- able.

The procedure for determining configurations with acceptable maximum wall temperature or inlet pressure is described next. For low-flux, folded-flow panels, the maximum wall temperature was plotted vs flow rate with fin geometry as a parameter (fig. 50) to find those geometries that had maximum wall tempera- tures below $1860^\circ R$ ($1033^\circ K$). This maximum wall temperature was based on the use of Concept I (fig. 51), where the heat exchanger and structural panel are combined into a single layer, and the maximum design value for cross section ΔT was $100^\circ R$ ($55.5^\circ K$). Reference to fig. 50 shows that folded-flow heat exchangers with 14 fins/in. (5.5 fins/cm) or less had acceptable maximum wall temperatures. The maximum wall temperature in the single-pass panel was less than $1860^\circ R$ ($1033^\circ K$) for all fin designs in fig. 48.

The maximum pressure drop for all low-flux panel systems was 2 psi (13.8 kN/m^2) with an outlet pressure of 300 psi (2070 kN/m^2). The average tempera- ture used for pressure drop calculation in the panel system with a folded-flow and a single-pass panel was obtained from the inlet and outlet temperatures to three flow lengths, each of 2 ft (0.61 m).

$$\text{Average } T_C = (T_{CI} + 2T_{HT} + 2T_{HM} + T_{CO})/6 \tag{20}$$

For the single-pass panels in parallel, the average temperature was obtained from:

$$\text{Average } T_C = (T_{CI} + T_{CO})/2$$

Inlet pressure for the system with a folded and a single-pass panel in series at high heat flux was found from eq. 21, as follows:

$$P_{CI} = P_{CO} + \Delta P_C = \left[P_{CO}^2 + \left(1 + \frac{\Delta P_m}{\Delta P_f} \right)(R) \left(\frac{T_{CI} + 2T_{HT} + 2T_{HM} + T_{CO}}{3} \right) \sigma \Delta P \right]^{0.5} \tag{21}$$

where the terms are defined in the nomenclature except $\sigma \Delta P$ is the product of pressure drop and density ratio for the entire 6-ft (1.83-m) hydrogen flow

40

length. About half of the overall $\sigma\Delta P$ occurs in the folded-flow panel with a flow length of 4 ft (1.22 m) and plain fins, and half occurs in the single-pass with a flow length of 2 ft (0.61 m) and offset fins.

Inlet pressure for the single-pass panels was calculated from eq. 22:

$$P_{CI} = P_{CO} + \Delta P_C = \left[P_{CO}^2 + \left(1 + \frac{\Delta P_m}{\Delta P_f} \right) (R)(T_{CI} + T_{CO}) \left(\frac{\sigma\Delta P}{\ell} \right) (\ell) \right]^{0.5} \quad (22)$$

APPLICATION TO SPECIFIC CONFIGURATIONS

Three basic concepts shown in fig. 51 were considered in depth over a range of environmental conditions in the tradeoff studies of ref. 1. Ranges of heat flux and pressure used as panel design points are summarized along with the resulting hydrogen flow and panel thickness and weight. Heat exchanger weight is noted to indicate the relative importance of minimizing this fraction of the total.

To permit panel weight minimization during concept evaluation and tradeoff studies presented in ref. 1, figs. 52 through 60 were prepared for single-pass panels. Either (1) design maximum wall temperature or (2) the difference between design maximum wall temperature and hydrogen outlet temperature is plotted vs fin height for a range of fin thicknesses or fins per inch. Where pressure containment could not be achieved by fins of minimum gage and spacing, the plots of hydrogen inlet pressure and fin allowable pressure were used. The heat transfer aspects for obtaining these curves are discussed here.

The boundary conditions established during the tradeoff studies and based on structural analysis include those listed in the Statement of Problem. A heat exchanger hydrogen outlet pressure of 300 psia (2070 kN/m^2) was used to allow a 50 psi (345 kN/m^2) outlet manifold pressure drop. A heat exchanger hot wall thickness of 0.010 in. (0.0254 cm) and thermal conductivity of 14.5 Btu/hr-$^{\circ}$F-ft (25.1 W/m-$^{\circ}$K) were used with the hydrogen outlet temperatures, dimensions, concepts, and heat fluxes noted in figs. 52 through 60. The maximum temperatures of the adiabatic structural panel were assumed equal to the selected values of hydrogen outlet temperatures.

The design maximum wall temperature was usually below the maximum value of 2000°R (1111°K), especially at the lower end of the heat flux and hydrogen outlet temperature range. If the maximum structural temperature of the hydrogen outlet had been allowed to increase and the design maximum wall temperature had been held constant, the hydrogen flow rate would have reduced from the values indicated, but the structure weight would have increased above the values noted in ref. 1.

Rectangular offset fins and plain round tubes were the heat exchanger geometries studied for Concepts 2 and 3, fig. 51. The geometries for Concept 1 are plain rectangular fins.

Inlet pressure for Concepts 1 and 2 was calculated by:

$$P_{CI} = P_{CO} + \Delta P_C = \left[P_{CO}{}^2 + \left(1 + \frac{\Delta P_m}{\Delta P_f} \right) (R) \; (T_{CI} + T_{CO}) \left(\frac{\sigma \Delta P}{\ell} \right) (\ell) \right]^{0.5} \quad (23)$$

where $\sigma \Delta P / \ell$ may be read at W/w from figs. 12 through 15 for all concepts.

Inlet pressure for Concept 3 was calculated by:

$$P_{CI} = P_{CO} + \Delta P_C = \left[P_{CO}^2 + \left(1 + \frac{\Delta P_m}{\Delta P_f} \right) (R)(0.9T_{CI} + 1.1T_{CO}) \left(\frac{\sigma \Delta P}{\ell} \right) (\ell) \right]^{0.5} \quad (24)$$

As indicated by eq. (24), the pressure drop for Concept 3 is always slightly higher than for Concept 2 because the hydrogen inlet temperature to the hot heat exchanger is higher by 10 percent of the hydrogen ΔT, thus reducing density. This ΔT represents a nominal heat leak to the cold structural protection heat exchanger. A value of 1.06 was used for the parameter $(1 + \Delta P_m/\Delta P_f)$ in all calculations of P_{CI}.

For Concept 3, the pressure drop in the cold structural protection heat exchanger was made negligible (less than 1 percent of hot-heat exchanger ΔP) by use of a plain aluminum fin with a height of 0.050 in. (0.127 cm). There was no incentive to design a minimum weight fin for the cold heat exchanger because elimination of the fin altogether produces a weight reduction of only 0.07 lb/ft^2 (0.34 kg/m^2). The hydrogen pressure in the cold heat exchanger will be near the design maximum of 1000 psia (6900 kN/m^2) because the lightest weight heat exchangers for high-flux panels are generally those having the highest permissible inlet hydrogen pressure and pressure drop. Thus, the fin geometry selected for hydrogen pressure containment strength in the cold heat exchanger is 20(7.9)R - 0.050(0.127) - plain - 0.005(0.013) - (7 - 3, $L_o/4r_h$ = 100,

constant T_W). This combination of fin spacing and fin thickness provides the metal cross section required for pressure containment.

Design maximum wall temperature for all concepts was calculated by:

$$T_{DMW} = T_{CO} + \Delta T_{fin} + \frac{2}{3} (T_{WH} - T_W) = T_{CO} + \frac{q/A}{\eta_o hA_T/w\ell} + \frac{2q/A}{3k} \quad (25)$$

where $\eta_o hA_T/w\ell$ may be calculated at T_{CO} by the method described in Appendix A or may be read at W/w from fig. 12 through 15 and modified by:

$$(\eta_o hA_T/w\ell) \text{ at } T_{CO} = \frac{(\eta_o hA_T/w\ell) \text{ at } 2000^\circ R \ (1111^\circ K) \text{ from figs. 12 through 15}}{C}$$

and

$$C = \frac{(\eta_o hA_T/w\ell) \text{ at } 2000^\circ R \ (1111^\circ K) \text{ from fig. 21}}{(\eta_o hA_T/w\ell) \text{ at } T_{CO} \text{ from fig. 21}} \quad (26)$$

Use of fig. 21 to obtain $\eta_o hA_T/w\ell$ at T_{CO} is required only when all of the thermal conductance data are at one temperature as in figs. 12 through 15. If thermal conductance is calculated at the hydrogen temperature of interest, then use of C is not required. Reasons for use of 2/3 $(T_{WH} - T_W)$ are discussed in ref. 1. In ref. 1, T_{DMW} was used to determine the fin material strength and fin allowable pressure of the various heat exchanger geometries considered.

44

The uniform heat fluxes shown on the curves for Concept 3 were used for the hot heat exchanger. As noted previously, 10 percent of this heat flux was assumed to pass through to the cold structural protection heat exchanger. Consequently, 10 percent of the hydrogen temperature change was assumed to occur in the cold structural protection heat exchanger. The remaining 90 percent of the hydrogen temperature change occurred in the hot heat exchanger. The heat transferred from the hot to the cold heat exchanger would cause an increase in cooling efficiency at less than infinite recovery temperatures.

The hydrogen inlet pressure P_{CI} is not usually indicated at a heat flux of less than 100 Btu/sec-ft^2 (1135 kW/m^2) because the hydrogen pressure drop is low enough to be practically negligible. For example, in Concepts 2 and 3 the hydrogen pressure drop at this heat flux was always less than 15 psi (103 kN/m^2) with an outlet pressure of 300 psia (2070 kN/m^2). The pressure drop is not reported for Concept 1 because the greatest pressure drop caused by any fin geometry selected for Concept 1 was 56 psi (386 kN/m^2). This pressure drop occurred for a length of 5 ft (1.53 m) with a fin geometry of 20(7.9)R - 0.050 (0.127) - 60(153) - 0.003(0.008) - (7 - 3).

For the plain, round, tubular heat exchanger geometry, curves for two different hydrogen flow rates are shown in figs. 57 and 58, even though only one panel length and heat flux were used for each figure. The 18-percent higher flow rate is based on the assumption that the heat flux may be increased by the ratio of total exposed area to panel projected area. This is commensurate with the heat exchanger geometry description given in the Symbols and Parameters table. A tube wall thickness of 0.010 in. (0.025 cm) was used to have the same hot wall thickness used for the corrugated-fin heat exchanger geometries.

To compare the performance of bimetal and single metal fins, performance was calculated for rectangular offset fins with a thermal conductivity of 100 Btu/hr-$^{\circ}$R ft (173 W/m$^{\circ}$K) and is reported in figs. 59 and 60 for the minimum weight geometries. The fin thickness was assumed to be made up of equal parts of copper and Hastelloy X. The pressure containment strength was based on the Hastelloy X portion of the fin only. While the higher fin conductivity produced lower design maximum wall temperatures, the reduction was not enough to produce lighter weight heat exchangers than for a thermal conductivity of 10 Btu/hr-$^{\circ}$R-ft (17.3 W/m$^{\circ}$K). The allowable fin pressure dictates the minimum weight design in fig. 59; the maximum hydrogen inlet pressure dictates minimum weight design in fig. 60.

For performance evaluation where the recovery temperature is 5000°R (2780°K), the hot-gas heat transfer coefficients were calculated by eq. 1. These heat transfer coefficients were used in the four-fluid heat exchanger analysis program, Appendix A, to calculate the data plotted in figs. 61 through 64 for a length of 2 ft (0.61 m). Hydrogen flow rate, cross-section ΔT, and pressure drop read from these figures at hydrogen outlet temperatures of 1400, 1600, 1760, and 1900°R (778, 888, 976, and 1055°K) were used to prepare figs. 65 through 69, which are plots of design maximum wall temperature and hydrogen inlet pressure as functions of heat exchanger geometry. On the low-flux curves, where pressure drop is not significant, the hydrogen pressure containment

capability of each geometry is noted at one value of design maximum wall temperature. At the higher fluxes, where pressure drop is significant, the allowable fin pressure is plotted as a curve.

A noteworthy characteristic of figs. 61 through 64 is that hydrogen flow rate is reduced with an increase in fin height and fin spacing only at fluxes above 10 Btu/sec-ft^2 (114 kW/m^2). Increased fin height and spacing cause lower thermal conductance, higher fin ΔT, and higher wall temperature along the entire panel length, thus reducing the heat flux into the panel. The hydrogen flow rates for the various geometries noted in figs. 61 through 68 for T_R of 5000°R (2780°K) are always less than for the similar size and nominal heat flux panel with infinite recovery temperature.

Off-Design Performance

Steady-state performance was calculated for minimum-weight-panel heat exchangers selected during the tradeoff studies at various design heat fluxes. The results of these calculations are presented in figs. 70 through 75; the fin geometry, design heat flux, and flow rate are noted on these figures. In all cases, the heat fluxes range between 10 and 100 percent of design heat flux since maximum thermal stresses occur at design heat flux. The minimum weight fins analyzed for Concept 1 are for a normal pressure differential of 6.95 psi (47.9 kN/m^2). The normal pressure has no effect on the other heat exchanger geometry selections. Constants for the heat exchanger geometries are hydrogen outlet temperature of 1600°R (888°K), flow length of 2 ft (0.61 m), infinite recovery temperature, and fin thermal conductivity of 10 Btu/hr-°R-ft (17.3 W/m-°K).

The design maximum wall temperature and cross section ΔT curves for plain fins in figs. 72 and 73 do not increase uniformly as flux increases, but have a maximum value at a flux less than design point flux. The heat transfer performance curves from fig. 7-3 of ref. 2 used in estimating the plain-rectangular-fin performance for Concept 1 have a sharp variation at Reynolds numbers in the transition region between laminar and turbulent flow. Transition begins at a Reynolds number corresponding to a heat flux of about 70 Btu/sec-ft^2 (796 kW/m^2). There is no similar sharp transition and inflection in the performance curve from fig. 10-61 of ref. 2 used for rectangular offset fins in Concepts 2 and 3. The design maximum wall temperature and cross section ΔT curves are, therefore, smoothly increasing functions of heat flux. The uncertainties in performance at transition Reynolds numbers for plain geometries are a compelling reason for exercising caution when designing for their use. Flow instability is a potential problem at high ratios of outlet-to-inlet temperature, and at laminar Reynolds numbers, especially in plain geometries.

46

APPENDIX C

METHOD OF MANIFOLD ANALYSIS

The flow rate parameter used for data presentation in connection with the manifold analysis combines heat flux and panel dimensions. The parameter is related to hydrogen flow rate, specific heat, and temperature change by eq. 27.

$$(q/A)(\ell/w) = \frac{(W/w)(c_p)(T_{CO} - T_{CI})}{w} \tag{27}$$

Eq. 27 was obtained by rearranging and dividing eq. 2, Appendix A, by w. The parameter $(q/A)(\ell/w)$ provides a method of indicating flow rate without requiring a separate curve for each flow rate in each panel width. Inspection of eq. 27 shows that a separate flow rate is associated with each curve of the type shown in fig. 38; but each flow rate applies to a broad range of combinations of panel heat flux and dimensions.

To calculate pressure drops, the manifold resistances were separated as shown in fig. 76. The pressure drop in the separate resistances was calculated by application or extrapolation of loss coefficient data from ref. 6 for incompressible flow in mitered bends with expansion or contraction; and from directly applicable data in ref. 2 for friction in plane rectangular channels. The pressure drops and the separate resistances were added and the results are plotted in fig. 77 for either inlet or outlet manifolds in three width-and-port-diameter combinations and for two manifold fin heights. The pressure drop data in fig. 77 is for any combination of heat flux and length-to-width ratio for fixed manifold widths. If a manifold is to be designed for a fixed heat flux and length-to-width ratio, then a cross plot of fig. 77 can be made as in fig. 78, which applies to a broad range of manifold widths at discrete values of the flow rate parameter, $(q/A)(\ell/w)$.

The pressure drop for both manifolds combined was calculated from eq. 28 and plotted in fig. 38, as well as in fig. 79, for a broad range of manifold widths and values $(q/A)(\ell/w)$.

$$\Delta P_M = \frac{\sigma \Delta P_{MI}}{\rho_{MI}} + \frac{\sigma \Delta P_{MO}}{\rho_{MO}} \tag{28}$$

The important geometric and hydrogen pressure and temperature limitations are noted in fig. 70. Calculations were made for both inlet and outlet manifolds but the resultant values for $\sigma \Delta P_{MI}$ and $\sigma \Delta P_{MO}$ never differed by more than 15 percent. Since a tolerance of ±15 percent on the calculated loss coefficients for the various resistances is realistic, the larger value was assumed to apply for both inlet and outlet manifolds.

Table 7 indicates the fraction of manifold pressure drop contributed by the various resistances in fig. 76 for three manifold widths. The bend-with-area-change and horizontal friction caused from 40 to 90 percent of the pressure drop

in both the inlet and outlet manifolds. The last three resistances in the outlet manifold caused from 81 to 94 percent of the pressure drop in both manifolds combined, since the inlet manifold causes only 3 percent of the combined pressure drop. Also, from table 7, the outlet port pressure drop was calculated to be 40 percent of the overall manifold pressure drop. The remaining 60 percent of the overall manifold pressure drop is inversely proportional to the square of the manifold fin height. The manifold fin height controls the free flow area, A_f, which in turn controls pressure drop according to eq. 29. Eq. 29 applies to subsonic incompressible flow as it exists in panel manifolds with reasonable pressure drop.

$$\Delta P = \frac{(\Sigma k)W^2}{A_f^2 2g_c \rho} \tag{29}$$

To calculate manifold fin height it was first necessary to determine manifold pressure drop as a function of the flow parameter $(q/A)(\ell/w)$ for the specific manifold widths to be used in the tradeoff studies of ref. 1. These manifold pressure drops are shown in fig. 36 for a hydrogen outlet pressure of 250 psi (1560 kN/m^2). The manifold fin height was then calculated by using eq. 30.

$$\text{new } h_{\text{fin M}} = \text{basic } h_{\text{fin M}} \left(\frac{0.6 \Delta P_c}{\Delta P_M - 0.4 \Delta P_c} \right)^{0.5} \tag{30}$$

where basic $h_{\text{fin M}}$ = 0.25 in. (0.635 cm)

ΔP_c = manifold pressure drop from fig. 36

ΔP_M = pressure drop allotted to outlet manifold of 45 psi (310 kN/m^2)

While the results discussed above show manifold pressure drop for uniform flow, the flow distribution resulting from existing pressure drop distributions can be calculated by similar methods. The analysis is iterative as used here.

In the analysis, uniform flow was assumed so that each flow path in the manifold from the longest at the edge to the shortest at the center received equal flow. The overall pressure drop of each local flow path, ΔP_{local}, through both manifolds and the core was calculated by eq. 29 and used to obtain a first trial flow-distribution profile, related to the shortest path by use of eq. 31.

$$\frac{W_{\text{local}}}{W_{\text{max}}} = \frac{W_{\text{local}}}{W_{\text{SP}}} = \left(\frac{\Delta P_{\text{local}}}{\Delta P_{\text{SP}}} \right)^{0.5} = \left(\frac{\Delta P_{\text{local}}}{\Delta P_{\text{min}}} \right)^{0.5} \tag{31}$$

To obtain eq. 31, the terms are eliminated from eq. 29 that are constant for any specific manifold and core geometry with any conditions of hydrogen flow rate, pressures, and temperatures. By use of the nonuniform flow profile obtained

48

from eq. 31, the pressure drop through all passages from the longest at the edge, ΔP_{LP} to the shortest at the center, ΔP_{SP} is calculated. A second non-uniform flow profile was then obtained by use of eq. 31 with the new pressure drop profile. This iterative procedure is continued until the same pressure drop is calculated for all flow paths. This process is based on the principle that all flow paths in parallel between two common plenums or pipes have the same pressure drop. The flow distribution profiles resulting from the above iterative calculation procedure are shown in fig. 39 for the three manifold widths. The set of typical operating conditions and manifold geometry shown in table 5 was selected to allow preparation of fig. 39.

APPENDIX D

MANIFOLD TESTS

This appendix describes the test apparatus and procedures used to evaluate manifold flow distribution and pressure drop. Data reduction methods, data presentation, and detailed test results are discussed.

Test Apparatus

The test unit, shown disassembled in fig. 80 and installed with instrumentation in fig. 81, consists of inlet and outlet plenums, inserts for two manifold fin heights, and a 65-tube core. The core is split to allow insertion of an orifice plate flow resistance. The installation of the orifice plate is optional, and thus permits operation at two levels of core flow resistance.

Overall inlet and outlet pressures are obtained by instrumenting each plenum with five static pressure taps. The core contains three rows of 16 static pressure taps on individual tubes. The larger (inlet) core section contains two rows of pressure taps from which are obtained core inlet pressure and pressure drop data. The smaller core section contains the core outlet row of pressure taps. Fig. 82 schematically depicts the instrumented test unit with the core geometry noted.

The readout of the static pressures at the inlet and outlet plenums, and the core inlet and outlet (Stations 2 and 4) is accomplished on a 48-port Scannivalve. This valve may be indexed to each port location; the indexing feature provides pressure correspondence between the center tap and the selected port. Station 3 pressures are fed to a common manifold and individually valved off by means of toggle valves. Core pressure differences were measured by selecting the appropriate Scannivalve and Station 3 locations. A water manometer board was used for core pressure drop readouts between Stations 2 and 3, and pressure gages and a mercury manometer board are used for all static pressure readouts.

The supporting apparatus consists of flow control, filtering, and measuring sections upstream of the test unit. Flow measurement is accomplished upstream of the test unit by means of a sharp-edged orifice. The isothermal airflow temperature is recorded at this measuring section.

Photographs of typical manifold test specimens are presented in figs. 83 and 84. Specimen geometries, as measured from the test specimens, are given in table 6. The flow distribution insert is described later in this section. The sequences of parameters that were compared are summarized in the following table.

.

Comparison parameter sequence	Specimen numbers
Port diameter	5, 2, and 4
Port-radius-to-diameter ratio	7, 6, and 2
Manifold width	3, 2, and I
Fin height and geometric similarity	12, 2, and I
Rectangular and tapered manifold comparison	II, 10, 2, and I
Flow distribution insert	I with insert

The manifold flow passages are formed with mitered, plain rectangular fins, sandwiched between two manifold plates. The fins would be brazed between thin sheets about 0.010 in. (0.025 cm) thick to provide adequate coolant pressure containment with light weight in a flight hardware application. Therefore, only Specimens I and II were tested without fins for reference. The fins were attached to one manifold plate with a rubber-base cement and removed as necessary for tests by soaking in toluene. Balsa wood inserts at the sides and bottom of the manifold were used between plates to prevent bypass leakage when fin configurations were bolted into the test unit.

Data Reduction Method

Flow distribution across the core was determined from the measured static pressure drop distribution between Stations 2 and 3. The basic equation relating measured pressure drop and local flow rate in any tube is:

$$\Delta P_{2-3} = \frac{W^2}{2g\rho_{a_{2-3}}A^2}\left[2\rho_{a_{2-3}}\left(\frac{1}{\rho_3} - \frac{1}{\rho_2}\right) + \frac{f\ell}{r_h}\right] \tag{32}$$

where the terms are defined in the table Symbols and Parameters and

$$A = 0.558 \text{ in}^2 \ (3.6 \text{ cm}^2)$$

$$\ell = 5 \text{ in. } (12.7 \text{ cm})$$

$$r_h = 0.1045/4 = 0.0261 \text{ in. } (0.0662 \text{ cm})$$

$$\rho_{a_{2-3}} = P_2 + P_3/R(T_2 + T_3)$$

The core friction factor, f, is calculated from core test results with a uniform airflow. The flow rate in each of 16 tubes with pressure taps is calculated from eq. 33, which is obtained from eq. 32.

$$W_{local} = \left[\frac{2g\rho_{a_{2-3}}\, \Delta P_{2-3}\, A^2}{2\rho_{a_{2-3}}\left(\dfrac{1}{\rho_3} - \dfrac{1}{\rho_2}\right) + \dfrac{f\ell}{r_h}}\right]^{0.5} \tag{33}$$

The flow distribution is plotted as

$$\frac{W_{local}}{W_{avg}} = \frac{65\, W_{local}}{W_{total}} \tag{34}$$

where 65 is the number of core tubes.

Eqs. 33 and 34 form the basis of a computer program that was used to reduce the flow distribution test data. The required input includes core geometric parameters, test static pressures and temperatures, total flow rate, and barometric pressure. Tables of core Fanning friction factor obtained from test unit calibration and tables of fluid properties are also included. The program prints out the core weight/flow distribution, as well as the distribution of associated parameters such as Mach number, Reynolds number, and total pressure and pressure drop. The arithmetic average core inlet and outlet total pressures are calculated from the core inlet and outlet static pressures and flow distribution. Using these average pressures and the test unit inlet and outlet total pressures calculated from test static pressures and flow, the program calculates the various total pressure drop parameters and entrance and exit loss coefficients. In addition, the program plots the flow and pressure distributions.

By choosing the plain tube core length between Stations 2 and 3 as the flow measuring section, the test friction factor calibration can be referenced to standard plain tube friction data (ref. 2). This referencing makes possible more accurate calibration data interpretation and extrapolation. Performance characteristics such as inlet and outlet manifold loss coefficients are determined by using Stations 1, 2, 4, and 5.

Test Results

Test unit calibration.--The tube Fanning friction factor is shown in fig. 85. This characteristic was obtained by calibrating the core with nominally uniform flow. The corresponding flow distribution profiles are shown in fig. 86 for various flow rates, with and without orifices in the tubes. The slightly nonuniform flow profiles (less than 5 percent) appear to be due to measurement scatter rather than to actual flow nonuniformity, since tests with a reversed flow direction also caused a reversal in flow profile tendencies. The flow profiles shown are for full core width. The left half of the core, where more uniform flow is indicated and where 11 of each group of 16 static pressure taps are concentrated, was used to calculate the flow distribution reported in figs. 41 and 42, as well as elsewhere in this report. This use of test results from the left half of the core is also justified because the test unit and all specimens are symmetrical about the centerline.

The test points in fig. 85 include data from both the smooth tube section of 5-in. length and 9-in. overall length without the 0.063-in.-diameter orifice plate. Data from ref. 2 for length-to-diameter ratios, $\ell/4r_h$, of 100 and infinity are plotted to assist in correlating the data. The actual length-to-diameter ratio between Stations 2 and 3 is 48, but the effective $\ell/4r_h$ is between 100 and infinity, since the tube entrance is 19 diameters upstream of Station 2. Agreement is good throughout the turbulent Reynolds number range. The test data near the transition Reynolds number range show a slight upward curvature not present in the reference curves.

Core flow profiles.--As mentioned above, only the test data from the left-hand half of the core were reduced (with the exception of the test unit calibration data). Fig. 87 is representative of the static pressure data obtained for half the core and used with the data reduction method described above to obtain the flow profile for Specimen I (see fig. 89). The 0.0 core flow width coordinate is at the edge of the core and the 1.0 coordinate is at the centerline of the core.

In general, the tests for which results are presented in fig. 88 through 93 have identical manifold specimens at the core inlet and outlet. For additional information, some flow distribution curves in fig. 92 are presented for Specimen I at the inlet only and at the outlet only; and individual Specimen I samples have been designated as Specimen IA and IB to indicate the effects of manufacturing tolerance. These figures include results from tests with the flow distribution insert. Design and test of the insert are discussed later in this section. As expected, tests on Specimens I and II with the manifold fin removed do not exhibit the flow peak at the core centerline present in tests with fins, as shown in fig. 90. Test results with Specimen I at the inlet and Specimen 2 at the outlet are similar to those obtained with Specimen I at both inlet and outlet.

Unless otherwise noted, all reported tests are with the core orifice resistance; all manifold loss coefficients are based on the core area; test manifold loss coefficients, K_I and K_0, are based on uniform flow in the core area and test unit inlet or outlet density (Stations 1 and 5, respectively).

The flow distribution is expressed as a ratio of local flow in the core to average flow in the core. The flow profiles in figs. 89 through 93 are at a nominal airflow rate of 4 lb/min (0.0303 kg/sec). Fig. 88 shows a set of representative flow profiles for Specimen 2 at various flow rates. The flow profiles are almost identical because the flow in all tubes is in the turbulent Reynolds number regime. The minimum Reynolds number in any tube during any test was about 6000, just below the lower edge of the turbulent regime.

Comparison of core and manifold flow profiles.--General data correlation is difficult for the wide range of geometric manifold parameters investigated, especially because of the hard-to-define relationship between core and manifold flow profiles. The manifold configuration (table 6) provides opportunity for crossflow along the channel formed at the right-angle joint between the core

and the manifold. The flow at this joint adjusts itself to accommodate the static pressure profile along the joint. Because of the existing inequality in resistance of manifold paths, this pressure profile decreases from the location of the shortest manifold path to that of the longest path in the inlet manifold and from the location of the longest path to that of the shortest path in the outlet manifold. The crossflow is away from the shortest path in the inlet manifold and toward the shortest path in the outlet manifold. This crossflow pattern causes both inlet and outlet manifold flow profiles to be less uniform than those in the core. Calculations show, for example, that the manifold centerline flow is twice the core centerline flow for inlet manifold Specimens I and II.

The core static pressure profiles are flat near the edge of the core for all specimens, which indicates that the crossflow there is small. Thus, the longest-path test loss coefficients reported in fig. 94 were evaluated assuming no crossflow at the core edge.

A knowledge of the centerline manifold flow for inlet Specimen I permits analysis of the shortest-path pressure losses. In the longest path, the high-pressure-loss components were found to be the horizontal fin friction and the horizontal-to-vertical fin miter joint. Neither of these high-loss components is present in the shortest path. Calculations showed that vertical fin friction and core entrance losses were not more than 15 percent of the measured total losses. The high pressure difference between the plenum and the core tube in line with the port centerline can be accounted for by postulating a nonuniform flow distribution in the inlet port; that is, flow through the inlet port adjacent to the shortest path is 3.5 times greater than the average port flow.

General data correlations.--A summary of test results for the various specimen configurations appears in table 8 and was used to prepare the data presentations. Figs. 41 and 42 are a summary of the experimental investigation. The curves are drawn to indicate trends using easily identifiable parameters rather than exact functional relationship. The general trend shown is that flow becomes more uniform as manifold pressure drop (resistance) is reduced. The maximum-to-minimum flow ratio (W_{max}/W_{min}) and core-to-overall total pressure drop ratio ($\Delta P_{2-4}/\Delta P_{1-5}$) are, respectively, the characteristic flow and flow resistance uniformity parameters. Since the shortest-to-longest manifold path flow resistance ratio is small, the manifold pressure drop is representative of the nonuniformity existing in the various overall test unit flow paths. Hence, the related parameter, $\Delta P_{2-4}/\Delta P_{1-5}$, is a measure of the uniformity of flow resistance in the various paths.

Calculated and test loss coefficients.--It is helpful to know loss coefficients for various parts of the manifold because flow distribution can be calculated if loss coefficients are known. Loss coefficients were calculated for comparison with test loss coefficients and to provide generally useful data for design of similar manifolds. In summary, calculated coefficients for the manifold longest path were from 0.87 to 1.84 times test coefficients (after friction was subtracted) for outlet manifolds and from 1.79 to 2.52 times test coefficients for inlet manifolds (fig. 94).

An indication of the relationships between calculated and test loss coefficients for the longest manifold path is shown in fig. 94. Both test and calculated coefficients are evaluated for the longest manifold path and are directly comparable. Test-effective loss coefficients (discussed in later paragraphs and presented in figs. 95 and 96) are related to the particular flow nonuniformity and, therefore, will have values that increase with increasing flow nonuniformity. For convenience in this analysis, the loss coefficients are based on the horizontal fin flow area because the majority of the longest path losses are related to this fin. The frictional loss characteristics available in ref. 2 for the horizontal fin are directly applicable and have been subtracted from the overall coefficient. The test coefficient was evaluated by using the measured local path pressure drop and airflow, assuming core and manifold longest path flow to be equal.

Since the resistance of the shortest manifold path is small in relation to that of the longest path, the resistance of the longest path is characteristic of the effective resistance of the manifold. A theoretical calculation of this longest-path resistance and its relationship to the experimentally determined effective manifold resistance can be used in the prediction of manifold pressure drop and, hence, of flow uniformity.

The calculated longest-path loss coefficients and pressure drops are presented in table 9. The pressure drops are calculated on the basis of a uniform 4 lb/min (0.0303 kg/sec) airflow through the manifold at a density of 0.0765 lb/ft^3 (1.225 kg/m^3). Also tabulated are the corresponding test-effective loss coefficients with a nonuniform test flow of 4 lb/min (0.0303 kg/sec). Refs. 6 and 2 were used to estimate the longest-path pressure drops by dividing the path into the pressure drop components shown in table 10. As indicated in this table, the effect of some of the longest-path components was approximated by the sum of two or more pressure drop components (loss coefficients) when a direct calculation of a single loss coefficient was unavailable.

The relationship between calculated and test loss coefficients is presented graphically in fig. 96. As previously mentioned, fig. 95 presents the experimental relationship between the test loss coefficient and the flow ratio. Even though the curves drawn are not considered definitive, the trends are indicated and, with the data points, can be used to predict the manifold losses and the flow nonuniformity of similar manifolds.

The theoretical manifold flow resistance correlation presented in fig. 94 shows the calculated longest-path resistance to be higher than the test-effective resistance. This tendency is qualitatively correct since the longest-path resistance is always greater than the effective average resistance. Also, the calculated longest-path resistance diverges farther from the test-effective resistance as the resistances increase. Because the shortest-path resistance is about the same for all specimens, an increasing manifold resistance means an increasing longest-path to effective-average resistance ratio, and thus a diverging resistance curve. This trend is in

qualitative agreement with fig. 95, where an increased manifold resistance is shown to be accompanied by an increasing flow nonuniformity.

Comparison of tapered and rectangular manifolds.--Figs. 90 and 91 show a comparison between finned-tapered and rectangular manifold flow profiles. A comparison of the associated manifold flow resistances is shown in fig. 95. Tapered and rectangular manifolds, Specimens 11 and 1, respectively, are similar in flow profile and flow resistance. This similarity is expected since the taper in Specimen 11 is small, and it approaches Specimen 1 in flow geometry. Tapered and rectangular manifolds, Specimens 10 and 2, respectively, however, exhibit considerable differences in flow profile and flow resistance. These differences are primarily a result of a narrower vertical fin flow path (between edges of the horizontal fin at the port) in Specimen 10 than in Specimen 2 (fig. 83). This increased core centerline (shortest path) flow resistance in Specimen 10 causes a greater flow through longer paths, increasing both pressure drop and flow uniformity. The same shortest-path resistance was assumed for all specimens while calculating the manifold pressure drop correlations in figs. 95 and 96. Hence, differences in shortest-path resistance, as emphasized by Specimen 10, cause data correlation scatter in these figures.

Uniform flow manifold design.--Uniform flow in the manifold can be obtained by equalizing the resistance through all manifold flow paths with an orifice plate inserted adjacent to the edge of the vertical manifold fin near the core. The holes in the orifice plate must be nonuniformly spaced or have various diameters, or both. Equal resistance in all paths ensures uniform manifold flow and pressure drop, independent of the core and other uniform series resistances.

A uniform-flow manifold design was based on test data for Specimen 1, a rectangular manifold with one port. Nonuniformity in flow path resistances is caused by

(a) A variation in flow length (especially in the horizontal fin)

(b) The absence of a right-angle mitered fin turn in the shortest manifold flow paths at the middle of the manifold

The insert design shown in fig. 84 was attached at the exposed edge of the vertical fin. For a uniformly distributed 4 lb/min (0.0303 kg/sec) flow, the required nonuniformity in orifice plate pressure drop, as calculated for Specimen 1, is shown in fig. 97. At the centerline, the flow paths have no right-angle bend, and this results in a step in the required pressure drop profile. The required pressure drops for both inlet and outlet manifolds are identical with the exception of those required near the core centerline. The difference at this location is due to the higher calculated loss encountered in flowing through the expanding bend at the inlet port, as compared with the contracting bend at the outlet port. The insert tested was the same for both inlet and outlet manifolds.

Fig. 98 shows the calculated pressure loss characteristics of the orifice plate. The required orifice area is obtained by using figs. 97 and 98 and is shown in fig. 99. Using 0.030-in. (0.076-cm) diameter holes with a minimum clearance between holes of 0.020 in. (0.051 cm), the maximum available area is 0.014 in^2 per inch of orifice strip (0.029 cm^2 per cm of orifice strip). To obtain the larger required areas, the ends of the orifice strip are cut to a taper. A linear taper approximating the actual area variation is used. The hole density was maintained at greater than 10 holes per inch by using 0.020-in. (0.051-cm) diameter holes in the more restrictive locations near the port.

Uniform Flow Manifold Tests

The test results for Specimen I with the flow distribution insert are shown in figs. 92 and 93. The flow was not uniform, although the maximum-to-minimum flow ratio was reduced from 4.5 without inserts to 2.8 with inserts. The significance of the nomenclature used to identify the various curves is as follows:

(a) Fig. 92

    (1) Inlet with outlet: Flow profile obtained with the basic manifold configuration of Specimen I, without flow correcting inserts.

    (2) No. IA inlet: Flow profile obtained with the basic manifold configuration of Specimen I, used at the test unit inlet only. The test unit outlet is formed by a plenum without fins or insert and has a uniform resistance.

    (3) No. IB inlet: Same as for No. IA inlet, using the outlet manifold from (1), above, in the inlet for comparison purposes.

    (4) No. IA outlet: Flow profile obtained with the basic manifold configuration of Specimen I, from (2), above, used at the outlet only. The inlet is formed by a plenum without fins or insert and has a uniform resistance.

    (5) No. IA inlet with insert: The configuration described in (2), above, with insert added.

(b) Fig. 93

    (1) Bottom curve: For basic manifold configuration of Specimen I, used in both inlet and outlet, with flow correcting inserts added to each, shown for comparison. Differences in the curve are due to manufacturing variances.

    (2) Top curve: For basic manifold configuration of Specimen I, with designated manifold ends run separately, the other end being at a uniform resistance.

Detailed modification of hole spacing can produce uniform flow. The insert was modified to improve the flow profile at the core center by enlarging the flow area in the center of the insert. The diameter of the seven center holes (approximately 0.5-in. (1.27-cm) span) was increased from 0.020 in. (0.051 cm) to 0.025 in. (0.0635 cm). Fig. 92 shows the flow distribution obtained. The maximum-to-minimum flow ratio was reduced from 2.8 with the basic insert design to 2.6 with the redrilled insert. The local change in profile, which was the purpose of the modification, was much more substantial. It does not appreciably affect the overall flow ratio because the maximum and minimum flows occur elsewhere. Further iteration in hole dimensions could be used to produce completely uniform flow in any manifold.

REFERENCES

1. Flieder, W. G.; Richard, C. E.; Buchmann, O. A.; and Walters, F. M.: An Analytical Study of Hydrogen-Cooled Panels for Application to Hypersonic Aircraft. NASA CR-1650, 1970.

2. Kays, W. M.; and London, A. L.: Compact Heat Exchangers. Second Ed., McGraw-Hill Book Co., Inc. (New York), 1964.

3. Anonymous: Properties of Parahydrogen. Report 9050-6S, Aerojet-General Corp., PRA-SA-DSA-30, September 1963.

4. Sparrow, E. M.; Lloyd, J. R.; and Hixon, C. W.: Experiments on Turbulent Heat Transfer in an Asymmetrically Heated Rectangular Duct. ASME Paper No. 65-HT-8.

5. Elam, B. F.: Heat Transfer in Honeycomb-Core Sandwich Panels. ASME Paper No. 65-HT-13.

6. Aero-Space Applied Thermodynamics Manual. Society of Automotive Engineers Committee A-9, January 1962.

7. Hendricks, R. C.; Graham, R. W.; Hsu, Y. Y.; and Freidman, R.: Experimental Heat Transfer Results for Cryogenic Hydrogen Flowing in Tubes at Subcritical and Supercritical Pressures to 800 psia. NASA TN D-3095.

8. Hendricks, R. C.; Graham, R. W.; Hsu, Y. Y.; and Medeiros, A. A.: Correlation of Hydrogen Heat Transfer in Boiling and Supercritical Pressure States. ARS Journal, February 1962, pp. 244-252.

TABLE I

HEAT EXCHANGER GEOMETRY LIMITS

Component	Governing condition	Affected parameter	Limitation
Heat transfer fin	Erosion of parent metal by braze filler alloy	Fin thickness	Minimum thickness: superalloy: .003 in. (.008 cm) aluminum: .004 in. (.010 cm)
	Collapse of fins due to braze fixture loads	Fin height, density, and thickness	Minimum collapsing load of 5 psi (34.5 kN/m^2) at 2100°F (1420°K) for superalloys
	Forming tools and material properties	Fin density and thickness	Fins/in. (Fins/cm) Max. fin thickness in. (cm) 40 (15.8) max. .003 (.008) 30 (11.8) .004 (.010) 20 (7.9) .006 (.016) 10 (3.94) .010 (.025)
	Fabrication, pressure drop	Fin height	.025 in. (.063 cm) min.
	Weight, fin ΔT		.100 in. (.254 cm) max.
Tubes	Fabrication (assembly and brazing)	Outside diameter	.050 in. (.127 cm) min. .100 in. (.254 cm) max.
Heat exchanger surface sheet (tube wall)	Handling, particle damage, fabrication	Thickness	Minimum thickness: superalloy: .010 in. (.025 cm) aluminum: .016 in. (.040 cm)
Coolant manifold pipes	Handling	Wall thickness	Minimum thickness .030 in. (.0762 cm)

TABLE 2

COOLING EFFICIENCY FOR FLOW ROUTING CONCEPTS

Heat flux, Btu/sec-ft² (kW/m²)	Recovery temperature, °R (°K)	Cooling efficiency		
		Single pass	Folded-in-depth	Folded-in-width
10 (114)	3000 (1670)	0.47	0.69	0.64
	5000 (2780)	.78	---	.84
	7000 (3890)	.83	.89	.94
250 (2840)	5000 (2780)	.81	---	.84
	7000 (3890)	.89	.86	.89
500 (5680)	5000 (2780)	.84	---	.86
	7000 (3890)	.86	.86	.88

TABLE 3

TYPICAL INSULATION PERFORMANCE AT T_R = 5000°R (2780°K)

Insulation ΔT, °F	0	500	0	500
Nominal q/A, Btu/sec-ft² (kW/m²)	250 (2840)	250 (2840)	500 (5680)	500 (5680)
T_{WH}, °R (°K)	2000 (1111)	2500 (1390)	2000 (1111)	2500 (1390)
T_{CO}, °R (°K)	1760 (978)	1760 (978)	1600 (888)	1600 (888)
h_G, Btu/sec-°R-ft² (kW/°K-m²)	0.0555 (1.13)	0.0555 (1.13)	0.111 (2.26)	0.111 (2.26)
Panel hot end q/A, Btu/sec-ft² (KW/m²)	167 (1900)	139 (1580)	333 (3780)	278 (3160)
Average T_{WH}, °R (°K)	1230 (684)	2030 (1128)	1460 (812)	2160 (1200)
Average q/A, Btu/sec-ft² (kW/m²)	209 (2370)	165 (1870)	393 (4460)	315 (3580)
W/A, lb/sec-ft² (kg/sec-m²)	0.036 (0.175)	0.028 (0.136)	0.074 (0.360)	0.059 (0.287)
Solid-plate insulation				
Thickness, t_i, in. (cm)		0.194 (0.493)		0.097 (0.246)
Weight, lb/ft² (kg/m²)		8.38 (40.8)		4.19 (20.4)
Fin and sheet insulation				
(includes t_{iw} of 0.010 in. (0.025 cm), t_{ifin} of 0.003 in. (0.008 cm), and N_{ifin} of 40/in. (15.8/cm)				
Thickness, t_i, in. (cm)		0.0378 (0.096)		0.0261 (0.0663)
Weight, lb/ft² (kg/m²)		0.690 (3.36)		0.628 (3.06)
Heat exchanger geometry				
Flow length	2 ft (0.61 m)			
Fins	20(7.9)R-0.070(0.178)-0.090(0.228)-0.006(0.015)-(10-61)		30(11.8)R-0.038(0.096)-0.060(0.153)-0.003(0.008)-(10-61)	

TABLE 4

MANIFOLD GEOMETRY FOR
TRADEOFF STUDIES

Flux, Btu/sec-ft^2 (kW/m^2)	Length, ft (m)	(q/A)(ℓ/w) Btu/sec-ft^2 (kW/m^2)	No. of manifold segments (ports)	Manifold segment width,in. (cm)	ΔP_M, psi (kN/m^2)	h_{Mfin}, in. (cm)	Port diameter, in. (cm)
250 (2840)	2 (.61)	250 (2840)	1	24 (61.0)	20 (138)	.142 (.36)	1.75 (4.45)
250 (2840)	3 (.914)	375 (4260)	1	24 (61.0)	42 (290)	.236 (.60)	1.75 (4.45)
500 (5680)	2 (.61)	1000 (11 350)	2	12 (30.5)	32 (221)	.193 (.49)	1.25 (3.18)
500 (5680)	3 (.914)	1500 (17 030)	2	12 (30.5)	72 (496)	.407 (1.03)	1.25 (3.18)
500 (5680)	3 (.914)	2250 (25 540)	3	8 (20.3)	55 (380)	.300 (.76)	1.00 (2.54)

TABLE 5

MANIFOLD GEOMETRY AND OPERATING CONDITIONS FOR CALCULATED FLOW DISTRIBUTION

Panel length, ft (m)	2 (0.61)
Heat flux, Btu/sec-ft^2 (kW/m^2)	250 (2840)
T_{CI}, $^{\circ}$R ($^{\circ}$K)	100 (55.5)
T_{CO}, $^{\circ}$R ($^{\circ}$K)	1600 (888)
W/w, lb/sec-ft (kg/sec-m)	0.0935 (0.139)
Core pressure drop, psi (kN/m^2)	40 (276)
P_{CI}, psia (kN/m^2)	500 (3450)

Manifold geometry:

    Horizontal fin

    8 (3.15)R - 0.164 (0.417) - plain - 0.004 (0.010)

    Vertical fin

    10 (3.94)R - 0.164 (0.417) - plain - 0.004 (0.010)

TABLE 6

MANIFOLD SPECIMEN GEOMETRY

Item	Description	Rectangular manifolds								Tapered manifolds	
a	Specimen number	1	2	3	4	5	6	7	12	10	11
b	Number of ports	1	2	3	2	2	2	2	1	2	1
c	Manifold width/total width	0.5	0.5	0.333	0.5	0.5	0.5	0.5	0.5	—	—
d	Diameter of ports, D, in. (cm)	0.406(1.03)	0.406(1.03)	0.406(1.03)	0.812(2.06)	0.313(0.795)	0.406(1.03)	0.406(1.03)	0.812(2.06)	0.406(1.03)	0.406(1.03)
e	Fin hole diameter, in. (cm)	0.56(1.42)	0.545(1.38)	0.56(1.42)	0.98(2.49)	0.43(1.09)	0.80(2.03)	0.915(2.32)	1.02(2.59)	0.52(1.32)	0.52(1.32)
f	Port radius ratio, r/D	0.1	0.1	0.1	0.1	0.1	0.4	0.692	0.1	0.1	0.1
g	Fin hole diameter = horizontal fin flow width, in. (cm)	0.55(1.40)	0.55(1.40)	0.53(1.35)	0.97(2.46)	0.45(1.14)	0.78(1.98)	0.98(2.49)	0.99(2.52)	0.57(1.45)	0.52(1.32)
h	Vertical fin flow length, in. (cm)	0.31(0.788)	→	→	→	→	→	→	0.31(0.788)	0.31(0.788)	0.31(0.788)
i	Fin height (plate spacing), in. (cm)	0.052(0.132)	→	→	→	→	→	0.052(0.132)	0.104(0.264)	0.052(0.132)	0.052(0.132)
j	Total width, in. (cm)	9.85(25)	→	→	→	→	→	→	9.85(25)	9.85(25)	9.85(25)
k	Fins per in. (cm)	20(7.9)	→	→	→	→	→	20(7.9)	10(3.9)	20(7.9)	20(7.9)
l	Fin thickness, in. (cm)	0.002(0.005)	→	→	→	→	→	0.002(0.005)	0.004(0.010)	0.002(0.005)	0.002(0.005)

+ Specimens I and II also tested without fins

Fin height (plate spacing)

Port radius, r

Core tubes
Vertical fin
Horizontal fin

.20 in. (.51 cm)

Vertical fin flow length

Manifold width

Port diameter, D

Fin hole diameter

Core tubes
Vertical fin
Horizontal fin

Rectangular

Horizontal fin flow width

Core tubes
Vertical fin
Horizontal fin

Manifold width

Port diameter, D

Fin hole diameter

Tapered
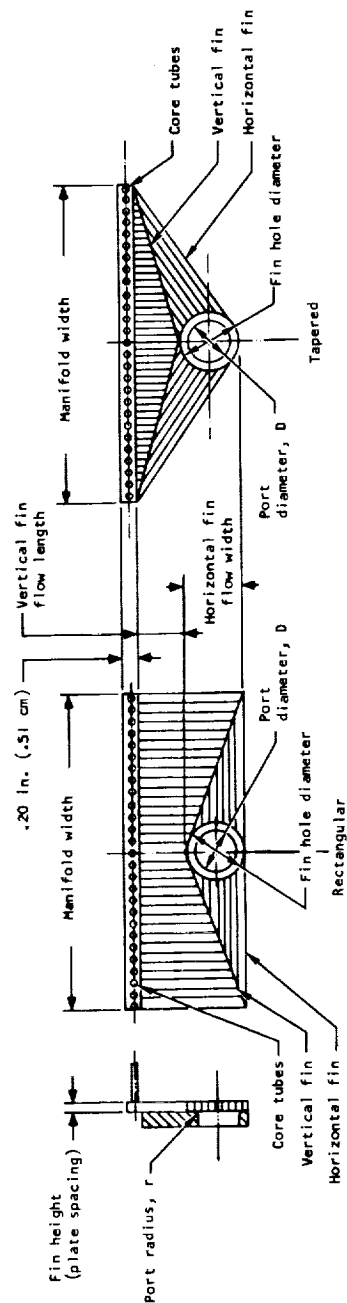
TABLE 7

MANIFOLD LOSS COMPONENTS

Loss components	Percent of overall manifold pressure drop		
	Manifold width, ft (m)		
	0.5 (.153)	1 (.305)	2 (.61)
Inlet manifold:			
Inlet port	14.0	10.1	5.2
Horizontal friction	20.1	31.3	48.4
90-deg turn and expansion	50.0	50.9	43.4
Vertical friction	2.2	.9	.3
Three 90-deg turns	9.6	4.7	1.9
Contraction at core inlet	4.1	2.1	.8
	100.0	100.0	100.0
Outlet manifold:			
Expansion at core outlet	4.4	2.2	.9
Three 90-deg turns	9.6	4.7	1.9
Vertical friction	2.2	.9	.3
90-deg turn and contraction	18.3	16.9	11.5
Horizontal friction	20.1	31.3	48.4
Exit port	45.4	44.0	37.0
	100.0	100.0	100.0

$(q/A)(\ell/w) = 250$ Btu/ft²-sec (2840 kW/m²)
Fin geometry = 10 (3.94)R - .250 (.635)- plain - .004 (.010)

TABLE 8

SUMMARY OF TEST RESULTS

Specimen	Airflow lb/min	Airflow kg/sec	$\frac{W_{max}}{W_{min}}$	$\frac{\Delta P_{2-4}}{\Delta P_{1-5}}$	K_I	K_0	ΔP_{1-5} psi	ΔP_{1-5} kN/m²	$\frac{\Delta P_{1-5}}{\Delta P_1}$ percent
1	4.08	0.0309	4.52	0.0181	215	171	67.9	478	78.5
2	4.08	.0309	1.88	.0686	46.7	43.2	24.7	170	48.8
2	6.00	.0454	1.81	.0802	45.6	41.3	35.7	246	57.4
2	8.02	.0607	1.82	.0669	43.4	40.5	48.4	336	60.0
3	4.05	.0306	1.41	.112	25.4	28.5	15.6	107	44.0
3	6.00	.0454	1.38	.0997	24.1	27.9	24.7	170	48.8
3	8.01	.0606	1.37	.103	23.7	26.9	34.3	236	51.9
4	4.03	.0305	1.37	.161	18.6	19.2	11.9	82	37.4
4	5.98	.0452	1.33	.174	16.0	18.4	18.3	126	41.0
4	8.06	.0610	1.32	.163	17.2	17.9	26.3	181	44.8
5	4.00	.0303	1.99	.0337	91.4	70.3	34.0	234	62.7
5	5.97	.0452	1.93	.0323	86.2	63.3	53.6	370	68.0
6	4.02	.0304	1.70	.107	35.3	27.3	16.5	114	45.5
6	6.00	.0454	1.66	.112	32.5	26.2	26.0	179	50.2
6	8.12	.615	1.65	.106	33.0	35.4	36.7	253	53.4
7	4.02	.0304	1.41	.145	21.9	20.6	12.7	87.6	39.0
7	5.96	.0451	1.36	.153	19.7	19.7	19.6	135	43.2
7	8.04	.0609	1.36	.157	19.9	18.9	27.8	192	46.7
10	4.05	.0306	1.78	.0387	75.9	66.2	32.0	221	61.7
10	6.01	.0455	1.71	.0355	78.1	63.4	50.5	348	66.0
10	8.08	.0611	1.70	.0351	73.9	61.2	68.9	475	68.3
11	4.07	.0308	3.79	.0102	278	175	72.0	496	76.8
11	4.09	.0309	3.37	.0106	262	176	71.8	495	76.7
12	4.04	.0306	1.69	.148	18.2	21.9	12.4	85.5	38.4
12	5.80	.0439	1.64	.146	15.7	22.0	18.5	128	41.8
12	8.05	.0609	1.62	.144	16.2	20.8	27.0	186	45.4
1 no fins	4.00	.0303	2.67	.0530	29.0	89.9	16.1	111	25.3
11 no fins	4.00	.0303	5.75	.0350	44.0	93.6	35.9	248	63.8
1 in, 2 out	4.03	.0305	3.85	.0300	325	43.1	32.3	223	34.4
1 insert*	3.19	.0241	3.01	.00238	604	521	63.7	440	56.2
1 insert**	3.20	.0242	2.86	.00193	635	490	62.9	434	55.9

*1B in, 1A out, no core orifice resistance
**1A in, 1B out, no core orifice resistance

70

TABLE 9
CALCULATED LONGEST-PATH AND TEST-EFFECTIVE MANIFOLD RESISTANCES AND LOSS COEFFICIENTS

Specimen	1	2	3	4	5	6	7	10	11	12
Inlet manifold components										
A. Port										
K (port)*	1.2	←		→	1.2	.75	.39	1.2	1.2	1.2
ΔP (psi)	9.3	2.3	1.0	0.1	6.5	1.4	0.8	2.3	9.5	0.6
(kN/m^2)	64.2	15.9	6.9	.69	44.8	9.7	5.5	15.9	65.5	4.1
B. Horizontal fin friction										
ΔP (psi)	103.3	12.9	4.1	4.1	19.3	6.4	4.1	12.0	115.8	4.6
(kN/m^2)	713.	89.	28.2	28.2	133.	44.2	28.2	82.8	799.	31.7
C. Fin miter joint										
K (horizontal fin)*	2.40	2.22	2.05	1.93	2.30	2.07	1.93	2.04	2.04	2.22
ΔP (psi)	95.3	22.2	9.9	6.3	34.4	10.2	6.1	19.0	90.1	9.0
(kN/m^2)	658.	153.	68.4	43.4	238.	70.4	42.1	131.	621.	62.1
D. Vertical fin friction										
ΔP (psi)	0.4	0.4	0.4	0.6	0.4	0.5	0.6	0.4	0.4	0.0
(kN/m^2)	2.76	2.76	2.76	4.14	2.76	3.45	4.14	2.76	2.76	0
E. Core entrance										
K (vertical fin)*	1.6	←							→	1.6
ΔP (psi)	0.9	←						→	0.9	0.3
(kN/m^2)	6.21	←						→	6.21	2.07
Overall										
Calculated longest path										
ΔP (psi)	209.2	38.7	16.3	12.0	61.5	19.4	12.5	34.6	216.7	14.5
(kN/m^2)	1442.	267.	112.	82.8	424.	134.	86.2	238.	1495.	100.
K$_I$* Calculated longest path	500.	92.4	38.9	28.8	147.2	46.5	30.0	82.6	516.	34.6
Test effective	215.	46.7	25.4	18.6	91.4	35.3	21.9	75.9	278.	18.2
Outlet manifold components										
A. Core exit										
K (vertical fin)*	1.6	←							→	1.6
ΔP (psi)	0.9	←						→	0.9	0.3
(kN/m^2)	6.21	←						→	6.21	2.07
B. Vertical fin friction										
ΔP (psi)	0.4	0.4	0.4	0.6	0.4	0.5	0.6	0.4	0.4	0.0
(kN/m^2)	2.76	2.76	2.76	4.14	2.76	3.45	4.14	2.76	2.76	0
C. Fin miter joint										
K (horizontal fin)*	2.08	2.06	2.01	1.97	2.07	2.02	1.97	1.88	1.72	2.06
ΔP (psi)	82.8	20.6	9.7	6.4	31.0	10.1	6.0	17.7	76.0	8.3
(kN/m^2)	571.	142	66.9	44.1	214.	69.6	41.4	122.	524.	57.2
D. Horizontal fin friction										
ΔP (psi)	103.3	12.9	4.1	4.1	19.3	6.4	4.1	12.0	115.8	4.6
(kN/m^2)	713.	89.	28.2	28.2	133.	44.2	28.2	82.8	799.	31.7
E. Port										
K (port)*	1.6	1.6	1.6	1.95	.15	0.74	0.50	1.6	1.6	1.6
ΔP (psi)	12.4	3.1	1.4	0.3	8.2	0.8	1.2	3.1	12.4	0.9
(kN/m^2)	85.5	21.4	9.65	2.07	56.6	5.52	8.28	21.4	85.5	6.21
Overall										
Calculated longest path										
ΔP (psi)	199.8	37.9	16.5	12.3	59.8	18.7	12.8	34.1	205.5	14.1
(kN/m^2)	1378.	262.	114.	84.9	412.	129.	88.3	235.	1415.	97.3
K$_0$* Calculated longest path	479.	90.6	39.6	29.4	143.	44.7	30.6	78.4	491.	33.6
Test effective	171.	43.2	28.5	19.2	62.7	27.3	20.6	66.2	175.	21.9

*See table 10 for areas used in calculating K values
Air flow = 4 lb/min (.0303 kg/sec)
Density ρ = .0765 lb/ft^3 (1.225 kg/m^3)

71

TABLE 10

LONGEST-PATH PRESSURE DROP ANALYSIS

Longest path components	Pressure drop components	Flow area based on dimensions in table 6 denoted by item letter
Inlet Manifold		
A. Port	90° round bend plus expansion from port to fin entrance	Port area $\pi (d)^2/4$
B. Horizontal fin	Friction for smooth, square ducts	Horizontal fin flow area 2 (i)(g)(b) less fin material
C. Fin miter joint	Miter bend plus expansion from horizontal to vertical fin	Horizontal fin flow area 2 (i)(g)(b) less fin material
D. Vertical fin	Friction for smooth, square ducts	Vertical fin flow area (i)(j) less fin material
E. Core entrance	90° miter bend	Vertical fin flow area (i)(j) less fin material
Overall		Core area
Outlet Manifold		
A. Core exit	90° miter bend	Vertical fin flow area (i)(j) less fin material
B. Vertical fin	Friction for smooth, square ducts	Vertical fin flow area (i)(j) less fin material
C. Fin miter joint	Miter bend plus contraction from vertical to horizontal fin	Horizontal fin flow area 2 (i)(g)(b) less fin material
D. Horizontal fin	Friction for smooth, square ducts	Horizontal fin flow area 2 (i)(g)(b) less fin material
E. Port	90° round bend plus contraction from fin exit to port	Port area $\pi (d)^2/4$
Overall		Core area

72
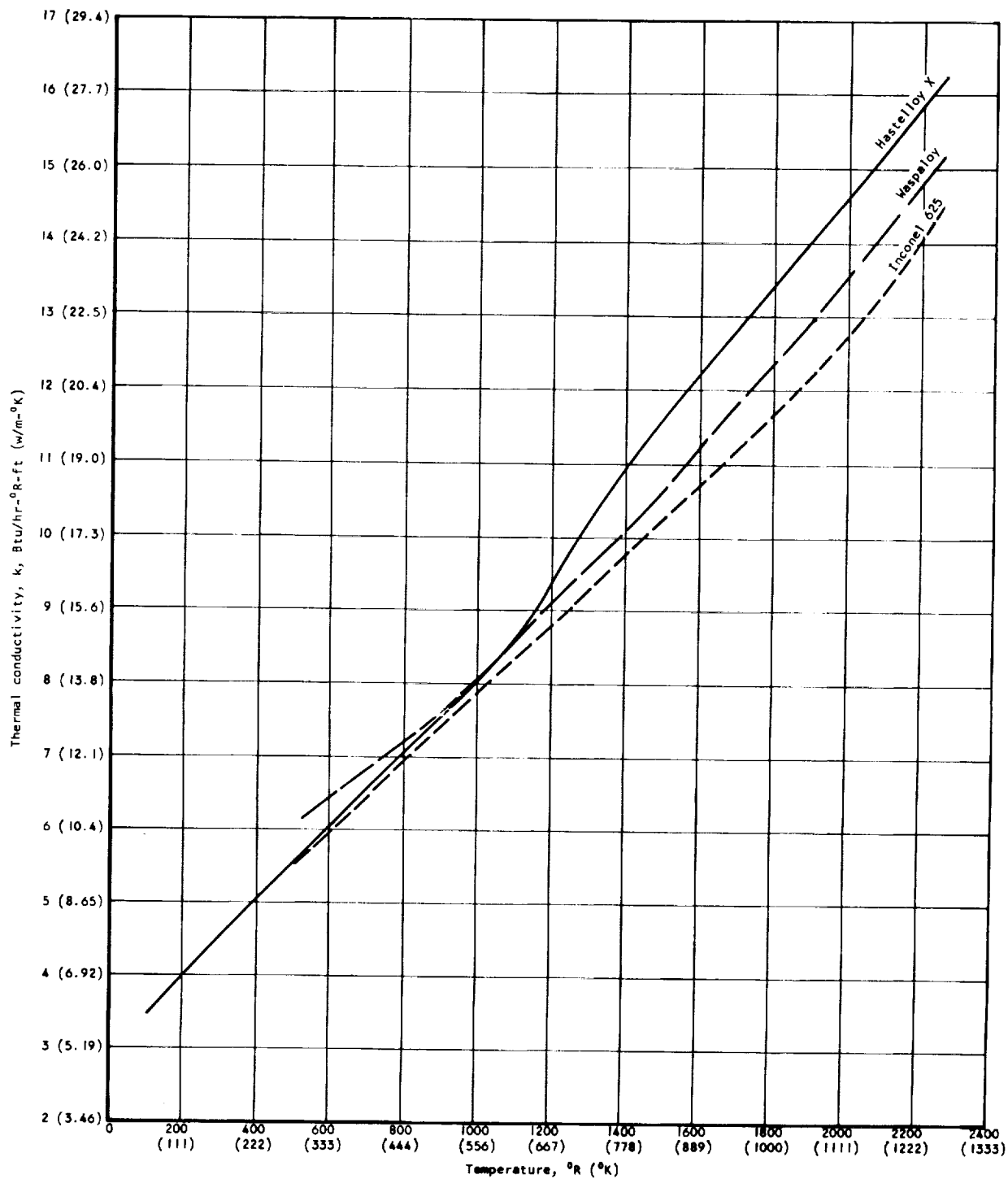
Figure 1. Thermal Conductivity of Panel Heat Exchanger Materials
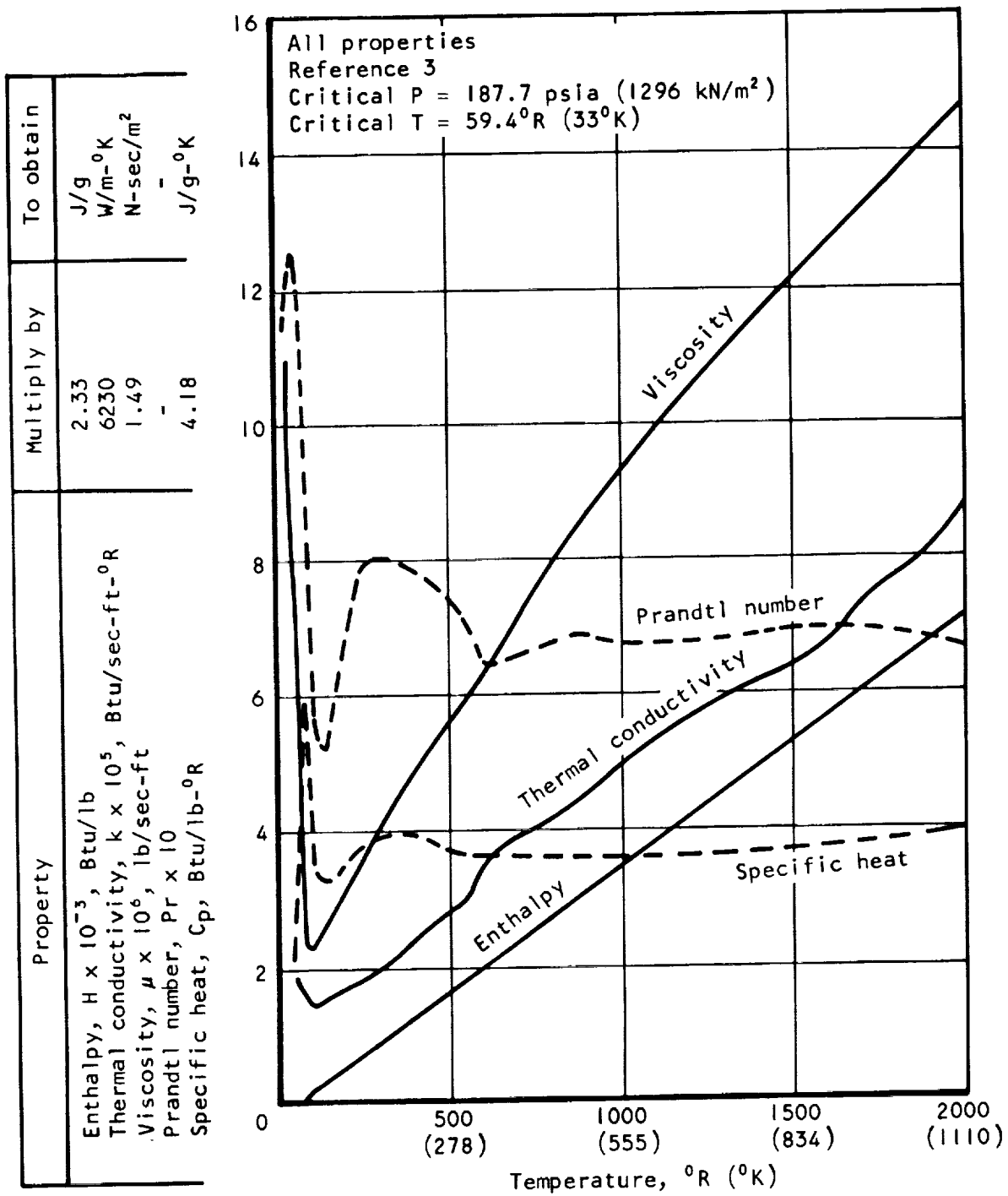
Figure 2. Transport Properties of Parahydrogen Gas
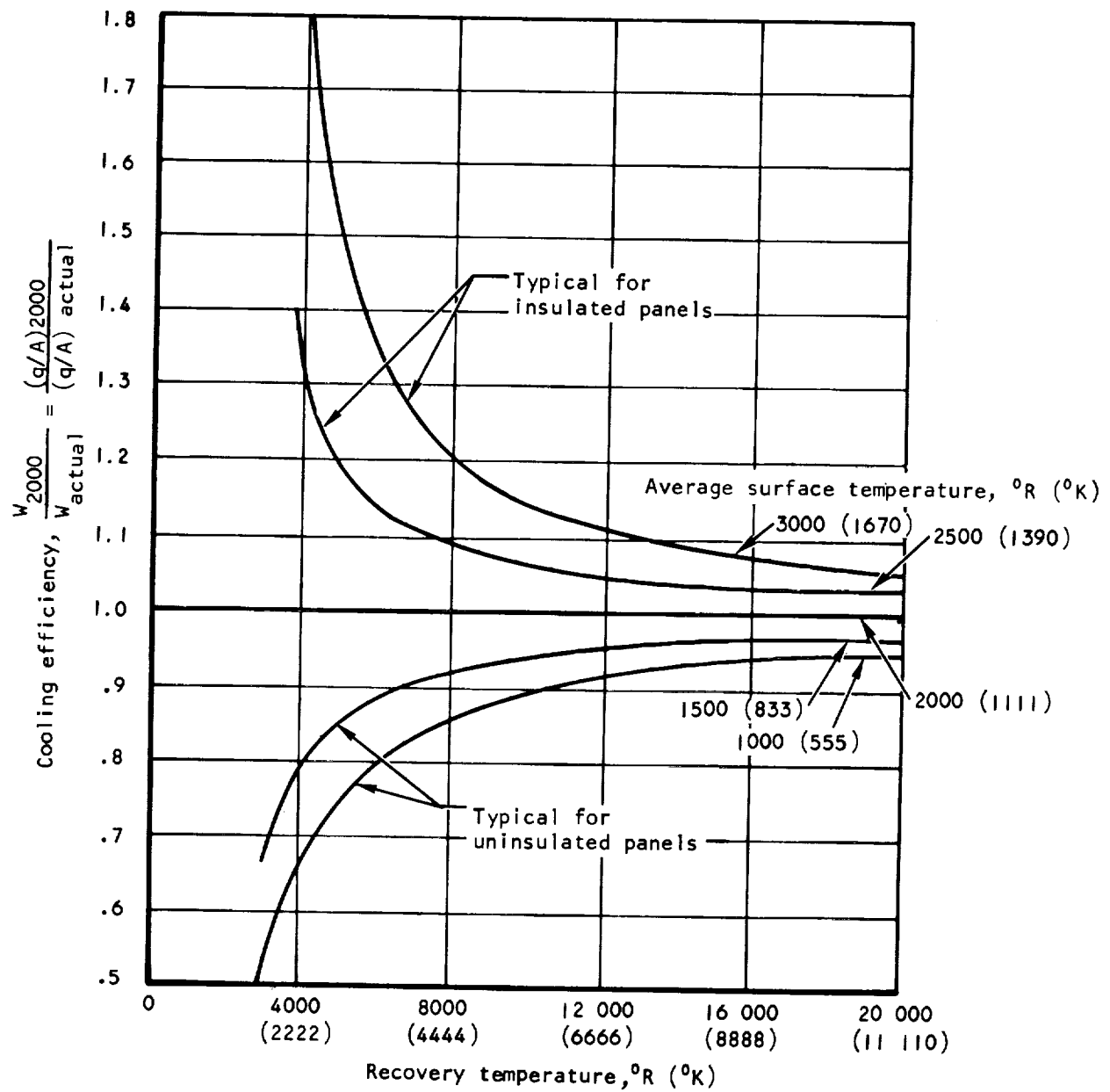
Figure 3. Cooling Efficiency
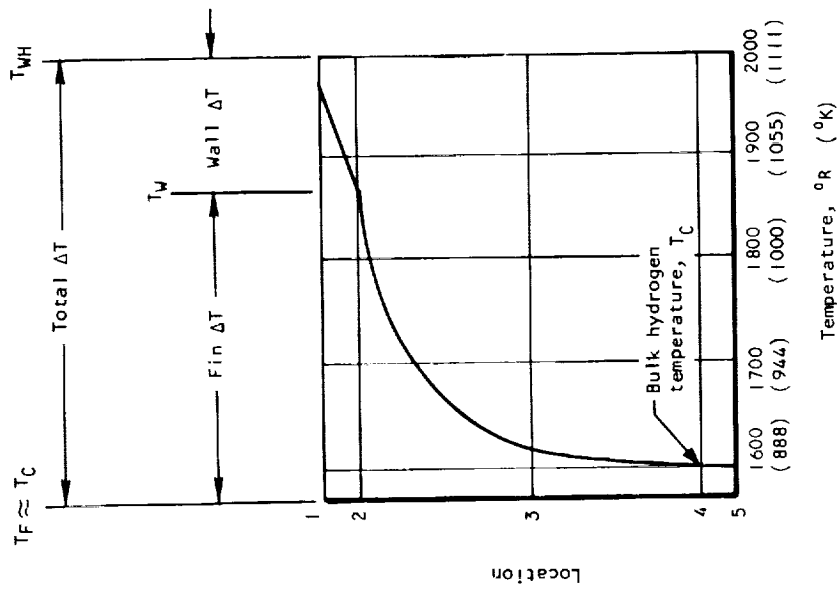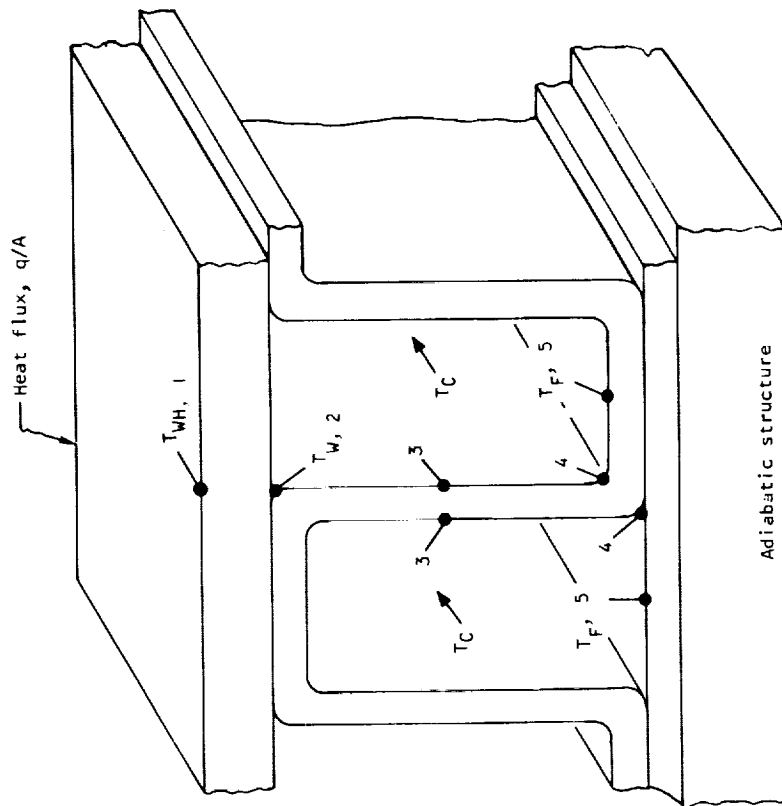
Figure 4. Heat Exchanger Cross Section Temperature Gradients
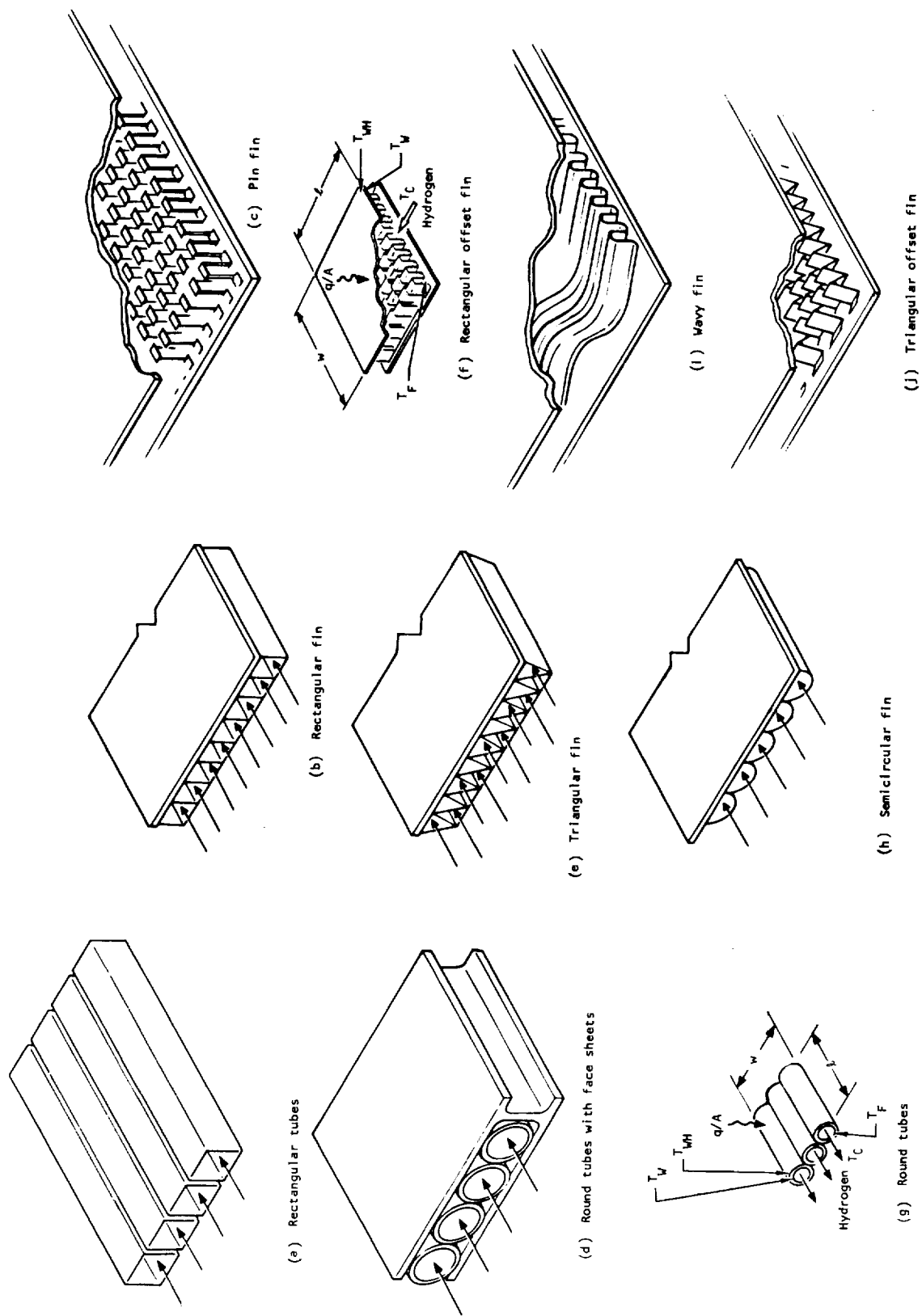
Figure 5. Heat Exchanger Geometry Concepts

(a) Rectangular tubes

(b) Rectangular fin

(c) Pin fin

(d) Round tubes with face sheets

(e) Triangular fin

(f) Rectangular offset fin

(g) Round tubes

(h) Semicircular fin

(i) Wavy fin

(j) Triangular offset fin
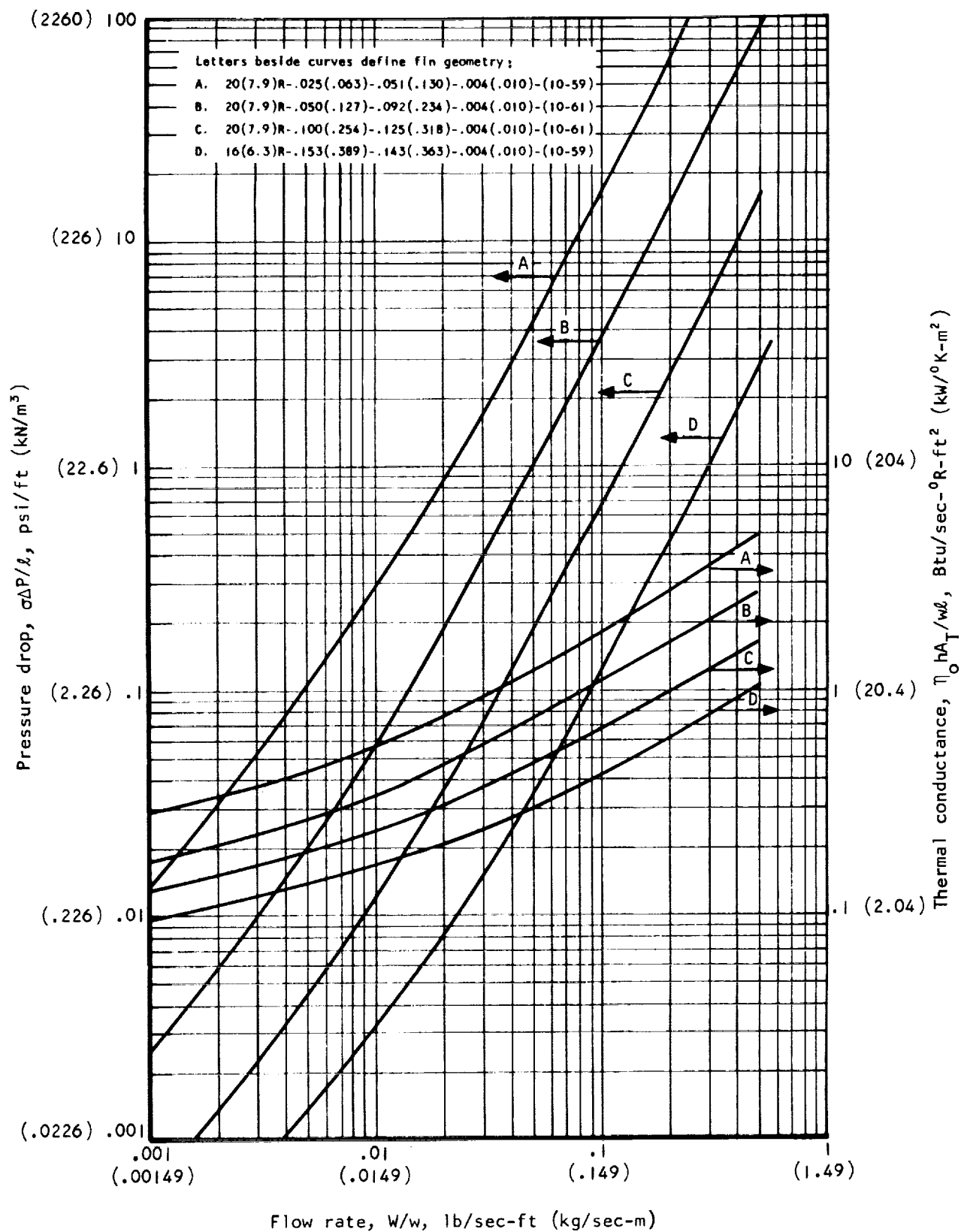
Figure 6. Effects of Fin Height on Heat Exchanger Performance

78
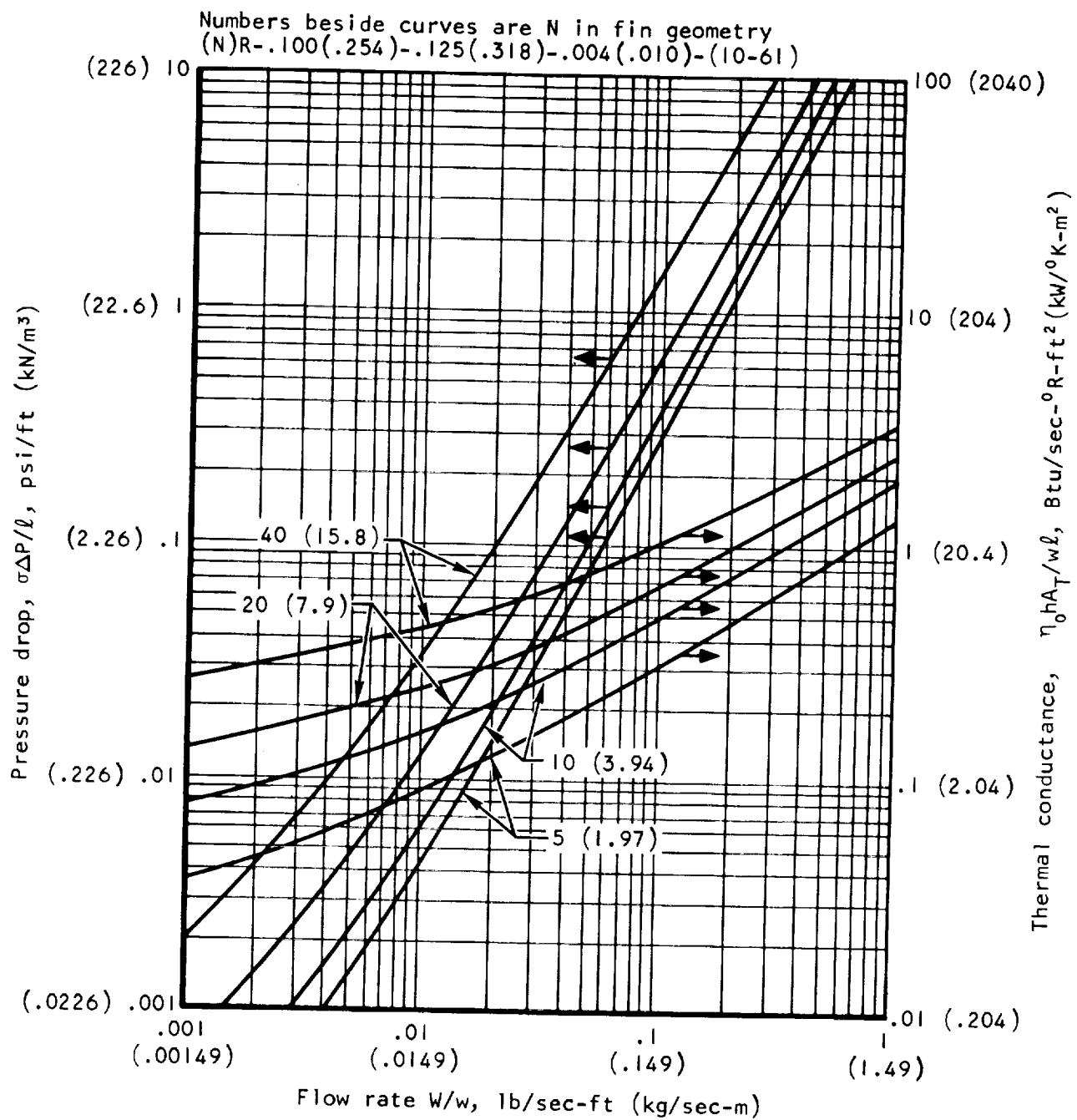
Figure 7. Effects of Fin Spacing on Heat Exchanger Performance

Letters beside curves define fin geometry:

A. 32 P(12.6)-.100(.254)-.020(.0510)-.010(.025)-(10-71)

B. 20 W(7.9)-.100(.254)-.375(.950)-.004(.010)-(10-67)

C. 20 R(7.9)-.100(.254)- $\geq$ 1.6(5.1)-0.004(.010)-(7-3, $L_o/4r_h$ = 100, constant T_W-T_F)

D. 20 T(7.9)-.100(.254)- $\geq$ 1.6(4.1)-.004(.010)-(10-33)

Pressure drop, $\sigma\Delta P/\ell$, psi/ft (kN/m³)

Thermal conductance, η_0 $hA_T/w\ell$, Btu/sec-°R-ft² (kW/°K-m²)

(2260) 100   100 (2040)

(226) 10   10 (204)

(22.6) 1.0   1.0 (20.4)

(2.26) .1   .1 (2.04)

(.226) .01   .01 (.204)

.001   .01   .1   1

(.0015)   (.0149)   (.149)   (1.49)

Flow rate, W/w, lb/sec-ft (kg/sec-m)

Figure 8. Effects of Cross Section Shape, Uninterrupted Flow Length, and Type of Flow-Length Interruption on Heat Exchanger Performance

80
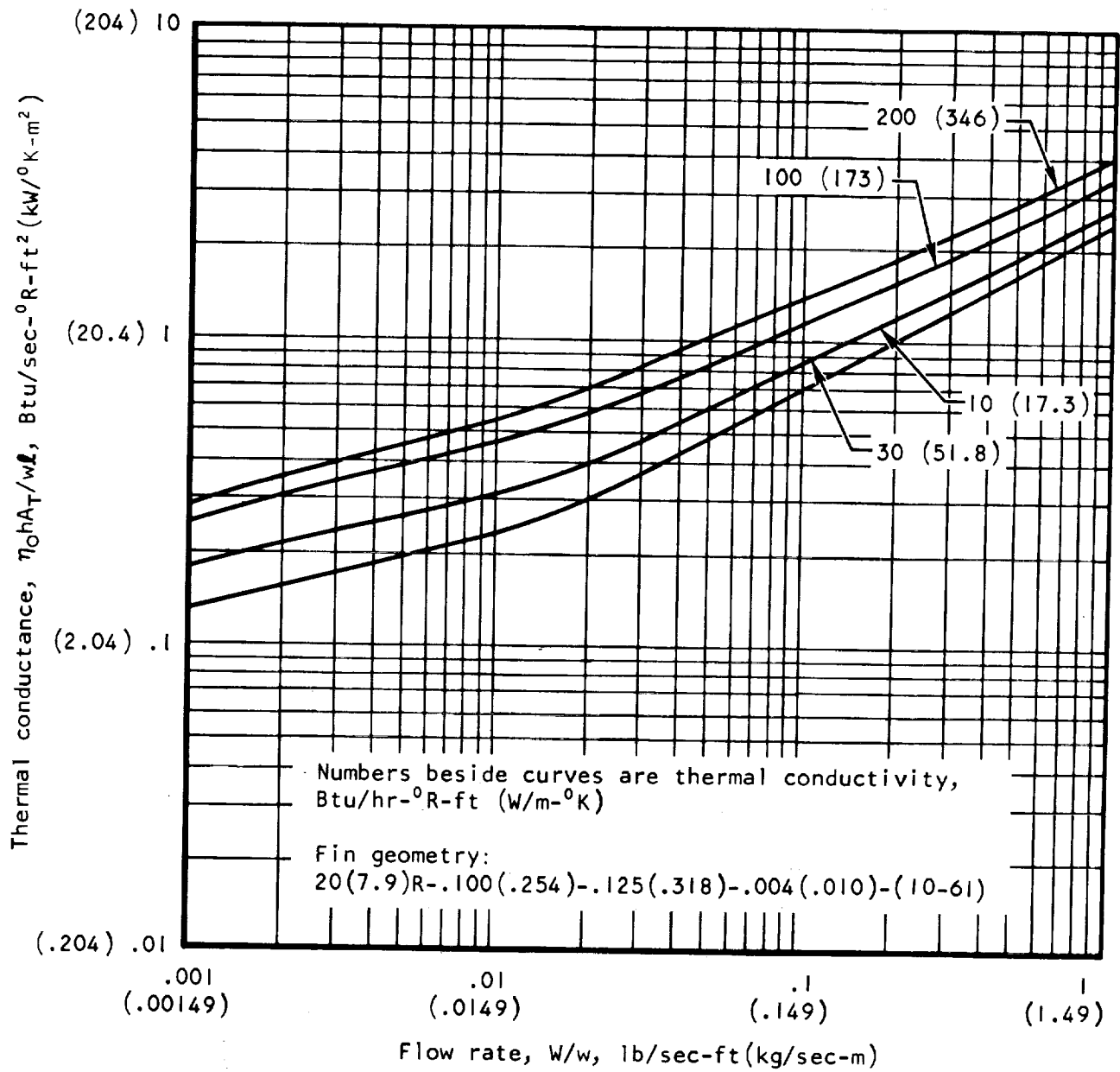
Figure 9. Effects of Fin Thermal Conductivity on Thermal Conductance

No braze fillets A. 40TB(15.8)-.050(.127)- ≥4(10.2)-.005(.013)-(7-1,L₀/4r$_h$=100,constant T$_w$)

.5 in. diam braze
fillets
  B. 20TB(7.9)-.100(.254)- ≥8(20.4)-.010(.025)-(7-1,L₀/4r$_h$=100,constant T$_w$)

  C. 40TB(15.8)-.050(.127)- ≥3(7.6)-.010(.025)-(7-1,L₀/4r$_h$=100,constant T$_w$)
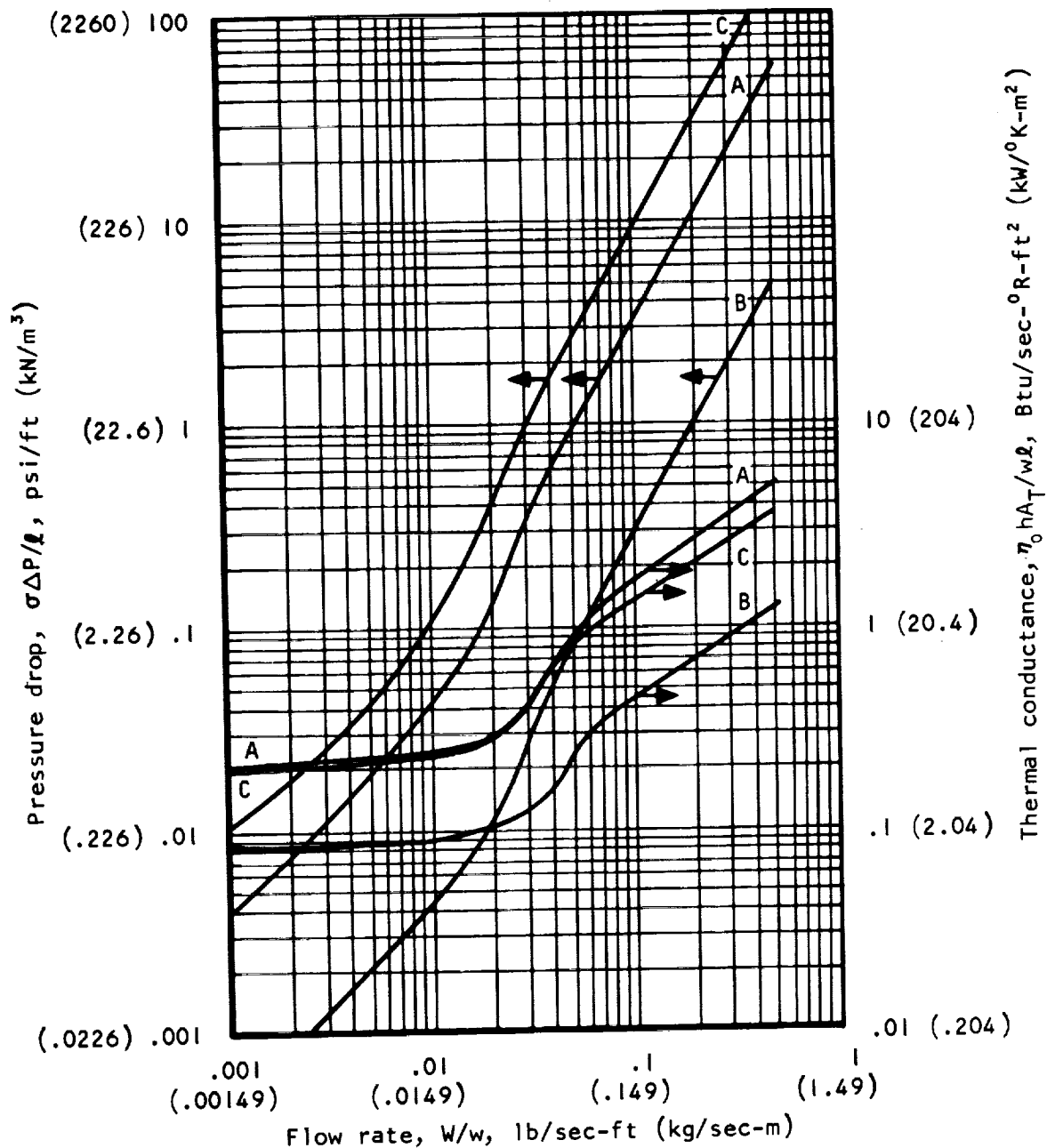
Figure 10. Effects of Fin Height, Spacing, and Thickness on Tubular
Heat Exchanger Performance
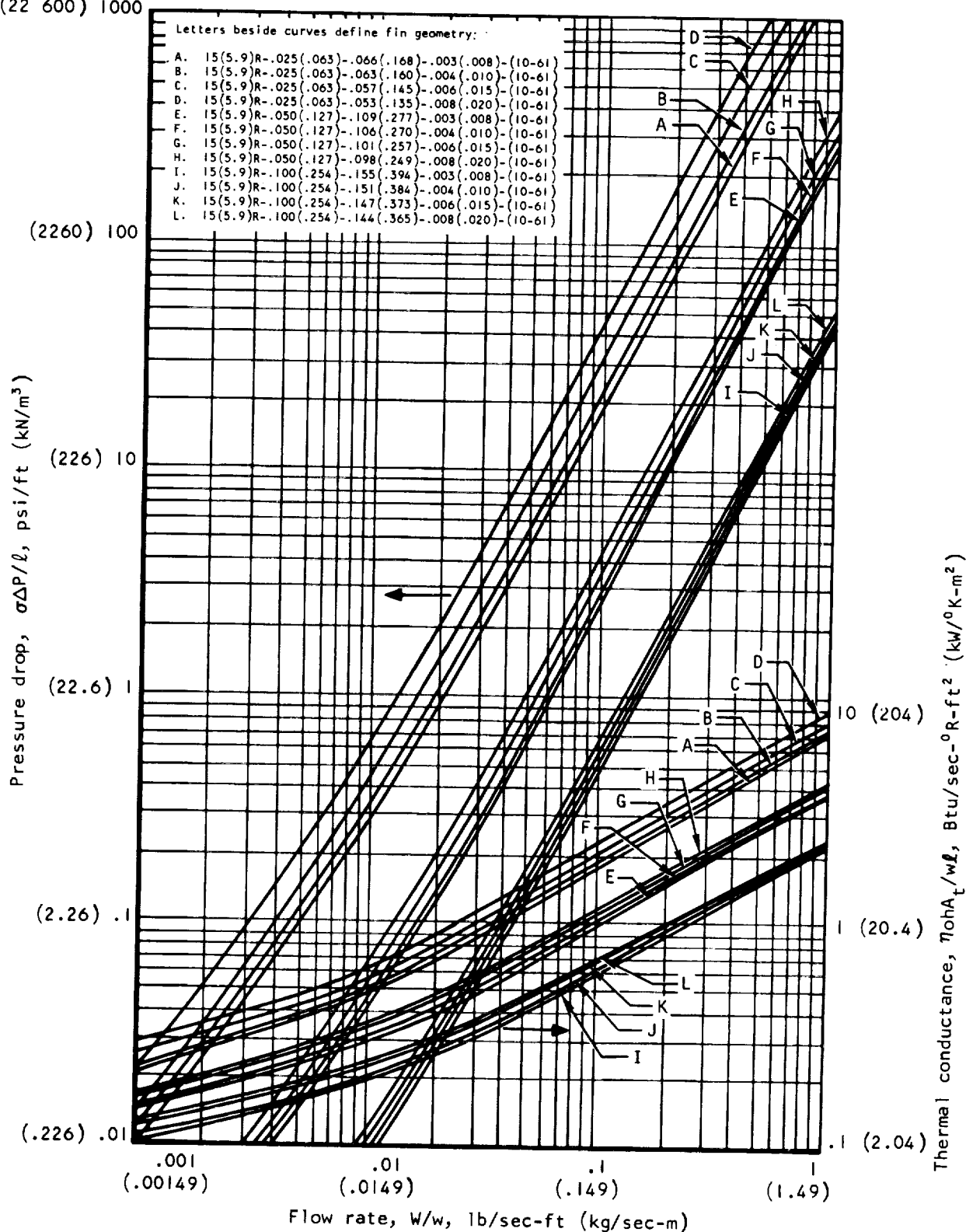
Figure 11. Rectangular Offset Fin Performance, N = 15
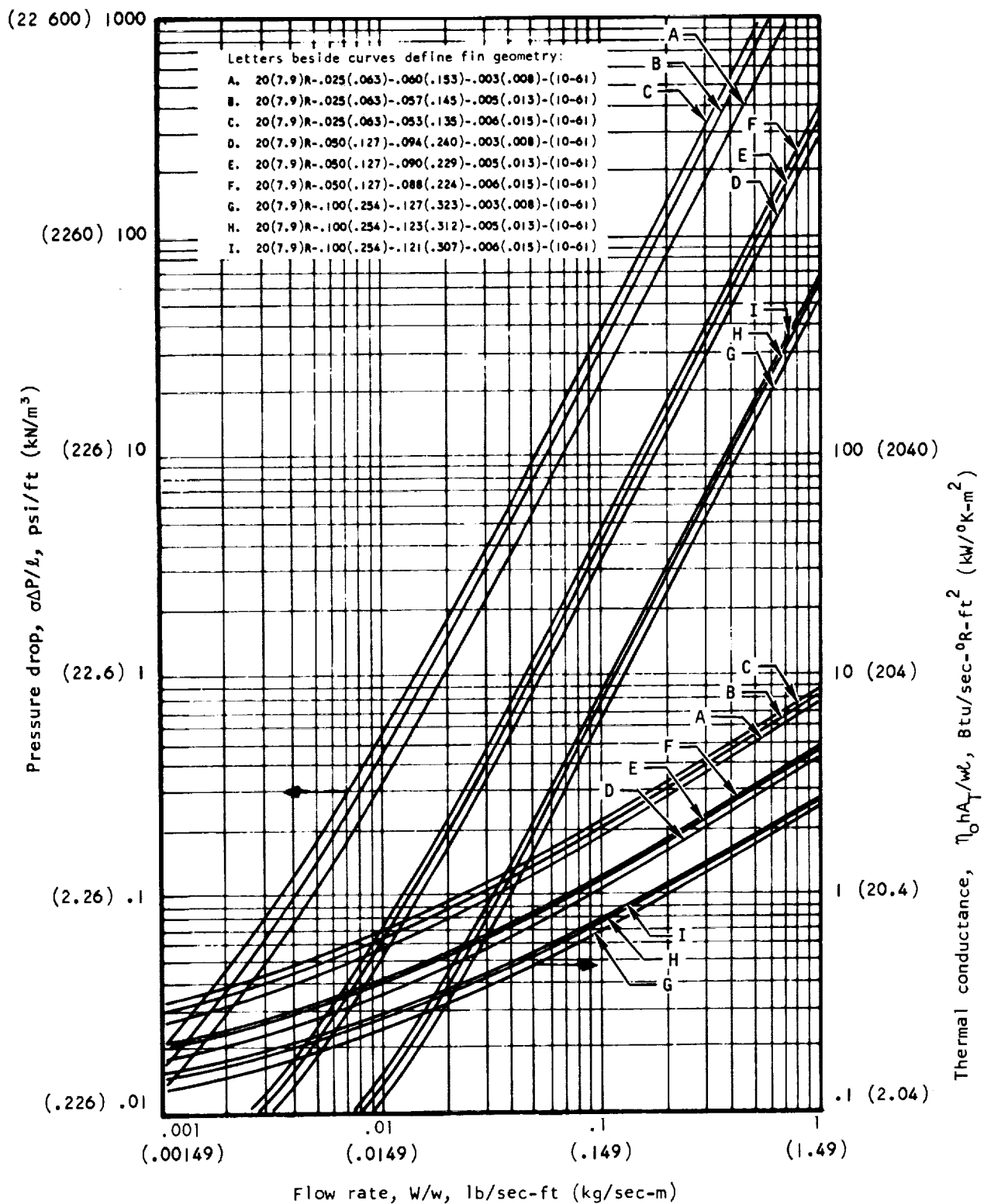
Figure 12. Rectangular Offset Fin Performance, N = 20
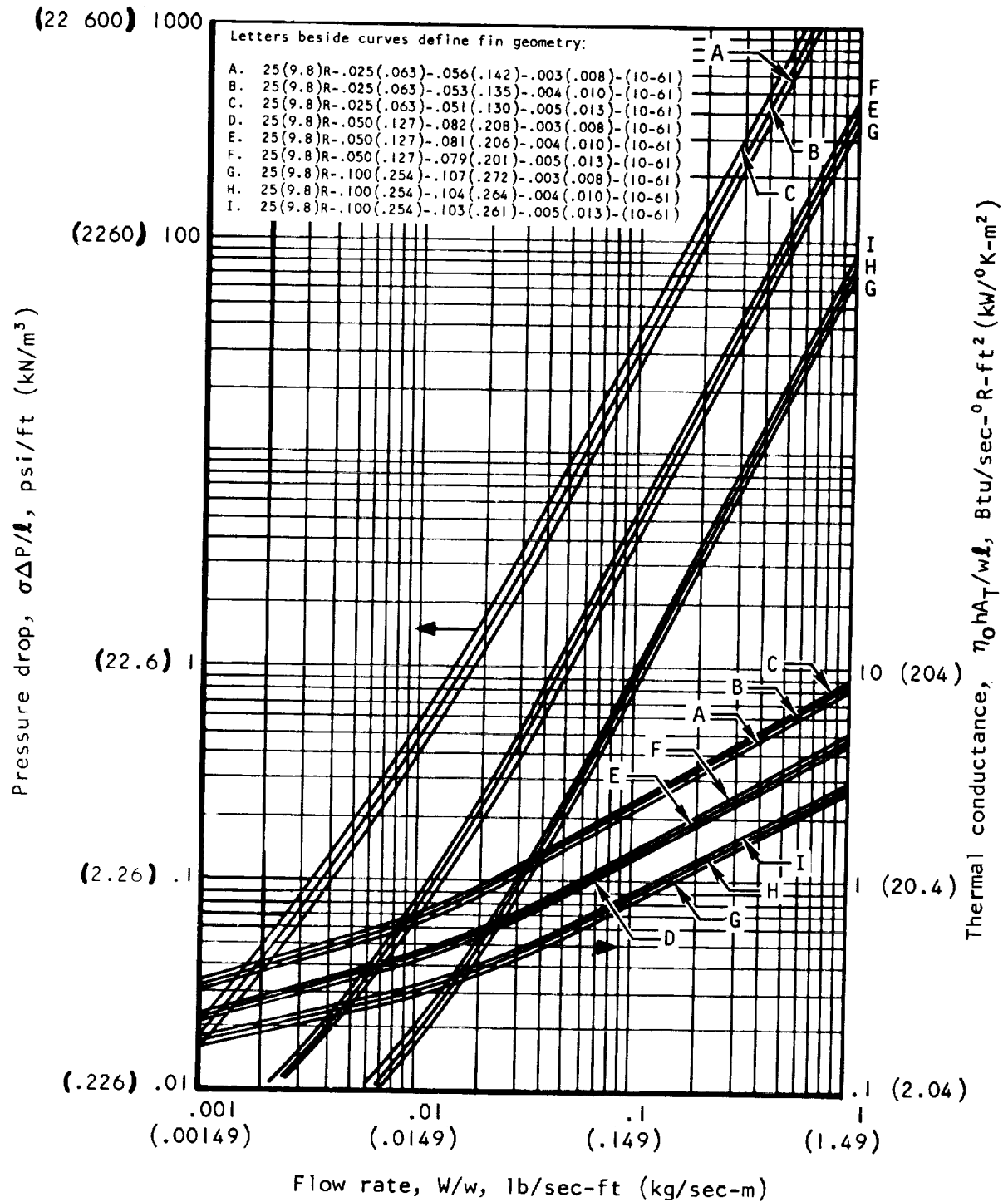
Figure 13. Rectangular Offset Fin Performance, N = 25

(22 600) 1000

Letters beside curves define fin geometry:

A. 30(11.8)R-.025(.063)-.051(.130)-.003(.008)-(10-61)
B. 30(11.8)R-.025(.063)-.049(.124)-.004(.010)-(10-61)
C. 30(11.8)R-.050(.127)-.074(.188)-.003(.008)-(10-61)
D. 30(11.8)R-.050(.127)-.072(.183)-.004(.010)-(10-61)
E. 30(11.8)R-.100(.254)-.092(.234)-.003(.008)-(10-61)
F. 30(11.8)R-.100(.254)-.090(.228)-.004(.010)-(10-61)

(2260) 100

Pressure drop, $\sigma\Delta P/\ell$, psi/ft (kN/m^3)

(226) 10

Thermal conductance $\eta_o h A_T/w\ell$, Btu/sec-$^\circ$R-ft^2 (kW/$^\circ$K-m^2)

(22.6) 1

10 (204)

(2.26) .1

1 (20.4)

(.226) .01

.1 (2.04)

.001   .01   .1   1
(.00149)   (.0149)   (.149)   (1.49)

Flow rate W/w, lb/sec-ft (kg/sec-m)

Figure 14. Rectangular Offset Fin Performance, N = 30

86
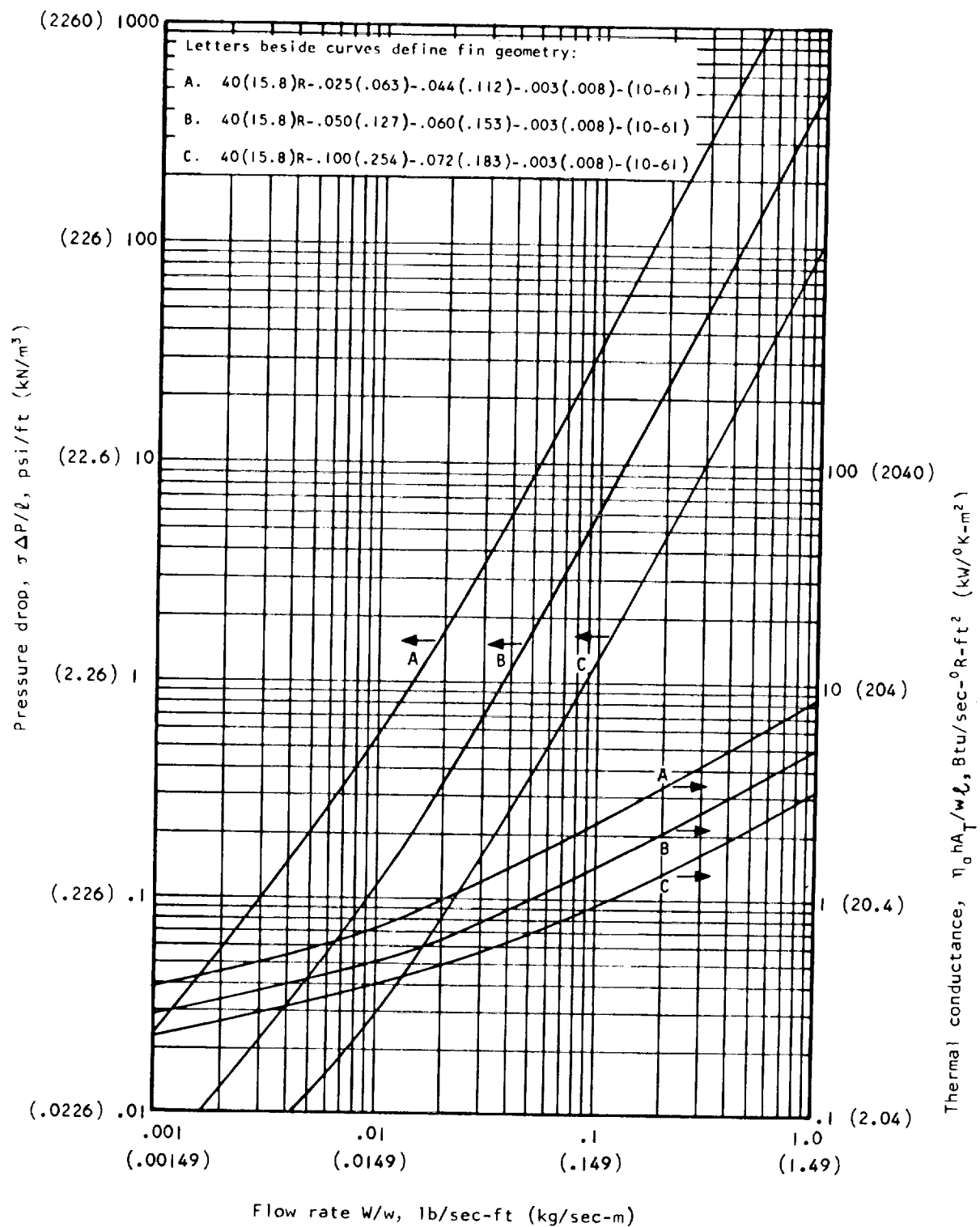
Figure 15. Rectangular Offset Fin Performance, N = 40

87

Numbers beside curves indicate flow lengths, ft(m)

Heat exchanger geometry: 20(7.9)R-.025(.063) -.051(.130)-.004(.010)-(10-59)
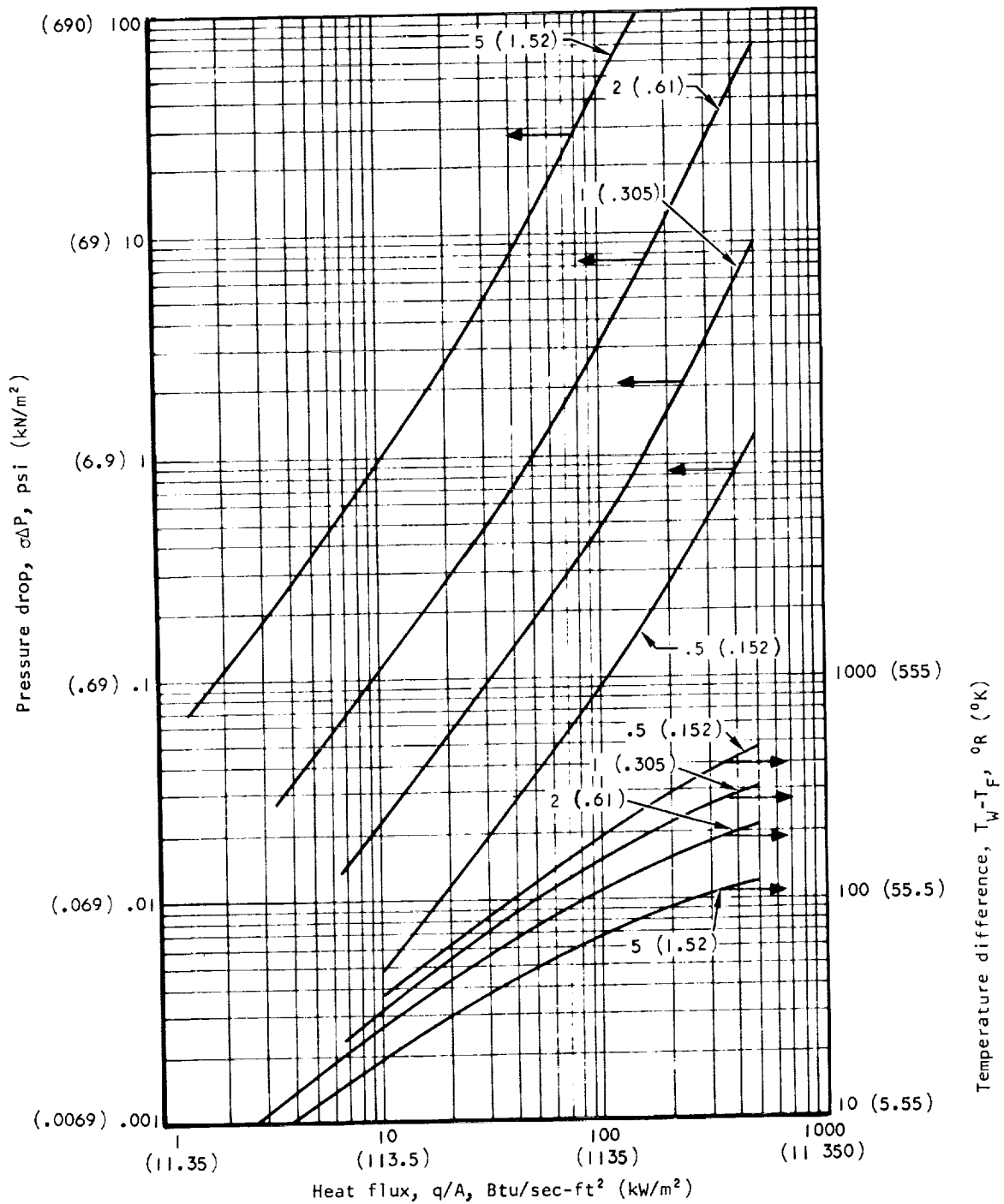
Figure 16. Heat-Flux and Flow-Length Effects on Heat Exchanger Performance, h_{fin} = 0.025 in. (0.063 cm)

Numbers beside curves indicate flow lengths, ft(m)

Heat exchanger geometry:
20(7.9)R-.050(.127)-.092(.234)-.004(.010)-(10-61)
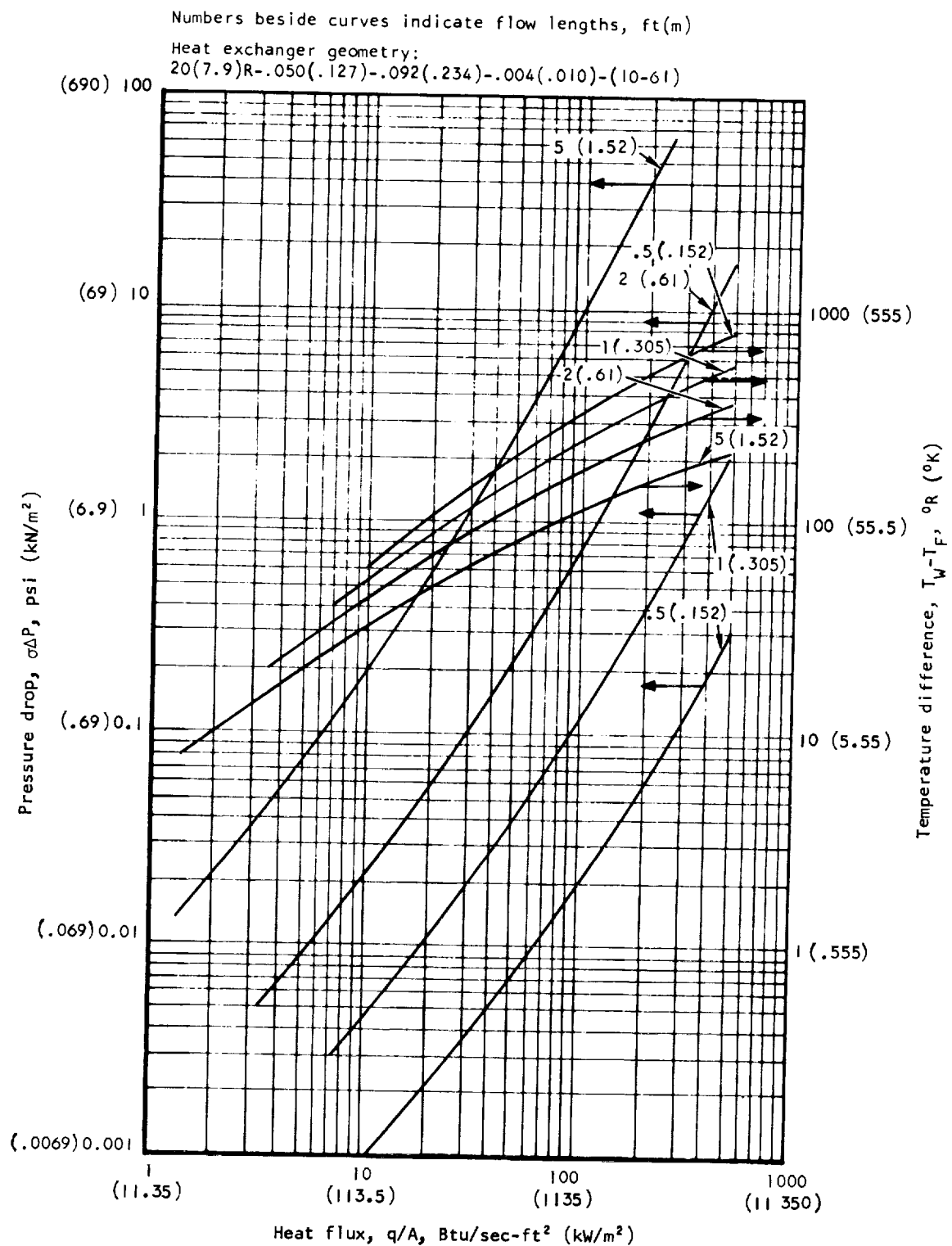
Figure 17. Heat-Flux and Flow-Length Effects on Heat Exchanger Performance, h_{fin} = 0.050 in. (0.127 cm)
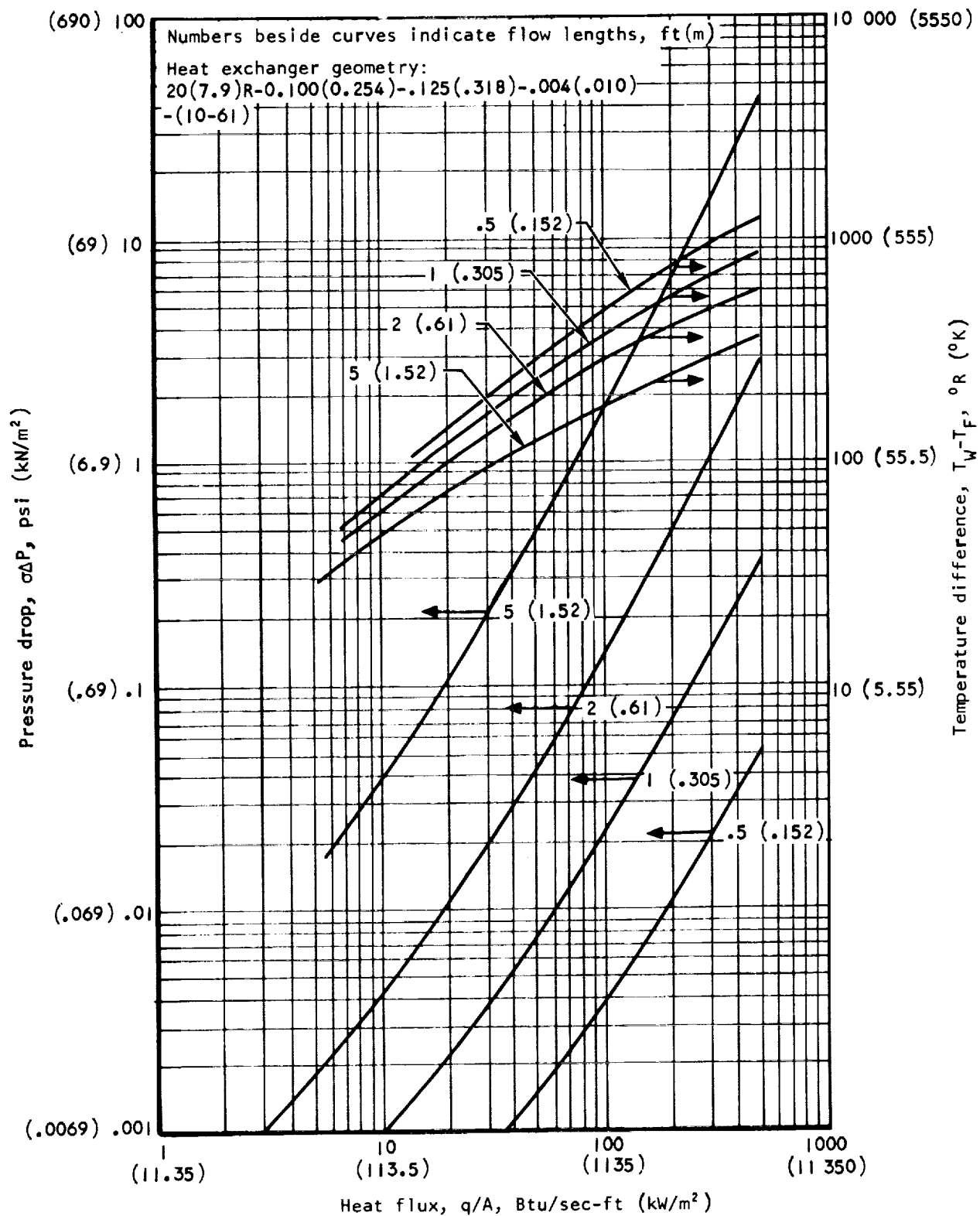
Figure 18. Heat-Flux and Flow-Length Effects on Heat Exchanger
Performance, h_{fin} = 0.100 in. (0.254 cm)
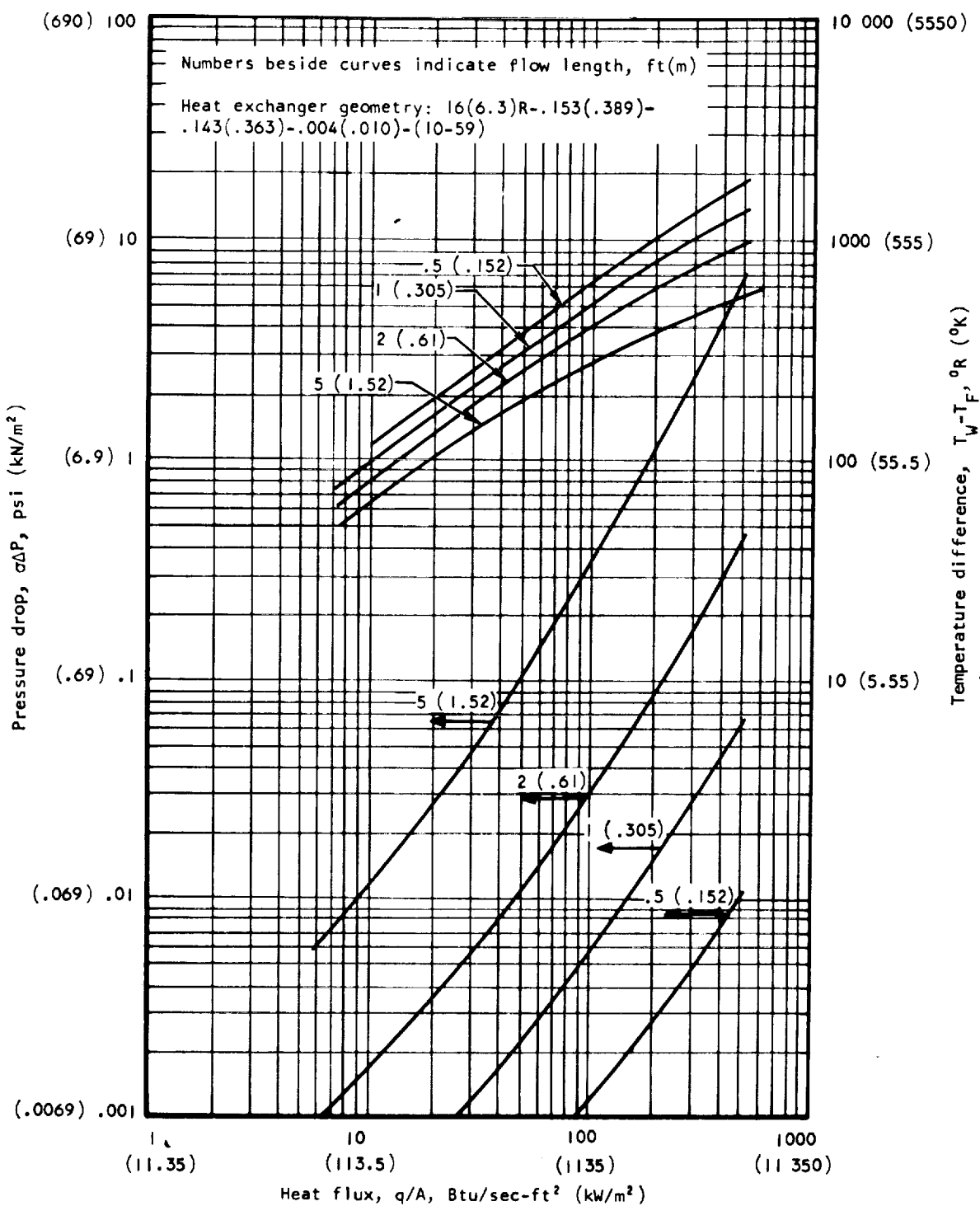
Figure 19. Heat-Flux and Flow-Length Effects on Heat Exchanger Performance, h_{fin} = 0.153 in. (0.389 cm)

91
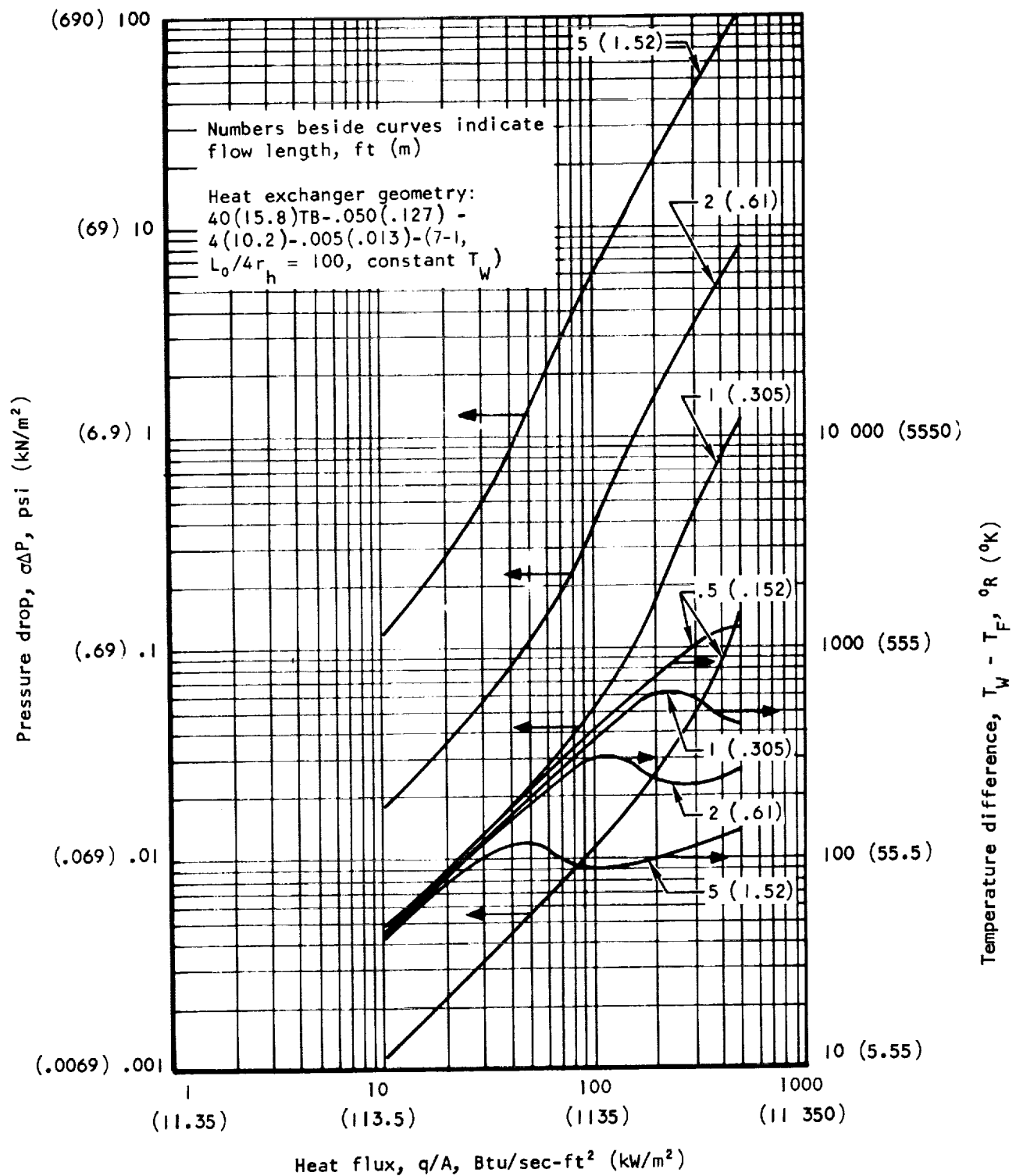
Figure 20. Heat-Flux and Flow-Length Effects on Tubular Heat Exchanger Performance
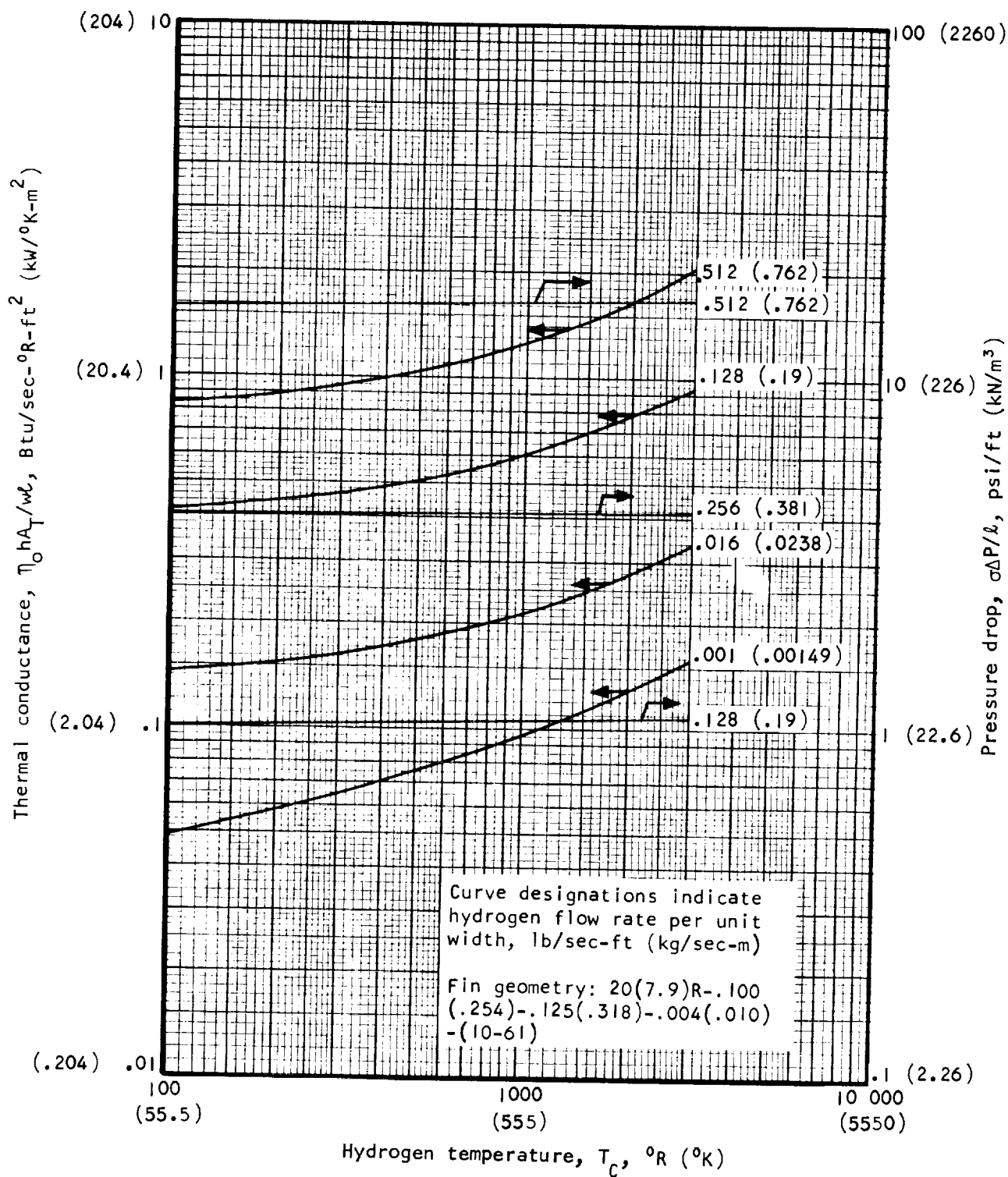
Figure 21. Effect of Hydrogen Temperature on Thermal Conductance

(a) Multiple inlets(single pass has only one inlet)

(b) Folded in depth

(c) Fold with injection

(d) Folded in width
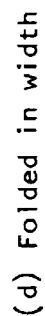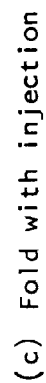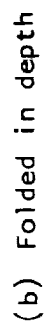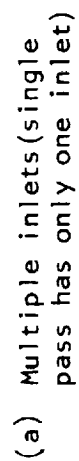
Figure 22. Coolant Flow Routing Concepts

94

(a) Adjacent inlet and outlet manifolds

(b) Common inlet and outlet
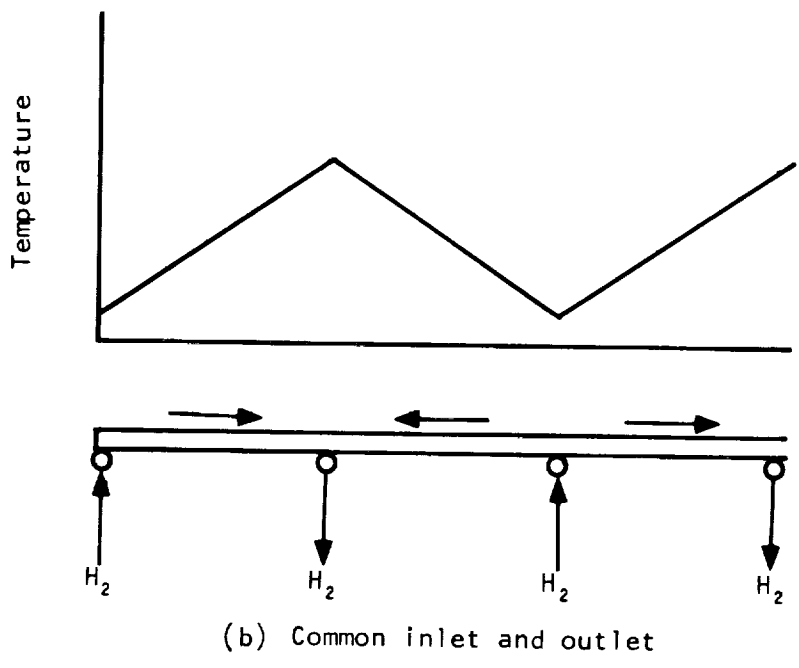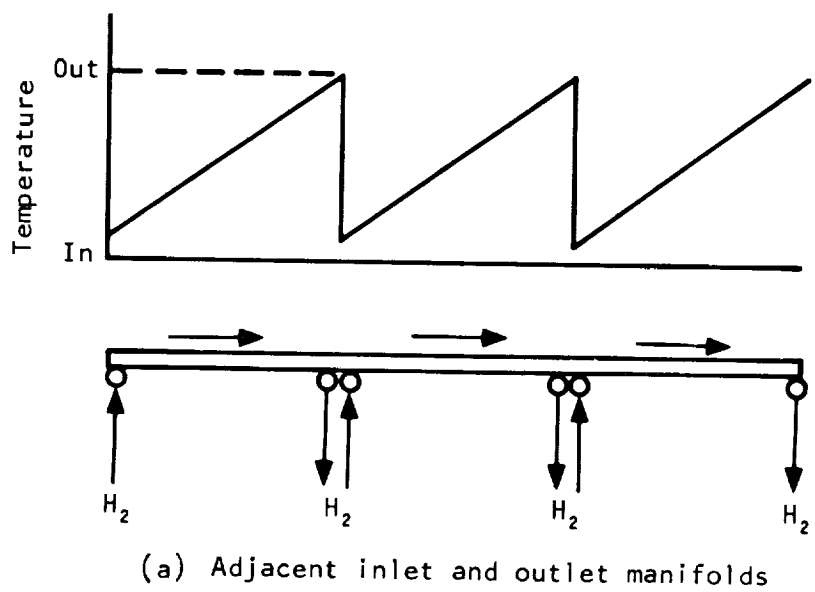
Figure 23. Multiple Manifold Flow Concepts

Legend:

⋈—● Valve and hot-temperature sensor
– – ▶ Low-temperature coolant
——▶ Intermediate-temperature coolant
—·▶ Maximum-temperature coolant

(a) Periodic coolant injection and removal

(b) Stepwise increment of fin height

(c) Periodic injection of low-temperature coolant
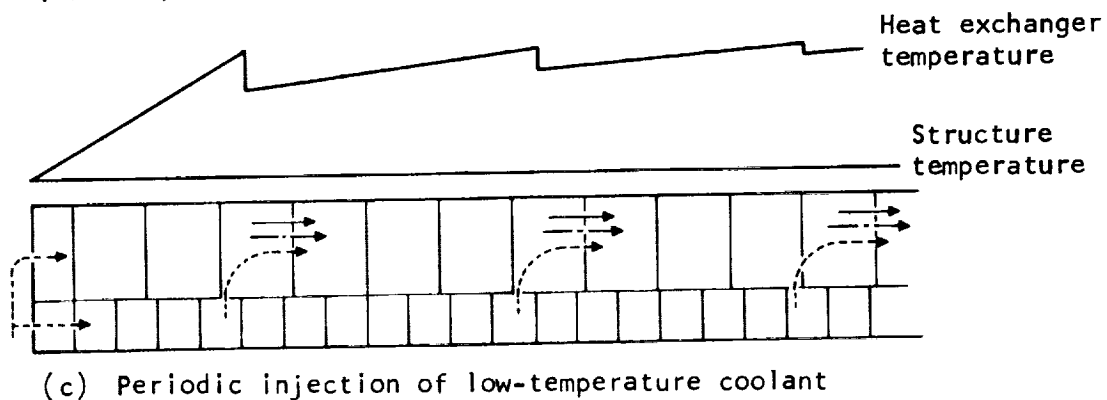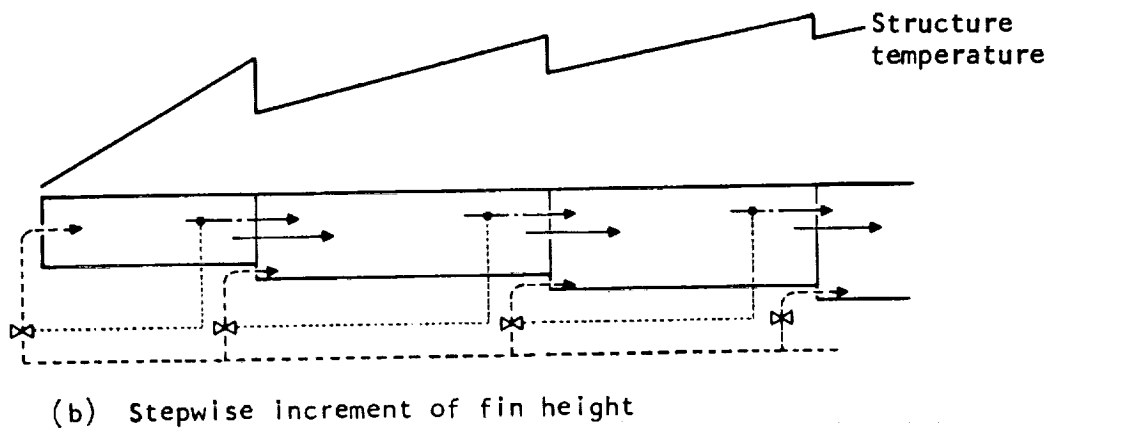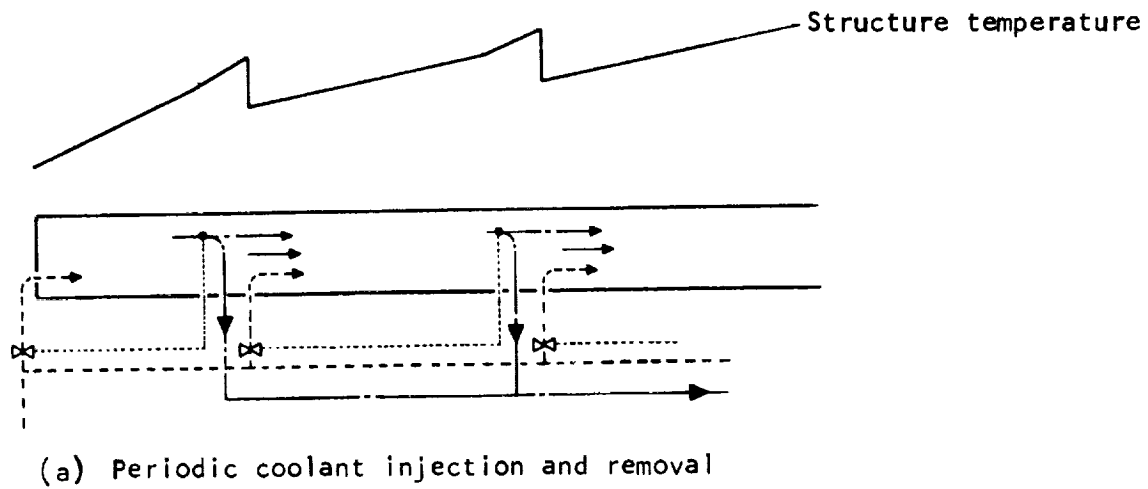
Figure 24. Multiple Inlet Concepts

Legend:

⋈----● Valve and hot-temperature sensor

-----► Low-temperature coolant

———► Intermediate-temperature coolant

——-—► Maximum-temperature coolant

Coolant temperature profile

Inlet

Inlet to next section

Outlet
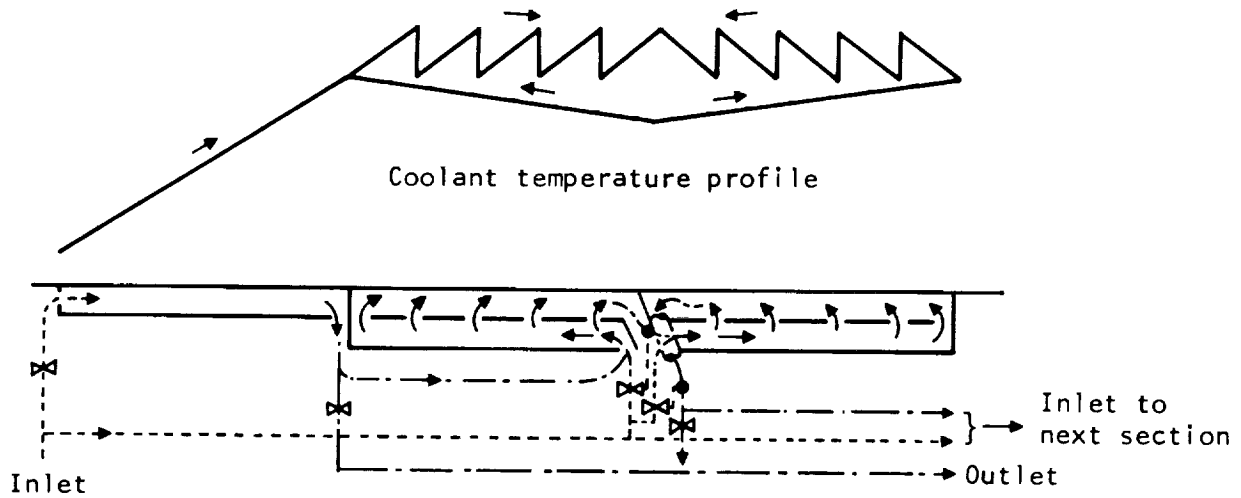
(a) Two fin rows plus manifold

Coolant temperature profile

Inlet

Inlet to next section

Outlet
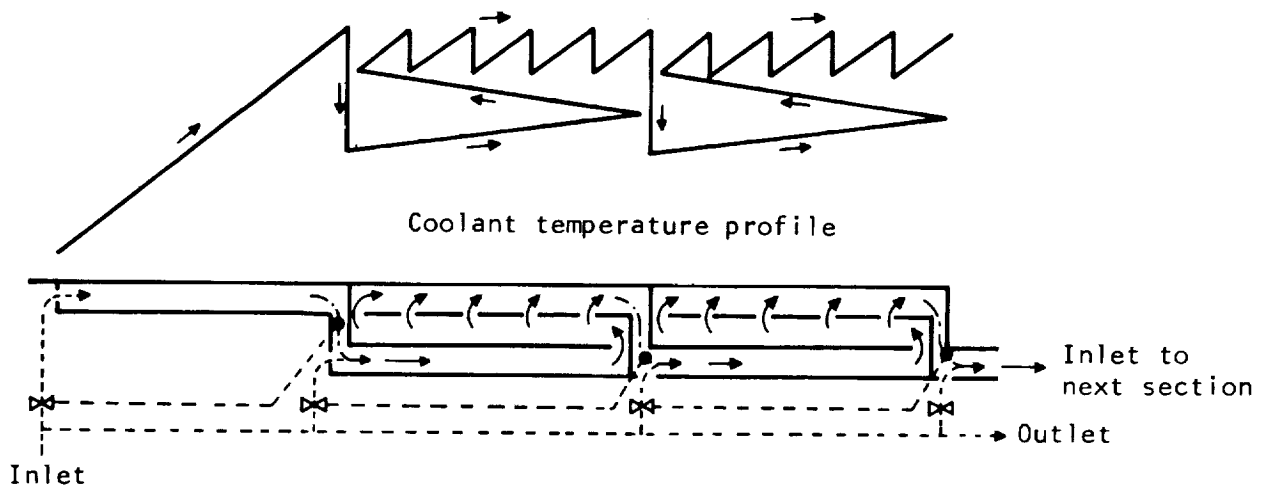
(b) Three fin rows

Figure 25. Folded Flow with Injection

NOTES:

1. Fin geometry:
   16(6.3)R-.153(.389)-plain-.004(.100)-(7-3, $L_o/4r_h$ = 100, constant T_W)

2. W/w = .00934 lb/sec ft (.0139 kg/sec-m)

3. $\sigma\Delta P$ < .04 psi (.276 kN/m^2) for entire combined length in each series

4. ————— indicates hydrogen temperature

   — — — — indicates wall temperatures, T_{DMW} and T_F
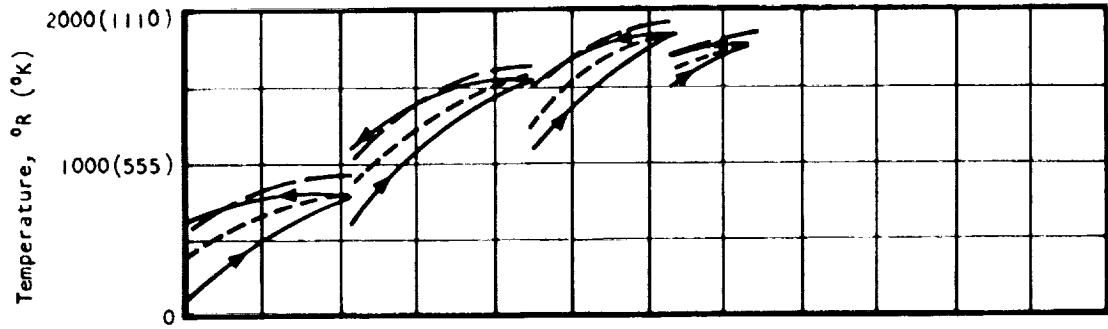
(a) T_R = 7000°R (3890°K), cooling efficiency = .94
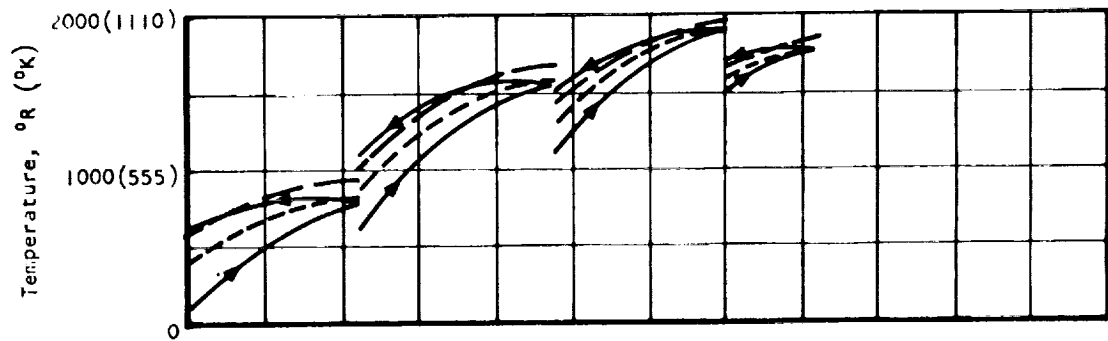
(b) T_R = 5000°R (2780°K), cooling efficiency = .84
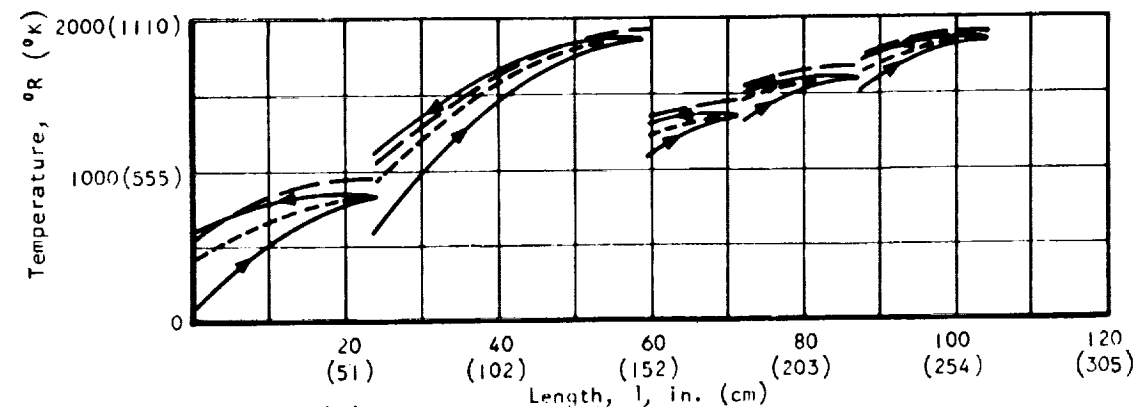
(c) T_R = 3000°R (1670°K), cooling efficiency = .63

Length, 1, in. (cm)

Figure 26. Temperature Profiles for Folded-in-Width Panels of Un Unequal Length with Nominal q/A = 10 Btu/sec-ft^2 (114 kW/m^2)

98

Note: At outlet of all single-pass panels and the hot end (180-deg turn) of folded-in-width panels:

	Low flux	High flux
T_{CO} or T_{HT}, °R (°K)	1760 (978)	1600 (888)
P_{CO}, psia (kN/m²)	300 (2070)	300 (2070)
T_{DMW}, °R (°K)	1860 (1033)	2000 (1111)

(a) Two single pass in parallel

		Low flux	High flux
T_{HM},	°R	935 to 967	880
	(°K)	(520 to 538)	(489)
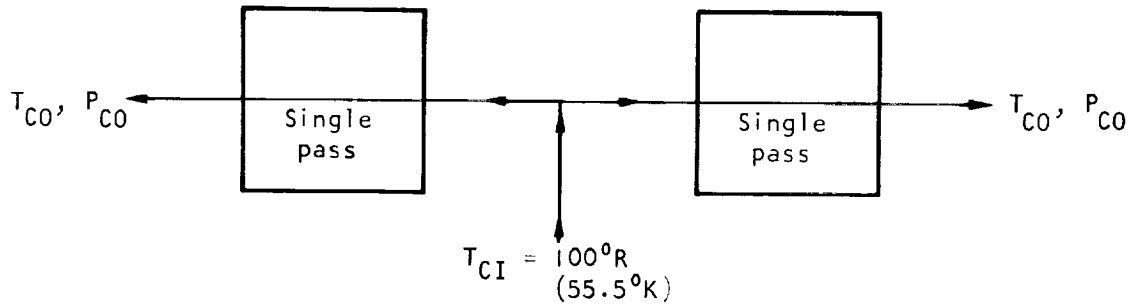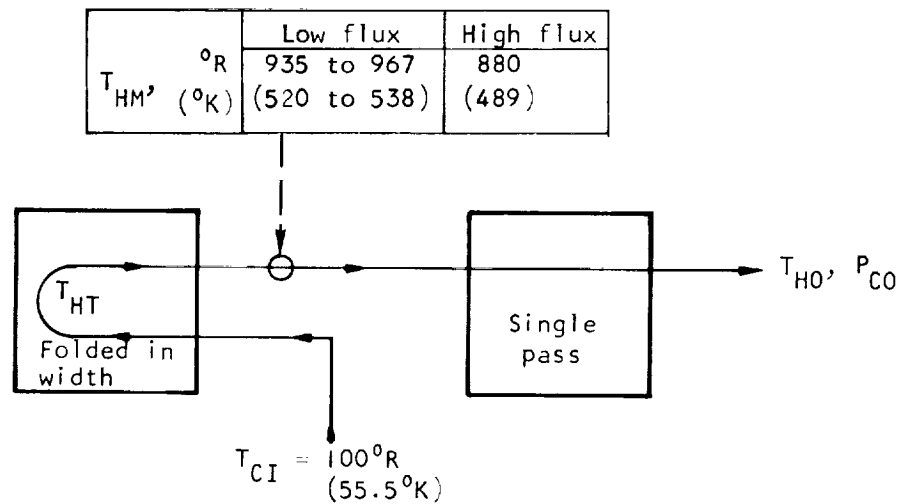
(b) Folded and single pass in series

Figure 27. Operating Conditions for Two-Panel Systems

Fin geometry:

q/A Btu/sec ft² (kW/m²)	Flow configuration	
250	single	$20(7.9)R$-h_{fin}-L_o-$.004(.010)$-$(10$-$61)$
250	folded	$20(7.9)R$-h_{fin}-plain-$.004(.010)$-$(7$-$3,\ L_o/4r_h =$ constant $T_w)$
500	single	$20(7.9)R$-h_{fin}-L_o-$.006(.015)$-$(10$-$61)$
500	folded	$20(7.9)R$-h_{fin}-plain-$.006(.015)$-$(7.3,\ L_o/4r_h = 100$, constant $T_w)$

Figure 28. T_{DMW} for High-Flux Folded-Flow and Single-Pass Systems per Figure 27

Notes:

1. h_{fin}, in. (cm) is noted beside points

2. Nominal q/A, Btu/sec ft² (kW/m²) is noted beside curves

3. ———— indicates folded and single pass in series

   — — — indicates single pass in parallel

4. Fin geometry:

q/A Btu/sec-ft² (kW/m²)	Flow configuration	
250	single	20(7.9)R-h_{fin}-L_o-.004(.010)-(10-61)
250	folded	20(7.9)R-h_{fin}-plain-.004(.010)-(7-3, $L_o/4r_h$ = constant T_w)
500	single	20(7.9)R-h_{fin}-L_o-.006(.015)-(10-61)
500	folded	20(7.9)R-h_{fin}-plain-.006(.015)-(7-3, $L_o/4r_h$ = 100, constant T_w)

Figure 29. P_{CI} for High-Flux Folded-Flow and Single-Pass Systems per Figure 27

curves (a) and (c):

q/A = 250 Btu/sec-ft² (2840 kW/m²)
N = 20 fins/in. (7.9 fins/cm)

curves (b) and (d):

q/A = 500 Btu/sec-ft² (5680 kW/m²)
N = 20 fins/in. (7.9 fins/cm)

(a) Folded with
t_{fin} = .004 in. (.010 cm)

(b) Folded with
t_{fin} = .006 in. (.015 cm)

(c) Single pass with
t_{fin} = .004 in. (.010 cm)

(d) Single pass with
t_{fin} = .004 in. (.010 cm)

Fin height, h_{fin}, in. (cm)

Hydrogen inlet pressure, P_{CI}, psi (kN/m²)

Fin allowable pressure

Design maximum wall temperature, T_{DMW}, °F (°K)
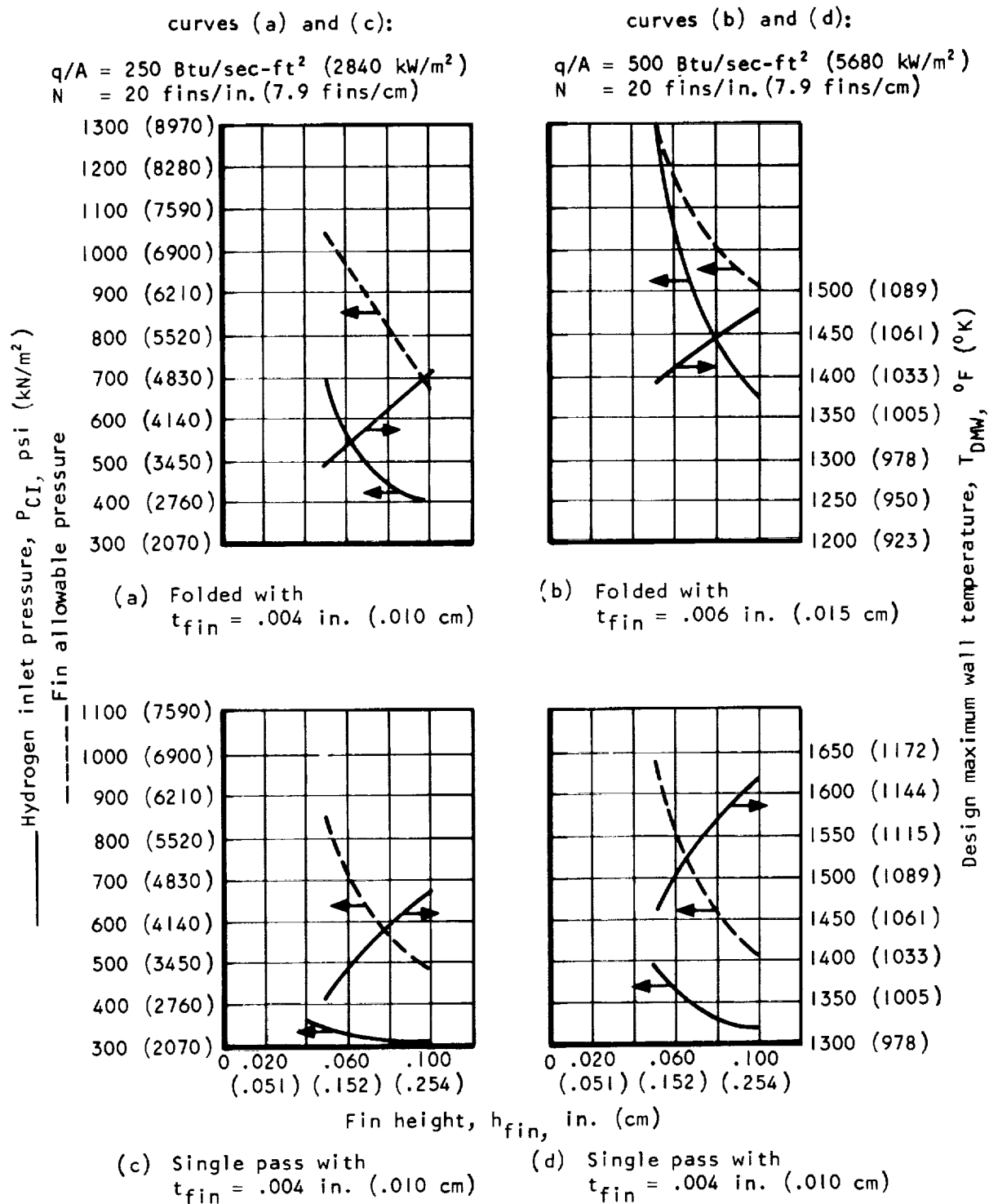
Figure 30. Strength Comparison of High-Flux Folded and Single-Pass
Heat Exchangers per Figure 27

102
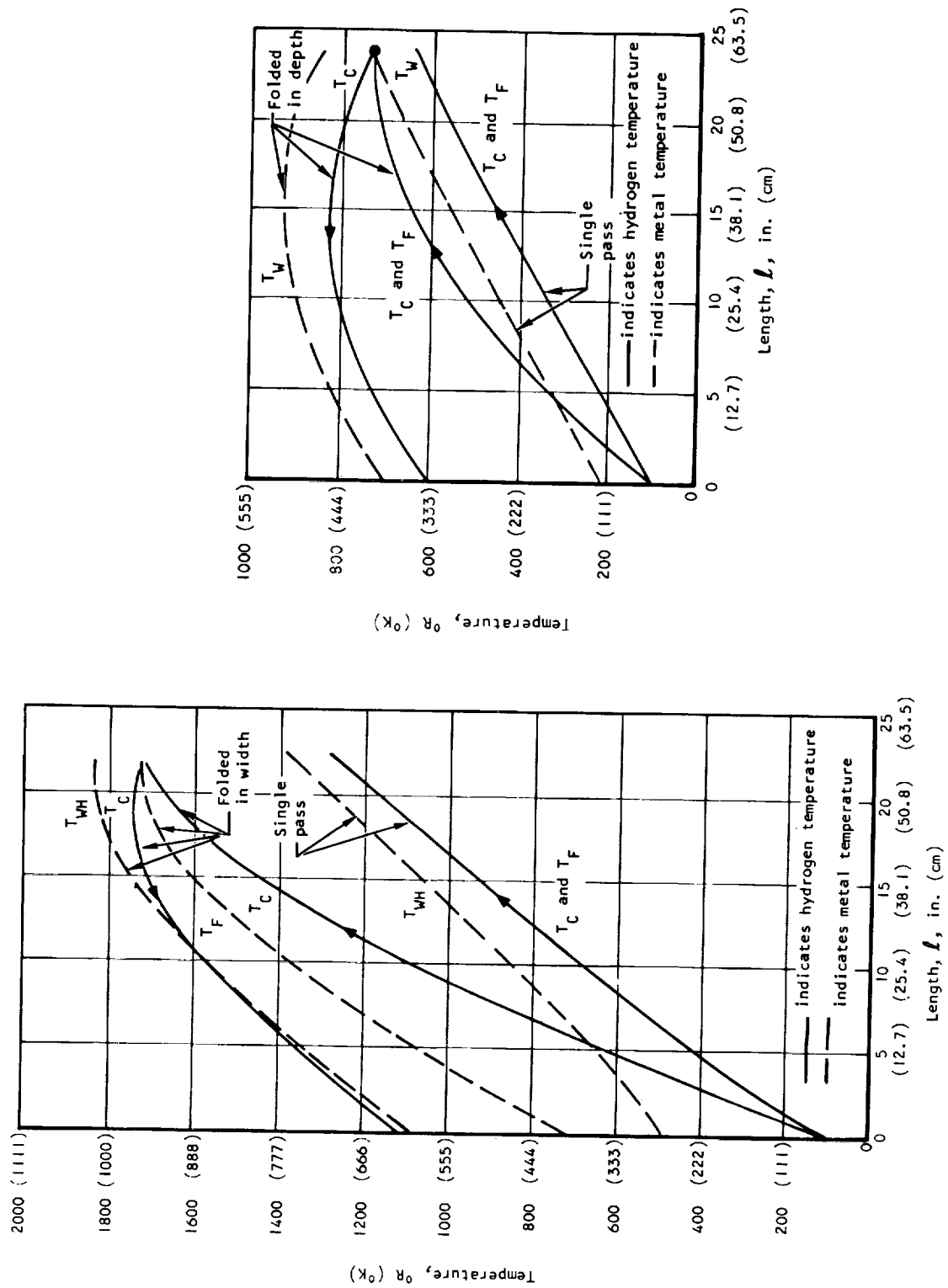
Figure 31. Temperature Profiles for Several Flow Routing Concepts
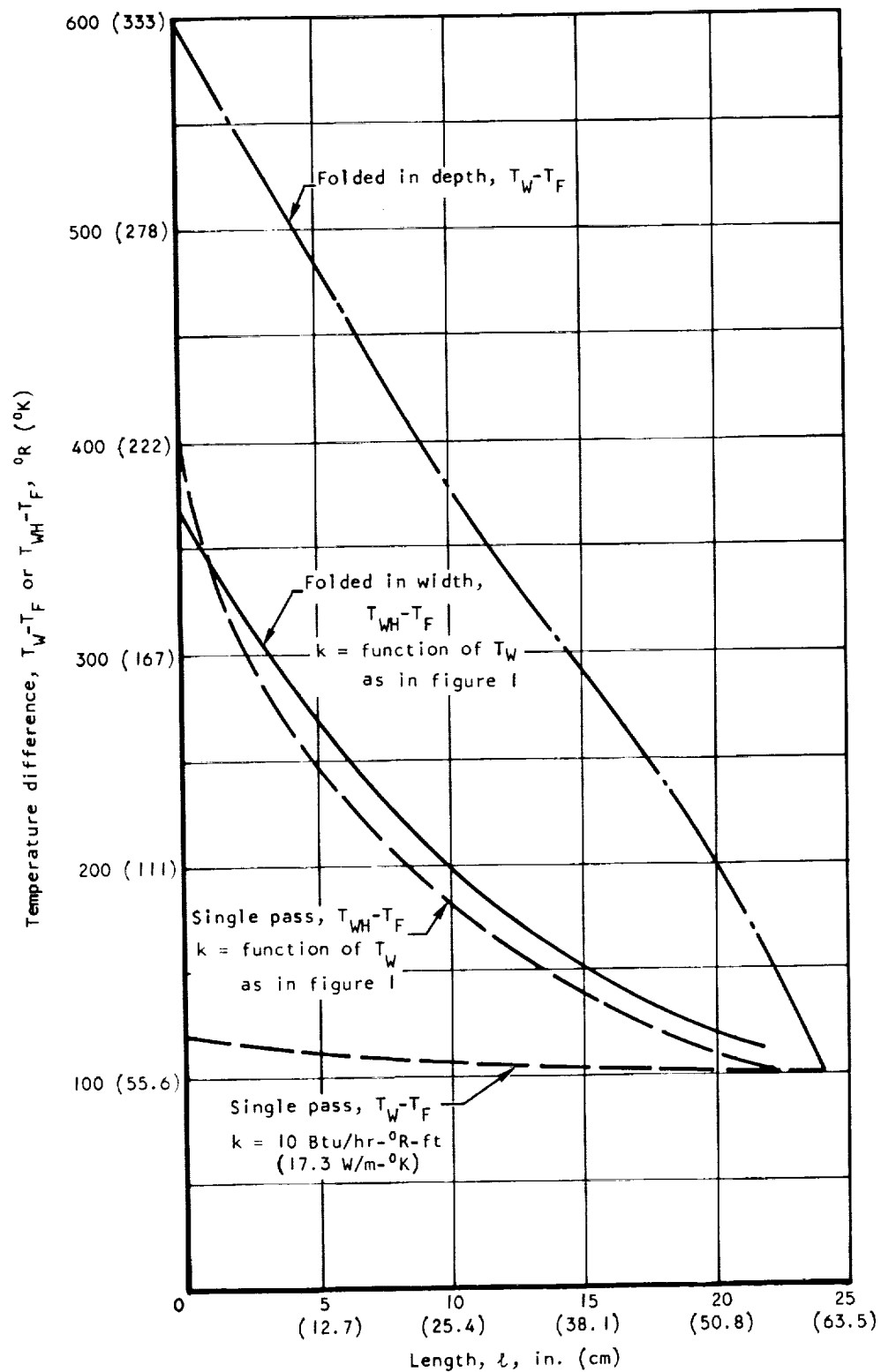
Figure 32. Typical Cross Section ΔT Profiles
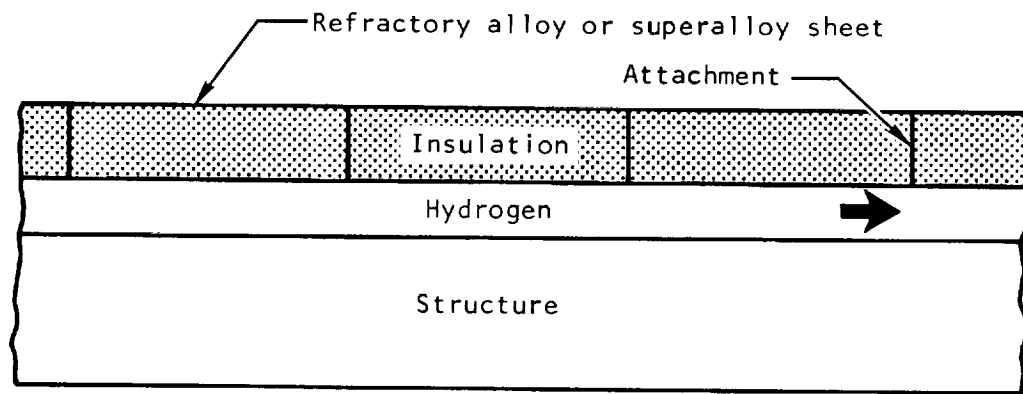
(a) Sheet metal covered insulation
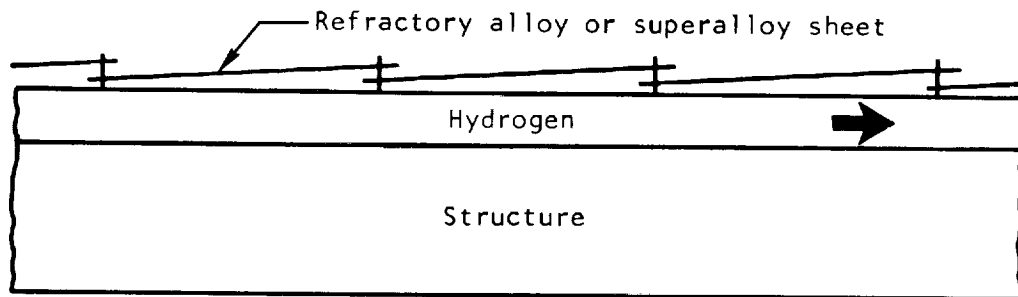
(b) Sheet metal shingle array
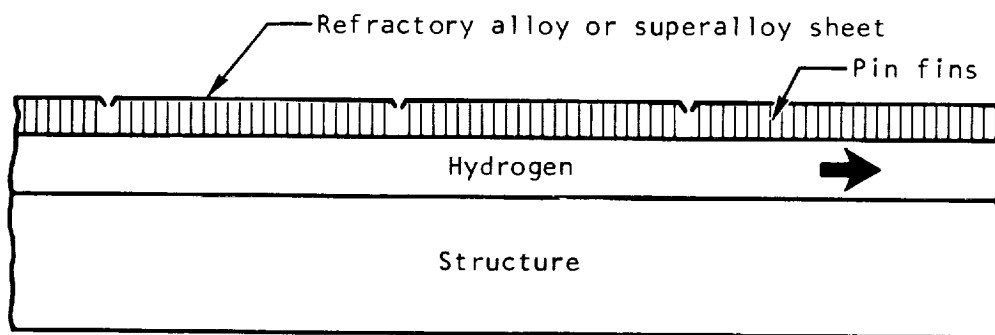
(c) Pin-fin insulation

Figure 33. Insulation Concepts
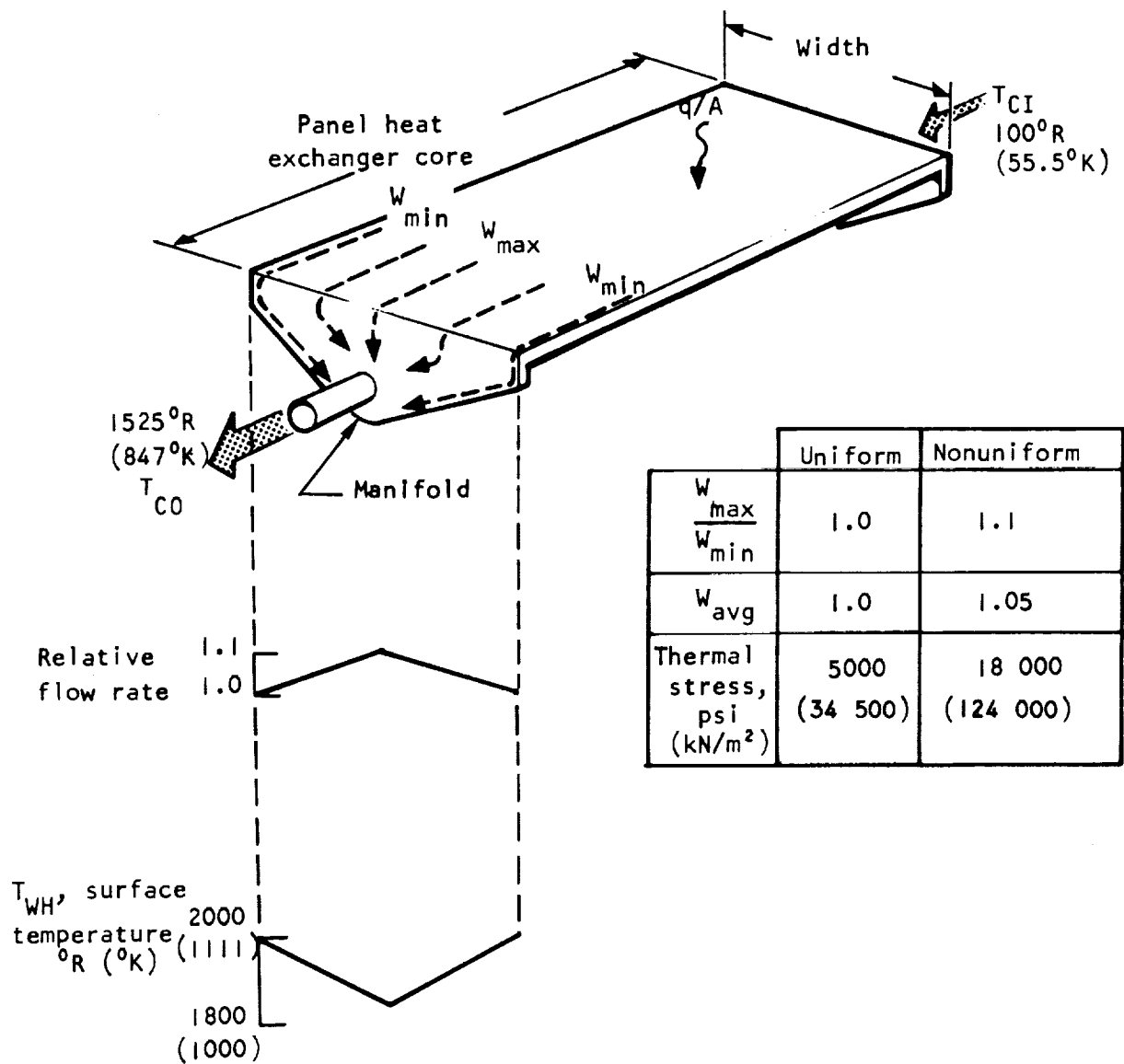
Figure 34. Flow Distribution Effects
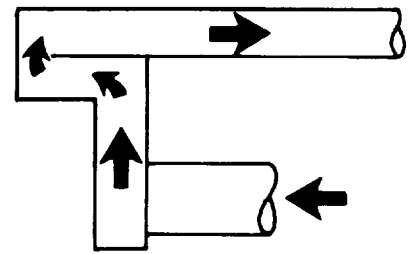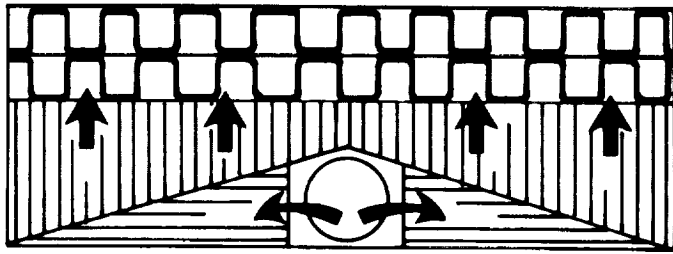
(a) Flat rectangular
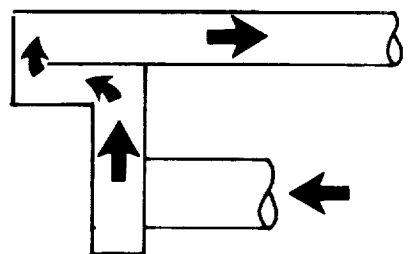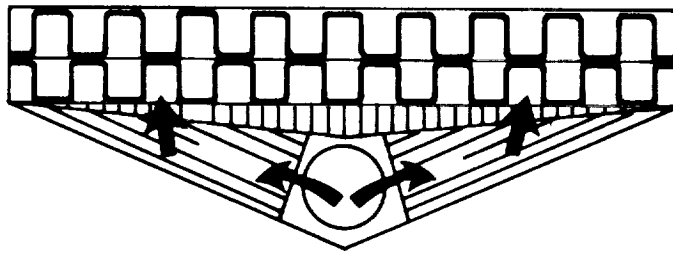
(b) Flat tapered
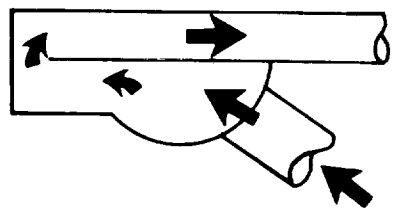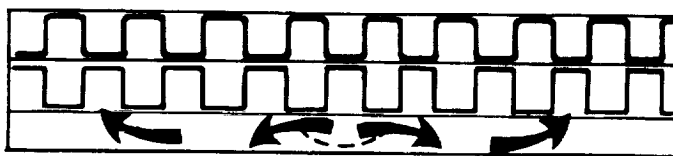
(c) Semicylindrical

Figure 35. Manifold Concepts
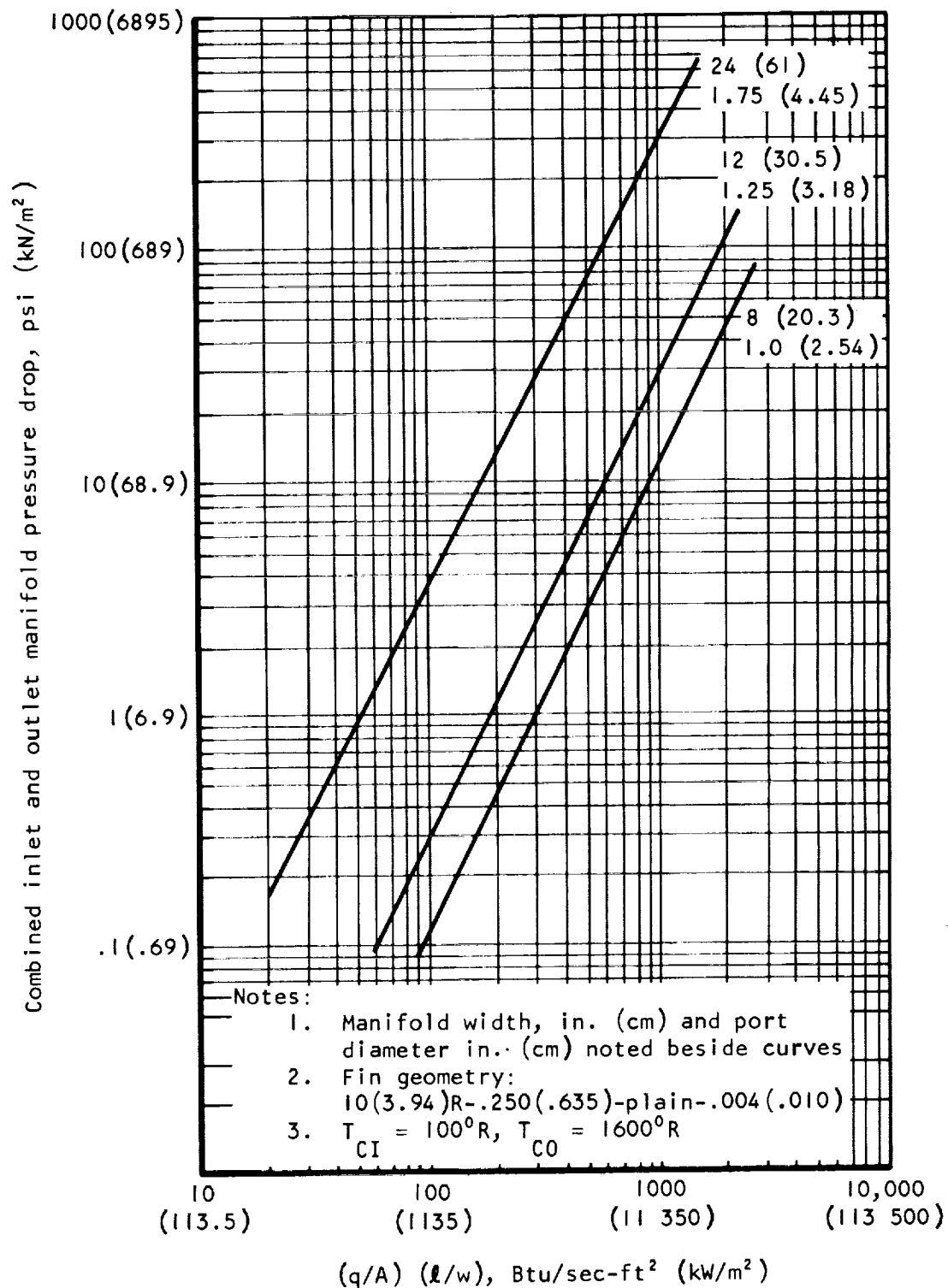
Figure 36. Manifold Pressure Drop

The chart axes and labels:
- Y-axis: Combined inlet and outlet manifold pressure drop, psi (kN/m²)
- Y-axis values: 1000(6895), 100(689), 10(68.9), 1(6.9), .1(.69)
- X-axis: (q/A) (ℓ/w), Btu/sec-ft² (kW/m²)
- X-axis values: 10 (113.5), 100 (1135), 1000 (11 350), 10,000 (113 500)

Curve labels:
- 24 (61), 1.75 (4.45)
- 12 (30.5), 1.25 (3.18)
- 8 (20.3), 1.0 (2.54)

Notes:
1. Manifold width, in. (cm) and port diameter in. (cm) noted beside curves
2. Fin geometry: 10(3.94)R-.250(.635)-plain-.004(.010)
3. $T_{CI} = 100°R$, $T_{CO} = 1600°R$

Notes:

1. h_{fin}, in. (cm) noted beside curves

2. Metal density = .3 lb/in³ (8300 kg/m³)

3. Fin geometry:

   $10(3.94)R-h_{fin}-plain-.004(.010)$
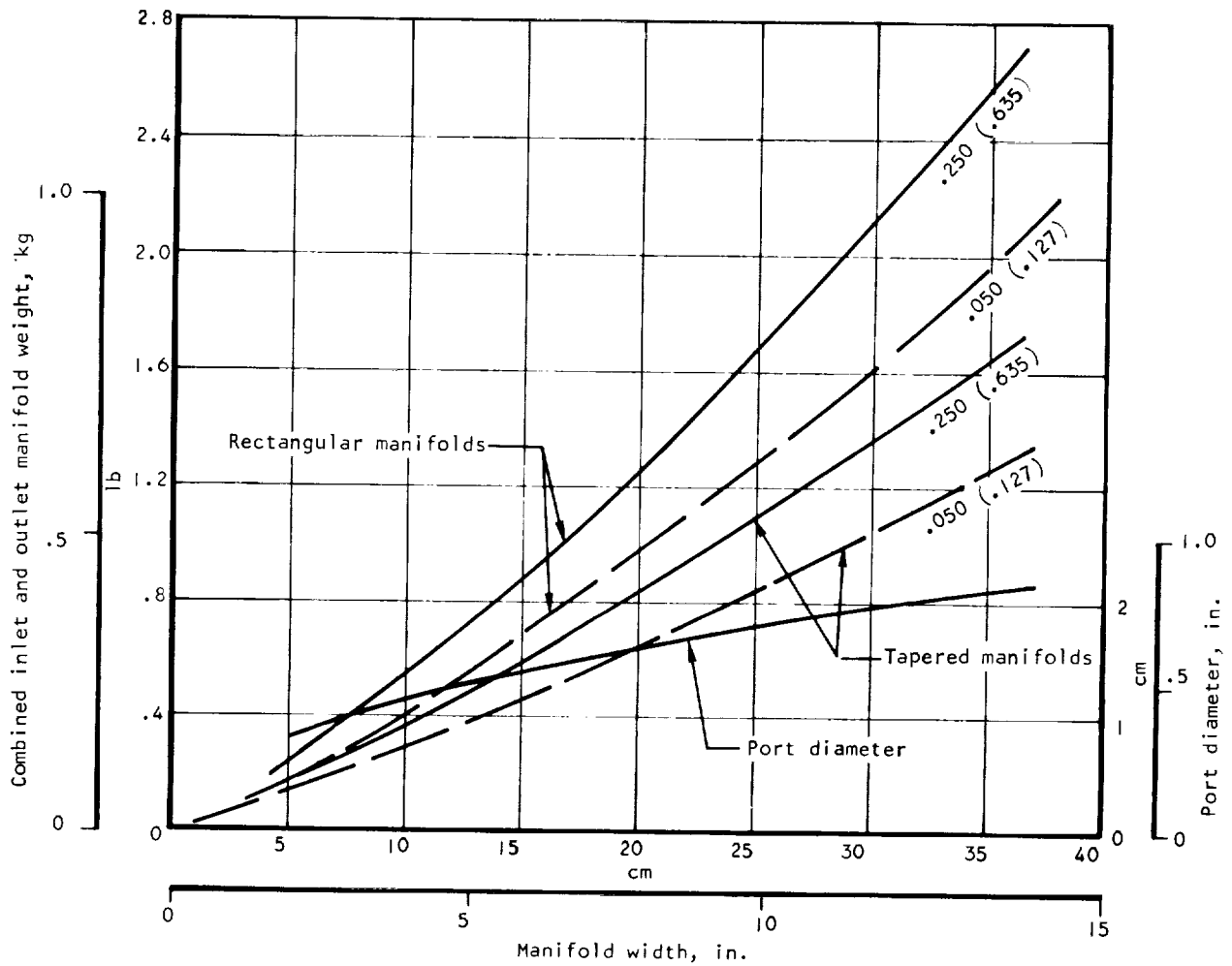
Figure 37. Manifold Weight
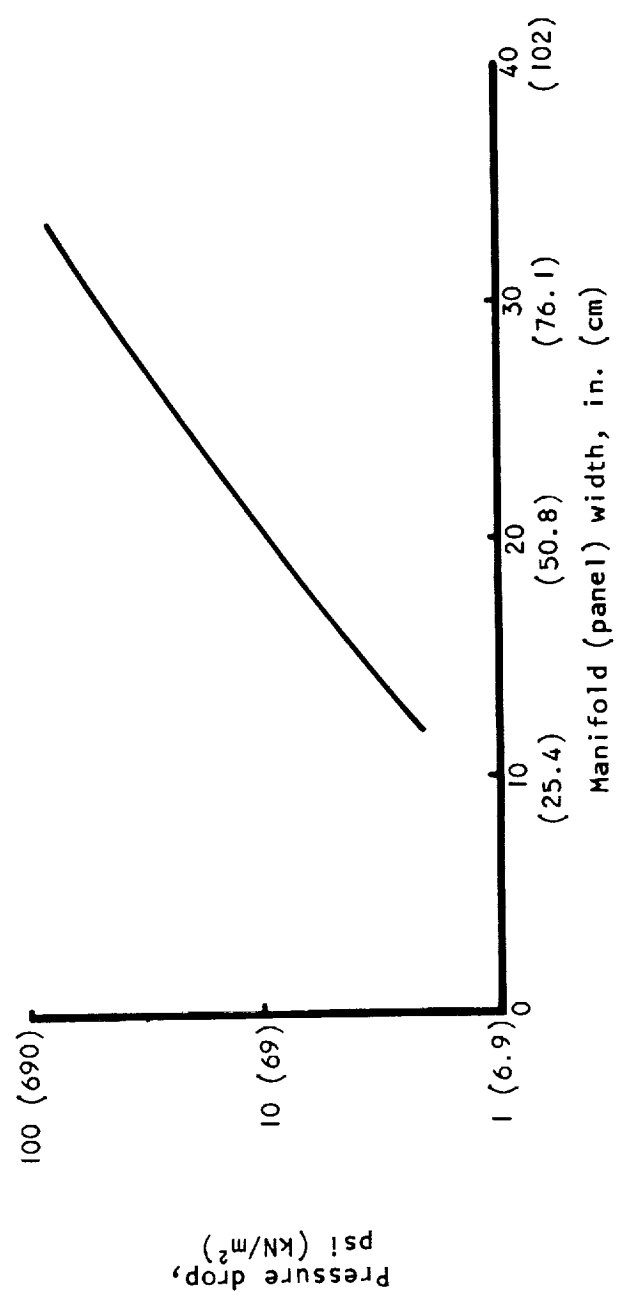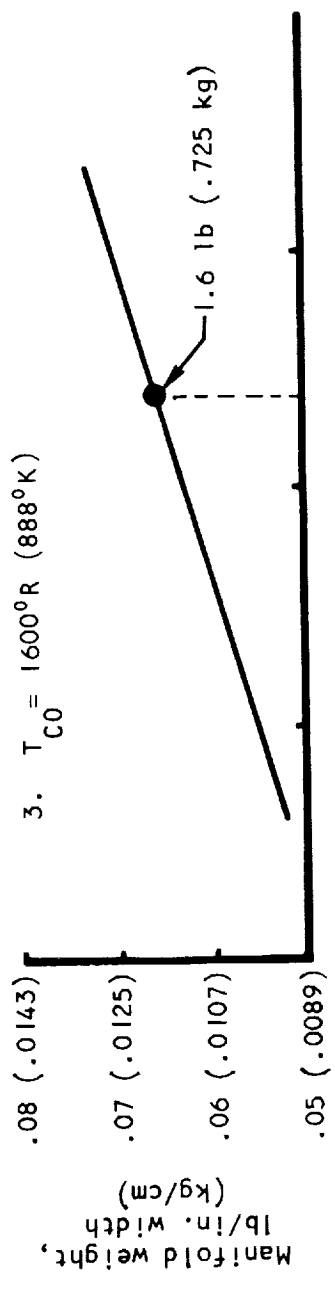
Figure 38. Manifold Performance
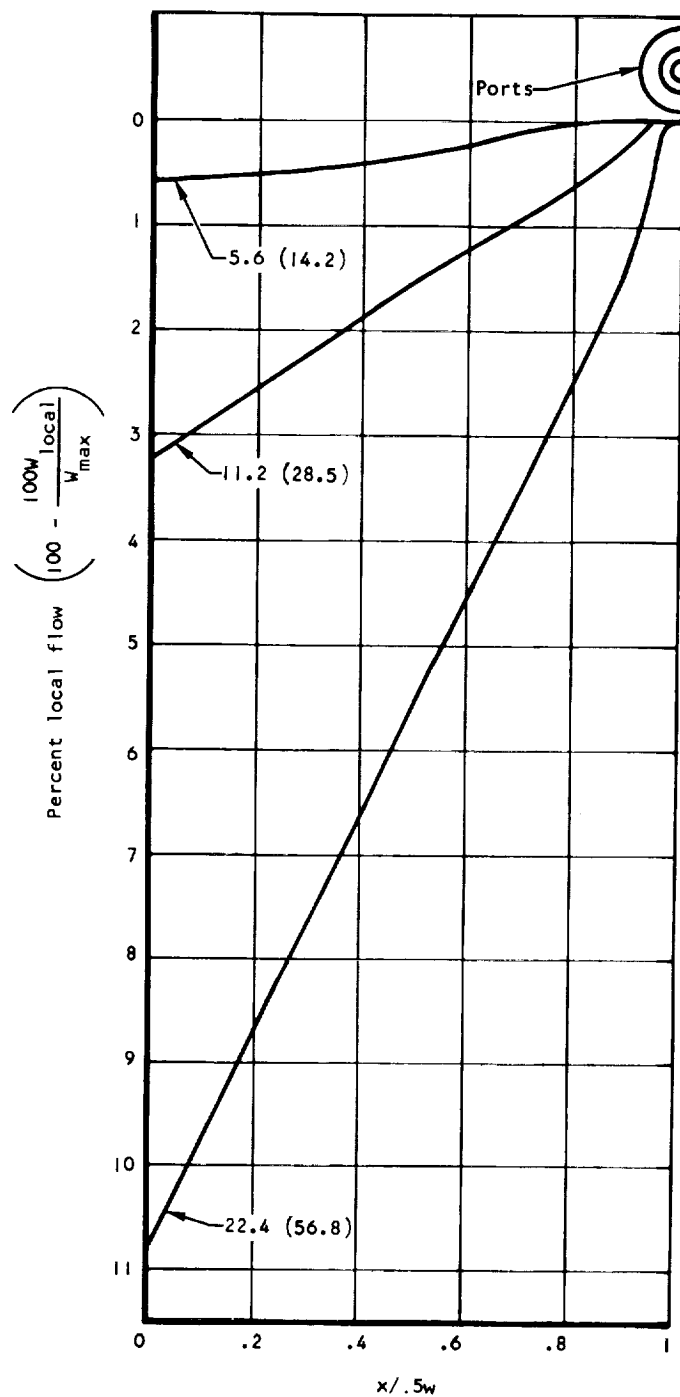
Figure 39. Calculated Flow Distributions
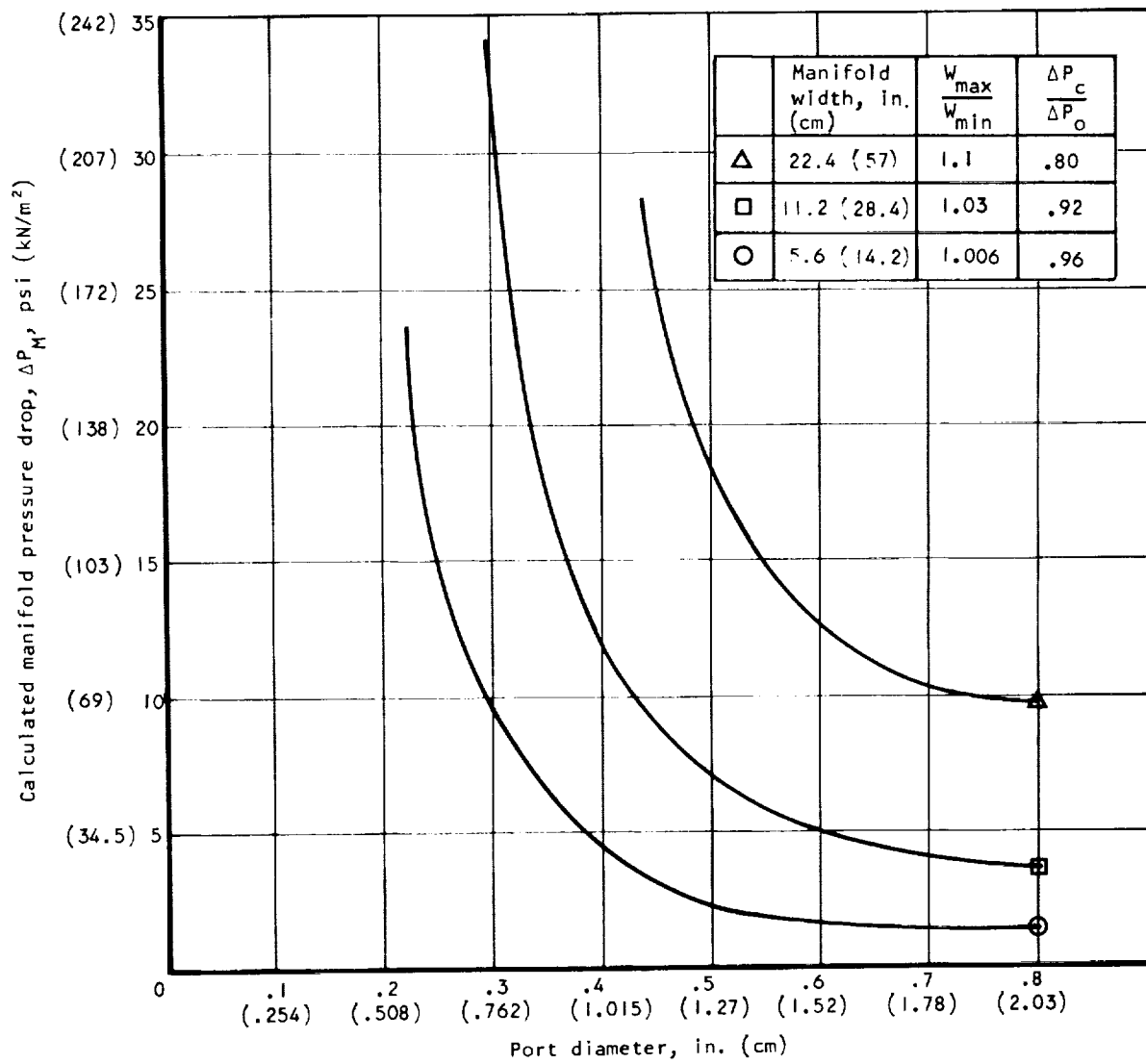
Figure 40. Calculated Inlet plus Outlet Manifold Pressure Drop
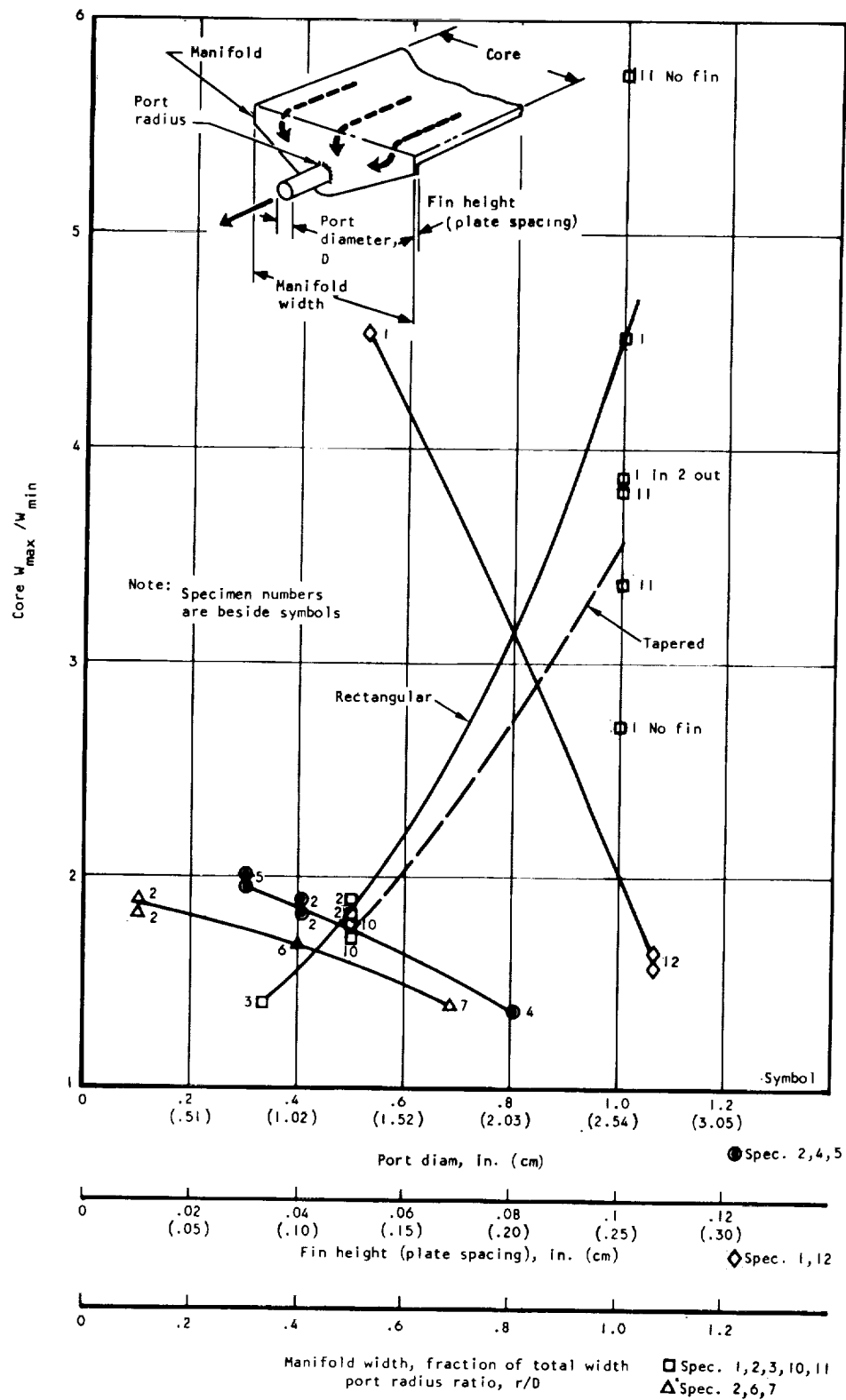
Figure 41. Effects of Manifold Geometry on Flow Distribution
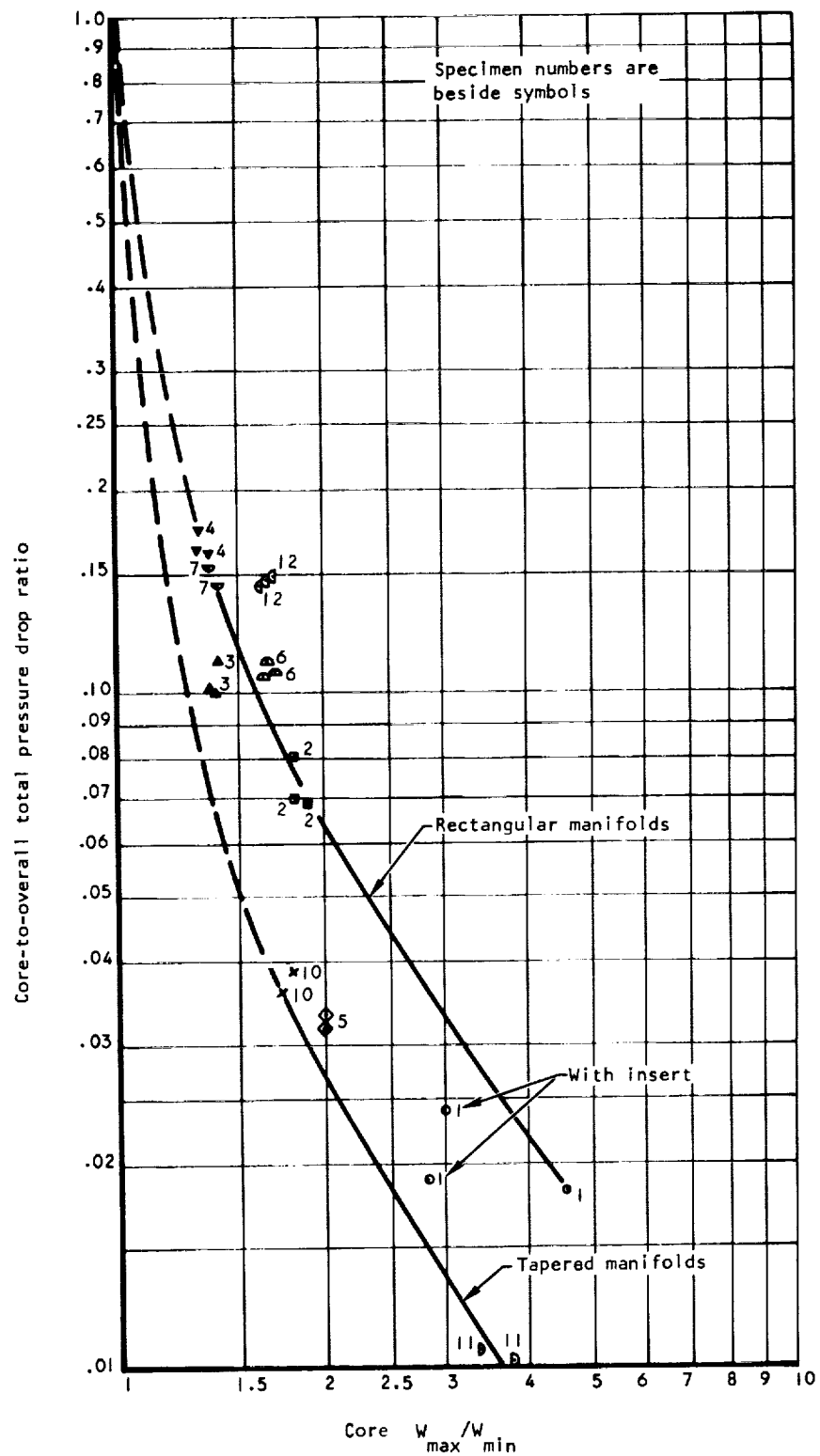
Figure 42. Effects of Pressure Drop Ratio on Flow Uniformity

114

Numbers beside curves indicate fins per inch and thickness, in.
(fins/cm, cm)
Hydraulic radius, r_h = .125 (L_o)
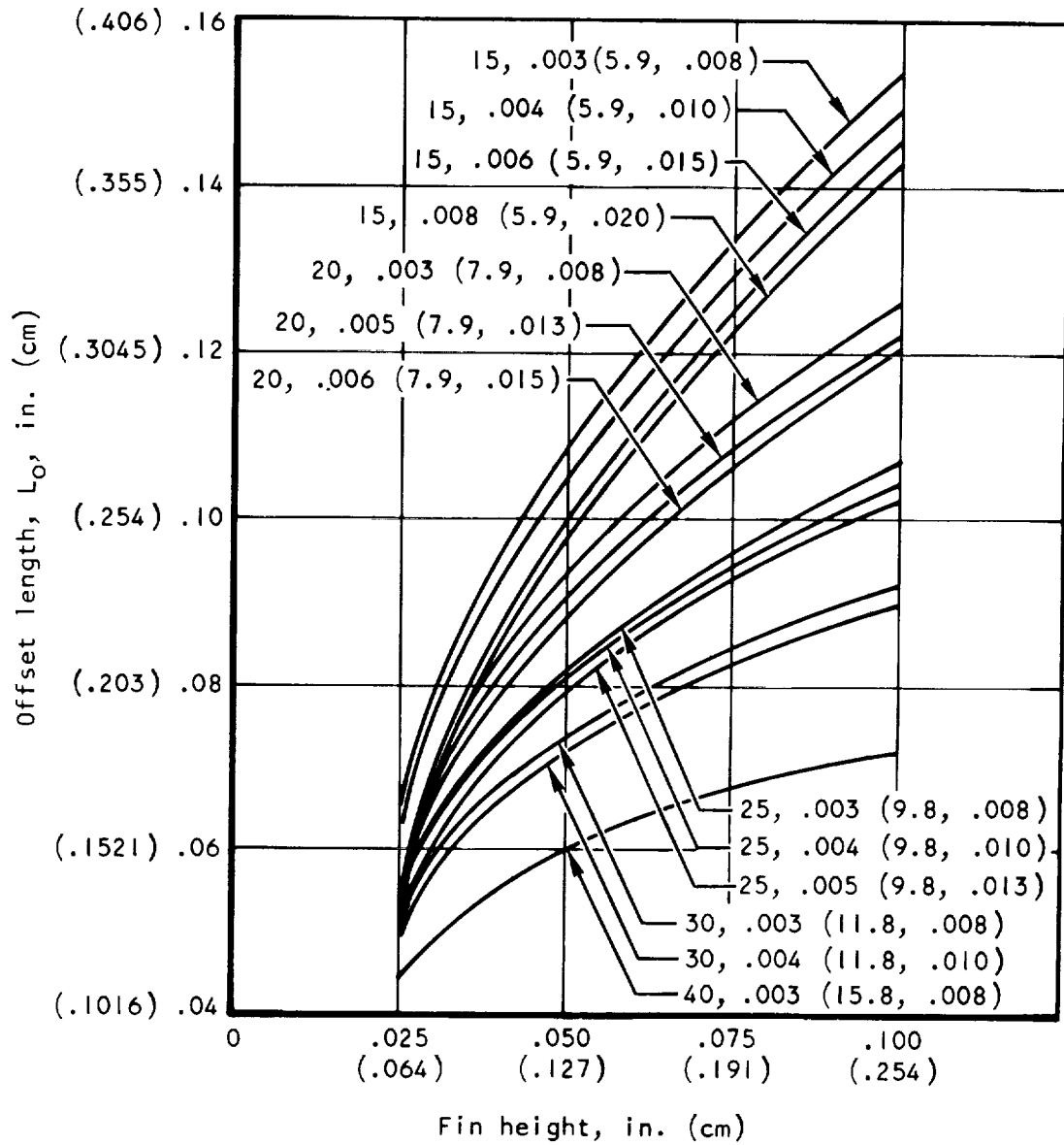
Figure 43. Geometry for Rectangular Offset Fins
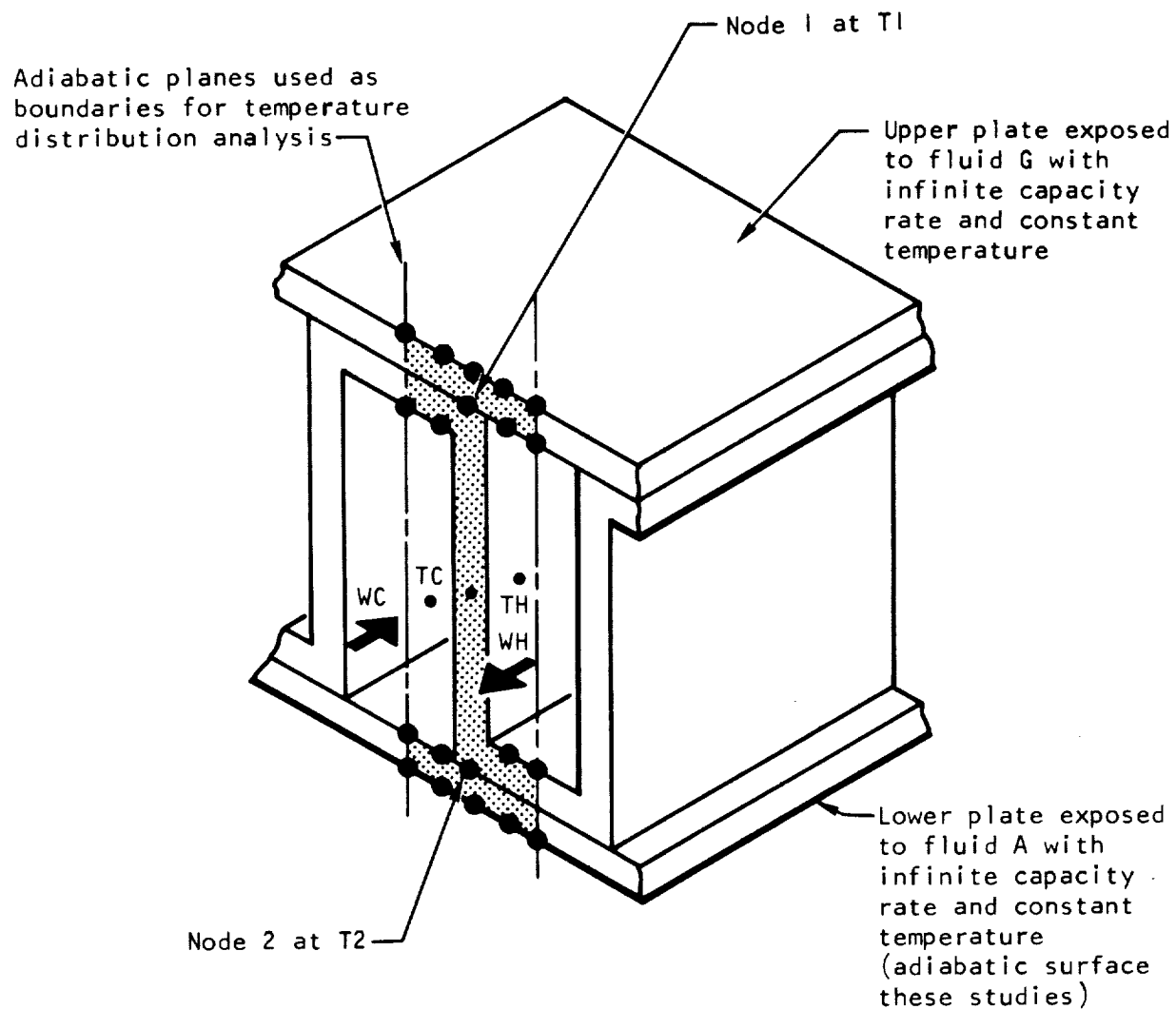
Figure 44. Locations of Temperatures in Computer Output

Numbers beside solid curves indicate flow rates,
W/w, lb/sec-ft (kg/sec-m)

Numbers beside dashed curves indicate hydrogen
outlet temperatures, $^{\circ}R$ ($^{\circ}K$)

Fin geometry:
20(7.9)-.075(.191)-plain-.003(.008)-(7-3,
$L_0/4r_h$ = 100, constant T_W)
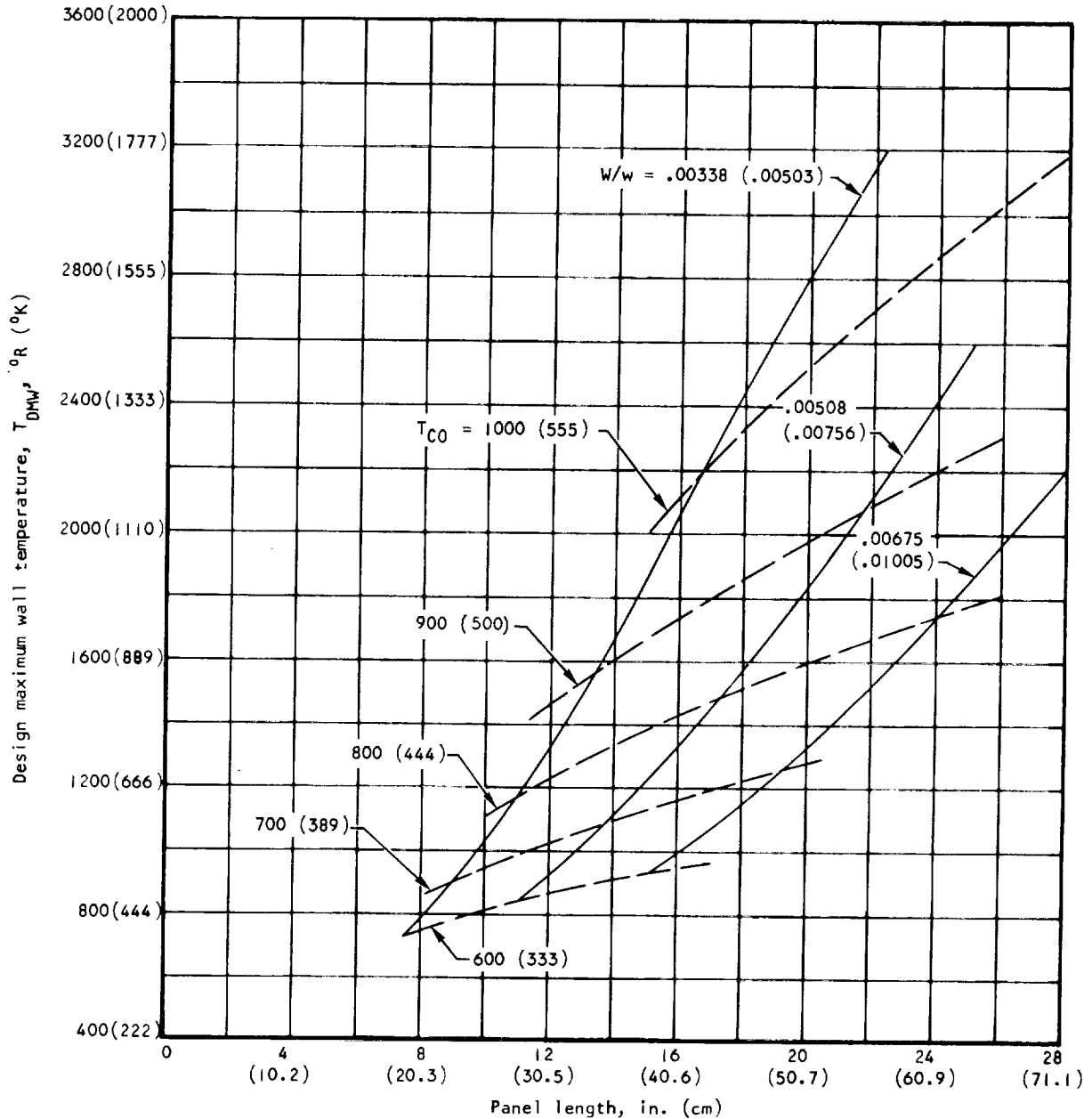
Figure 45. T_{DMW}, T_{CO}, and W/w as Functions of Panel Length for Folded-in-Width Panel, at Normal q/A = 10 Btu/sec ft² (114 kW/m²)

N and h_{fin} noted beside curves

Fin geometry:

$(N)R-h_{fin}$-plain-.003(.008)-(7-3, $L_0/4r_h$ = 100, constant T_W)
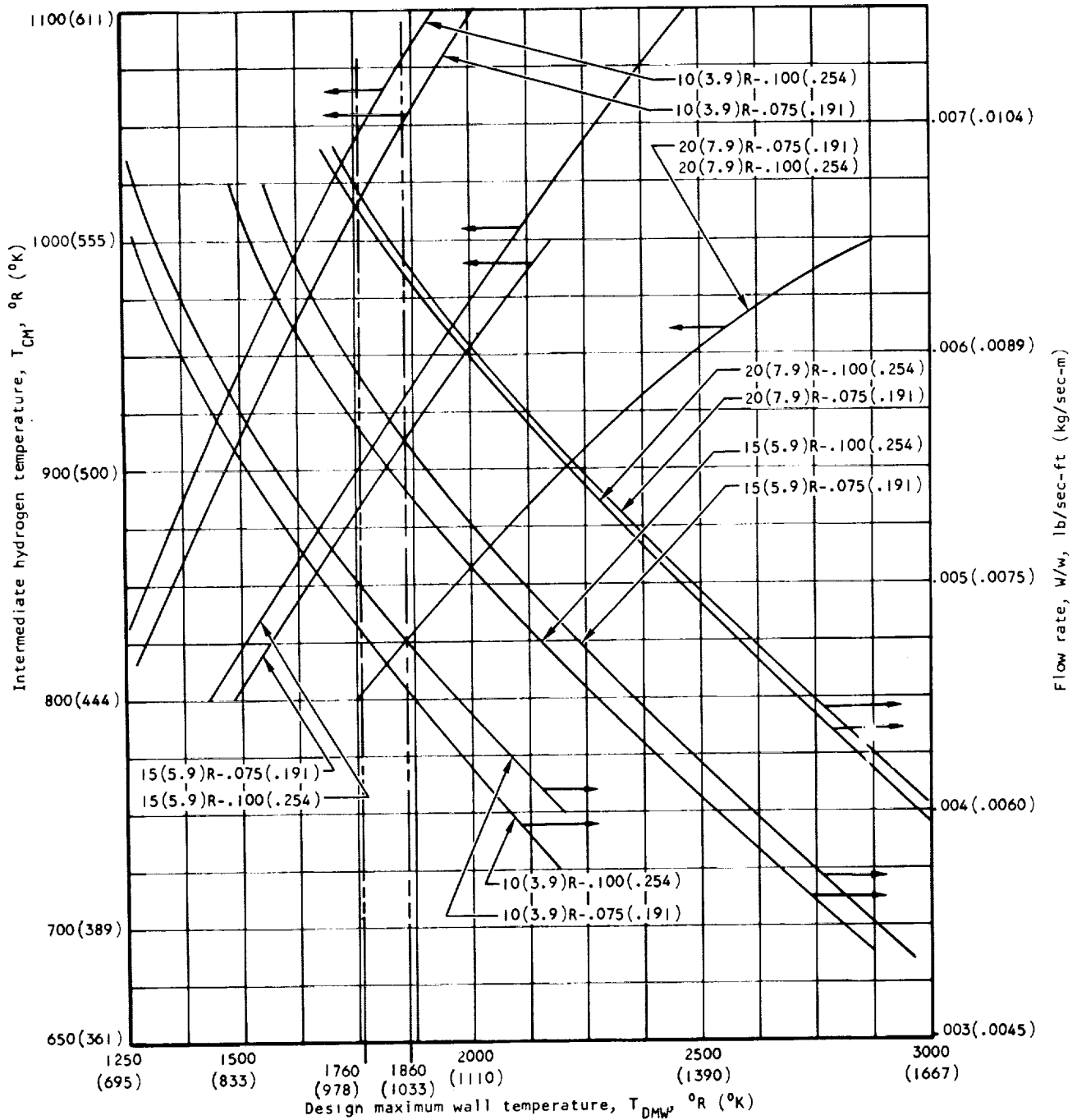
Figure 46. W/w and T_{CM} for Folded-in-Width Panel Only, at Nominal
q/A = 10 Btu/sec-ft² (114 kW/m²) and ℓ = 2 ft (0.61 m)
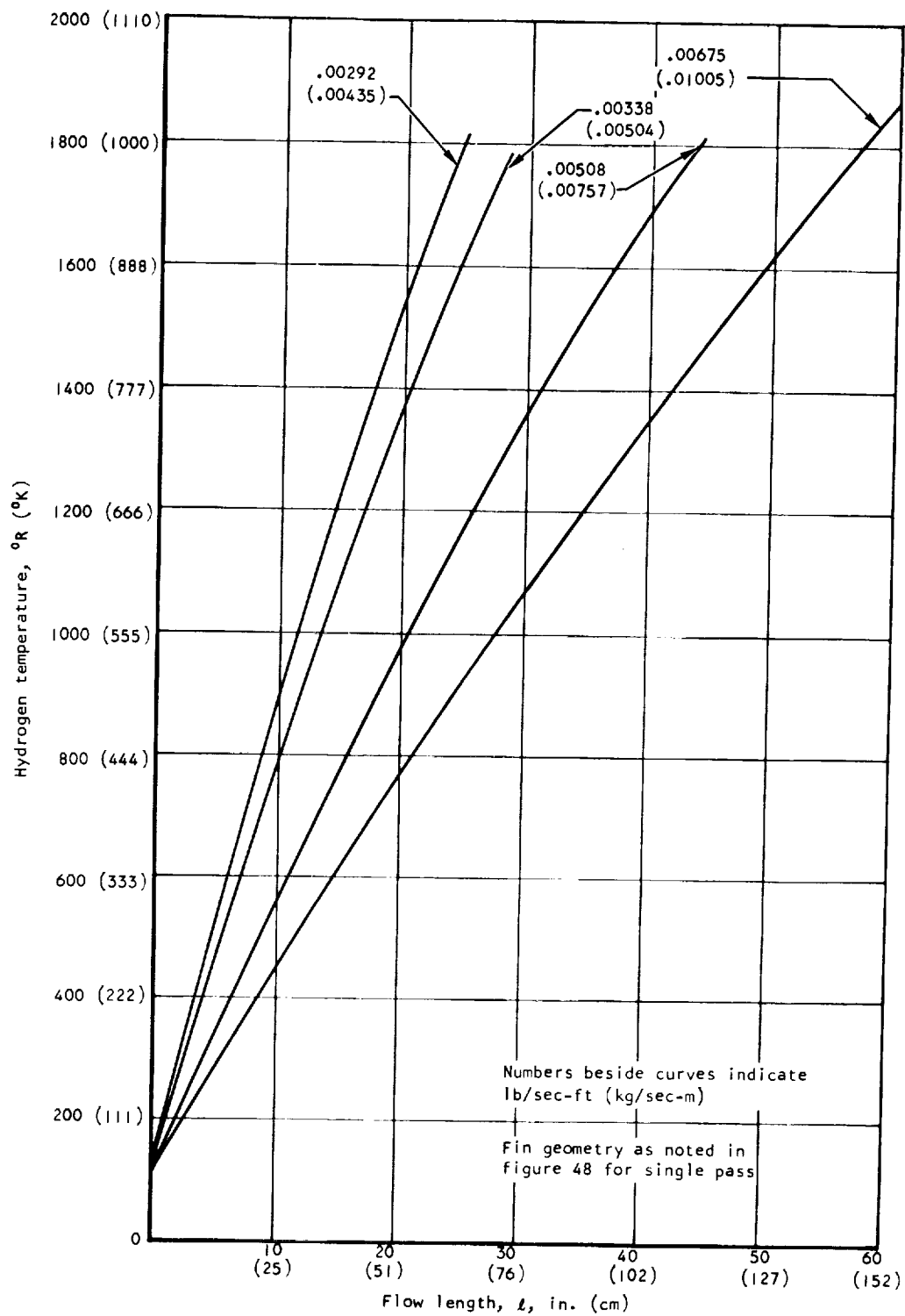
Figure 47.   Hydrogen Temperature in Single-Pass Panels with Nominal
q/A = 10 Btu/sec-ft² (114 kW/m²)
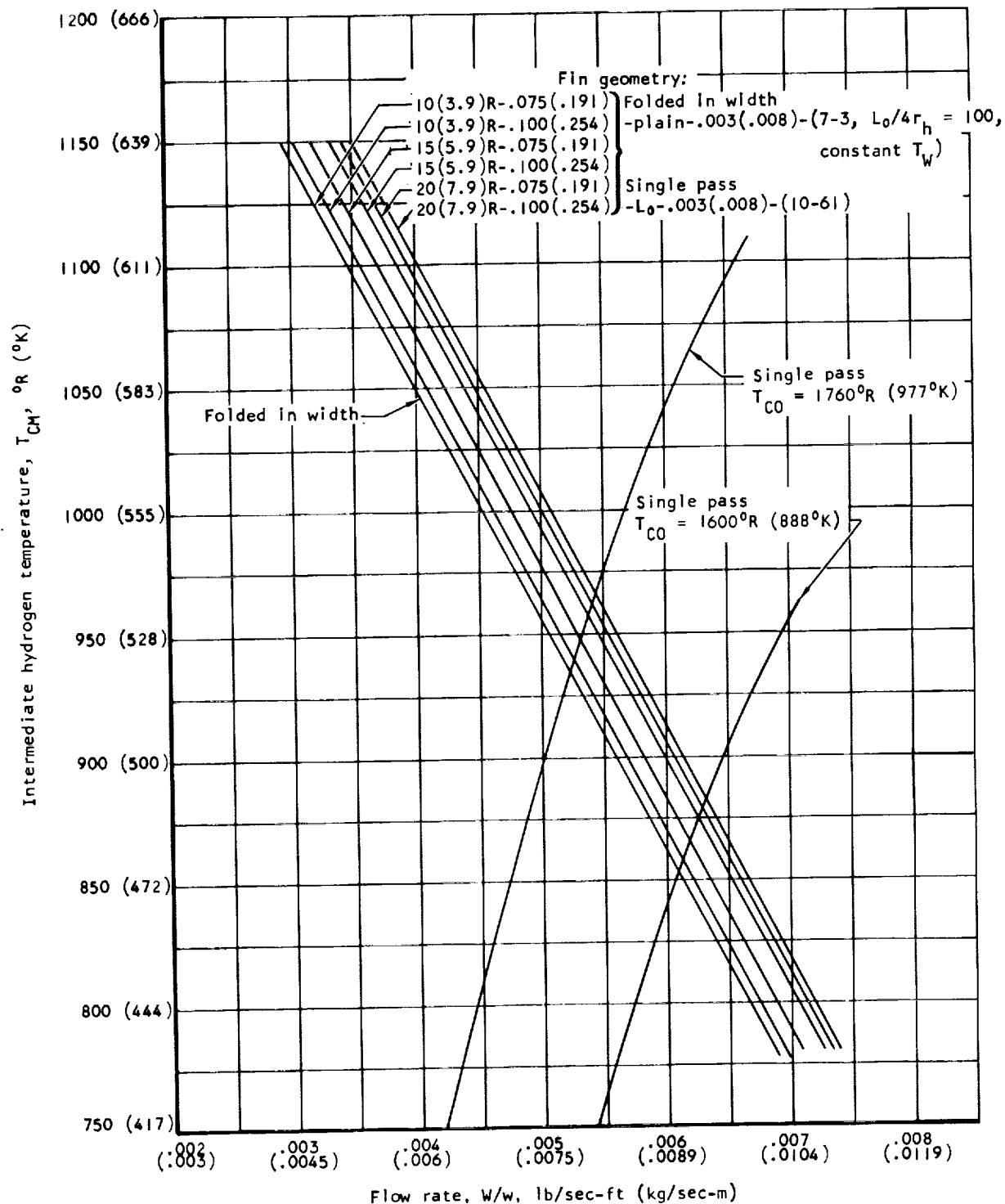
Figure 48. T_{CM} between Folded-in-Width and Single-Pass Panels in Series at Nominal $q/A = 10$ Btu/sec-ft^2 (114 kW/m^2) and $\ell = 2$ ft (.61 m)

120

h_{fin}, in. (cm) is noted beside curves

t_{fin}, in. (cm) noted beside curves for nominal q/A of 500 Btu/sec-ft^2 (5680 kW/m^2)

Fin geometry:

q/A Btu/sec-ft^2 (kW/m^2)	Flow configuration	
250(2840)	single	20(7.9)R-h_{fin}-L_0- .004(.010)-(10-61)
250(2840)	folded	20(7.9)R-h_{fin}-plain-.004(.010)-(7-3, $L_0/4r_h$ = 100, constant T_w)
500(5680)	single	20(7.9)R-h_{fin}-L_0-t_{fin}-(10-61)
500(5680)	folded	20(7.9)R-h_{fin}-plain-t_{fin}-(7-3, $L_0/4r_h$ = 100, constant T_w)
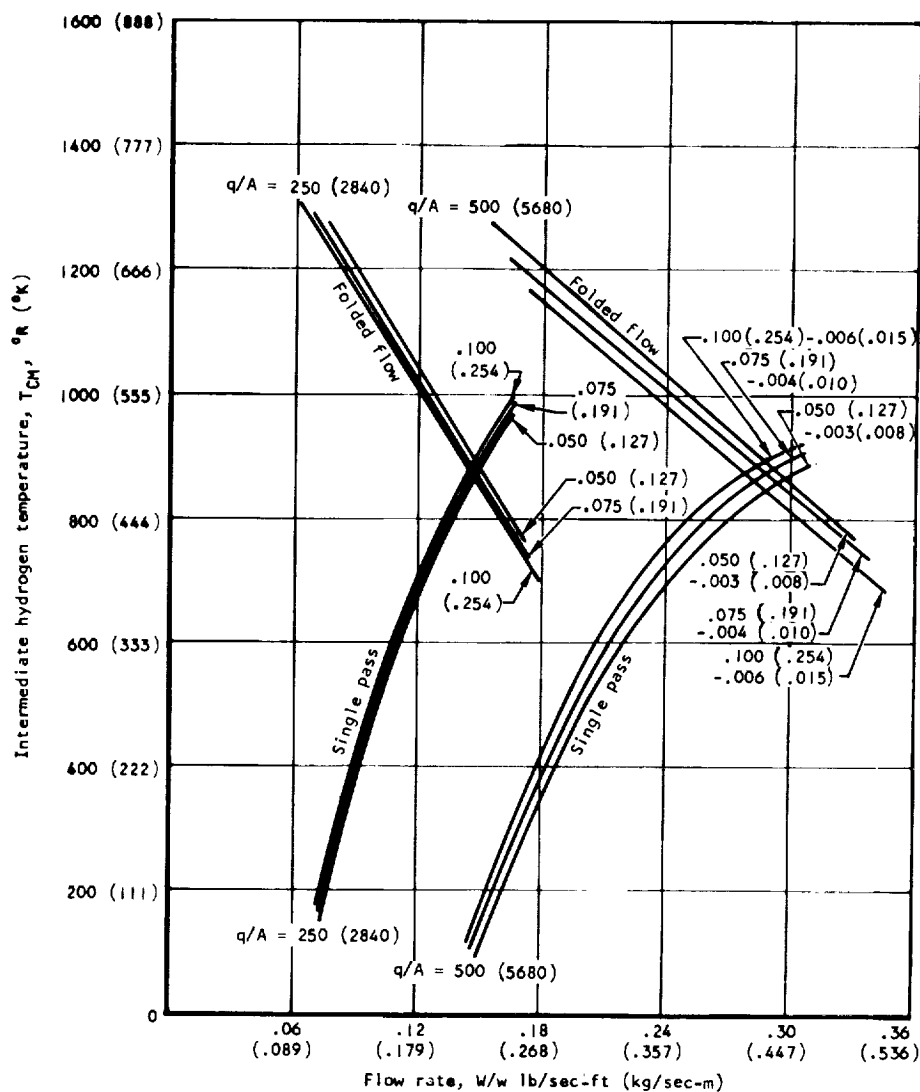
Figure 49. T_{CM} between Folded-in-Width and Single-Pass Panels at Nominal q/A = 250 and 500 Btu/sec-ft^2 (2840 and 5680 kW/m^2) and ℓ = 2 ft (.61 m)
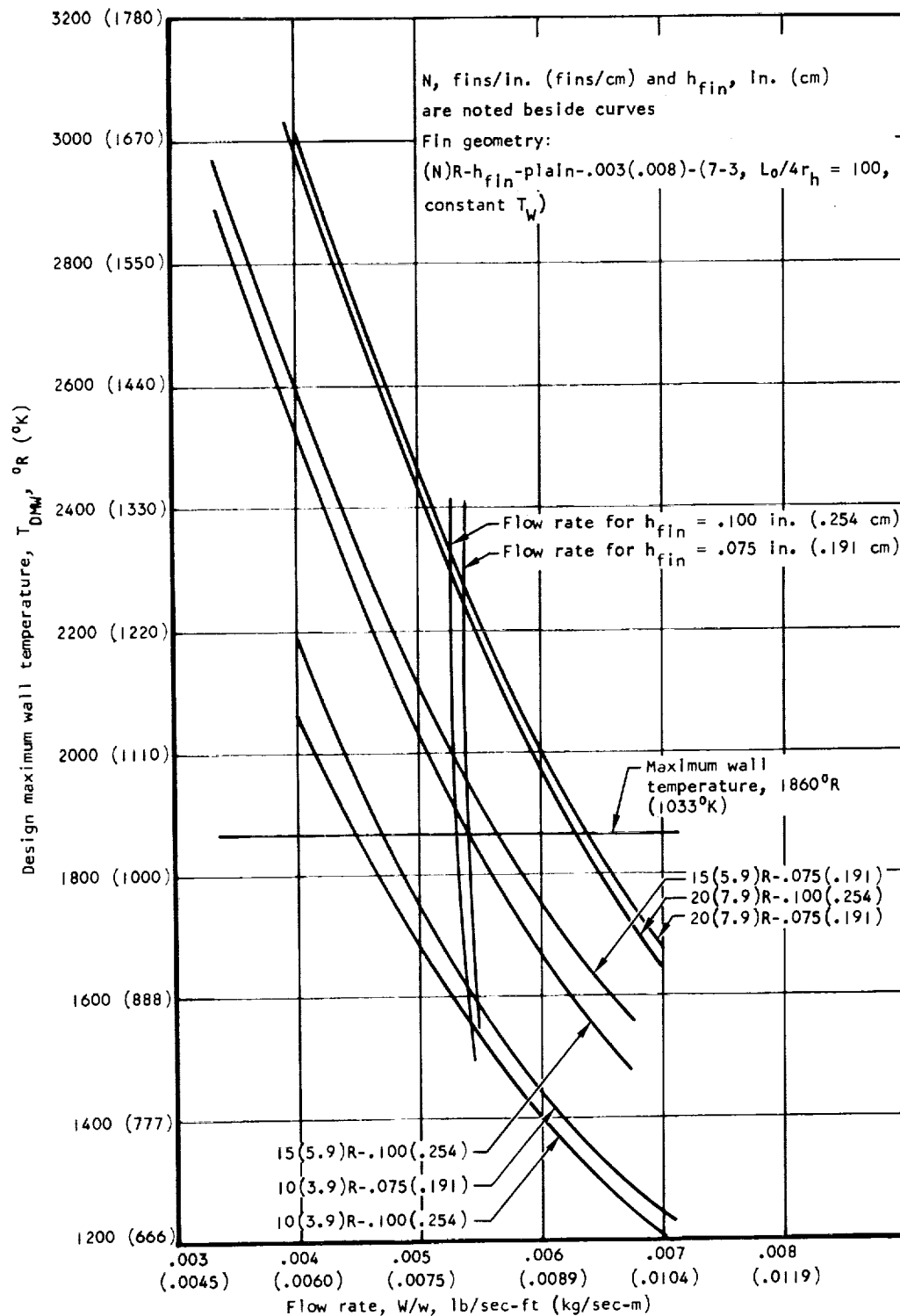
Figure 50. Fin Geometry Selection for Folded-Flow Only at Nominal q/A = 10 Btu/sec-ft^2 (114 kW/m^2) and ℓ = 2 ft (.61 m)

Heat flux, q/A, Btu/sec-ft² (kW/m²)	10 to 100 (114 to 1140)	50 to 500 (570 to 5680)	50 to 500 (570 to 5680)
Pressure, P, psia (kN/m²)	7 to 100 (48 to 690)	50 to 250 (345 to 1720)	50 to 250 (345 to 1720)
Heat exchanger weight, lb/ft² (kg/m²)	1.2 to 1.5 (5.9 to 7.3)	.7 to .9 (3.4 to 4.4)	1.1 to 1.40 (5.4 to 6.9)
Total weight, lb/ft² (kg/m²)	1.8 to 4 (9 to 20)	5 to 10 (24 to 49)	5 to 8 (24 to 39)
Thickness, t, in. (cm)	1 to 3 (2.5 to 7.6)	2 to 5 (5.1 to 12.7)	3.5 to 6.5 (9 to 16.5)
Hydrogen flow rate, lb/sec-ft² (kg/sec-m²)	.0008 to .008 (.0039 to .039)	.008 to .08 (.039 to .39)	.008 to .08 (.039 to .39)
	Concept 1, Integral	Concept 2, Bonded	Concept 3, Nonintegral

Figure 51. Operating Conditions and Configurations for Regeneratively Cooled Panel Applications

	T_{CO}		W/w		Allowable hydrogen pressure only for fin 20(7.9)R-.025(.063)-.053 -(.135)-.003(.008)-(10-61)	
	°R	(°K)	lb/sec-ft	(kg/sec-m)	psig	(kN/m²)
A.	1900	(1058)	.00314	(.00468)	332	(2290)
B.	1760	(979)	.00338	(.00504)	587	(4050)
C.	1600	(890)	.00374	(.005575)	852	(5880)
D.	1400	(778)	.00435	(.00649)	960	(6620)

Fin geometry (N)r-h$_{fin}$ - L$_o$ - .003(.008)-(10-61)

10 fins/in.
(4 fins/cm)

15 fins/in.
(5.9 fins/cm)

20 fins/in.
(7.9 fins/cm)

20 fins/in. (7.9 fins/cm)
k_{fin} = 100 Btu/hr-°R-ft
(173 W/m-°K)

30 fins/in. (11.8 fins/cm)
k = 100 Btu/hr-°R-ft
(173 W/m-°K)

Temperature difference, $(T_{DHW} - T_{CO})$, °R (°K)

Fin height, in. (cm)
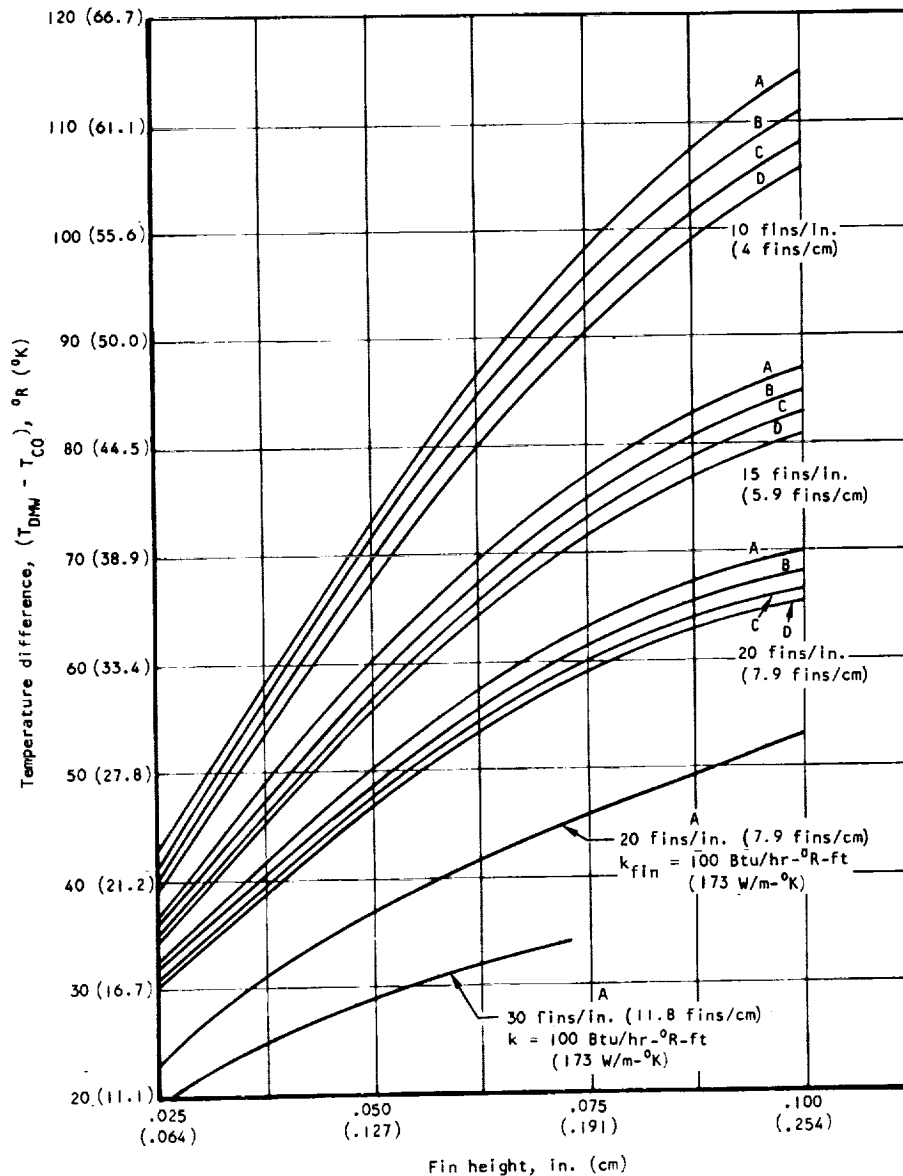
Figure 52. Heat Exchanger Performance for Concepts 1 and 2, ℓ = 2 ft (.61 m), $T_R = \infty$, q/A = 10 Btu/sec-ft² (114 kW/m²)

124

Numbers beside curves indicate fins/in. (fins/cm)

Fin geometry: $(N)R-h_{fin}-L_o-.003(.008)-(10-61)$

$W/w = .0374$ lb/sec-ft $(.0557$ kg/sec-m$)$

Fin height, in. (cm)
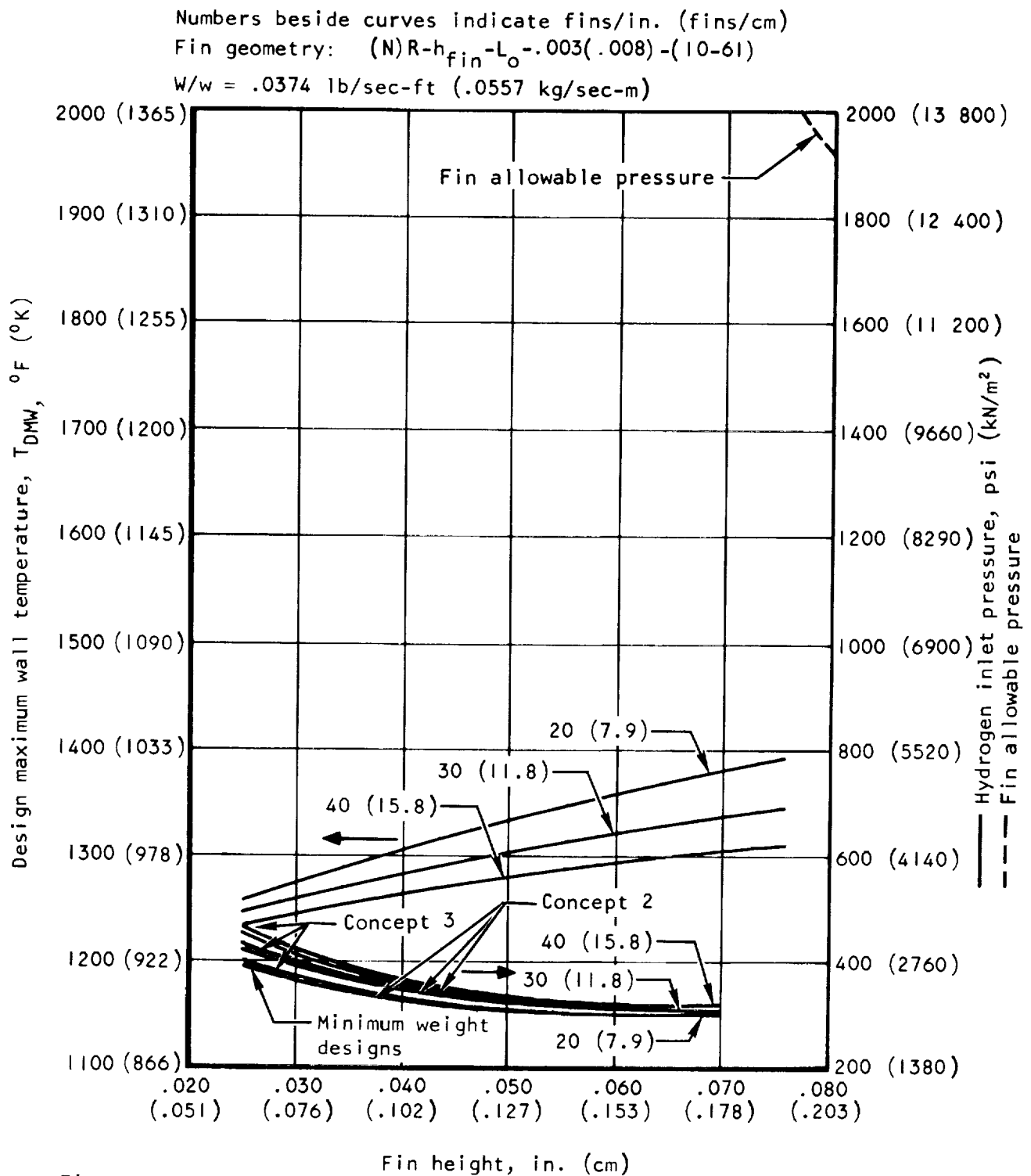
Figure 53. Heat Exchanger Performance for Concepts 2 and 3, $\ell = 2$ ft $(0.61$ m$)$, $T_R = \infty$, $q/A = 100$ Btu/sec-ft^2 $(1135$ kW/m$^2)$, $T_{CO} = 1600°R$ $(888°K)$

Figure 54. Heat Exchanger Performance for Concepts 2 and 3, $\ell = 2$ ft (0.61 m), $T_R = \infty$, $q/A = 250$ Btu/sec-ft^2 (2840 kW/m^2), $T_{CO} = 1400°R$ (778°K)
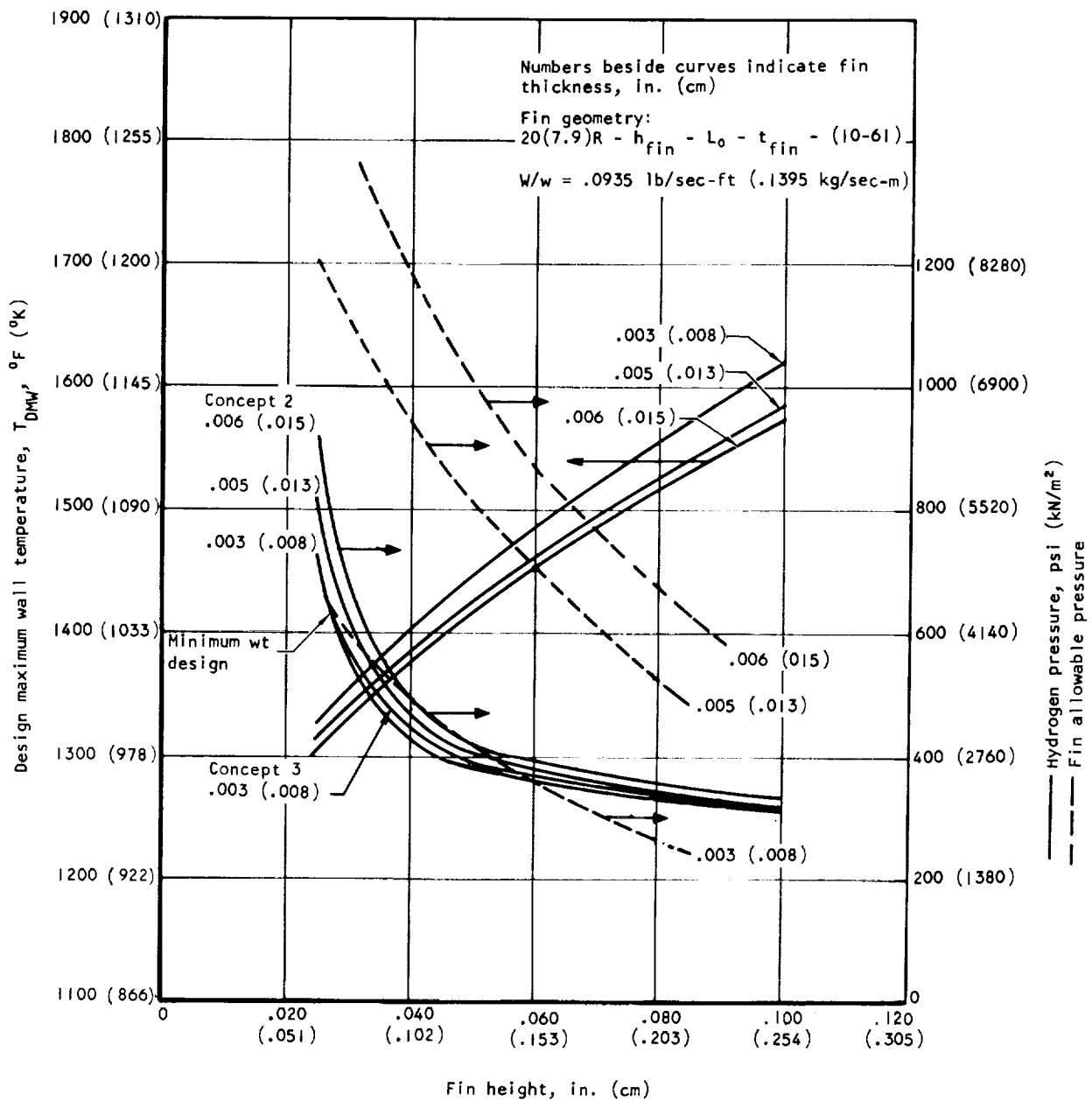
Figure 55. Heat Exchanger Performance for Concepts 2 and 3, $\ell = 2$ ft (0.61 m), $T_R = \infty$, q/A = 250 Btu/sec-ft^2 (2840 kW/m^2), $T_{CO} = 1600°R$ (888°K)

Fin geometry: 40 (15.8)R-h$_{fin}$-L$_o$-.003(.008)-(10-61)

W/w = .187 lb/sec-ft (.278 kg/sec-m)

Minimum weight design

Concept 2

Concept 3

Design maximum wall temperature, T$_{DMW}$, °F (°K)

Hydrogen inlet pressure, psi (kN/m²)

Fin allowable pressure

Fin height, In. (cm)
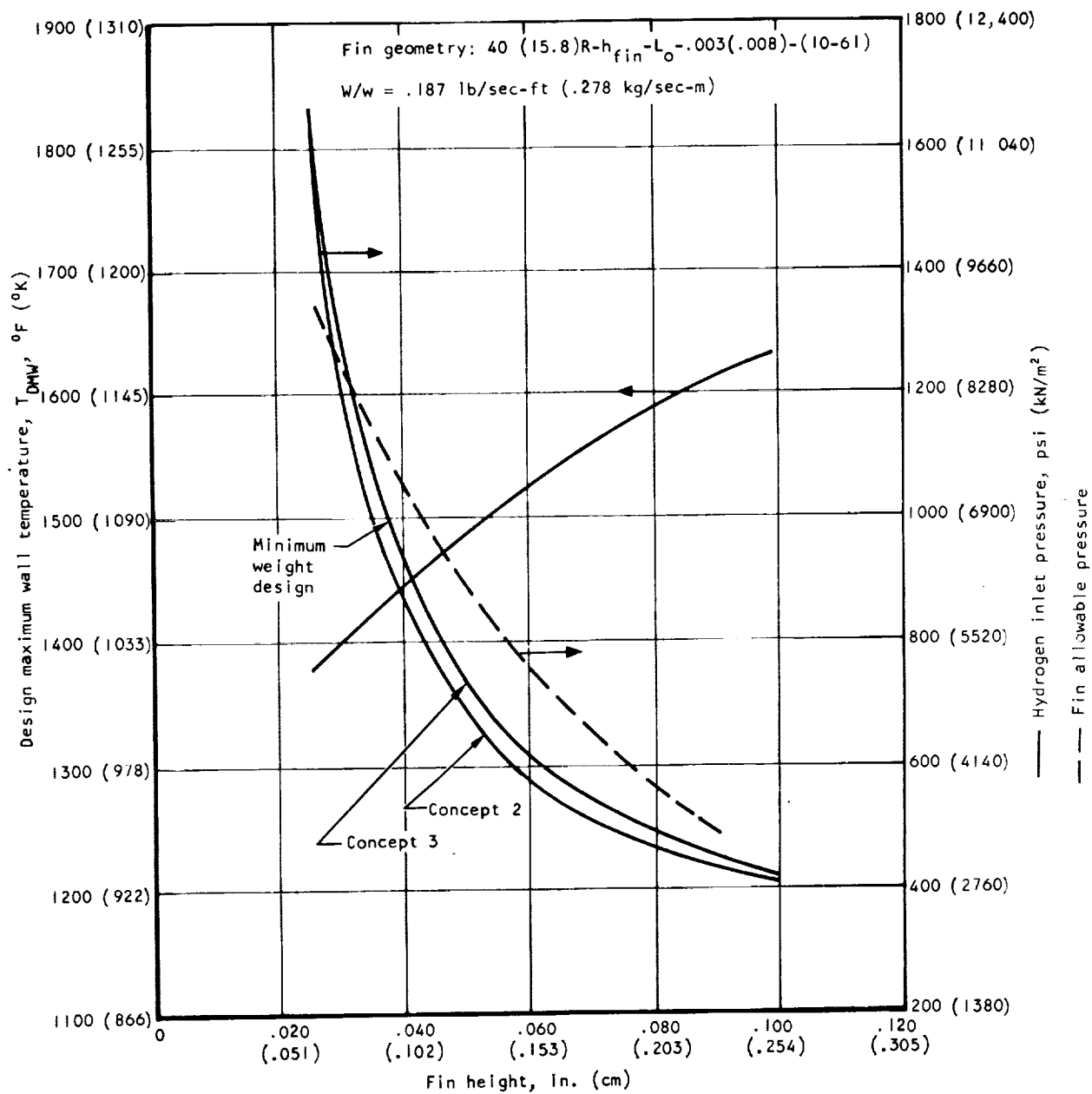
Figure 56. Heat Exchanger Performance for Concepts 2 and 3, ℓ = 2 ft (0.61 m), T$_R$ = ∞, q/A = 500 Btu/sec-ft² (5680 kW/m²), T$_{CO}$ = 1600°R (888°K)

128

W/w is noted beside curves, lb/sec-ft (kg/sec-m)

Tube geometry:

$(N)TB-h_{fin}-plain-.010(.025)-(7-1, L_o/4r_h = 100, constant T_w)$
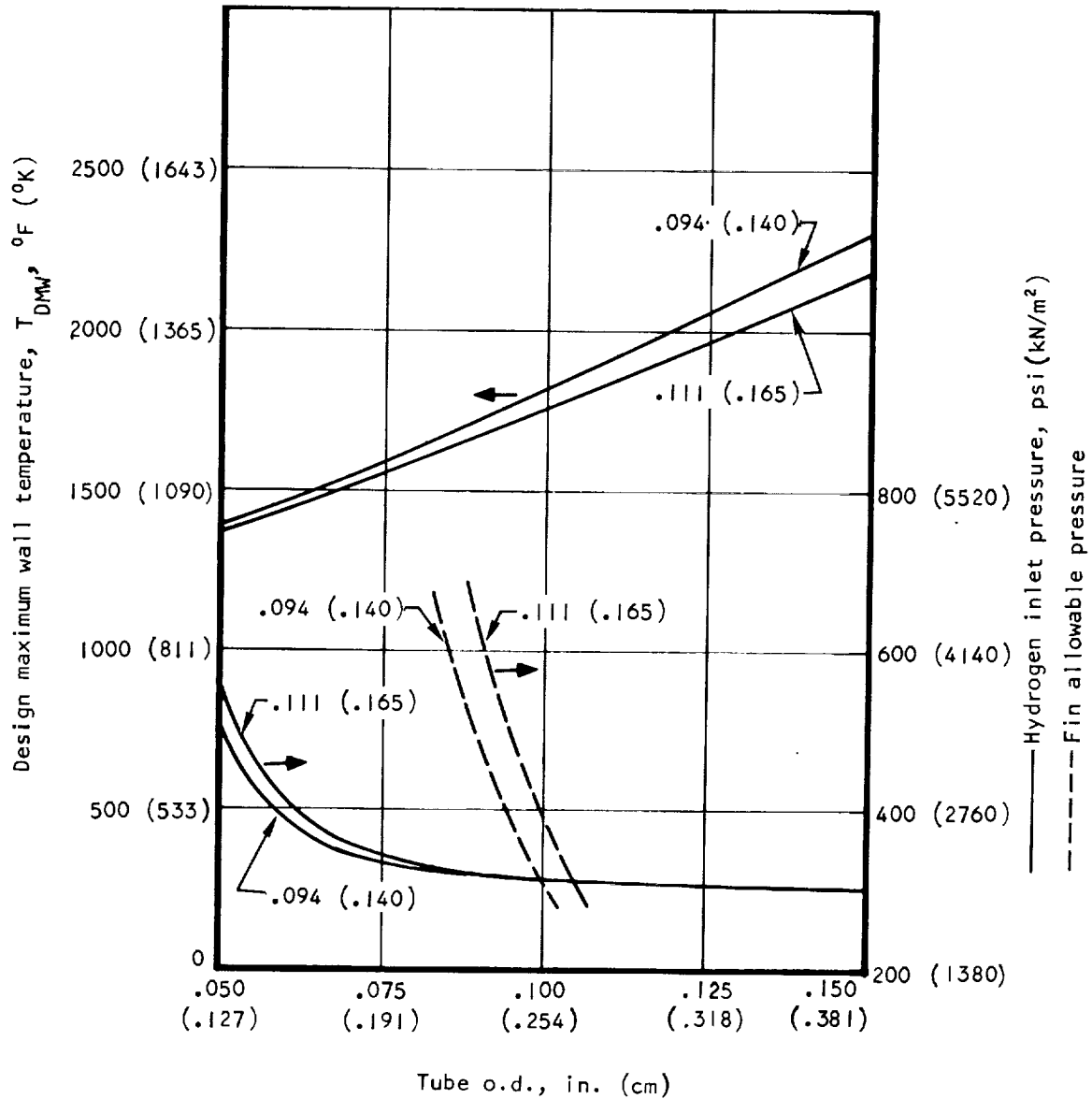
Figure 57. Tubular Heat Exchanger Performance for Concept 2, ℓ = 2 ft (.61 m), T_R = ∞, q/A = 250 Btu/sec-ft² (2840 kW/m²)

W/w is noted beside curves, lb/sec-ft (kg/sec-m)

Tube geometry:

(N)TB-h_{fin}-plain-.010(.025)-

(7-1, $L_o/4r_h$ = 100, constant T_w)
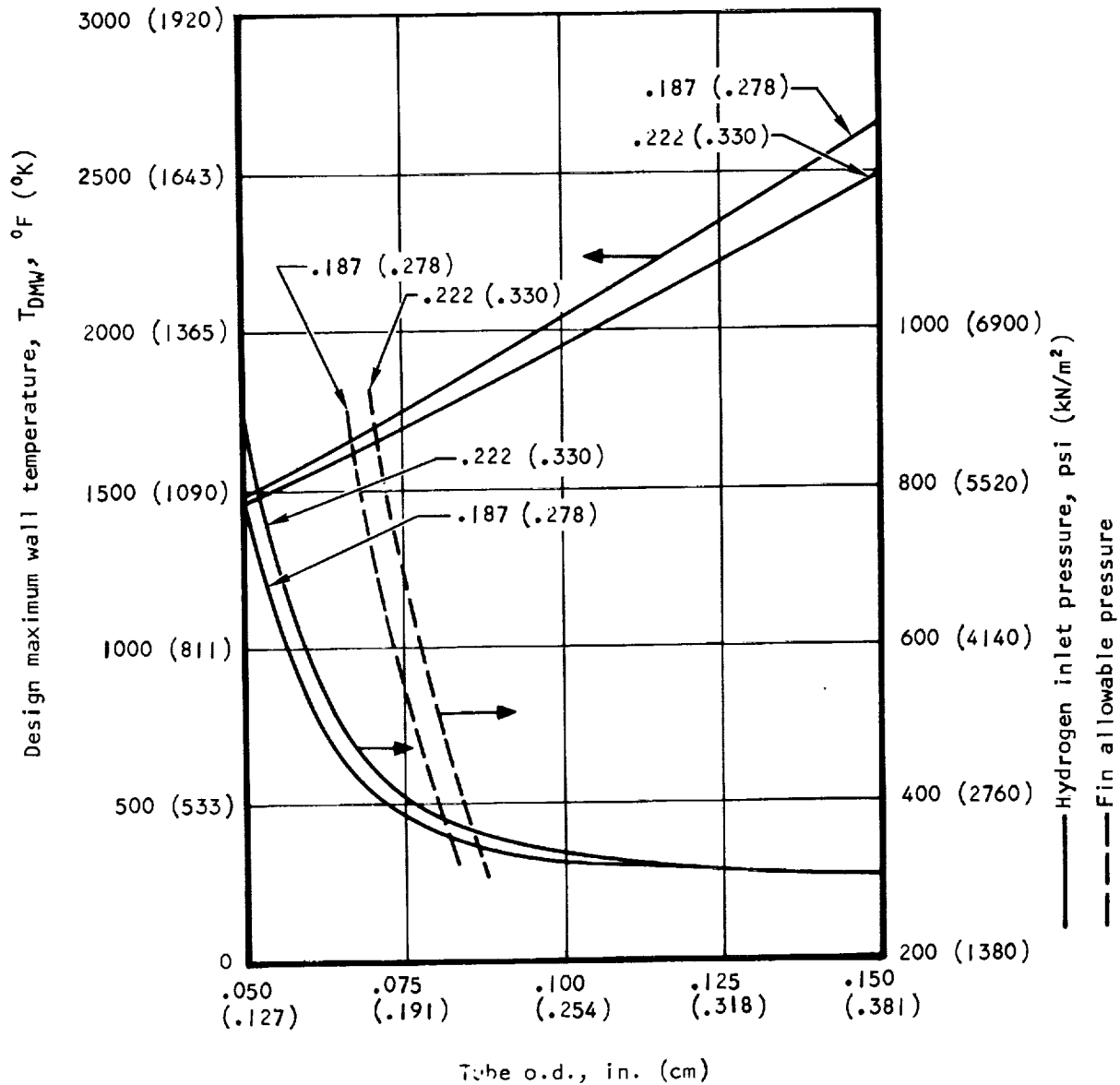
Figure 58. Tubular Heat Exchanger Performance for Concept 2, ℓ = 2 ft (.61 m), T_R = ∞, q/A = 500 Btu/sec-ft^2 (5680 kW/m^2)

Fin thickness noted beside curves, in. (cm)

Fin geometry:
20 $(7.9)R-h_{fin}-L_0-t_{fin}-(10-61)$

$W/w = .0935$ lb/sec-ft-(.139 kg/sec-m)
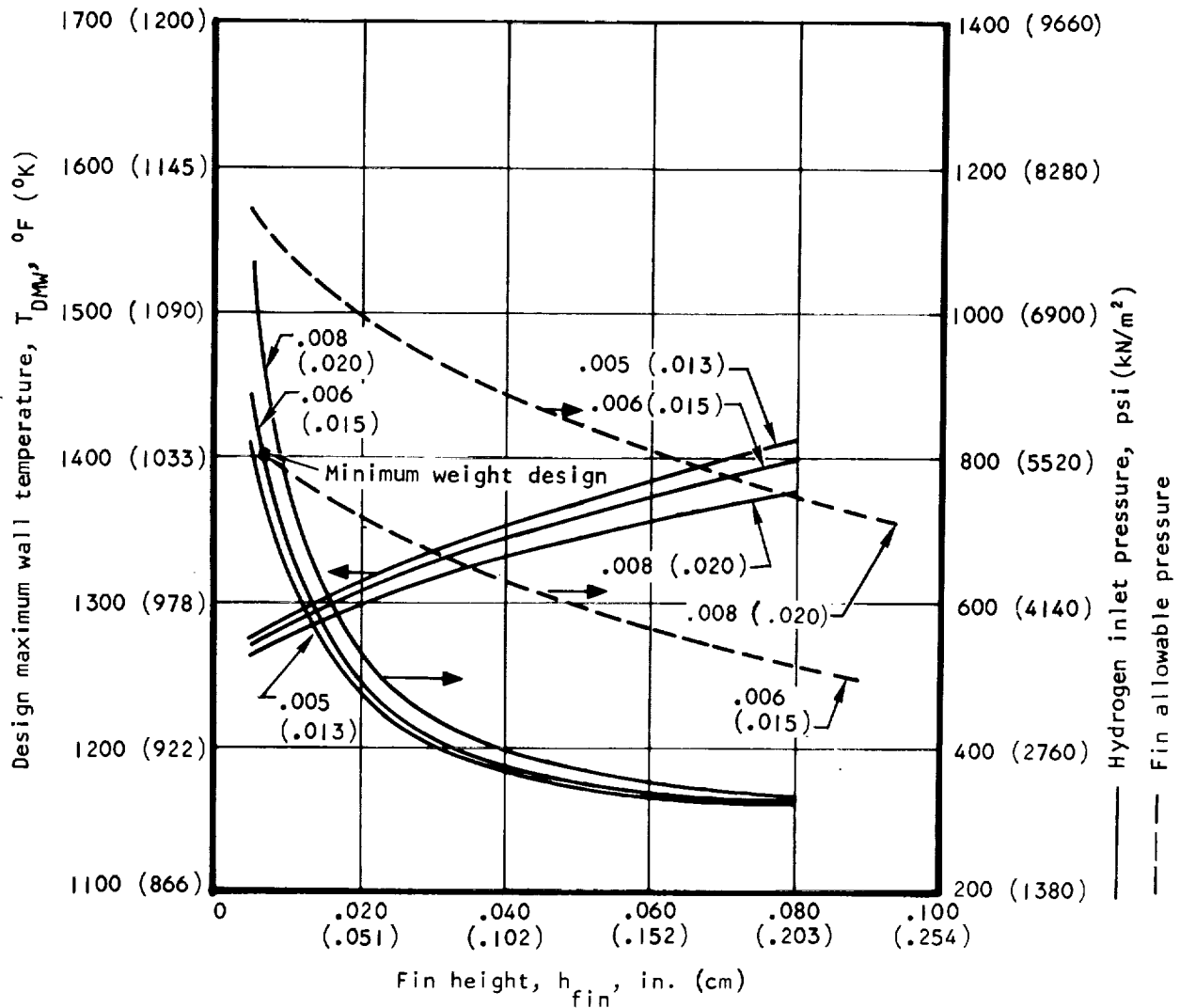
Figure 59. Heat Exchanger Performance for concept 2, $l = 2$ ft (0.61 m), $T_R = \infty$, $q/A = 250$ Btu/sec-ft^2 (2840 kW/m^2), $T_{CO} = 1600°R$ (888°K), and Metal Thermal Conductivity = 100 Btu/hr-°R-ft (173 W/m-°K)

131
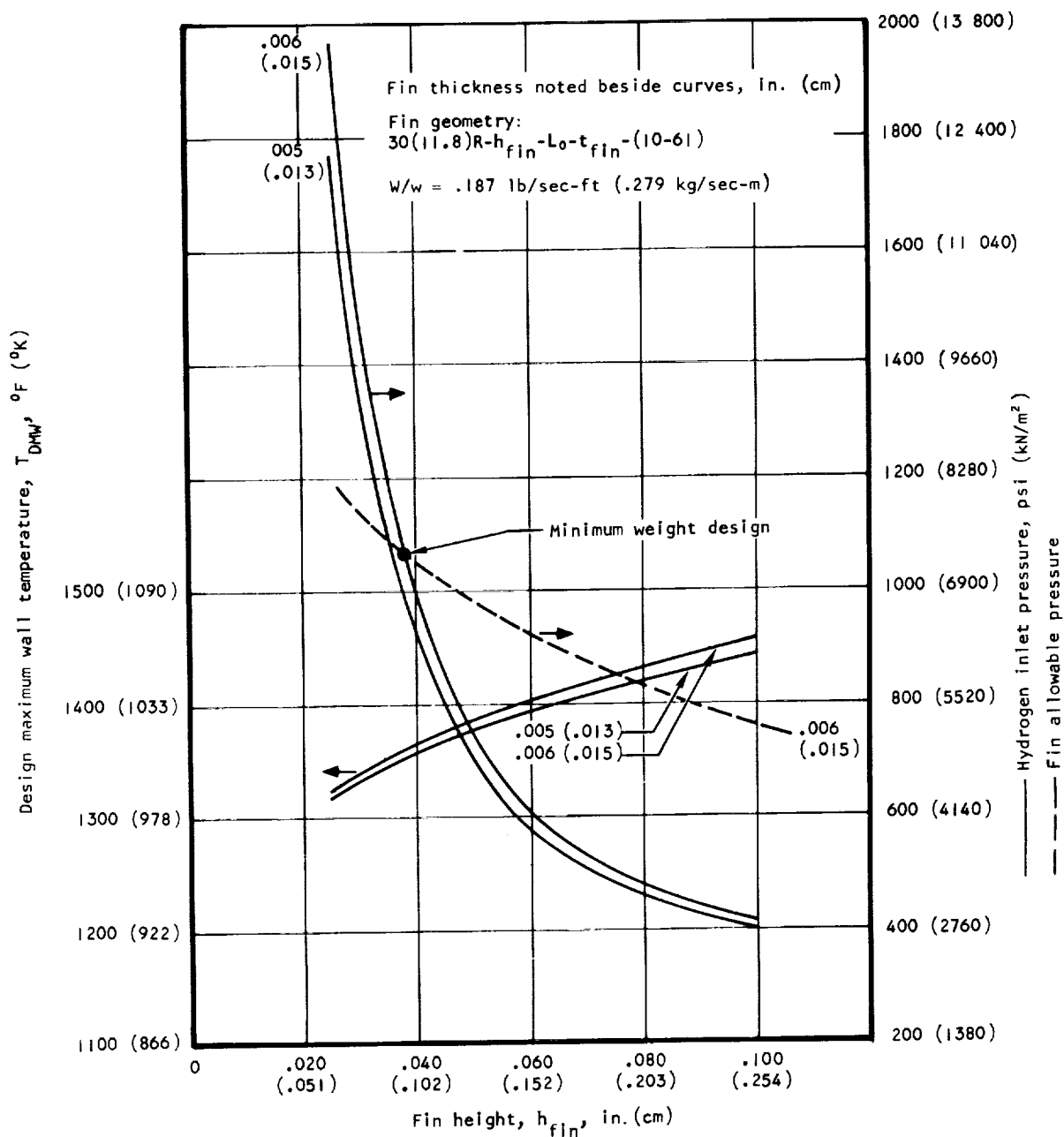
Figure 60. Heat Exchanger Performance for Concept 2, $\ell = 2$ ft $(0.61m)$, $T_R = \infty$, $q/A = 500$ Btu/sec-ft^2 (5680 kW/m^2), $T_{CO} = 1600^\circ$R $(888^\circ K)$, and Metal Thermal Conductivity = 100 Btu/hr-$^\circ$R-ft $(173 W/m-^\circ K)$

N and h_{fin} are noted beside curves

Fin geometry: $(N)R-h_{fin}-L_0-.003(.008)-(10-61)$
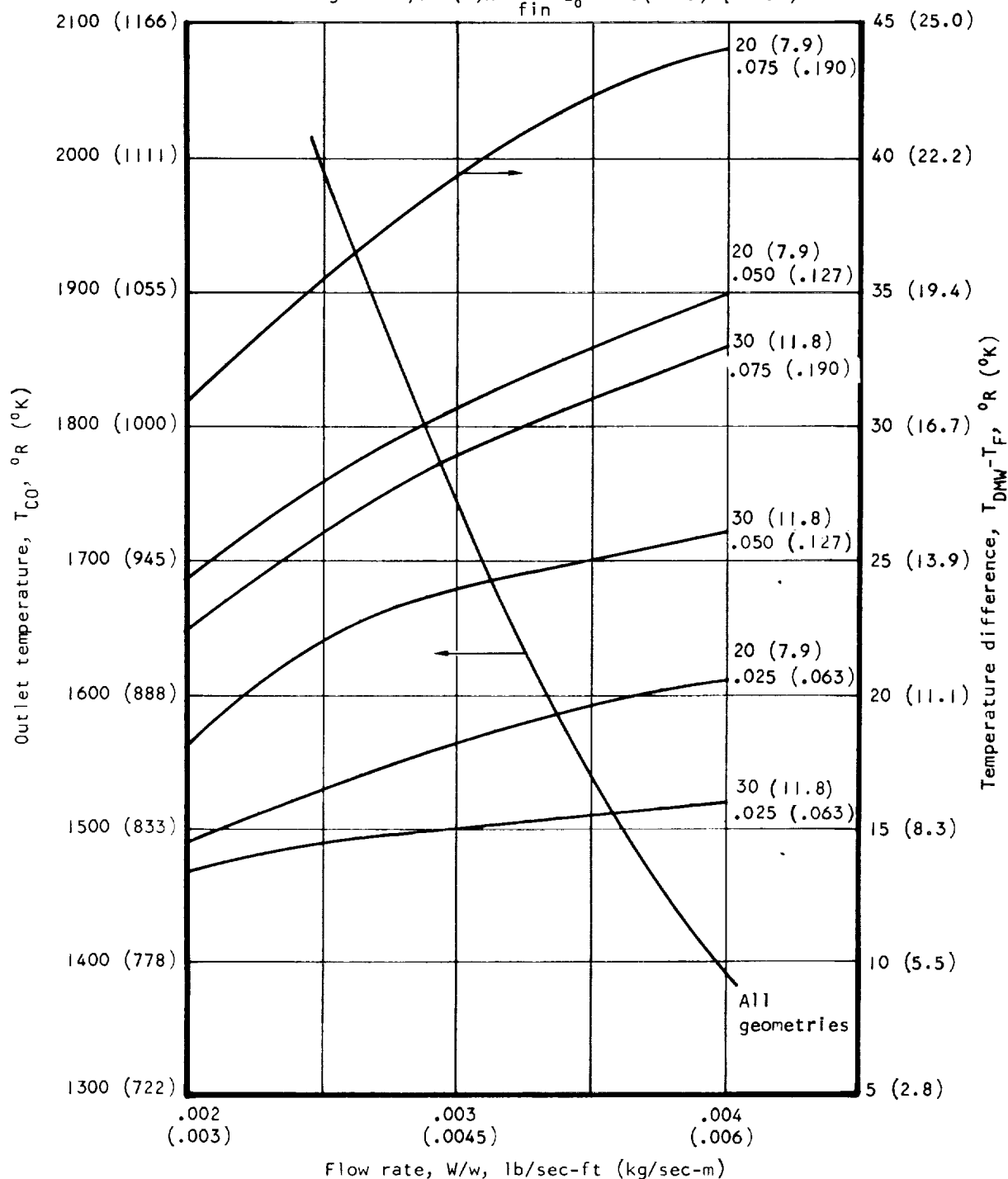
Figure 61. T_{CO} and $T_{DMW} - T_F$ for $T_R = 5000°R$ $(2780°K)$, $q/A = 10$ Btu/sec-ft^2 (114 kW/m^2), Various Flow Rates and Fin Geometries
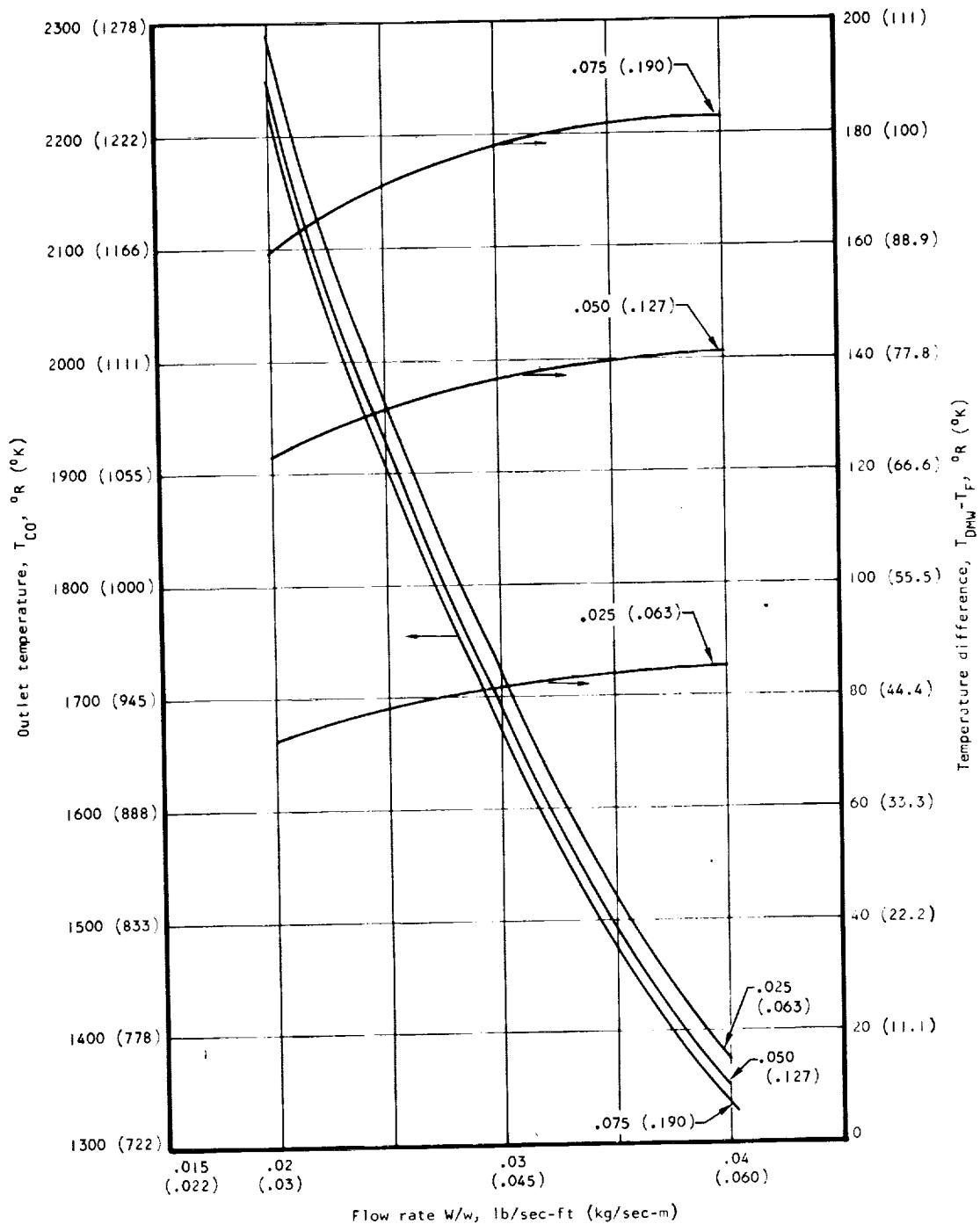
Figure 62. T_{CO} and $T_{DMW} - T_F$ for $T_R = 5000°R$ (2780°K), q/A = 100 Btu/sec-ft^2 (1135 kW/m^2), Various Flow Rates and Fin Geometries with 20 Fins/in. (7.9 Fins/cm)

h_{fin} is noted beside curves

Fin geometry: $20(7.9)R-h_{fin}-L_o-.003(.008)-(10-61)$
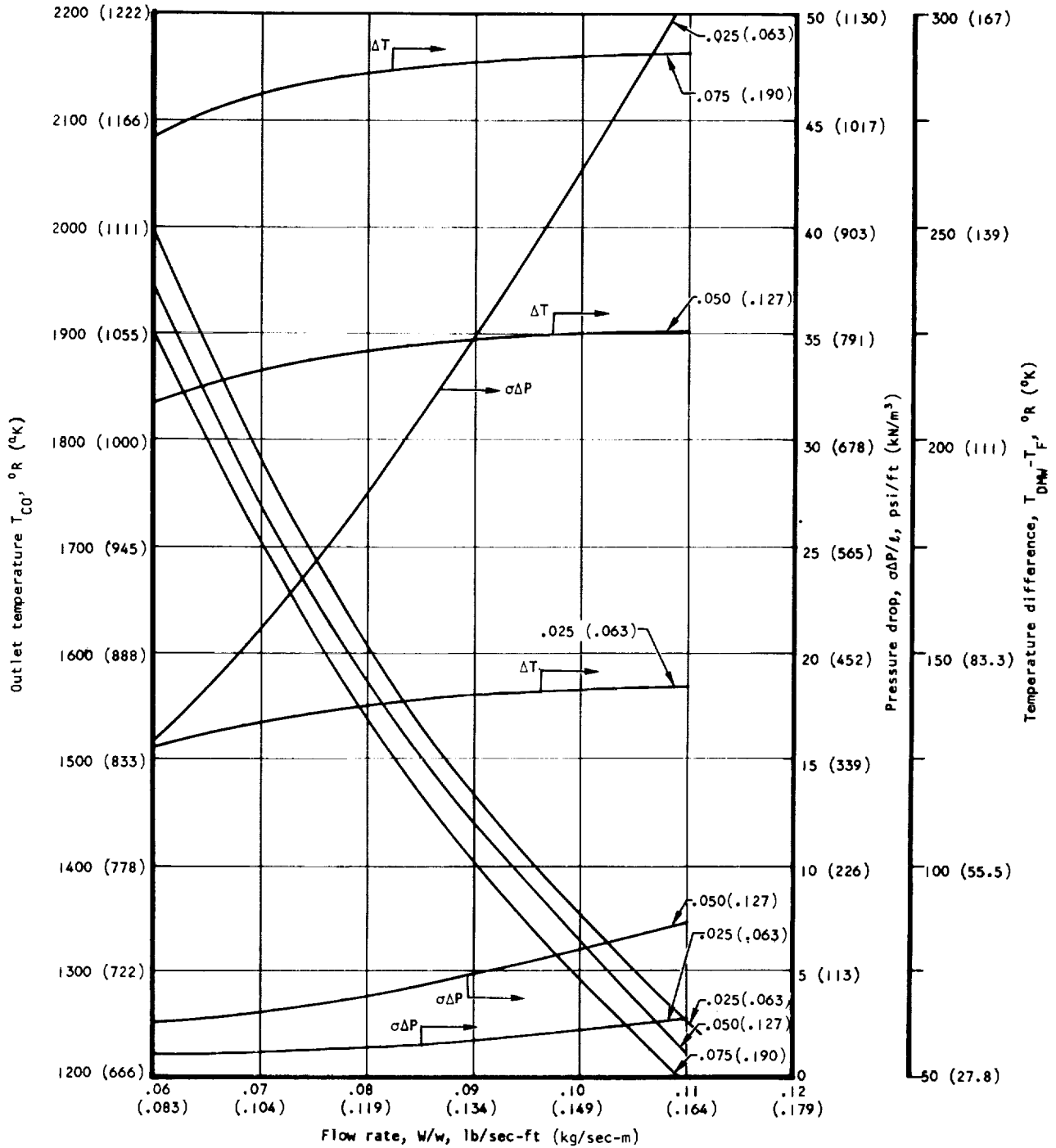
Figure 63. T_{CO} and $T_{DMW} - T_F$ for $T_R = 5000°R$ $(2780°K)$, $q/A = 250$
Btu/sec-ft^2 $(2840$ kW/m$^2)$, Various Flow Rates and Fin
Geometries with 20 Fins/in. $(7.9$ Fins/cm$)$
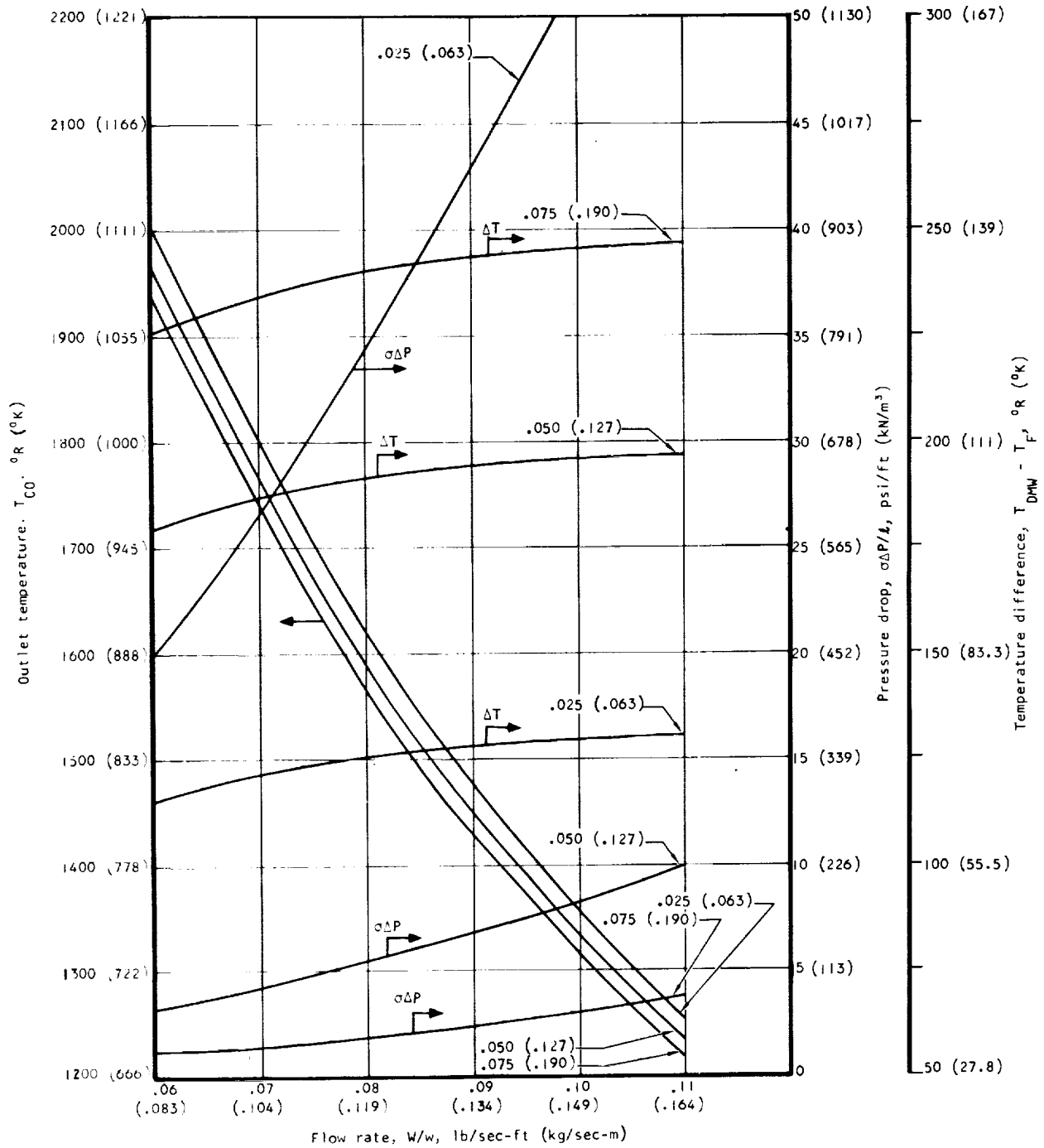
Figure 64. T_{CO} and $T_{DMW} - T_F$ for $T_R = 5000°R$ $(2780°K)$, $q/A = 250$
Btu/sec-ft² $(2840\ kW/m²)$, Various Flow Rates and Fin
Geometries with 30 Fins/in. $(11.8\ Fins/cm)$

Figure 65. Heat Exchanger Performance for $T_R = 5000^oR$ (2780^oK),
10 Btu/sec-ft² (114 kW/m²)

Fin geometry:

Concept 1, 20(7.9)R-.075(.190)-(plain)-.003(.008)-(7-2, $L_0/4r_h$ = 100, constant T_W)

Concept 2, 20(7.9)R-.025(.063)-.060(.153)-.003(.008)-(10-61)

$T_R = \infty$, T_{CO} = 1600°R (888°K), ℓ = 2 ft (.61 m)

Figure 70. Concepts 1 and 2 Off-Design $T_{DMW} - T_F$ and $\sigma\Delta P/\ell$ for Design q/A = 10 Btu/sec-ft² (114 kW/m²)

Fin geometry:

Concept 1, 20(7.9)R-.075(.191)-(plain)-.003(.008)-(7-2, $L_o/4r_h$ = 100, constant T_w)

Concept 2, 20(7.9)R-.025(.063)-.060(.153)-.003(.008)-(10-61).

T_R = ∞ , T_{CO} 1600°R (888°K), l = 2 ft (.61 m)

At design heat flux

Concept	P_{CI}, psia (kN/m²)
1	300.3 (2072)
2	302 (2084)
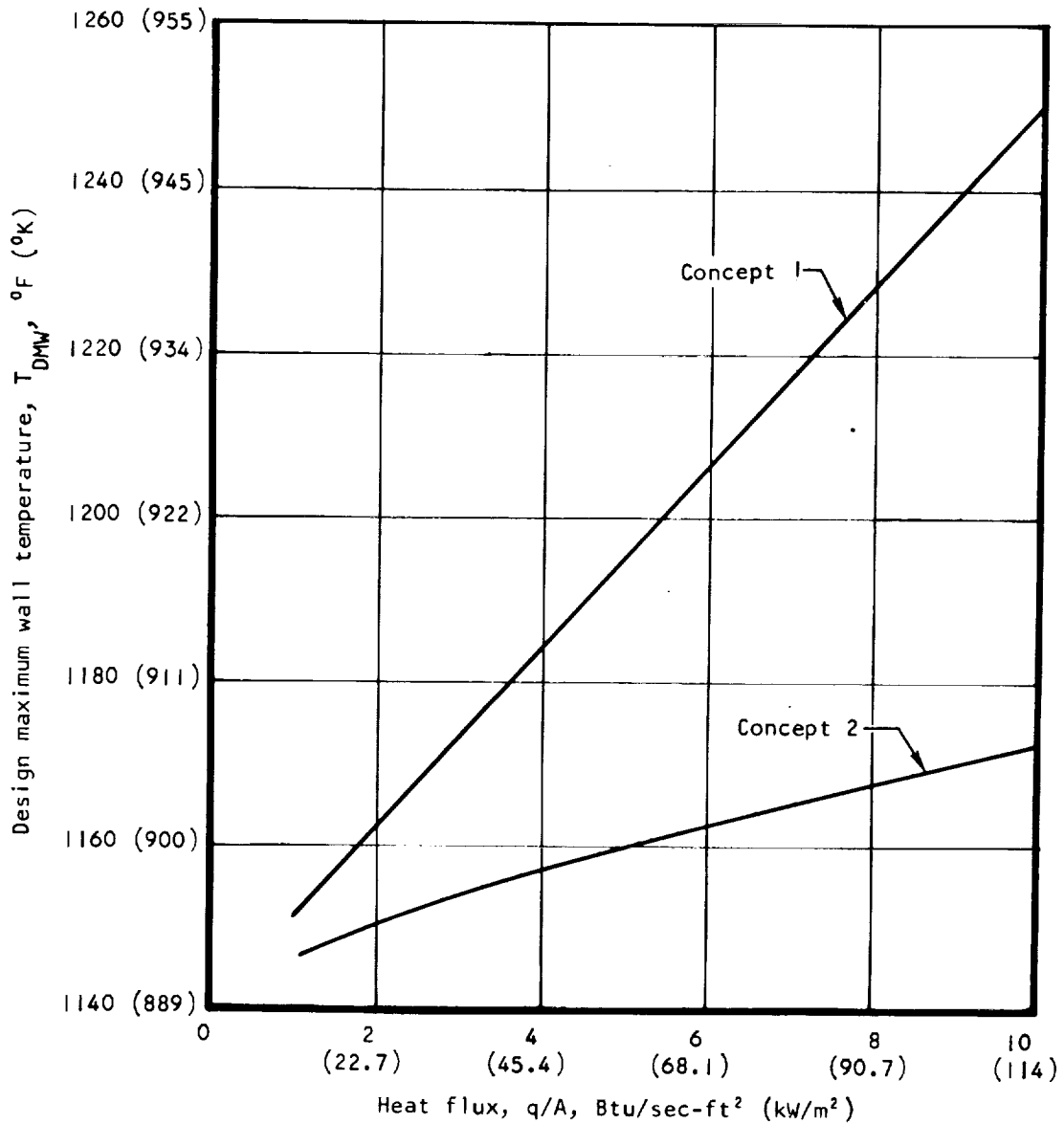
Figure 71.   Concepts 1 and 2 Off-Design T_{DMW} for Design q/A = 10
Btu/sec-ft² (114 kW/m²)

143

Figure 74. Concepts 2 and 3 Off-Design $T_{DMW} - T_F$ and $\sigma\Delta P/\ell$ for Design q/A = 500 Btu/sec-ft^2 (5680 kW/m^2)

146

Fin geometry:

Concept 2, 40(15.7)R-.038(.097)-.055(.140)-.003(.008)-(10-61)

Concept 3, 40(15.7)R-.039(.099)-.056(.142)-.003(.008)-(10-61)

$T_R = \infty$, $T_{CO} = 1600°R$ (888°K), $\ell = 2$ ft (.61 m)
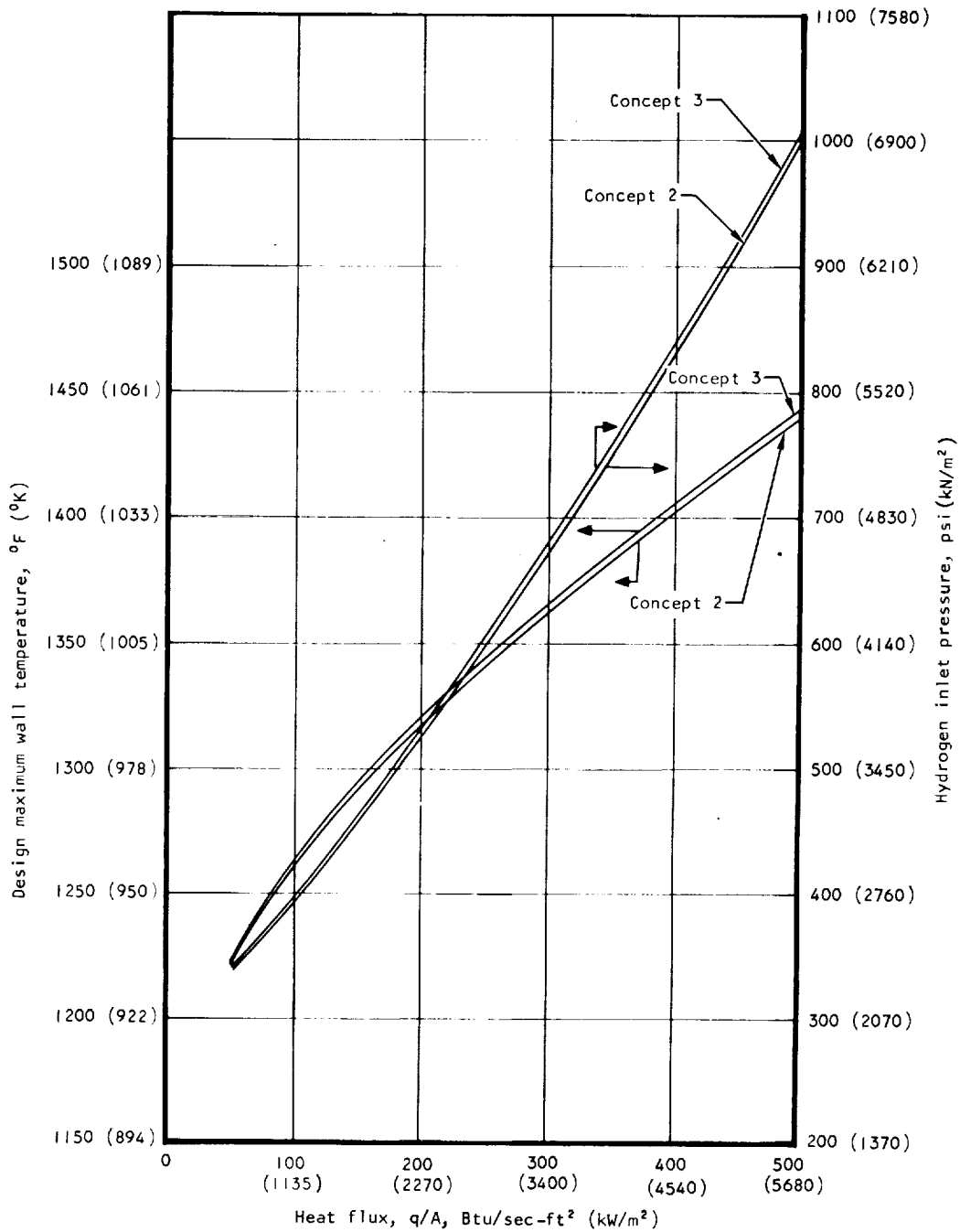
Figure 75. Concepts 2 and 3 Off-Design T_{DMW} and P_{CI} for Design
q/A = 500 Btu/sec-ft² (5680 kW/m²)
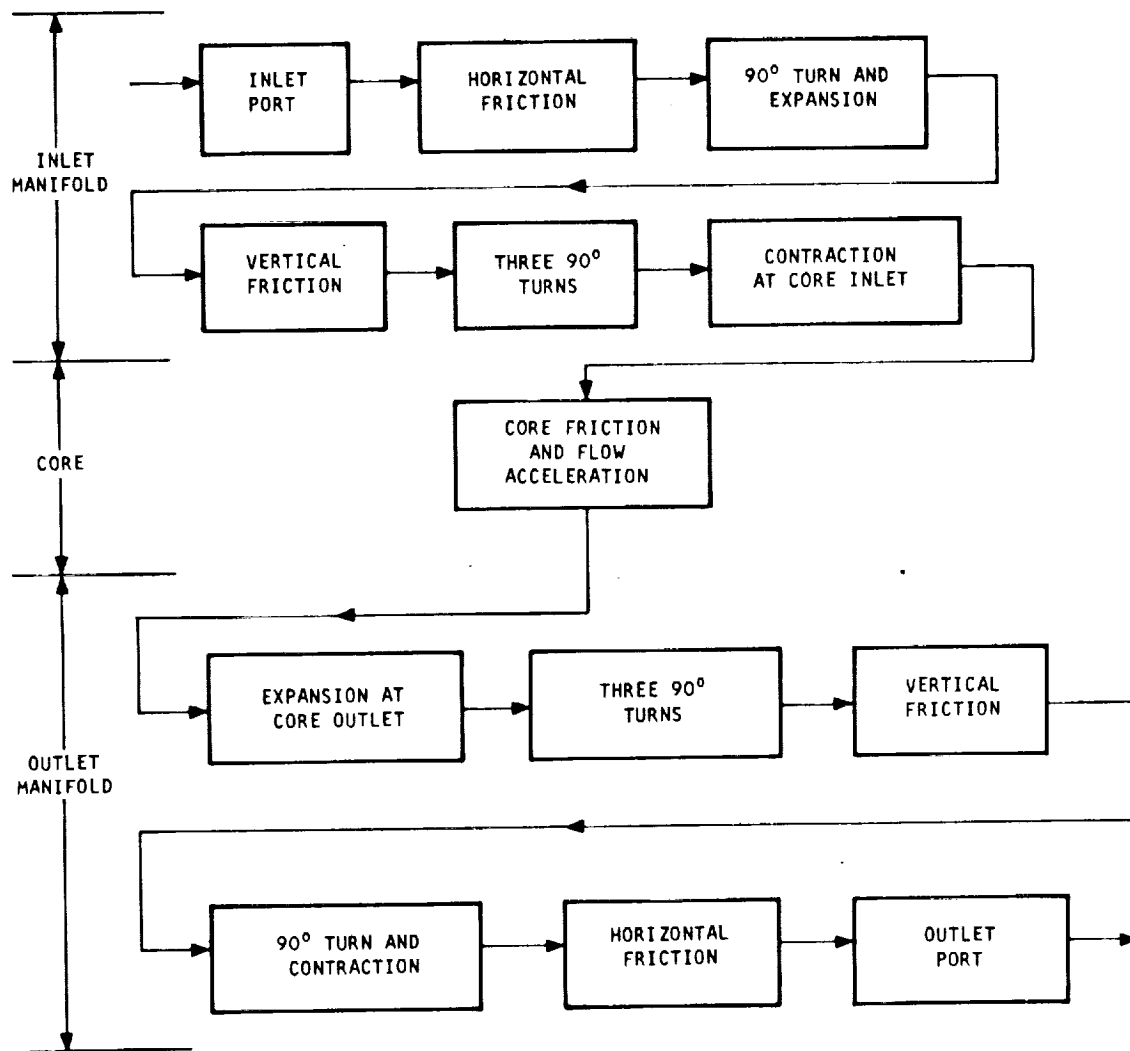
Figure 76. Pressure Drop Sources in Rectangular Manifolds

Values beside curves are w, ft (m);

h_{fin}, in. (cm), port diameter, in. (cm)

Fin geometry:

10(3.94)R-.250(.635)-plain-.004(.010)-

(7-3, $L_o/4r_h$ = 100, constant T_w)
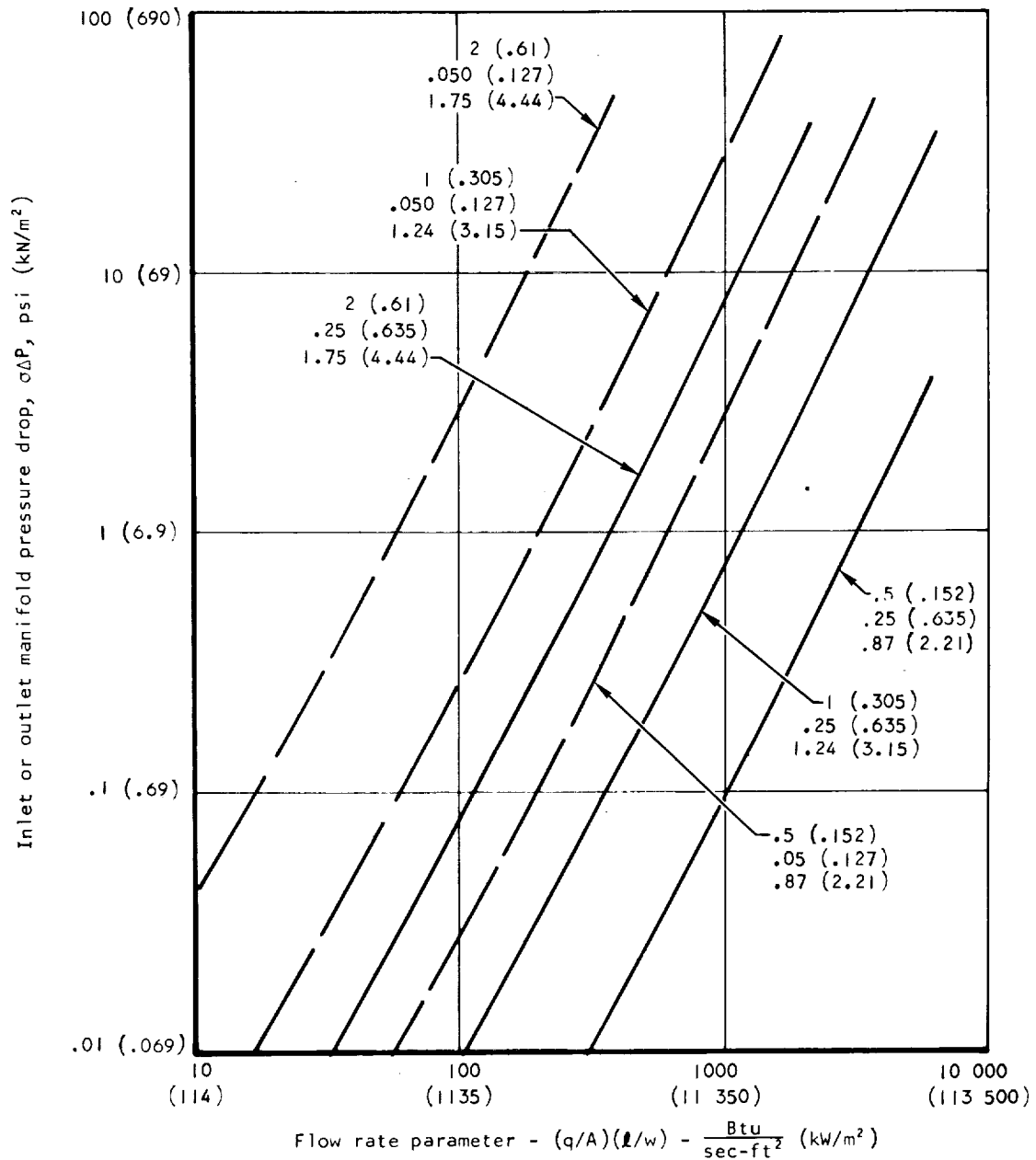
Figure 77. Density-Adjusted Manifold Pressure Drop vs (q/A) (ℓ/w)
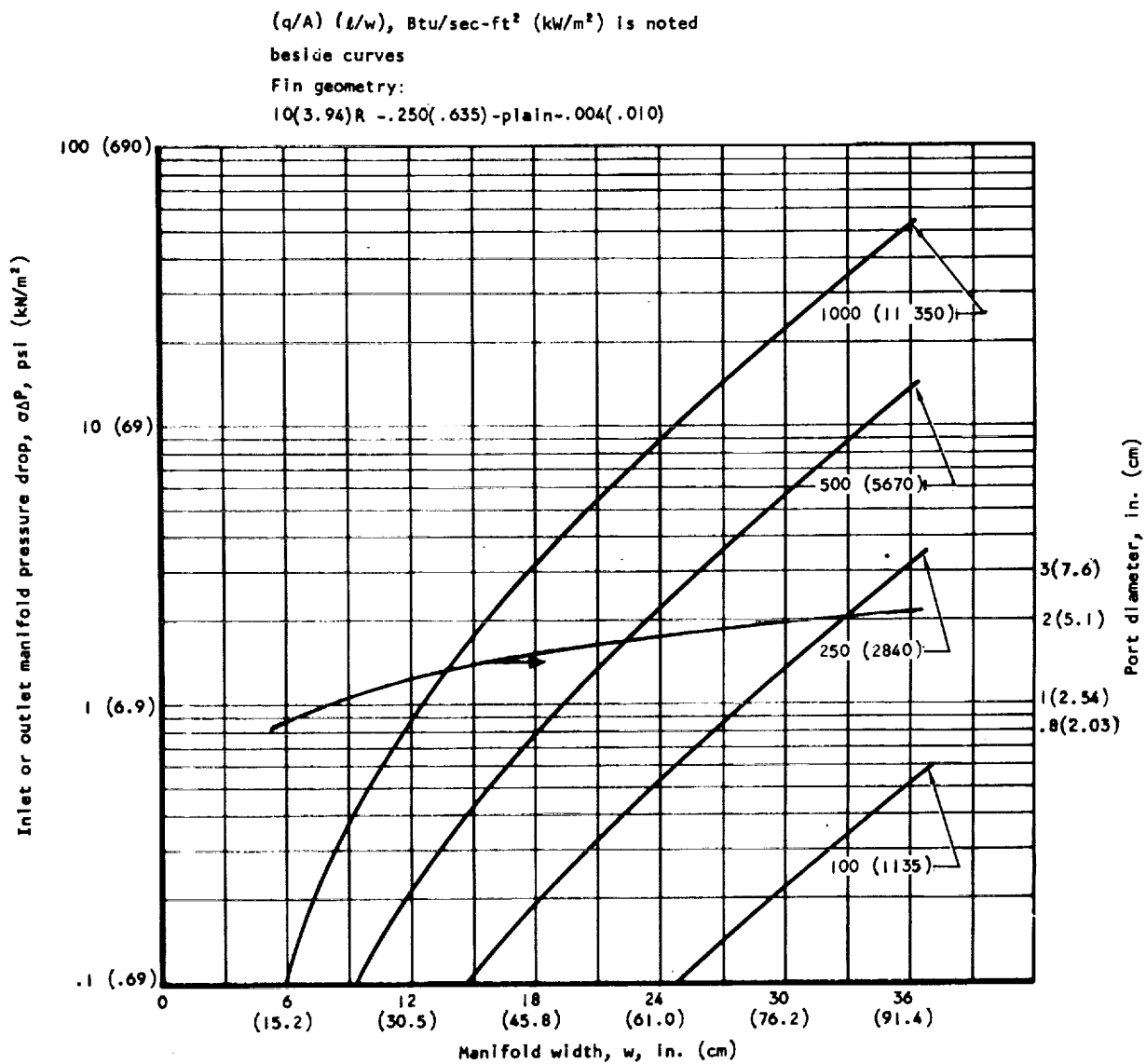
Figure 78. Density-Adjusted Manifold Pressure Drop vs Manifold Width

(q/A) (ℓ/w), Btu/sec-ft^2 (kW/m^2) and h_{fin}, in. (cm)
are noted beside curves

Fin geometry:

$10(3.94)R-h_{fin}-plain-.004(.010)$

σ_I = .939 at 500 psia (3450 kN/m^2) and 100°R (55.5°K)

σ_o = .0293 at 250 psia (1725 kN/m^2) and 1600°R (888°K)
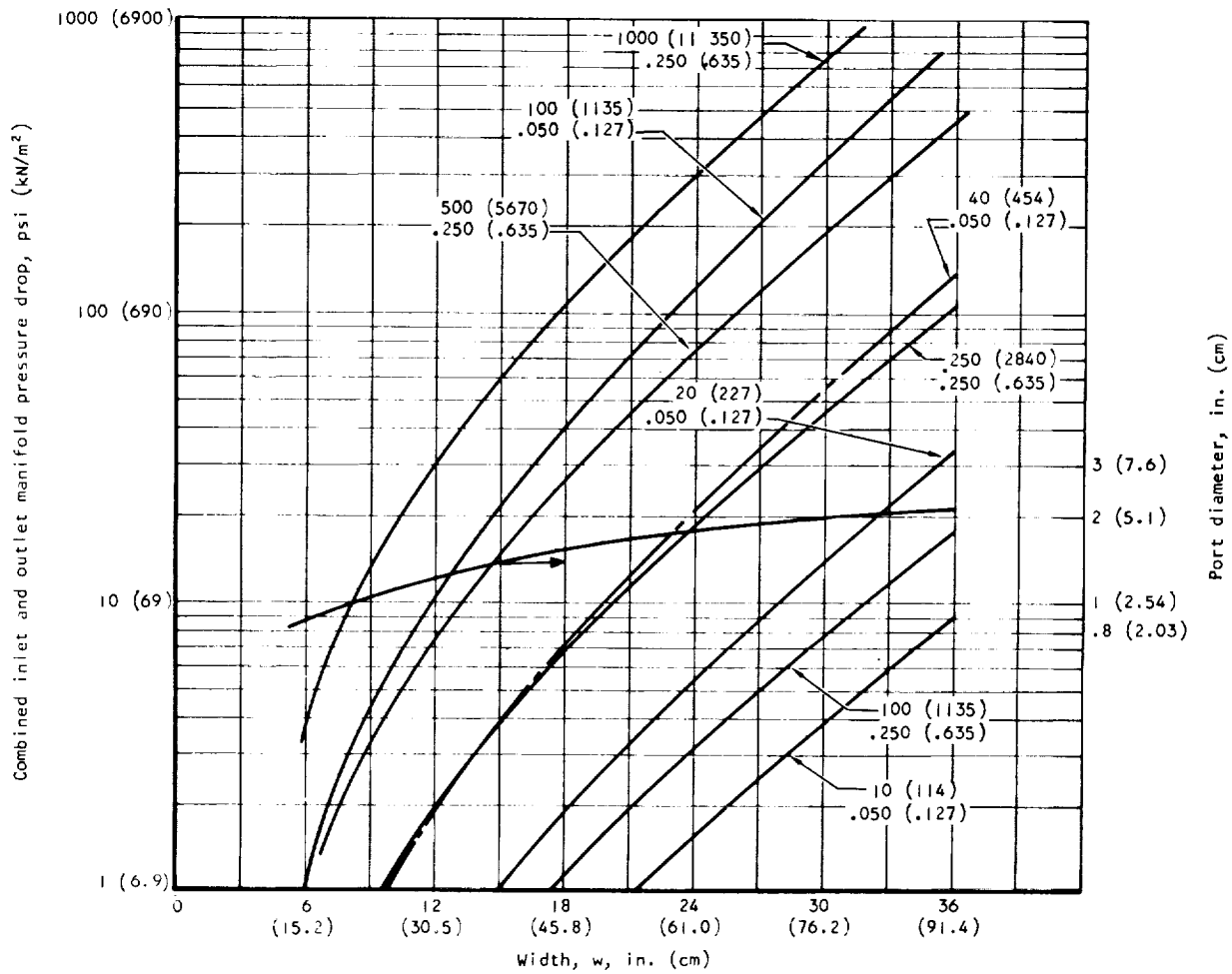
Figure 79.   Manifold Pressure Drop vs Manifold Width
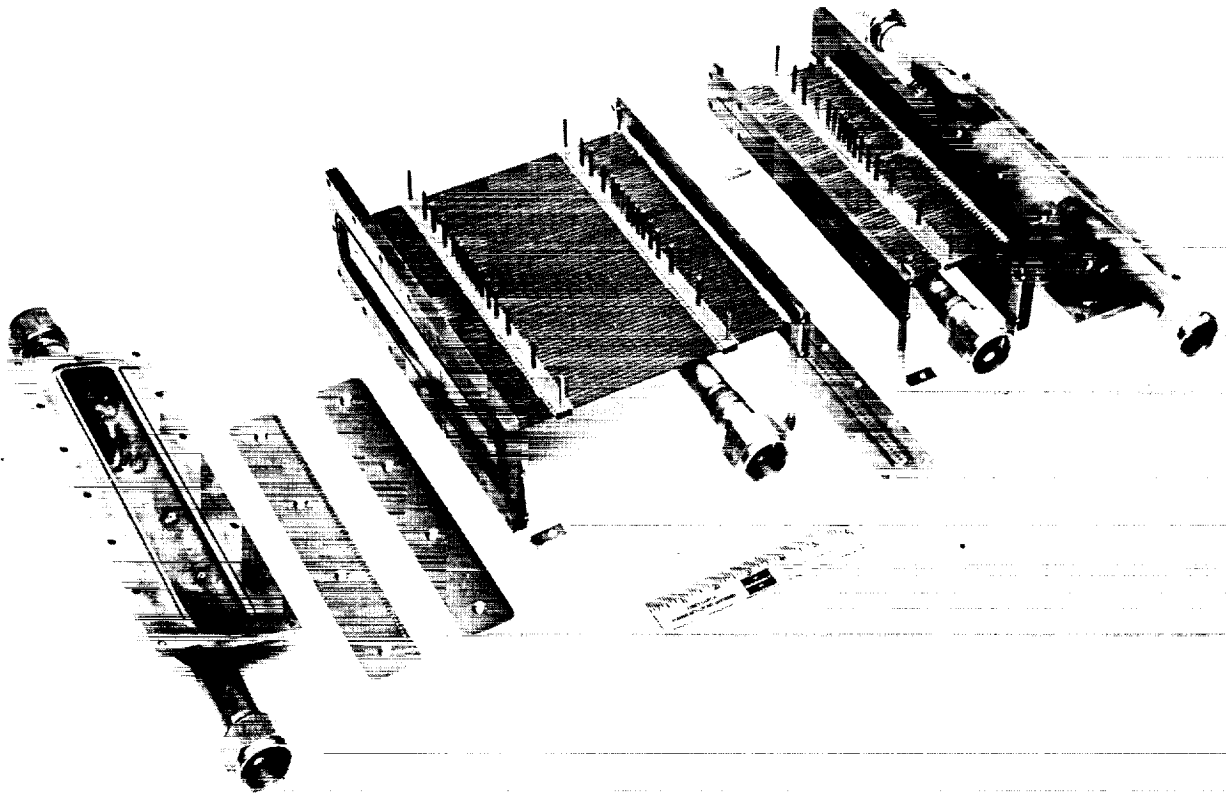
Figure 80. Flow Distribution Test Unit, Drawings 181643 and 181644
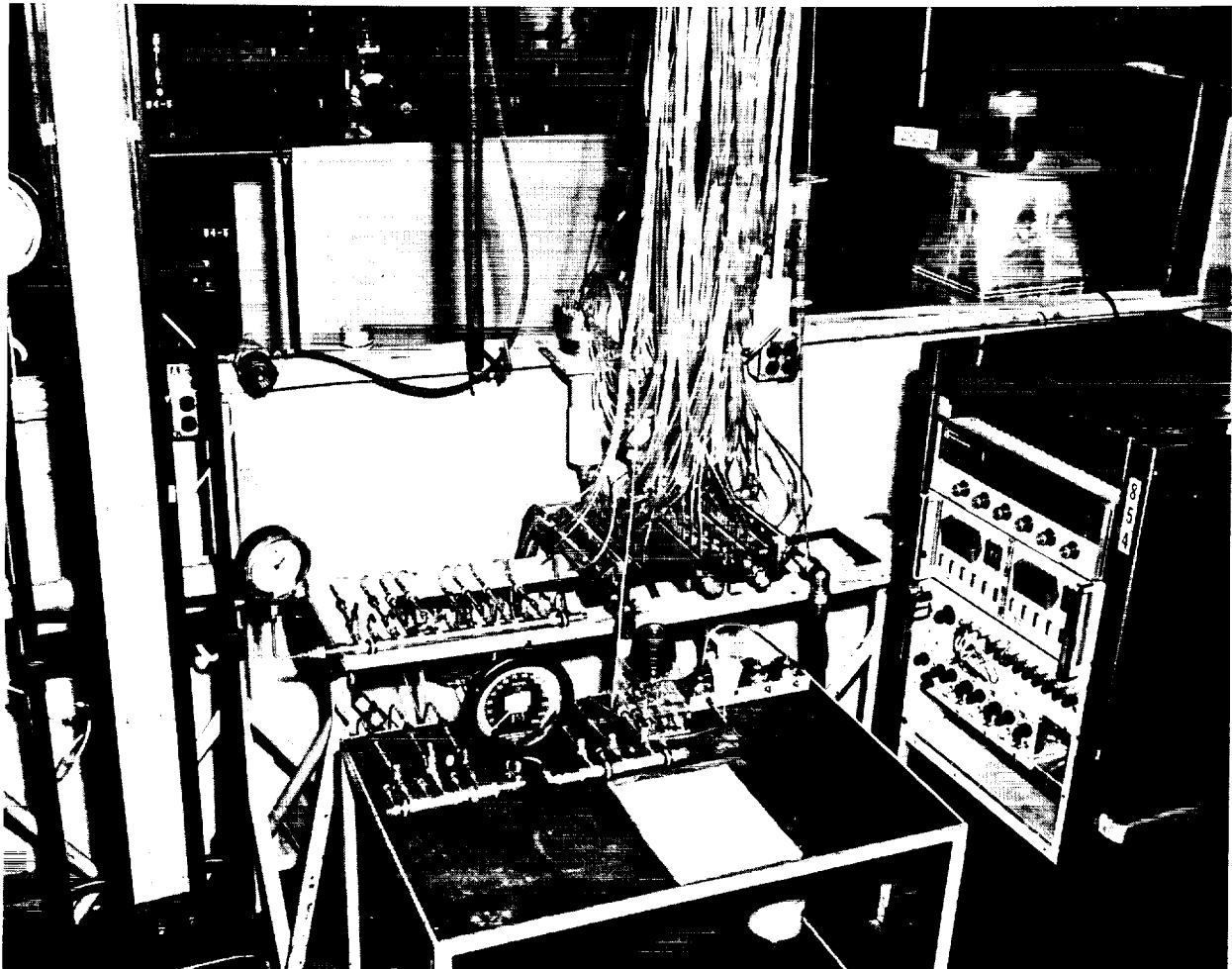
Figure 81. Test Setup, Showing Instrumentation and Connected Test Unit
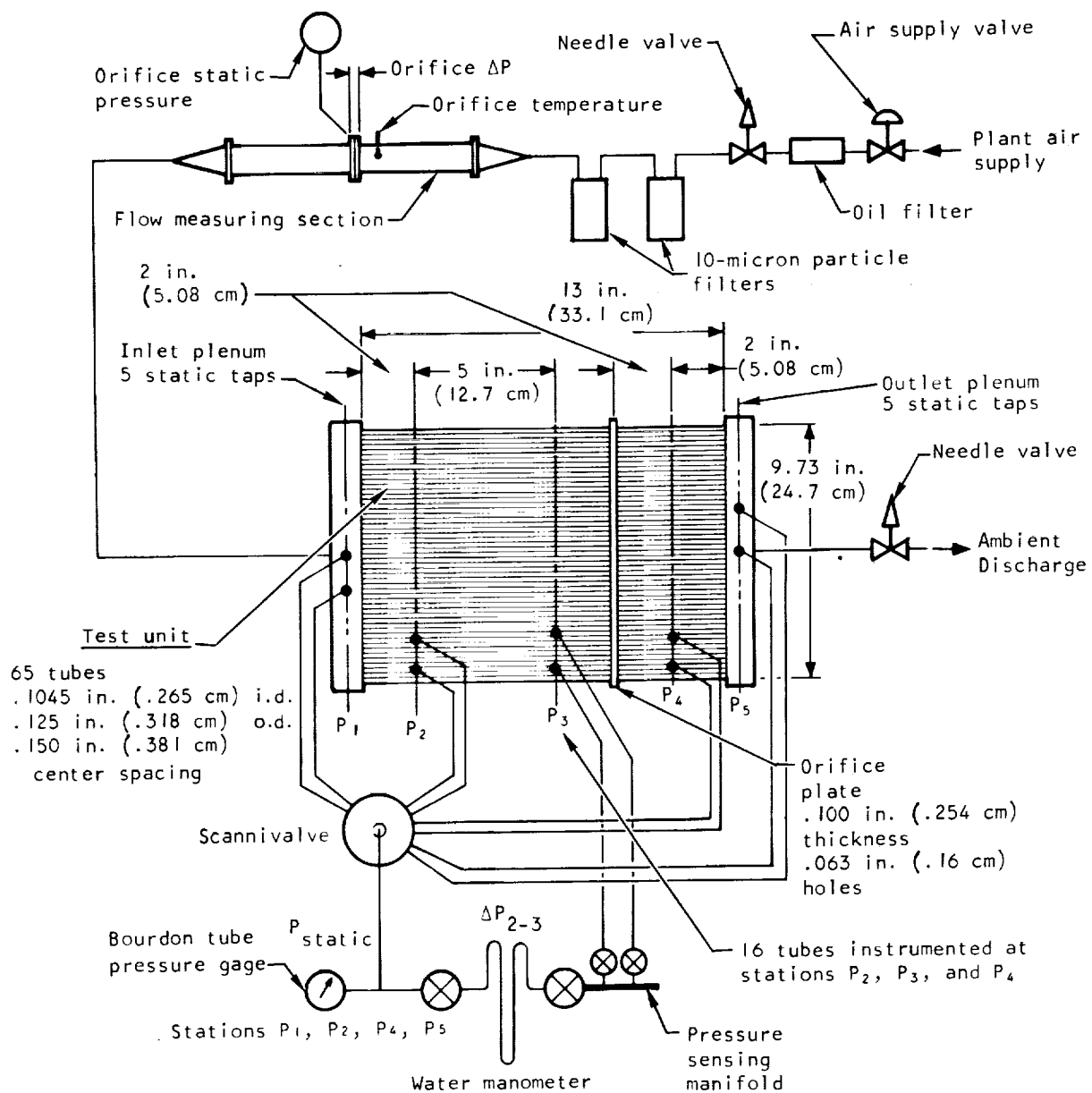
Figure 82. Flow Distribution Test Setup, Schematic Diagram

SPECIMEN NO. 11

SPECIMEN NO. 10

SPECIMEN NO. 2
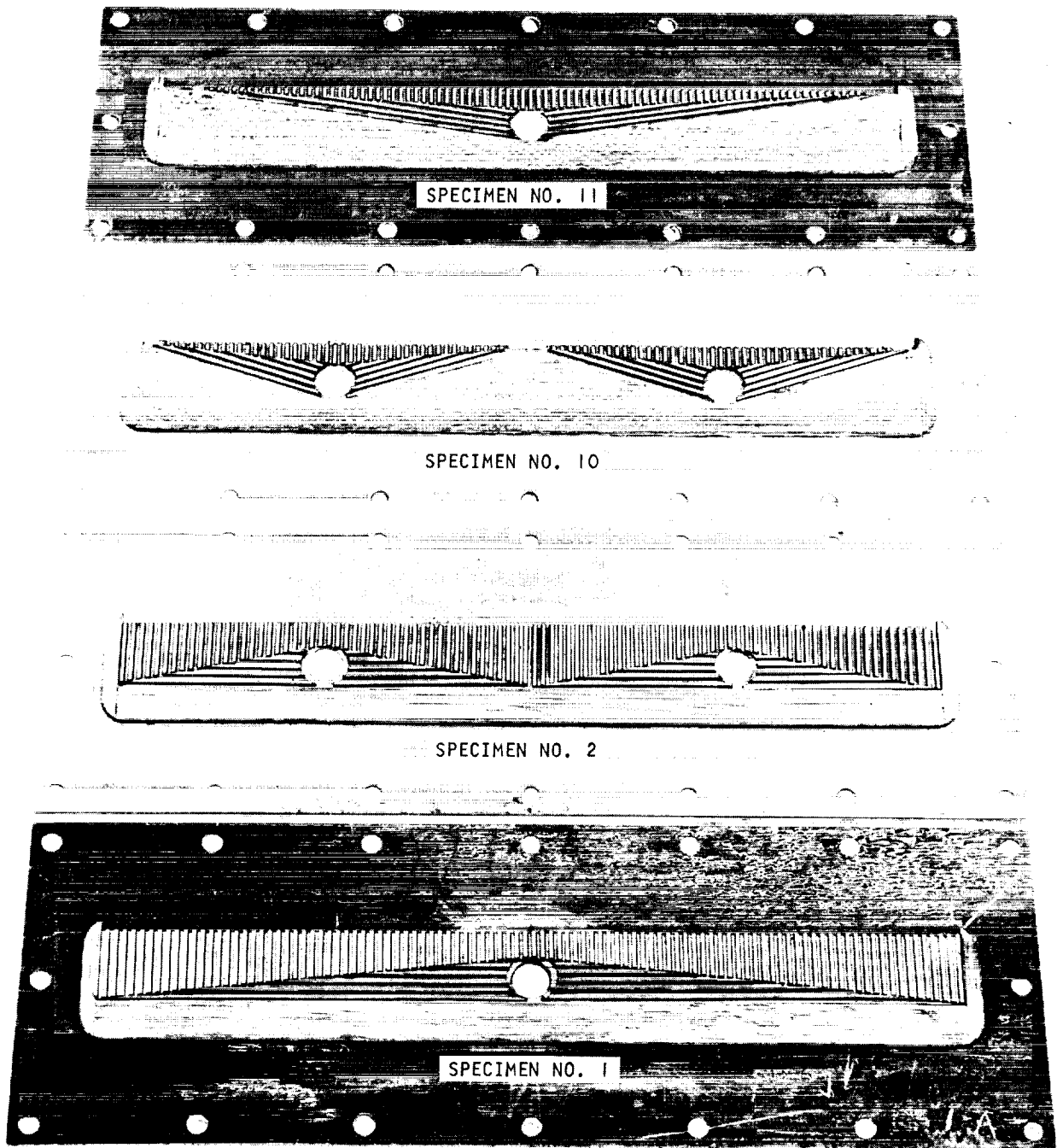
SPECIMEN NO. 1

Figure 83.   Manifold Test Specimens No. 11, 10, 2, and 1, Rectangular
and Tapered Manifold Comparison

155
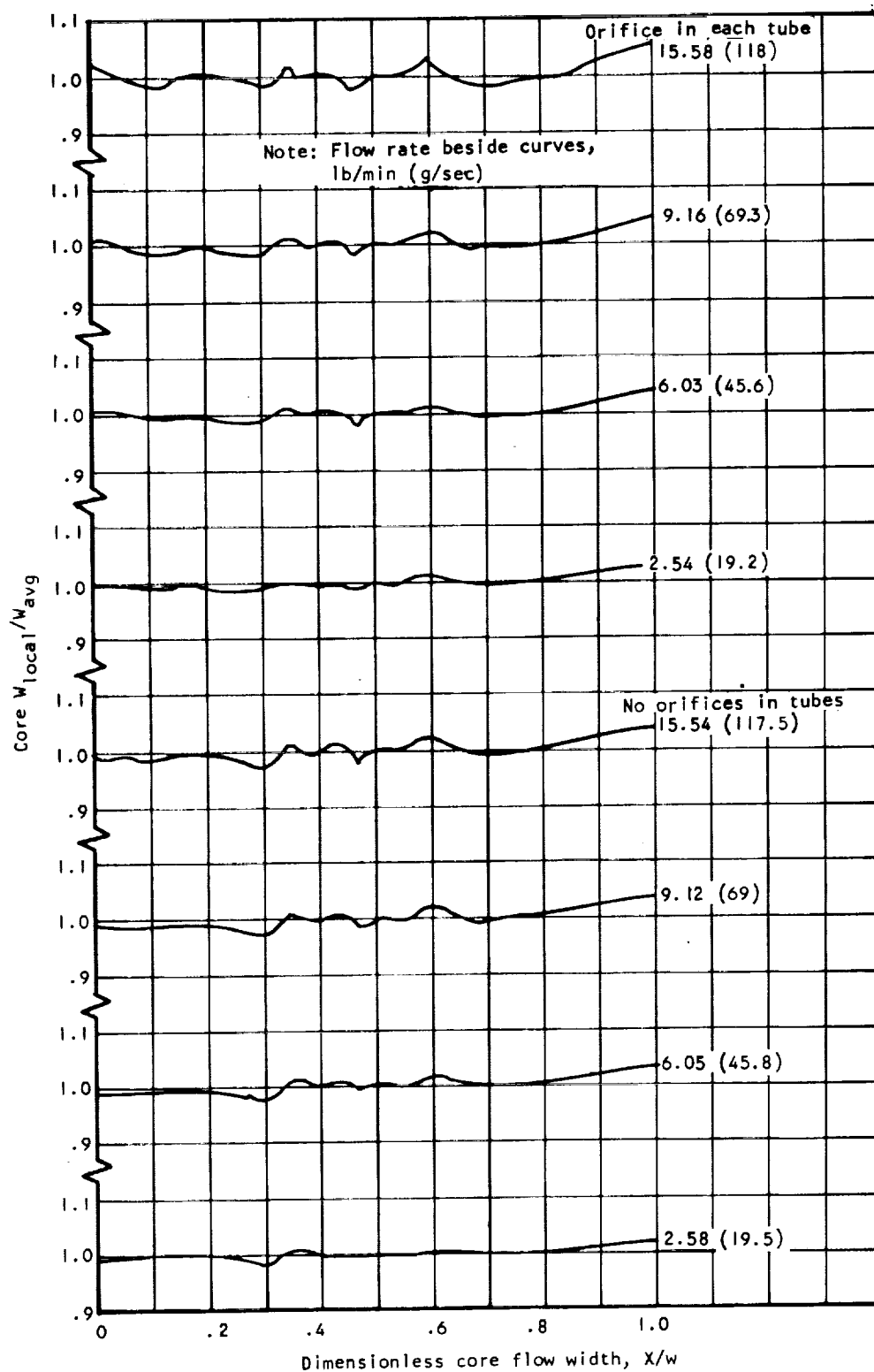
Figure 86. Calibration with Plenum and Core Tubes Only
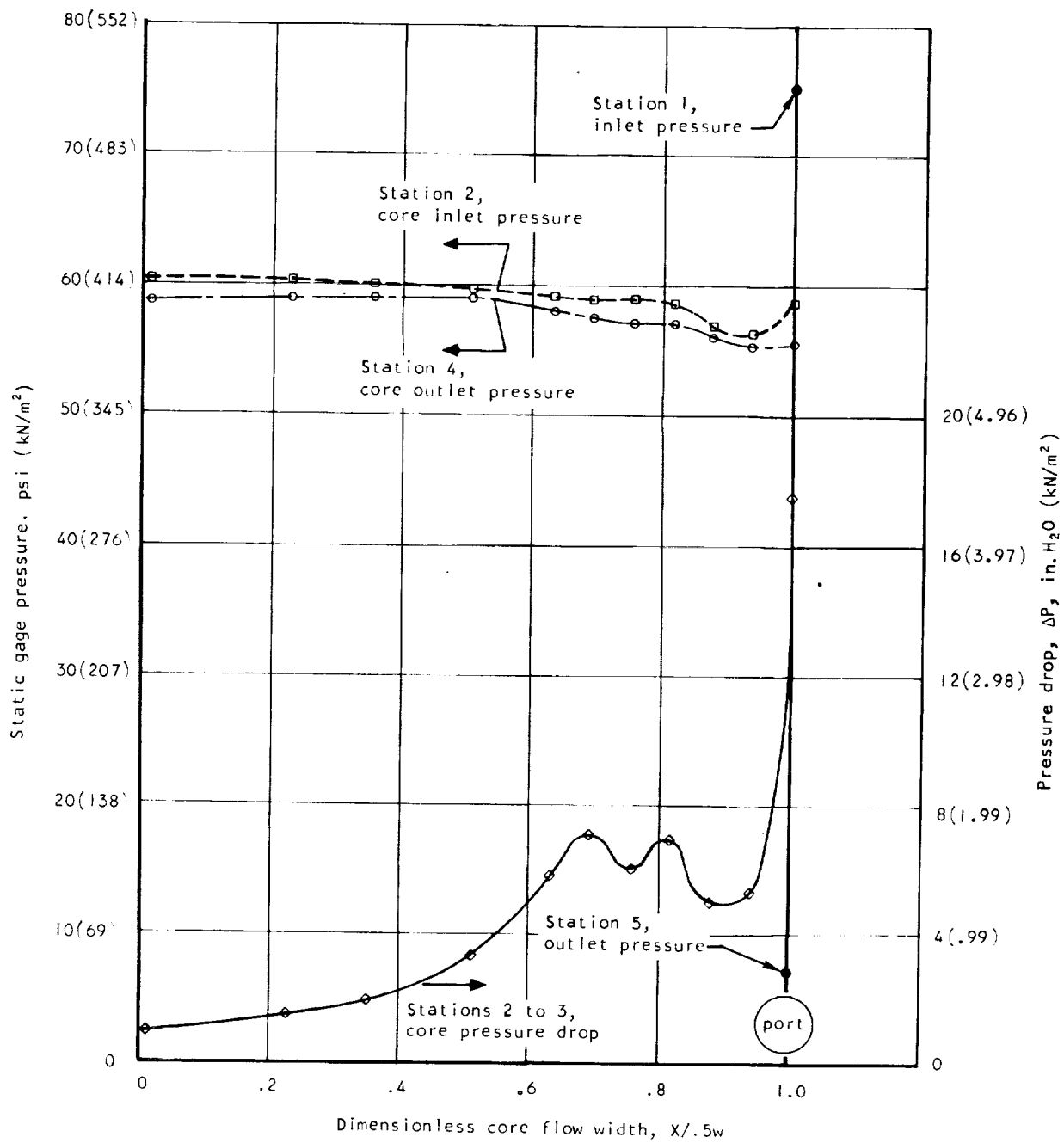
Figure 87.   Pressure and Pressure Drop Profiles for Specimen No. 1
at Inlet and Outlet
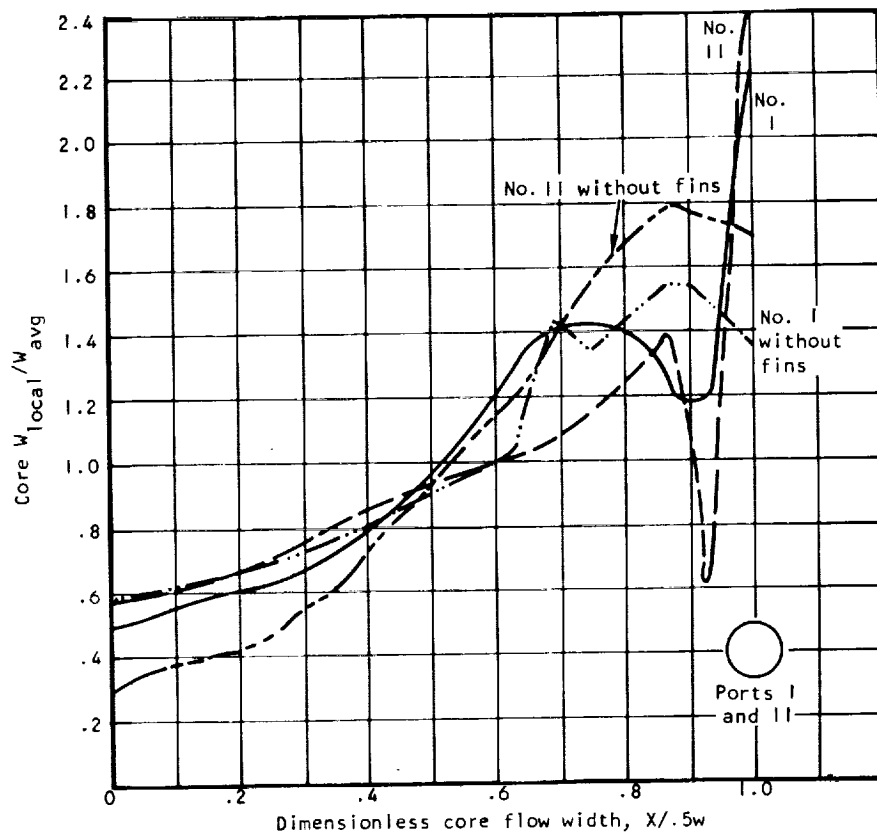
Figure 90. Flow Profiles for Specimens No. 1 and 11, Rectangular and Tapered with One Port Each
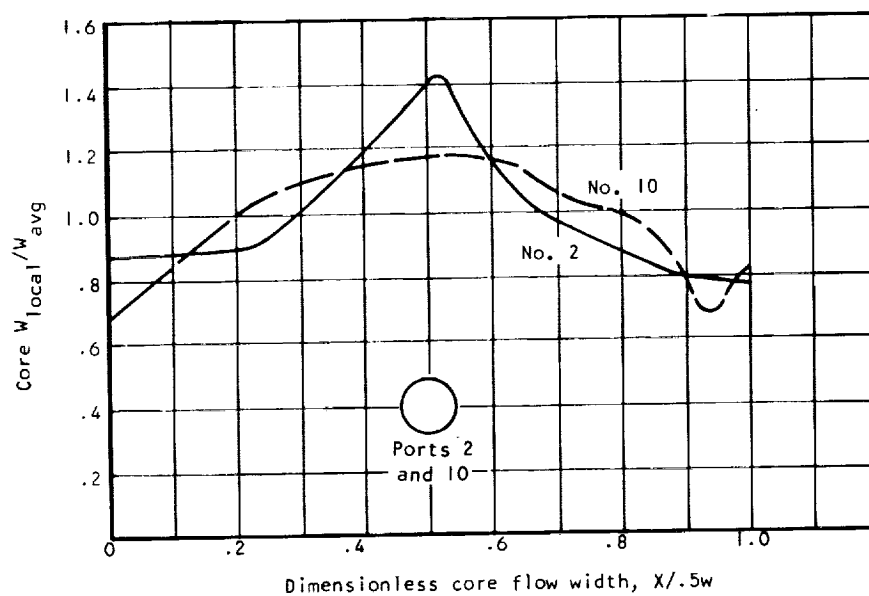
Figure 91. Flow Profiles for Specimens No. 2 and 10, Rectangular and Tapered with Two Ports Each

162
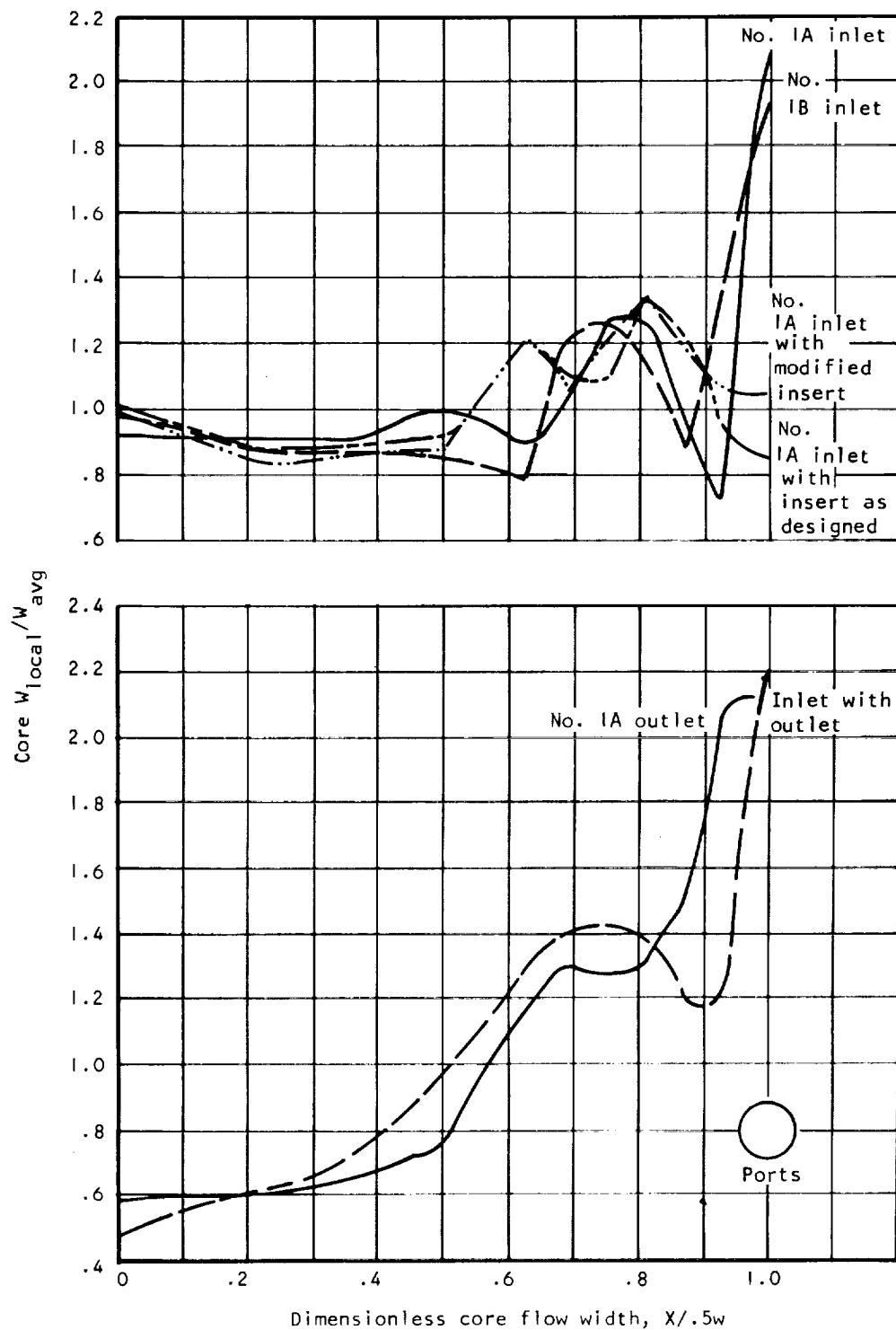
Figure 92. Flow Profiles for Specimen No. 1, Inlet or Outlet Only
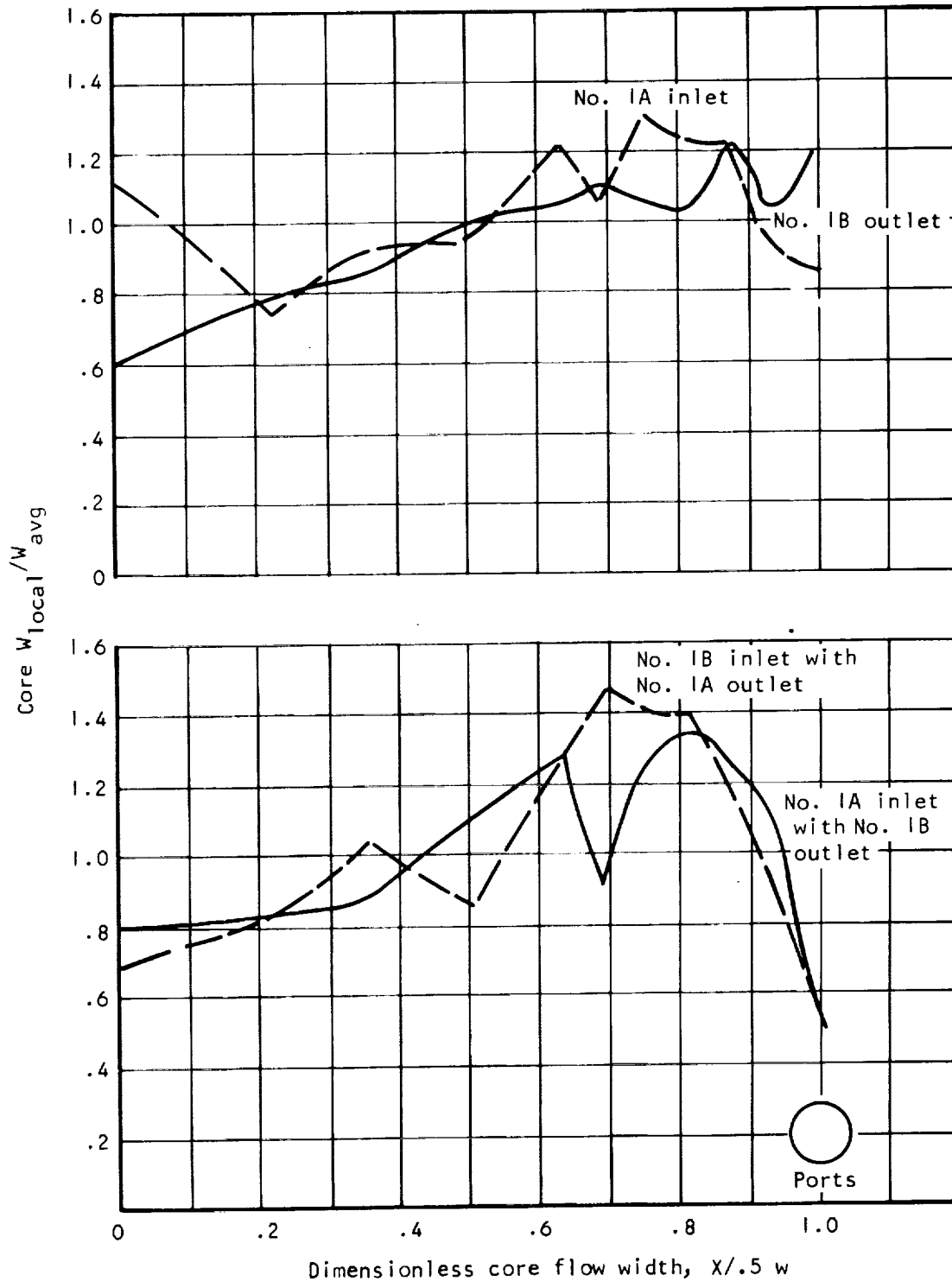
Figure 93. Flow Profiles for Specimen No. 1 with Flow Distribution Insert (without Tube Orifices)
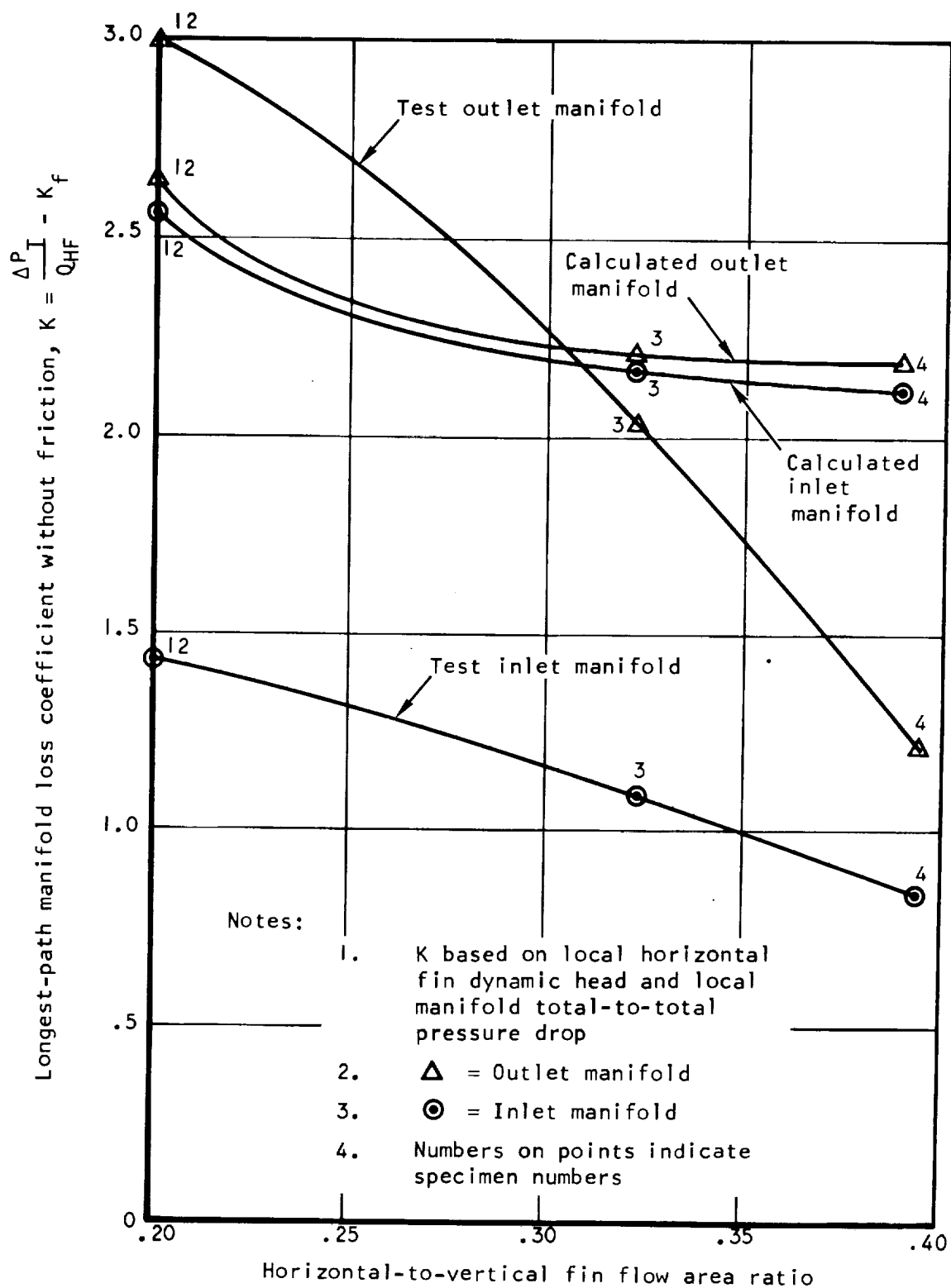
Figure 94. Longest-Path Manifold Loss Coefficients without Friction
vs Horizontal-to-Vertical Fin Flow Area Ratio
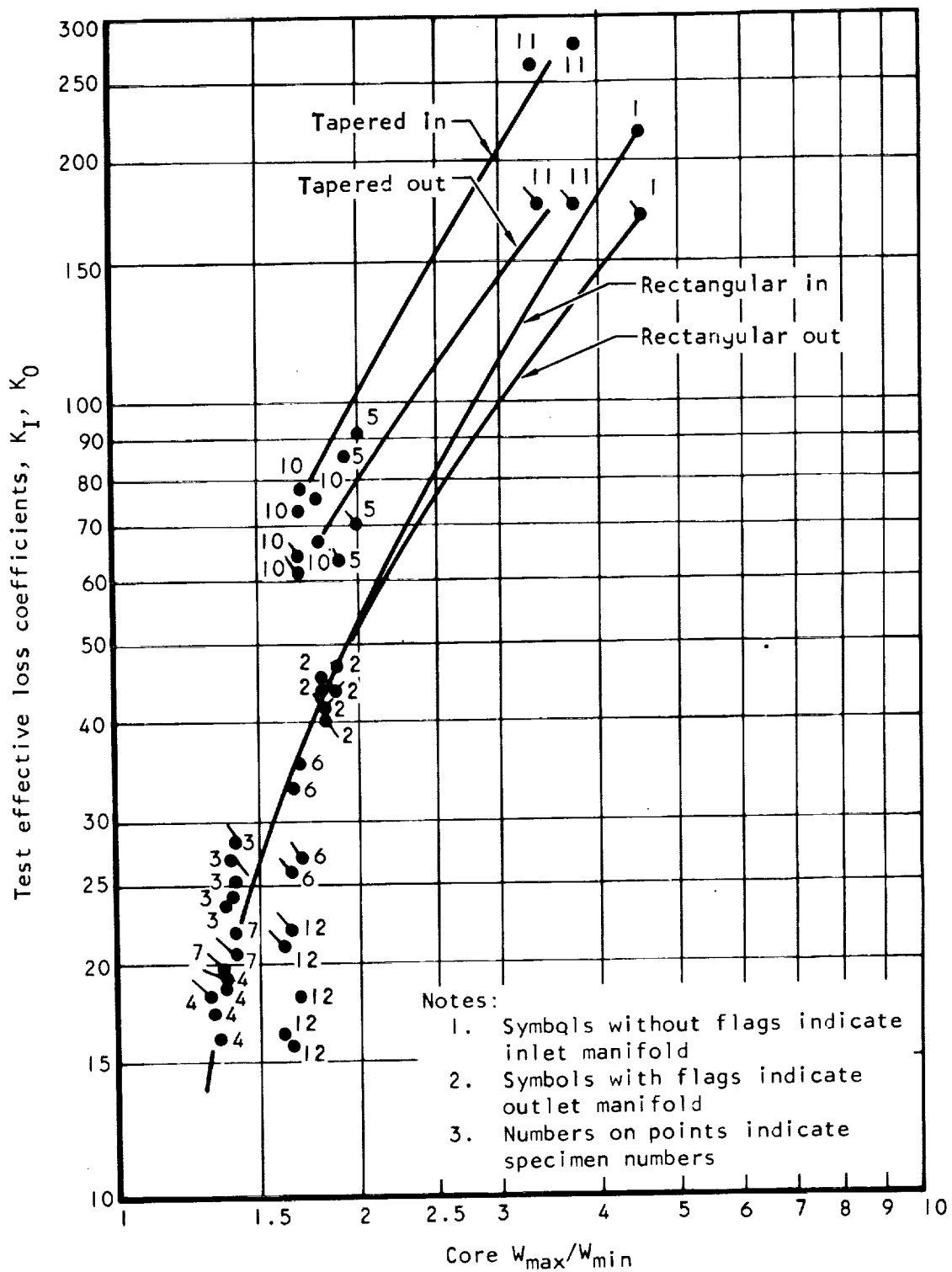
Figure 95. Manifold Pressure Drop Loss Coefficients vs Flow Ratio
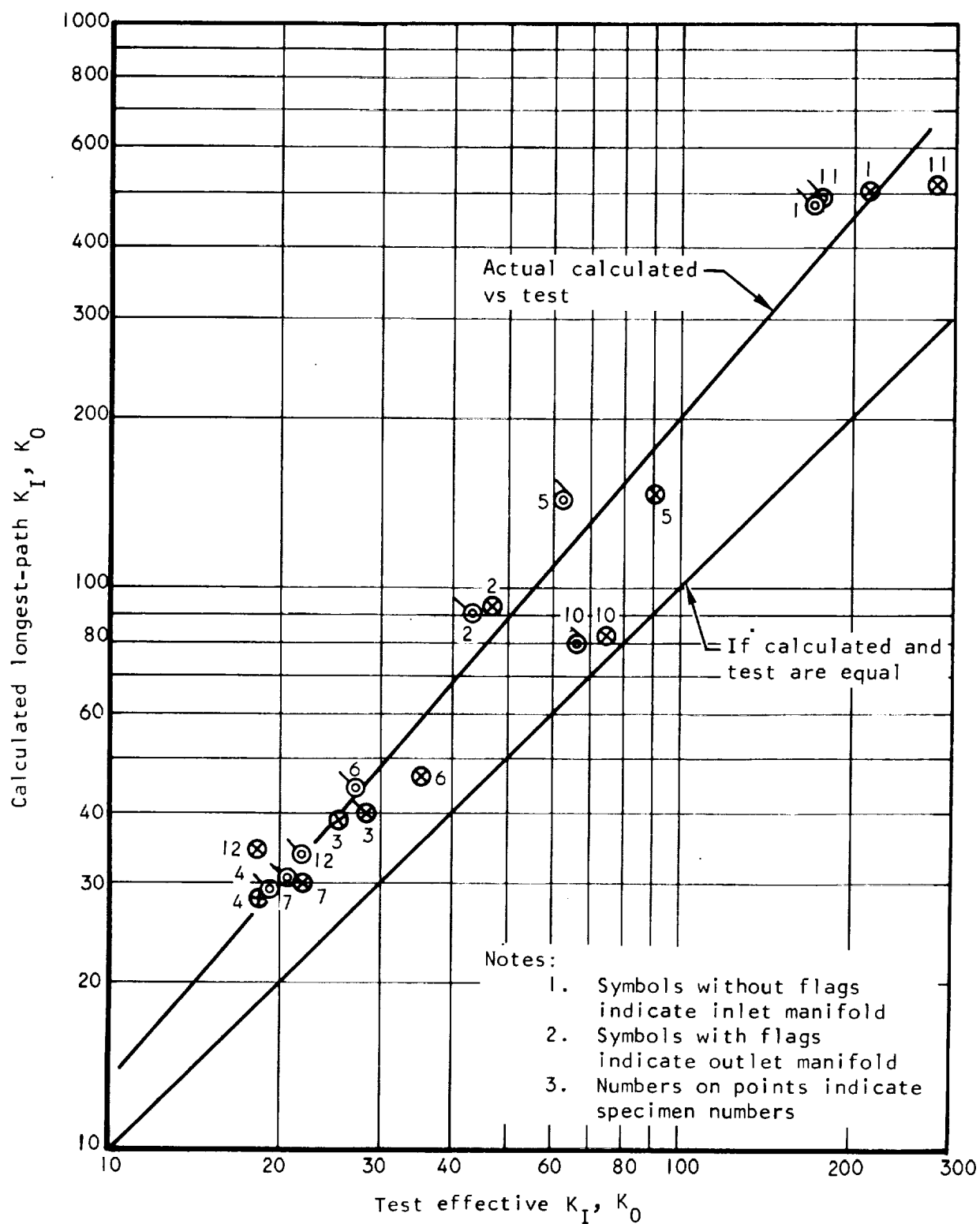
Figure 96.   Calculated Longest-Path K_I, K_0 vs Test Effective K_I, K_0
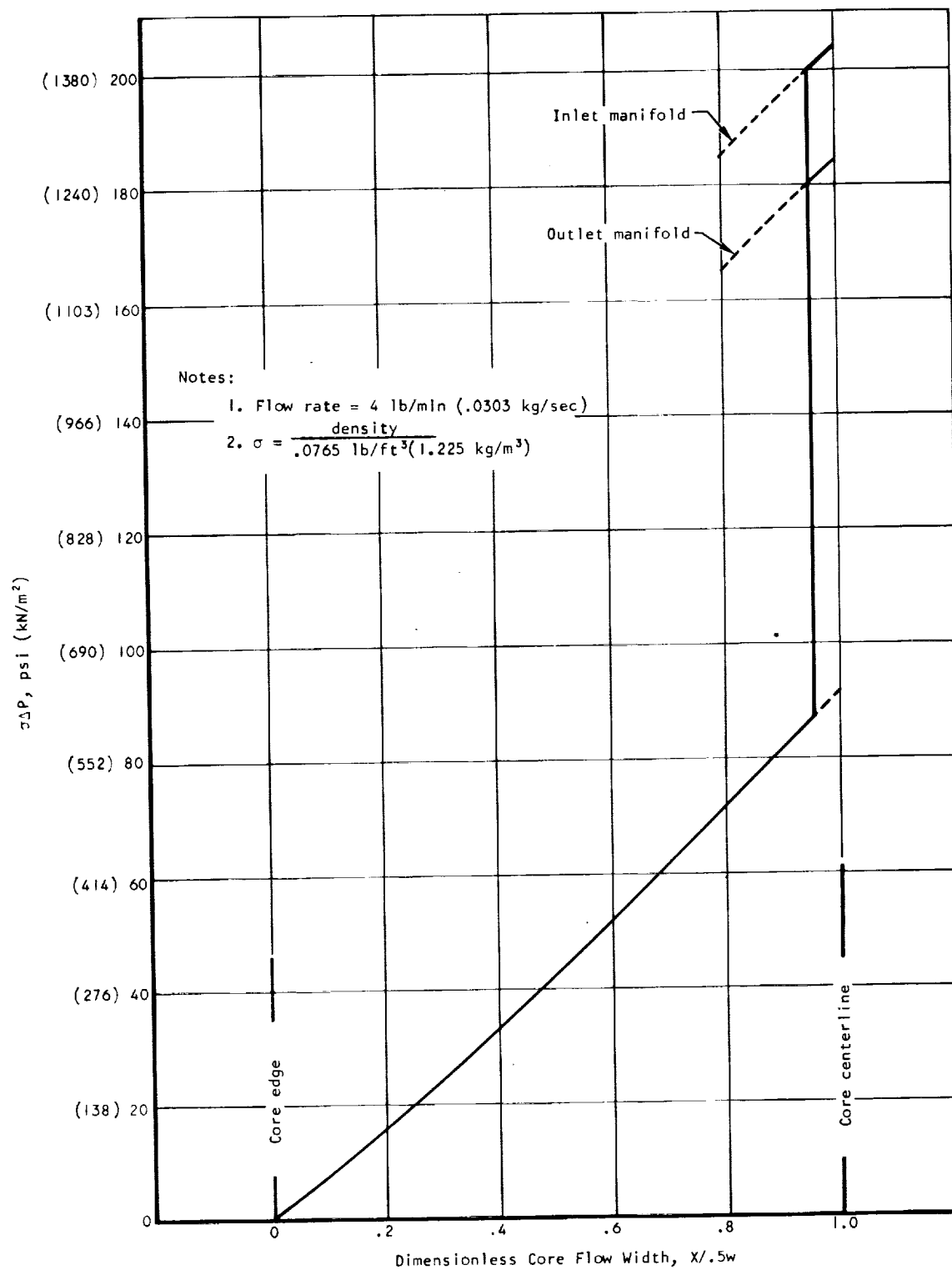
Figure 97.   Insert Pressure Drop for Uniform Flow in Specimen No. 1

Notes:
1. Flow rate = 4 lb/min (.0303 kg/sec)

2. $\sigma = \dfrac{density}{.0765\ lb/ft^3 (1.225\ kg/m^3)}$
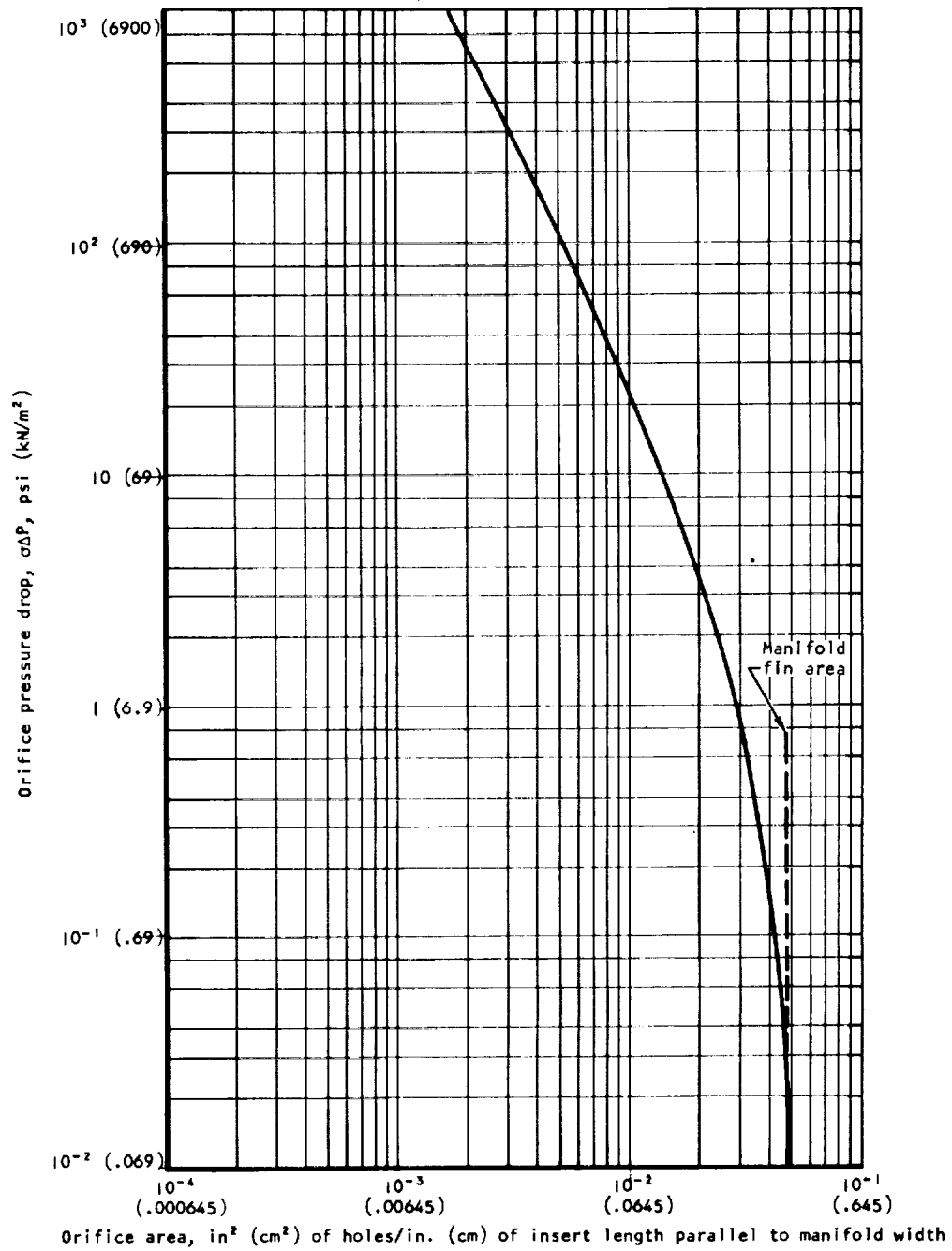
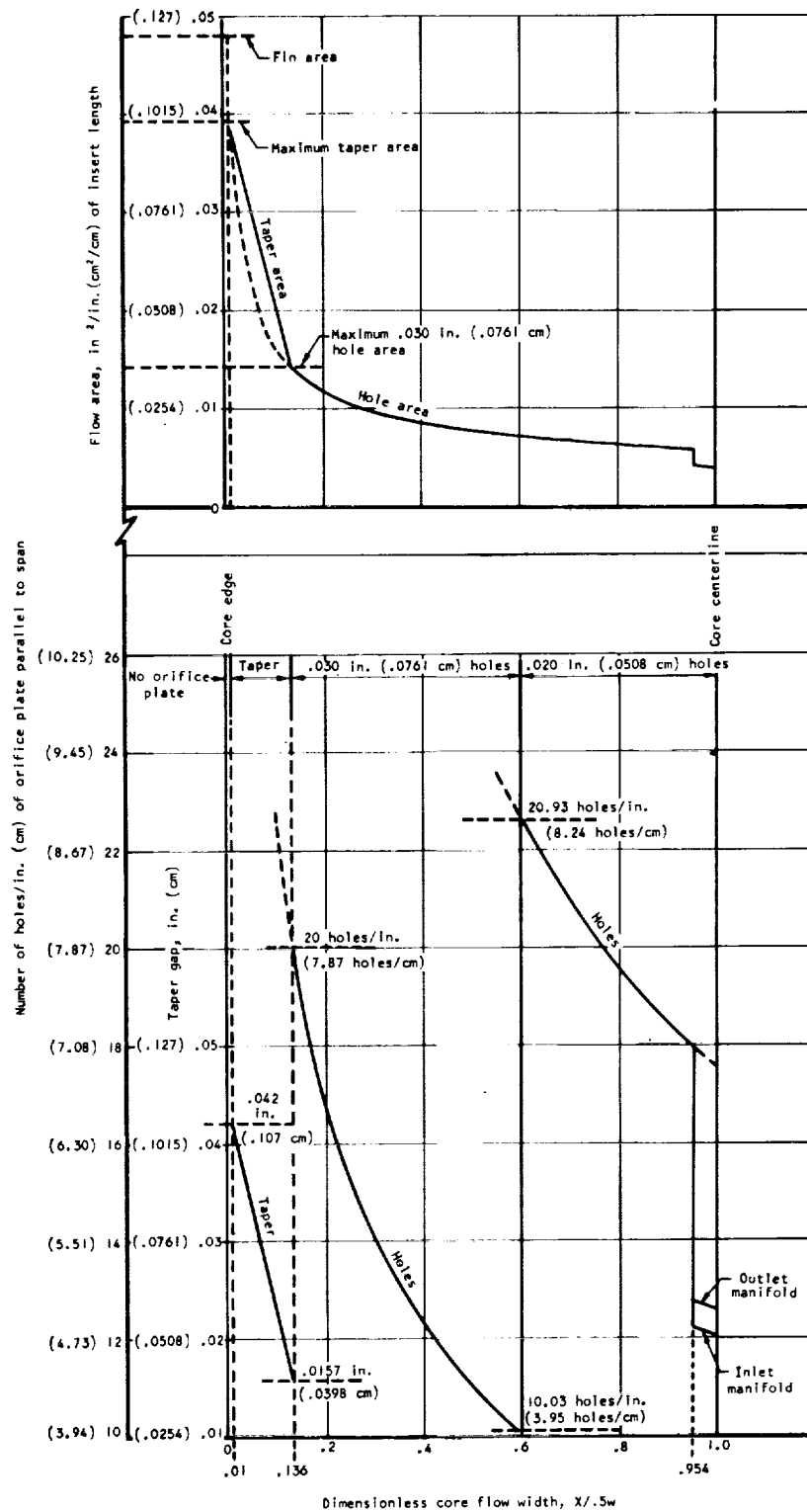3. Loss coefficient, K = .9

Figure 98. Flow Distribution Insert Pressure Drop

Figure 99. Insert Strip Area Distribution